

CCD photometry of variable stellar sources

Data reduction workflow, assessment of accuracy, case studies

Taavi Tuvikene

Promotor: Christiaan Sterken





Vrije Universiteit Brussel

FACULTEIT WETENSCHAPPEN EN
BIO-INGENIEURSWETENSCHAPPEN

CCD photometry of variable stellar sources

Data reduction workflow, assessment
of accuracy, case studies

Proefschrift ingediend met het oog op het behalen
van de graad van Doctor in de Wetenschappen

Taavi Tuvikene

Promotor: Dr. Christiaan Sterken

AUGUST 2012



This study was carried out at Vrije Universiteit Brussel, Belgium.

Jury members: Prof. Dr. Catherine De Clercq (Chair) – *Vrije Universiteit Brussel*
Prof. Dr. Jean-Pierre De Greve – *Vrije Universiteit Brussel*
Prof. Em. Dr. Walter Van Rensbergen – *Vrije Universiteit Brussel*
Prof. Dr. Philippe Cara – *Vrije Universiteit Brussel*
Prof. Dr. László Szabados – *Konkoly Observatory, Hungary*
Dr. Herman Hensberge – *Royal Observatory of Belgium*
Dr. Christiaan Sterken (Promotor) – *Vrije Universiteit Brussel*

Public defence: August 17, 2012
Vrije Universiteit Brussel, Belgium

Acknowledgements:

This work was made possible by the financial support from FWO (Fonds Wetenschappelijk Onderzoek – Vlaanderen); the Flemish Ministry for Foreign Policy, European Affairs, Science, and Technology is acknowledged for research grants in the framework of *Bilateral scientific and technological cooperation* with Chile and South Africa. The author also acknowledges financial support from the Estonian Ministry of Education and Research, the Estonian Research Council (former Estonian Science Foundation), and the EU FP7 project EstSpacE. The South African Astronomical Observatory and Universidad Católica del Norte (Chile) are thanked for allotting observing time.

Cover illustration: panorama of Cerro Armazones, Chile, July 2005

Front cover: Observatorio Cerro Armazones

Back cover: the Cerro Armazones mountaintop that has been selected as the site for the European Extremely Large Telescope

Insets on back cover: the SAAO 1.0-m telescope dome, CCD image of the open cluster NGC 3293, light curve of CY Aquarii

Cover design and images by the author

© Taavi Tuvikene 2012

Published by the Tartu Observatory, Estonia
Printed at TT Print OÜ, Estonia

ISBN 978-9949-30-595-7 (print)
ISBN 978-9949-30-596-4 (PDF)

Preface

In September 2003, a scientific meeting “Stellar Photometry: Past, Present and Future” was held in Vilnius, Lithuania. I had just started on my graduate studies at the University of Tartu, Estonia, and I was affiliated with the Tartu Observatory where I carried out observations with the local telescopes. During the meeting, my senior colleague, the late Izold Pustõlnik, introduced me to Chris Sterken, who was looking for a PhD student to work on the photometry of the southern open cluster NGC 3293. And so it happened that in May 2004 I left Tartu for several years to come, and began my studies at Vrije Universiteit Brussel in Belgium.

I am greatly indebted to my supervisor Chris Sterken, who has taught me a lot on my way to become a scientist. I appreciate the speed with which Chris has given feedback on my writings, and the help that he has provided in solving administrative issues. I really enjoyed discussions over joint lunches with Chris and others in the workgroup: Yacine Bouzid, Jianning Fu, and Alessandro Ederoclite. I kindly remember fellow PhD students Lars Freyhammer and Christina Papadaki, whose experience was very valuable, as they completed their studies before me. I thank Lars for welcoming me and my wife in Mechelen, a beautiful city that eventually became my own hometown during my stay in Belgium.

Part of my PhD work involved carrying out new observations of my research subjects – mostly stars in the southern sky – that called for travelling to observatories in the Southern Hemisphere. I thank Chris for the opportunities to visit the South African Astronomical Observatory on four occasions and Observatorio Cerro Armazones in Chile on two missions. The personnel at both of these observatories is thanked for their hospitality.

My observing run at Cerro Armazones in July 2005 coincided with a stellar occultation by Pluto’s moon Charon. This event brought me in collaboration with Bryce Babcock, Michael Person, and Joseph Gangestad from the MIT–Williams College team. I thank them for the great time that we spent setting up observations with the portable POETS instrument, and for letting me use the instrument to obtain unique light curves of my own targets.

I would like to express my thanks to Chris Koen for discussions on photometry of blended stellar images and for data that allowed me to carry out comparative tests of data reduction. Tõnis Eenmäe is thanked for close and fruitful collaboration that led to two papers and a chapter in this thesis.

The last almost four years that I have been working at the Tartu Observatory have been great thanks to many wonderful colleagues. I am indebted to Anu Reinart and Laurits Leedjärv for making my return to Tartu very smooth and pleasant, and to Anti Hirv for very kindly helping me move from Belgium to Estonia. Many thanks go to my supervisor from my undergraduate studies, Indrek Kolka, who has given me good advice on scientific questions as well as on general matters. I highly value discussions with Elmo Tempel, who has inspired me in my work and given me good advice on technical matters. I expect to continue collaboration with Elmo on studies of galaxies and beyond. I appreciate lively discussions with fellow students and colleagues in the current temporary office: Tiina, Boris, Jaan, Tõnis, Antti, Elmo, Juhani, Tiit, Rain, Teet, Kristiina, and Jasper.

Finally, I am deeply grateful to my loving wife, Anu, who has been patient and supportive during my PhD studies, and who has spent lots of time with our three sons, Arlo Leon, Eero Sven, and Tim Ilmar, while I was busy with finishing my manuscript.

Taavi Tuvikene

Tartu, July 2012

Contents

Preface	v
List of acronyms	xi
Foreword	1
I CCD photometry workflow	3
1 Workflow concept, design, and implementation	5
1.1 Workflow concept	5
1.2 Principles of CCD data reduction	6
1.2.1 Bias level	6
1.2.2 Dark current	7
1.2.3 Flat field	7
1.2.4 Calibration of science frames	8
1.2.5 Magnitude extraction	8
1.3 Workflow design	9
1.4 Workflow implementation	12
2 Comparative tests of data reduction procedures	15
2.1 Rationale	15
2.2 Time of observation	15
2.3 Magnitude extraction	17
2.3.1 PHOTWORK, IRAF/DAOPHOT, and MOMF	17
2.3.2 PHOTWORK and DoPHOT	19
2.4 Discussion	20
II Case studies	25
3 Observations of a stellar occultation by Charon	27
3.1 Stellar occultations	27
3.2 Observations	28
3.3 Light curves and occultation times	30

3.4	Charon's radius and density	31
3.5	Related work	32
4	GSC 08613–02122, a new δ Scuti star in Carina	33
4.1	Introduction	33
4.2	Observations and data reduction	34
4.2.1	CCD photometry	34
4.2.2	Photoelectric photometry	36
4.3	Results	37
4.3.1	Average magnitudes and colour indices	37
4.3.2	Light and colour curves	37
4.3.3	Frequencies	37
4.3.4	Amplitude variations	41
4.3.5	Period and phase variations	42
4.4	Discussion	43
4.4.1	Location of GSC 08613–02122 in the spectral-classification dia- gram	43
4.4.2	Nature of the erratic variations	44
4.5	Conclusions	45
5	GSC 04778–00152, a contact binary with a visual companion	47
5.1	Introduction	47
5.2	Observations and data reduction	48
5.2.1	CCD photometry	48
5.2.2	Photoelectric photometry	50
5.2.3	Spectroscopy	51
5.3	Results	53
5.3.1	CCD astrometry	53
5.3.2	Primary and secondary minima	54
5.3.3	Phase diagrams	54
5.3.4	Peculiarities	55
5.4	Analysis	55
5.4.1	Spectral type	55
5.4.2	Stellar parameters	58
5.4.3	Light-curve solution	58
5.5	Conclusions	59
6	On the light variability of CY Aquarii	61
6.1	Introduction	62
6.2	Observations and data reduction	63
6.2.1	USNO	64
6.2.2	TASS	64
6.2.3	Skinakas Observatory	64
6.2.4	Observatorium Hoher List	64
6.2.5	Mount Laguna Observatory	64
6.2.6	Crimean Laboratory of the Sternberg Astronomical Institute .	65

6.2.7	Observatorio Cerro Armazones	65
6.2.8	MDM Observatory	67
6.2.9	South African Astronomical Observatory	67
6.2.10	Realgymnasium Bruneck	67
6.2.11	Strömgren Automatic Telescope	69
6.2.12	Miscellaneous sources	71
6.3	Times of maximum, new ephemeris and $O - C$ diagram	71
6.3.1	Times of maximum light	71
6.3.2	Ephemeris and resulting $O - C$ diagrams	73
6.3.3	Additional times of maximum from the literature	75
6.4	Conclusions	76
7	Photometric monitoring of the open cluster NGC 3293	81
7.1	Stellar identifications	81
7.2	Telescopes and instruments	85
7.3	Contribution to a multi-site campaign	87
7.4	Observing strategy	87
7.5	Observing logs and statistics	88
7.6	Atmospheric extinction, seeing	91
7.7	Selection of comparison stars	99
7.8	Quantification of variability	106
7.9	Ensemble photometry	109
7.10	Long-term variability in NGC 3293	112
7.10.1	Bright stars BVC 4, 5, 6, 7, 10	116
7.10.2	Be stars	121
7.10.3	β Cep stars	129
7.10.4	SPB-star candidates	133
7.10.5	Other stars	135
7.11	Conclusions	138
Summary		141
Samenvatting		145
Appendices		147
A Other publications		149
B PHOTWORK user guide		153
B.1	Introduction	153
B.1.1	Installation	153
B.1.2	Getting started	153
B.2	The main menu	155
B.3	Creating master files	156
B.3.1	Overscan correction	156

B.3.2	Creating a master bias	156
B.3.3	Creating a master dark	157
B.3.4	Creating a master flat	158
B.4	Calibration of object frames	159
B.5	Processing of frame headers	160
B.6	Aperture photometry	162
B.7	Identification of stars	164
B.7.1	Graphical user interface	164
B.7.2	Creating a reference field	166
B.7.3	Manual identification	167
B.7.4	Automatic identification	168
B.7.5	Tracking	169
B.7.6	Batch-identification	170
B.8	Annotating data	171
B.9	Constructing light curves	172
B.10	Configuration files	175
B.11	Database structure	182
B.12	Acknowledgements	185

List of acronyms

ADU	analog-to-digital unit
ASAS	All Sky Automated Survey
ASCII	American Standard Code for Information Interchange
CCD	charge-coupled device
CD	Cordoba Durchmusterung (catalogue)
CPD	Cape Photographic Durchmusterung (catalogue)
DFOSC	Danish Faint Object Spectrograph and Camera
EB	eclipsing binary
ESO	European Southern Observatory
FITS	Flexible Image Transport System (file format)
FOV	field of view
FWHM	full width at half maximum
GCVS	General Catalogue of Variable Stars
GSC	Guide Star Catalog
HC	heliocentric correction
HD	Henry Draper (catalogue)
HJD	heliocentric Julian date
IDL	Interactive Data Language
IRAS	Infrared Astronomical Satellite
JD	Julian date
LJD	local Julian day number
MDM	Michigan-Dartmouth-MIT (observatory)
MJD	modified Julian date
MOMF	Multi-Object Multi-Frame (software)
NSV	New Catalogue of Suspected Variable Stars
OCA	Observatorio Cerro Armazones
POETS	Portable Occultation, Eclipse, and Transit System (camera)
PSF	point-spread function
RA	right ascension
SAAO	South African Astronomical Observatory
SAT	Strömgren Automatic Telescope
SNR	signal-to-noise ratio
UT	Universal Time
WCS	world coordinate system

Foreword

Photometric studies of variable stars nowadays involve observations with CCD cameras. CCD cameras have many useful properties, such as a nearly linear response to the incident light, high quantum efficiency, and the ability to record many stellar images in a single exposure. At the same time, handling of CCD data needs care, if high accuracy and precision of results are required. Also, one has to deal with large amounts of data, especially if there are hundreds of stars in the field of view and observations are carried out over long time spans.

Working with large amounts of CCD frames necessitates a highly automated data reduction approach. As data often originate from a variety of telescopes and instruments, the same reduction steps cannot always be applied to all data. Thus, what is needed is not a fully automated pipeline, but rather a workflow, an organised and consistent set of reduction procedures. A workflow for reducing heterogeneous CCD data was developed in the framework of this thesis.

The main goal for this study was to collect new, but also archival, photometric data on a number of objects, all of which have some observational parameters at their extreme limits (e.g. very small or large amplitude, very fast rise time or steep eclipses, or a close visual companion) and, as such, pose a challenge either in observing, data reduction, or analysis. The developed workflow was applied to the data reduction of most of these objects.

The motivation for our systematic and thorough approach is driven by our desire to disentangle the minute physical variations in light and colour from effects of instrumental origin, data reduction, calibration, and standardisation. Such an approach is of great importance, because the breakthroughs in contemporary front-line astrophysical research rely not only on very large telescopes, but even more on the aforementioned aspects of observational and data-reduction procedures. This is especially true for studies that deal with objects at cosmological distances or with phenomena that are caused by exotic physical processes. Never in the past has the science of calibration had such prominent impact on the conclusions as it has today.

Part I of this thesis describes our workflow concept, design, and implementation in data reduction. An important aspect is the assessment of accuracy, which is dealt with in Chapter 2, by carrying out comparative tests of different data reduction procedures. The discussion in Part I is accompanied by Appendix B that provides a user guide

to the developed workflow tool, PHOTWORK, describing its modular setup, usage, and database structure.

Part II is devoted to case studies of variable stellar sources. Chapter 3 deals with the determination of the radius of Pluto’s moon Charon by observing a stellar occultation. The combined light from a background star, Pluto, and Charon varies due to Charon passing in front of the star. Recording such an event requires fast photometry together with accurate timing of CCD exposures. The same observing technique was also applied to the pulsating star CY Aquarii, producing a unique high-resolution light curve over nearly two periods (see Chapter 6).

Chapter 4 focuses on a newly-discovered δ Scuti star GSC 08613–02122. The star lies in the vicinity of the open cluster NGC 3293, and was found to be variable during the photometric monitoring of the cluster. Such a star may be considered a classical case, but our results reveal the presence of erratic amplitude and phase variations, which we show not to be of instrumental nor procedural origin.

A deep study of the close binary star GSC 04778–00152 is presented in Chapter 5, including spectroscopic and astrometric observations. The star was found to have a 1-magnitude fainter visual companion about 2 arcsec away from the binary, complicating data reduction, as the companion was not resolved in most of CCD images. The parameters of the binary system were derived from light-curve modelling.

Chapter 6 deals with the light variability of the SX Phoenicis star CY Aquarii. The star has a short period (87.9 min) and a large amplitude (0^m71 in V), with a very steep rise to maximum light. In this Chapter, data from the 2010 and 2011 seasons are combined with a large set of observations, previously obtained at 10 observatories worldwide over an entire decade. The resulting times of maximum are presented in an $O - C$ diagram, together with timings spanning more than 75 years, which reveal a long-term period change of CY Aquarii. The final set of data from the 2011 season illustrates how a careful and consistent approach in observing as well as in data reduction yields $O - C$ residuals that are very small as compared to any other substantial dataset from the last decade.

Finally, in Chapter 7 the workflow is applied to a target for which it was initially designed – the open cluster NGC 3293, known to contain 11 β Cephei-type pulsators and numerous other variable stars. The cluster was photometrically monitored for a time span of ten years (1997–2007), resulting in a massive set of over 22 000 CCD frames. Careful reduction and analysis led to the conclusion that truly constant stars among brighter cluster members are rather rare. Special focus is given to the long-term variability of the cluster stars.

In Appendix A, we present abstracts of seven papers that deal with a wide range of subjects, from a cataclysmic star to the Andromeda galaxy. All these studies involve CCD photometry, but with different requirements on observations and subsequent data reduction.

Part I

CCD photometry workflow

Chapter 1

Workflow concept, design, and implementation

1.1 Workflow concept

Workflow, in general, is used as a term for a systematic pattern of activity. Workflow management techniques have mainly been developed for business processes, but many successful approaches have also been implemented in scientific applications, especially in bioinformatics and cheminformatics.¹ In this work we apply the workflow concept to CCD photometry in variable-star research.

Following van der Aalst & van Hee (2002, Chap. 1), we use the workflow terms *case*, *process*, and *task*.

- A task is a unit of work that is carried out by a single resource, i.e. a person, machine, or a group of persons or machines. A task may also be called a step. Examples of tasks in CCD photometry include bias subtraction, creation of a master flat frame, and extraction of stellar magnitudes from a CCD frame.
- A process consists of a number of linked tasks and a set of conditions that determine the order of the tasks.
- A case is something that is produced or modified, or it may be something more abstract, like reduction of a batch of CCD frames in order to construct a light curve. Determining standard magnitudes of stars in an open cluster is another example of a case. Each case is discrete in nature, thus having a beginning and an end, and involves carrying out a process.

Tasks are linked together in a process with four basic mechanisms: *sequence*, *selection*, *parallelisation*, and *iteration*. Two or more tasks that have to be carried out in strict succession, are called a sequence, e.g. creation of a master bias and subtraction of the master bias from science frames. Sometimes there are tasks that do not need

¹Bioinformatics and cheminformatics are scientific disciplines in which computer science and information technology are applied to the fields of biology and chemistry.

to be carried out, or a choice between two or more tasks is made. This is called a selection. An example is omitting subtraction of a dark frame if dark current is very low. Parallelisation involves performing two or more tasks in parallel; these tasks must all complete before the following task can begin. Iteration means repetition of one or more tasks.

Using CCD photometry workflow is not new, as everyone who systematically reduces CCD data in order to carry out stellar photometry has his or her own workflow. Sky surveys, like the Sloan Digital Sky Survey (SDSS) and the All Sky Automated Survey (ASAS), have their own data reduction workflows in order to cope with large amounts of data. However, the workflow concept may also be useful in smaller-scale studies to improve efficiency and to get consistent results.

Large data volumes are often handled by using *pipelines*. A pipeline is a contiguous set of tasks in which the output of one task is used as an input for the next task. Automated data reduction pipelines are especially useful if the same reduction tasks need to be repeated with lots of data, e.g. in sky surveys that are carried out with a fixed set of instruments and in space missions that require on-board data reduction.

In the following Section we describe the principles of CCD data reduction. A workflow design for variable-star research is proposed in Section 1.3. The workflow design is implemented in a software package that we introduce in Section 1.4 and apply to most of the case studies presented in Part II.

1.2 Principles of CCD data reduction

CCD photometry involves several data reduction steps that need to be carried out, in order to retrieve useful information from raw CCD frames. Here we discuss the reduction steps and review different methods.

1.2.1 Bias level

CCD cameras are designed in such a way that even without any detected photons, all pixels have positive values at read-out. The bias level, introduced by the CCD electronics, can be measured from a *bias frame*, a zero-length exposure with the camera shutter closed. Professional CCD cameras usually allow for additional readings of the read-out register beyond the actual number of columns in the CCD matrix. These additional readings form an *overscan strip* on one or on both sides of CCD frames, providing information about the bias level in each frame. The bias level can then be corrected by subtracting the mean overscan value from the entire frame or by subtracting the overscan value on a row-by-row basis.

Quite often the bias level is not uniform across the CCD, exhibiting a low-level fixed pattern, a *bias structure*, that can be corrected with a bias frame. The bias structure, $B_0(x, y)$, is obtained by subtracting the mean overscan value, B_s , from the raw bias frame, $B(x, y)$:

$$B_0(x, y) = B(x, y) - B_s, \quad (1.1)$$

where (x, y) refers to frame coordinates (columns and rows).

In order to suppress read-out noise, it is useful to median-average multiple bias frames into a *master bias*, denoted by $B_m(x, y)$. In this process, each pixel of the master bias is assigned the median of the values taken from the same pixel of individual bias frames.

1.2.2 Dark current

A *dark frame* contains thermal electrons that accumulate in CCD pixels during an exposure. The rate at which they accumulate strongly depends on the CCD temperature, and the resulting dark current is proportional to the integration time. Dark frames are obtained by taking exposures with the shutter closed and with the CCD operating at the same temperature as when taking science frames.

In order to eliminate cosmic rays and in order to suppress the read-out noise, the individual dark frames may be median-averaged into a *master dark*. The mean overscan value, D_s , and the master bias may be subtracted from dark frames before combining them:

$$D_0(x, y) = D(x, y) - D_s - B_m(x, y) \quad (1.2)$$

In this way the master dark, $D_m(x, y)$, can be scaled to the integration time of science frames.

Dark frames that have the same integration time as science frames, can be used for simultaneously subtracting the bias level and the dark current from the frames.

1.2.3 Flat field

Flat fielding is a calibration step that corrects for pixel-to-pixel variations of the CCD and for non-uniform illumination of the detector. The variations in pixel response depend on wavelength, and result from small structural irregularities of the CCD. The uneven illumination is caused by telescope optics and by obstacles in the light path, like dust on the filters and on the CCD window.

Obtaining *flat field frames* means pointing the telescope to a uniform light source and taking exposures. There are generally two approaches:

1. *dome flats* – the telescope is pointed towards a reflective screen inside the dome, while the screen is illuminated with a lamp;
2. *sky flats* – twilight or night sky is used as a flat-field source; the exposures of the twilight sky are taken shortly after sunset and/or before sunrise; if the night sky is used then multiple exposures with spatial offsets are required in order to eliminate star images.

However, in practice it is very difficult to achieve a uniform light source that has the same wavelength distribution over the filter passband as that of the objects in science frames. Projector lamps and twilight skies do not have the same spectral energy distribution as the observed stars. To overcome this problem, Stubbs & Tonry (2006) have devised and demonstrated a flat-fielding technique, where a screen is illuminated by monochromatic light from a tunable laser, and the light level is monitored at

the entrance pupil of the telescope by a calibrated photodiode. A series of flat-field exposures is then recorded at discrete wavelengths over the passband of the instrument. Brown et al. (2007) extend the same idea by developing a self-luminous calibration screen that can cover the entrance of the telescope. The radiating element is a “side-emitting” optical fiber excited by a pulsed tunable laser. They expect to reach a calibration precision at 1% level.

Flat fields often exhibit illumination gradients that do not characterise the instrumental response of the telescope optics and detector. These gradients are caused by the unevenness of the light source or by scattered light reaching the focal plane. Using such flat-field frames in the data reduction process, may yield position-dependent systematic errors in the resulting photometry. Several authors (Manfroid 1995; Laggalys et al. 2004; Freudling et al. 2007; Boyle & Janusz 2007) have discussed flat-field corrections on the basis of standard-star observations or shifted-field photometry.

Flat field frames should be processed first by subtracting the mean overscan value, F_s , master bias, and master dark (scaled with the integration time):

$$F_0(x, y) = F(x, y) - F_s - B_m(x, y) - \frac{t_f}{t_d} D_m(x, y), \quad (1.3)$$

where $F(x, y)$ is the raw flat frame, t_f and t_d are the integration times of the flat frame and the master dark, respectively. The processed flats, $F_0(x, y)$, are scaled to unity and the *master flat*, $F_m(x, y)$, is derived through median-averaging of the individual frames, a procedure that eliminates stellar images and cosmic rays.

1.2.4 Calibration of science frames

Once all the necessary calibration frames have been obtained and properly processed, then science frames can be calibrated with the following scheme:

$$S_0(x, y) = \frac{S(x, y) - S_s - B_m(x, y) - \frac{t_s}{t_d} D_m(x, y)}{F_m(x, y)}, \quad (1.4)$$

where $S_0(x, y)$ is the calibrated frame, $S(x, y)$ denotes the raw science frame, S_s is the mean overscan value, t_s and t_d are the integration times of the science and dark frames, and $B_m(x, y)$, $D_m(x, y)$, $F_m(x, y)$ are the master bias, the master dark and the master flat, respectively.

1.2.5 Magnitude extraction

In this data reduction step, calibrated frames are analysed in order to locate stars and determine their instrumental magnitudes. Basically the following three tasks are involved:

1. determination of the centroids of stellar images (*image centring*);
2. estimation of the sky-background level;
3. calculation of the flux contained within the stellar images.

Stone (1989) compares five one-dimensional centring algorithms: the Gaussian fit, moment, modified moment, median, and derivative search. He finds that the Gaussian fit and the median algorithms work well, while the moment and the derivative-search methods are inferior. A modification of the moment analysis that suppresses the sky background is found to be the best method when the sky-background level is significant.

To estimate the sky-background level under a stellar image, a common technique is to analyse pixel values in an annulus around the source. For a good statistical determination of the background level, the size of the annulus has to be sufficiently large, containing at least three times more pixels than the source aperture (Merline & Howell 1995). However, in real cases the optimal size of the background annulus may be affected by the crowding of the stellar field, or by the non-uniformity of the background.

For measuring the signal within stellar profiles, three approaches can be used: aperture photometry, point-spread function (PSF) fitting, and the combined PSF–aperture photometry:

1. Aperture photometry means straightforward counting of analog-to-digital units (ADUs) in apertures centred on stellar images. Circular apertures are the most common, but other shapes may also be used, e.g. rectangular apertures (Chapter 3). This method is justified when the field is not crowded and stars are well exposed.
2. PSF photometry works by obtaining a model PSF from one or several (isolated) stars, fitting the model profile to each star on the frame, and integrating the function over the areas of the stellar images. Analytical, semi-empirical, and empirical PSFs can be used. PSF photometry is best suited for crowded fields where the stellar images overlap, and for faint stars that are poorly exposed. Aperture and PSF photometry are both implemented in the widely-used computer program DAOPHOT (Stetson 1987).
3. The third approach combines aperture and PSF photometry, applying aperture photometry on the residuals after PSF fitting. This is applicable in semi-crowded fields and is implemented in the software package MOMF (Kjeldsen & Frandsen 1992).

The instrumental magnitude of a star is given by:

$$m = -2.5 \log_{10} (I_{\text{total}} - n_{\text{pix}} B_{\text{sky}}) + C, \quad (1.5)$$

where I_{total} is the sum of pixel values within a given aperture, n_{pix} is the number of pixels in the aperture, B_{sky} is the mean sky-background value, and C is a constant.

1.3 Workflow design

By using data reduction steps as building blocks, it is possible to create custom workflows for different cases. In this Section we propose a workflow for the reduction of CCD frames with the aim of producing differential light curves. The proposed

workflow is suitable for variable-star research where data may originate from a variety of telescopes and instruments.

The workflow consists of the following tasks:

1. evaluation of bias frames and identifying data batches for which a single master bias can be constructed;
2. creating master biases;
3. evaluation of dark current and the need for dark-frame subtraction; identifying data batches for which a single master dark can be constructed;
4. creating master darks for each combination of integration time and CCD temperature;
5. evaluation of flat frames and identifying data batches for which a single master flat can be constructed;
6. creating master flats for each passband and data batch, identified in task 5;
7. calibrating science frames (Eq. 1.4);
8. creating an empty database for storing photometric data as well as information (metadata) about science frames;
9. parsing the headers of science frames and storing the metadata in the database; calculating the Julian date and the heliocentric correction based on the time of observation in the frame header;
10. extracting magnitudes from all science frames (a sub-workflow):
 - (a) determining the sky background in a frame;
 - (b) locating stellar sources in the frame and determining centroids of the sources;
 - (c) determining the full width at half maximum (FWHM) of stellar images in the frame;
 - (d) carrying out aperture photometry in the frame for all sources found in task 10b, using a number of different aperture radii scaled with the FWHM value;
 - (e) storing instrumental magnitudes in the database;
11. building a list of stars in the observed field and establishing reference coordinates for these stars;
12. manually identifying one or more stars in a frame;
13. establishing coordinate transformation between the current frame and reference field (as set up in task 11); automatically identifying all stars in the frame, based on the reference field and the coordinate transformation;
14. automatically identifying all stars in the rest of the frames, based on the reference coordinates and the coordinate transformation of the first frame in the sequence, assuming that the telescope pointing does not change significantly between two exposures; if automatic identification fails, then returning to task 12;

15. evaluating the quality of data by inspecting the instrumental magnitude versus air mass plots (Bouguer plots) and individual CCD frames;
16. assigning flags to data, based on the result of data evaluation (task 15) and using the scheme in Table 1.1; storing flags in the database;
17. choosing one or more comparison stars;
18. choosing the aperture that gives the highest signal-to-noise ratio for the specific program star, comparison stars, and passband;
19. constructing a differential light curve in one passband by subtracting the comparison-star magnitudes from the program-star magnitudes;
20. checking the light curve for seeing effects by inspecting the differential magnitude versus seeing plot; if magnitude is correlated with seeing then establishing the maximum seeing limit and repeating task 19 with the seeing limit;
21. repeating tasks 19–20 for other passbands;
22. outputting the constructed light curves.

Magnitude extraction in this workflow is carried out on a frame-by-frame basis, thus no assumption is made on the field rotation, pixel scale, or pointing offsets at this stage. Only for the automatic identification of stars (task 14), it is assumed that the field rotation and pointing offsets in a frame sequence are small.

The identification scheme based on a reference field may be modified to make use of the world coordinate system (WCS) representation in FITS files (Greisen & Calabretta 2002). The WCS allows for determination of physical (celestial) coordinates, e.g. right ascension (RA) and declination (DEC), for each pixel in a frame. Therefore, if the CCD frame (in FITS format) has the required WCS keywords, assigned either before or after calibration, then the stellar centroids can be transformed into RA and

Table 1.1: Scheme for assigning flags to data, based on atmospheric extinction and other criteria.

Flag	Description	Atm. extinction	Other criteria
-1	bad (rejected) data	> 1 mag (clouds)	cosmic ray hit in aperture satellite trail in aperture severely out-of-focus images severe instrumental problems
0	no flags assigned	—	—
1	very-low-quality data	< 1 mag (clouds)	very high sky background very poor focus significant tracking error
2	low-quality data	variable	high sky background tracking error telescope pointing offset
3	normal data	variable / unknown	—
4	good data	small variations	—
5	excellent data	constant	—

DEC, and star identifications (names) can be assigned on the basis of the celestial coordinates.

The workflow presented above can also be modified for PSF photometry by substituting the magnitude extraction sub-workflow (task 10) with relevant tasks, e.g. choosing isolated stars, constructing the PSF based on the chosen stars, fitting the PSF to all stellar images, and determining instrumental magnitudes.

1.4 Workflow implementation

We have implemented the above-described workflow by developing a software package, named PHOTWORK, and using the software for data reduction in a number of case studies. The programs in the package are written in the Interactive Data Language (IDL) and rely on astronomy-specific routines available in the IDL Astronomy User's Library² (Landsman 1995). Detailed description and instructions on the usage of PHOTWORK are provided in the user guide (Appendix B).

²<http://idlastro.gsfc.nasa.gov/>

Table 1.2: Usage of PHOTWORK in case studies: application of frame calibration steps, the number of reduced frames, and the number of measured star images (thousands of magnitudes) in data batches. Frames that have been calibrated with other software than PHOTWORK, are marked with 'n/a'.

Case study (Chapter)	Data batch	Frame calibration				Frames	Mags. (10 ³)
		Overscan	Bias	Dark	Flat		
GSC 08613-02122 (4)	SAAO	+	+	-	+	1489	364
GSC 04778-00152 (5)	OCA 2006	-	+	-	+	776	24
	MDM	+	+	-	+	141	10
	Tartu	+	-	+	+	271	9
	SAAO 2007	+	+	-	+	899	34
CY Aqr (6)	SAI	-	-	+	-	1259	7
	OCA 2005	-	-	+	+	2093	44
	OCA POETS	-	-	-	-	18000	312
	MDM 2005	+	-	-	+	124	3
	SAAO 2005	+	+	-	+	381	4
	RGB 2008	-	-	+	-	5926	116
	RGB 2010	-	-	+	-	2561	71
	RGB 2011	-	-	+	+	3494	94
	NGC 3293 (7)	n/a	n/a	n/a	n/a	7618	1120
	SAAO 2001	n/a	n/a	n/a	n/a	1589	379
	Danish	n/a	n/a	n/a	n/a	2292	650
	SAAO 2005	+	+	-	+	785	202
	OCA 2006	-	+	-	+	2975	2033
	SAAO 2006	+	+	-	+	2491	573
	SAAO 2007	+	+	-	+	3676	750

The emphasis in the development of PHOTWORK has been put on efficient data handling. The extracted magnitudes are stored in a database together with various information about observations, e.g. date and time of observation, heliocentric Julian date, integration time, air mass, seeing, etc., which allows for efficient selecting of data based on various criteria. As PHOTWORK programs are open-source, it is possible to modify the programs or build upon them by writing custom scripts that execute specific programs from the package.

The usage of PHOTWORK in case studies is summarised in Table 1.2. Data batches in this work vary in size from about 100 to 18 000 science frames, with typical sizes of a few thousand frames. We have calibrated the majority of CCD frames with PHOTWORK, with the exception of early data of NGC 3293 (the Dutch-telescope, the SAAO 2001, and the Danish-telescope data batches), which were calibrated by individual observers. PHOTWORK was used for determining stellar magnitudes with aperture photometry, flagging the data, and construction of light curves in all listed cases. The number of star images in frames that were detected and measured, varied from a few to several hundred, typically producing a few hundred thousand measurements per data batch, where each measurement consisted of 12 magnitudes, one for each aperture radius. The largest database resulted in the study of NGC 3293, with a total of 5.7 million measured star images.

In the next Chapter, differential light curves, obtained with PHOTWORK, are compared to the results of other data reduction software, viz. IRAF/DAOPHOT, MOMF, and DOPHOT.

References

- Boyle, R. P. & Janusz, R. 2007, in Astronomical Society of the Pacific Conference Series, Vol. 364, *The Future of Photometric, Spectrophotometric and Polarimetric Standardization*, ed. C. Sterken, p. 563
- Brown, Y. J., Stubbs, C. W., Henry, E. T., & Bailes Brown, L. 2007, in Astronomical Society of the Pacific Conference Series, Vol. 364, *The Future of Photometric, Spectrophotometric and Polarimetric Standardization*, ed. C. Sterken, p. 571
- Freudling, W., Romaniello, M., Patat, F., et al. 2007, in Astronomical Society of the Pacific Conference Series, Vol. 364, *The Future of Photometric, Spectrophotometric and Polarimetric Standardization*, ed. C. Sterken, p. 113
- Greisen, E. W. & Calabretta, M. R. 2002, A&A, 395, 1061
- Kjeldsen, H. & Frandsen, S. 1992, PASP, 104, 413
- Landsman, W. B. 1995, in Astronomical Society of the Pacific Conference Series, Vol. 77, *Astronomical Data Analysis Software and Systems IV*, ed. R. A. Shaw, H. E. Payne, & J. J. E. Hayes, p. 437
- Laugalys, V., Kazlauskas, A., Boyle, R. P., et al. 2004, Baltic Astronomy, 13, 1
- Manfroid, J. 1995, A&AS, 113, 587

- Merline, W. J. & Howell, S. B. 1995, Experimental Astronomy, 6, 163
- Stetson, P. B. 1987, PASP, 99, 191
- Stone, R. C. 1989, AJ, 97, 1227
- Stubbs, C. W. & Tonry, J. L. 2006, ApJ, 646, 1436
- van der Aalst, W. & van Hee, K. 2002, Workflow Management: Models, Methods, and Systems (MIT Press)

Chapter 2

Comparative tests of data reduction procedures

This Chapter is based on

A Comparative Test of CCD Reduction Procedures

T. Tuvikene, M. Y. Bouzid, A. Ederoclite, and C. Sterken,
2007, in ASP Conference Series, Vol. 364, *The Future of Photometric,
Spectrophotometric and Polarimetric Standardization*, ed. C. Sterken, p. 579

2.1 Rationale

At first glance, reducing CCD images is a straightforward and technical process, yet there is no standard way to follow. Numerous approaches exist for bias subtraction, flat fielding, and magnitude extraction, the choice depending on the requirements of the project, the availability of software, and also on the user preferences.

Comparisons of CCD photometry software are rather scarce in the literature, with only a few sources available (O'Donoghue et al. 2000; Becker et al. 2007). When the published comparisons give emphasis on evaluating scatter in the resulting light curves, then in this Chapter we concentrate on systematic errors and discrepancies between the results obtained with various software packages.

Also, care has to be taken in handling time of observation – extracting timestamps from FITS files, applying mid-exposure correction, and calculating heliocentric Julian dates. Errors in these steps occur easily but they are difficult to spot, except when comparing independent reductions of the same data by different users.

2.2 Time of observation

We compared independent reductions of CCD frames, obtained with the 1.0-m and 1.9-m telescopes at SAAO, Sutherland, South Africa. The raw FITS headers provided

timestamps of the beginning of exposures, both in UT as well as converted to modified Julian dates (MJD). The raw UT timestamps had been rounded to integer seconds by the acquisition software and the MJDs were given with five decimals.

Fig. 2.1a illustrates a case in data reduction where the exposure times of CCD frames were not taken into account correctly, leading to systematic errors in HJD of up to 20 seconds. In Fig. 2.1b, the correct approach was followed, and the residuals are smaller than the rounding error of the time of observation (1s). Another comparison revealed a one-second jump in heliocentric correction to occur at midnight UT, when the integer part of MJD changes (Fig. 2.1c). In this case, one of the reductions was done with constant heliocentric correction for the whole calendar date. The same systematic error is seen in Fig. 2.1d, where an additional sub-second effect is due to the fact, that one of the reductions was based on UT timestamps and the other on MJD values.

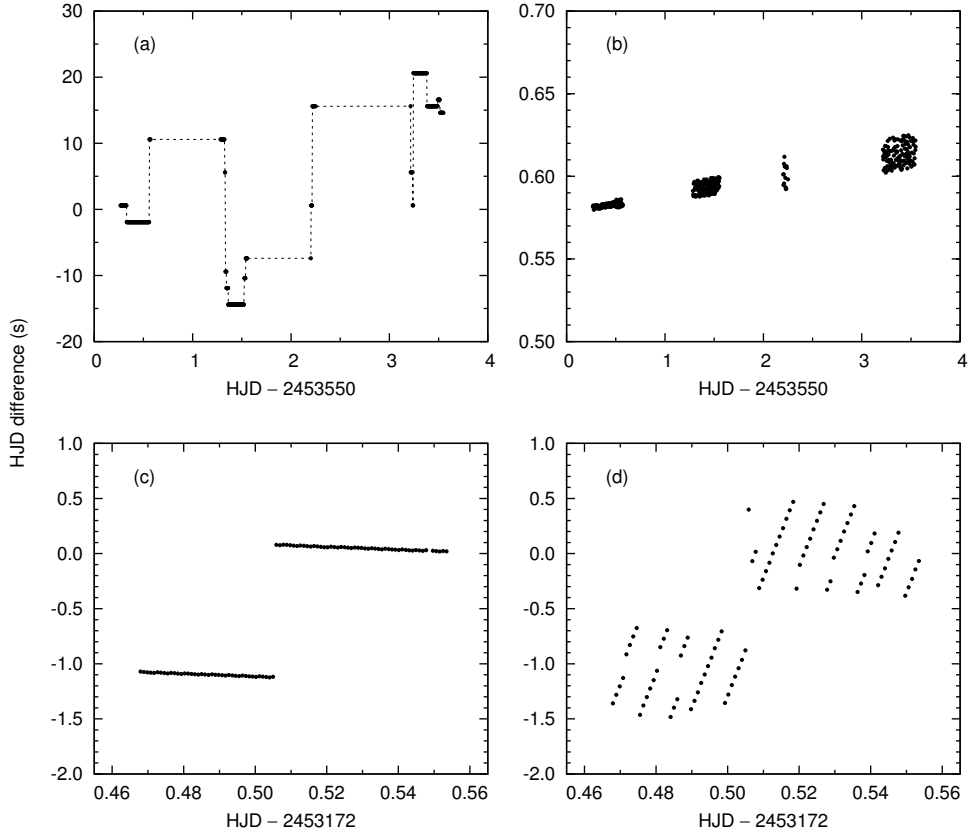


Figure 2.1: Differences in HJD of the same light curves, derived from two independent reductions: (a) systematic error due to neglecting changes in exposure times; (b) proper mid-exposure and heliocentric correction; (c) a jump in heliocentric correction at midnight UT; (d) same as (c), with sub-second effects due to rounding of seconds.

2.3 Magnitude extraction

2.3.1 PHOTWORK, IRAF/DAOPHOT, and MOMF

In the first test, a batch of flat-fielded CCD frames of the open cluster NGC 3293 were reduced independently by three users, each applying different reduction software: (1) PHOTWORK (aperture photometry), (2) DAOPHOT package in IRAF (PSF photometry), and (3) MOMF (combined PSF/aperture photometry). The frames had been obtained with the SAAO 1.0-m telescope, yielding a pixel size of 0.31 arcsec.

The reduction workflow with PHOTWORK is described in Sections 1.3–1.4. Magnitudes were extracted in 12 apertures with radii ranging from 1.0 to $3.75 \times \text{FWHM}$. The sky background was estimated in an annulus between 5.0 and $7.0 \times \text{FWHM}$. The optimal aperture-scaling factor was determined by minimising the scatter in differential magnitudes of constant stars.

An independent reduction was carried out with the IRAF/DAOPHOT package¹. Approximate FWHM of stellar images and sky-background levels were determined with the IRAF task `daoeedit`. A semi-empirical PSF model was obtained using nine isolated stars. The PSF was allowed to vary quadratically across the image.

The reduction package MOMF (Kjeldsen & Frandsen 1992) applies an empirical point-spread function and carries out aperture photometry on the residuals. Isolated PSF stars were selected by the user. Aperture radii for each program star were chosen according to the lowest point-to-point scatter in the light curves during good nights.

We compared the differential magnitudes of three isolated stars (BVC 5, 33, 64) in NGC 3293, using BVC 26 as a comparison star (see Sect. 7.1 for stellar identifications in NGC 3293). These stars cover 4 magnitudes of the brightness scale, BVC 5 being nearly 2 mag brighter, BVC 33 being 0.5 mag fainter, and BVC 64 about 2 mag fainter than the comparison star. In most of the frames, BVC 5 was exposed as high as possible, without reaching the CCD saturation limit, typically with the highest pixel value between 40,000 and 60,000 ADU.

The differences between the obtained light curves are plotted in Fig. 2.2. The results from MOMF and PHOTWORK agree well for brighter stars, whereas the magnitudes of the fainter star (BVC 64) differ systematically. PSF photometry with IRAF/DAOPHOT introduces large scatter in our test and leads to shifts and strong night-to-night changes in the mean magnitudes. Large deviations during the third night (JD 2453474) are related to poor seeing. Fig. 2.3 illustrates the difference of light curves as a function of seeing (FWHM).

Determination of the seeing itself varies from one method to the other, as shown in Fig. 2.4. Comparing MOMF with IRAF/DAOPHOT (left panel), MOMF produces half a pixel higher values in good seeing conditions (up to about 8 px, or 2.5 arcsec), whereas with poor seeing there is a strong discrepancy between the two methods. As can be seen in the right panel of Fig. 2.4, there is a trend in PHOTWORK measurements, while at about 7 px both MOMF and PHOTWORK yield the same FWHM.

¹<http://iraf.net/irafdocs/daorefman/>

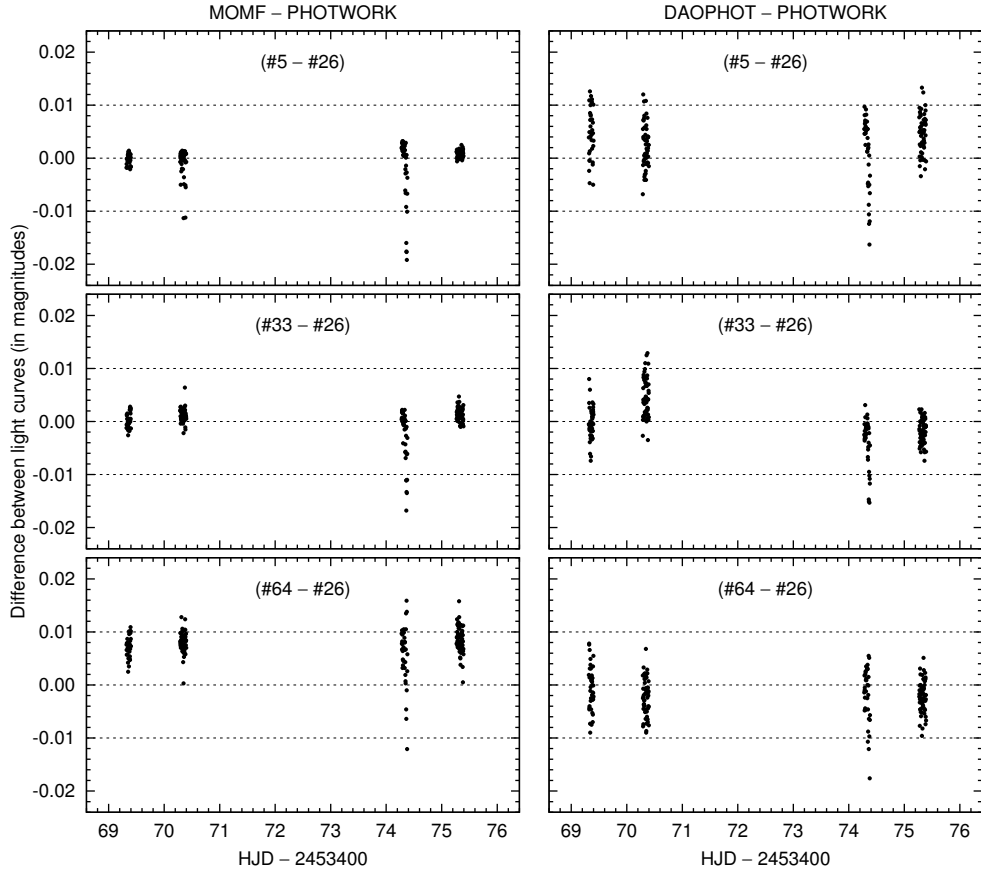


Figure 2.2: Comparison of differential light curves (in magnitudes), *top*: (BVC 5)–(BVC 26), *middle*: (BVC 33)–(BVC 26), *bottom*: (BVC 64)–(BVC 26), *left*: MOMF minus PHOTWORK, *right*: IRAF minus PHOTWORK. Star BVC 5 (top) is the brightest and BVC 64 (bottom) is the faintest in the sample.

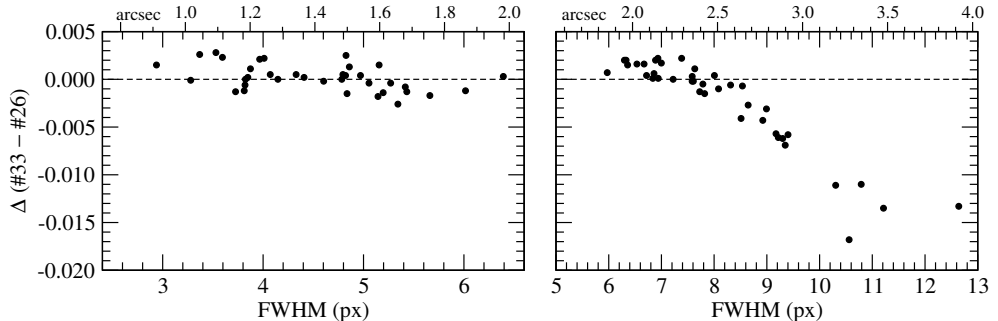


Figure 2.3: Difference in (BVC 33)–(BVC 26) light curves. MOMF minus PHOTWORK as a function of FWHM during a night with good seeing (JD 2453469, left) and poor seeing (JD 2453474, right).

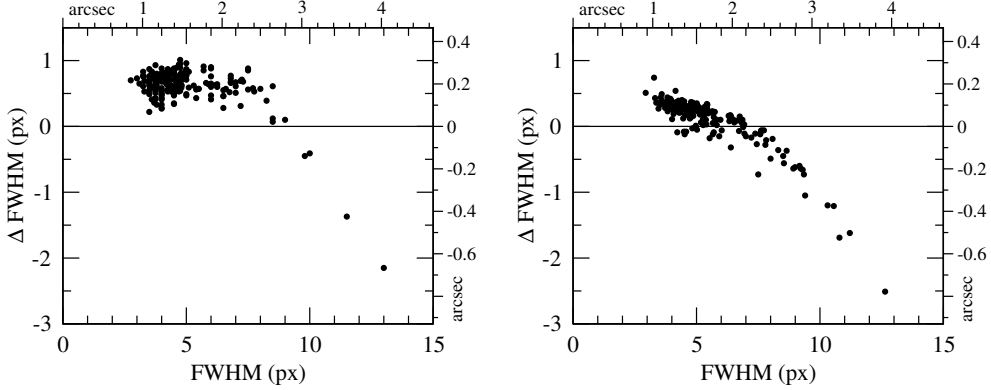


Figure 2.4: Comparison of FWHM measurements. *Left:* MOMF minus IRAF/DAOPHOT, *right:* MOMF minus PHOTWORK.

2.3.2 PHOTWORK and DOPHOT

In the second test, light curves from PHOTWORK were compared with the results from DOPHOT, a commonly used CCD photometry package (Schechter et al. 1993). DOPHOT carries out PSF photometry with analytical point-spread functions that are not allowed to vary across the image. DOPHOT also gives estimates of aperture magnitudes for stars with adequate signal-to-noise ratio.

The frames were obtained with the SAAO 1.9-m telescope, using *I* filter and 2×2 binning with the resulting pixel size of 0.29 arcsec. Raw frames were handled

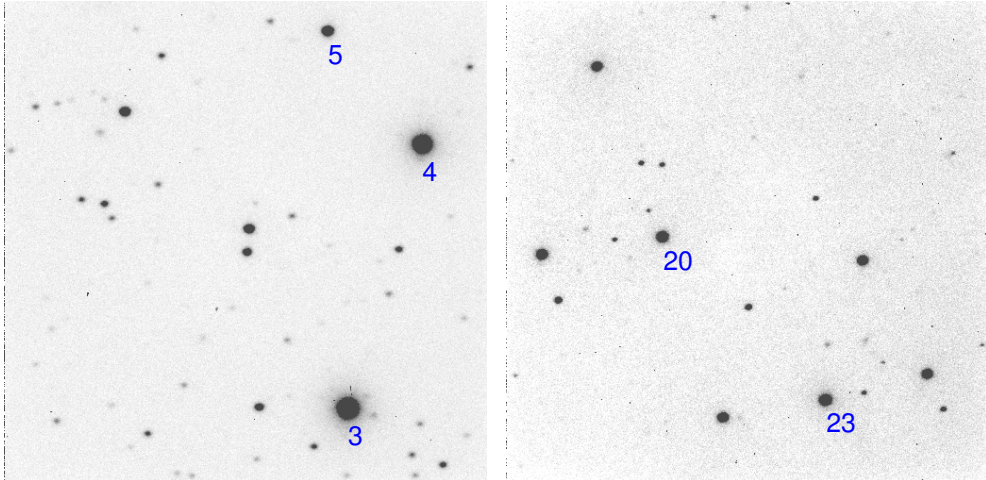


Figure 2.5: Sample CCD frames in *I* passband, with the centre coordinates (J2000) $\alpha = 17^{\text{h}}05^{\text{m}}48^{\text{s}}$, $\delta = -5^{\circ}16'46''$ (left panel) and $\alpha = 22^{\text{h}}04^{\text{m}}08^{\text{s}}$, $\delta = -56^{\circ}47'55''$ (right panel). North is up and east is left. Field of view is 2.5 arcmin.

independently by two users, from bias subtraction and flat fielding to extracting of magnitudes. Observations of two sparsely populated fields were taken into study. The sample CCD frames are shown in Fig. 2.5.

In the first field, the brightest stars (#3 and #4) were exposed to peak ADU values between 15,000 and 30,000. The light curves of these well-exposed stars are compared in the left panels of Fig. 2.6. Aperture photometry produces less scatter, while there is a systematic difference of a few millimagnitudes between PHOTWORK and DOPHOT light curves. PSF photometry from DOPHOT gives a light curve with higher scatter and the difference with PHOTWORK is both larger and not constant throughout the night. The right panels of Fig. 2.6 are dedicated to light curves with a 2-mag fainter star with a bright comparison star (#5 minus #4). As expected, PSF photometry works better for less-exposed stars and gives a more favourable light curve, while systematic differences between methods persist. Aperture photometry from DOPHOT gives much larger scatter than PHOTWORK, which uses an optimal aperture size.

In the second field (Fig. 2.5, right), light curves of equally-exposed stars (#23 minus #20) were compared, and the results for two nights are presented in Fig. 2.7. Aperture photometry from PHOTWORK and PSF photometry from DOPHOT give comparable results in terms of scatter, while DOPHOT's aperture photometry is clearly inferior. Systematic differences of about 5 mmag are present between the PHOTWORK and DOPHOT light curves. During the second night, JD 2452770, the DOPHOT PSF photometry produces an 8 mmag shift in a differential light curve, which cannot be seen in either aperture photometry results. The shift is attributable to a change in exposures, as the peak value of star #23 varies between 10,000 and 20,000 ADU in the first half of the night, and between 20,000 and 30,000 ADU in the second half. At the same time, seeing does not change considerably.

2.4 Discussion

We find systematic discrepancies between differential light curves obtained with various software packages. This means that stars on CCD frames get treated differently in the course of data reduction. While we did not carry out extensive comparisons, it is evident that systematic errors are rather common. Possible causes for systematic effects:

1. flat-fielding errors (cannot explain systematic effects in the first test, where the same flat-fielded frames were used);
2. differences in estimating sky-background values;
3. variable PSF across frames not taken into account properly.

Larger discrepancies between the PHOTWORK and MOMF light curves in poor seeing conditions may be attributed to the fact that MOMF works well only in the FWHM range from 3 px to 7 px.

While estimating FWHM is important for aperture photometry, high accuracy of FWHM values is not crucial in extracting magnitudes, as the same scaled apertures are applied to all the stars on a CCD frame and the optimal aperture-scaling factor

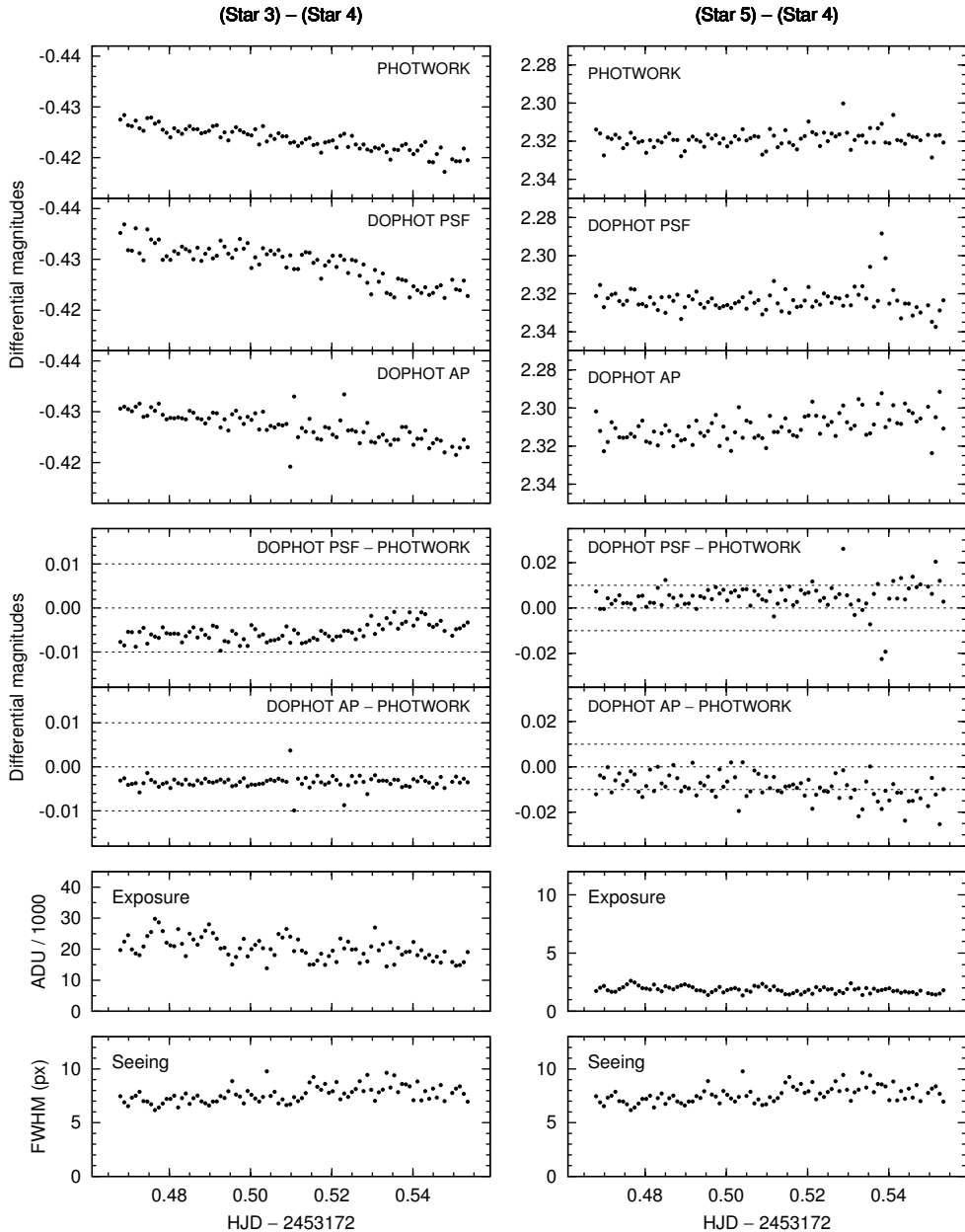


Figure 2.6: Comparison of differential light curves, obtained with the PHOTWORK and DOPHOT software (PSF and aperture photometry). Left panels correspond to a pair of well-exposed stars (#3 minus #4), while right panels correspond to a pair of stars with different brightness (#5 minus #4). The exposure panels give the peak ADU values of stars #3 and #5 on CCD frames.

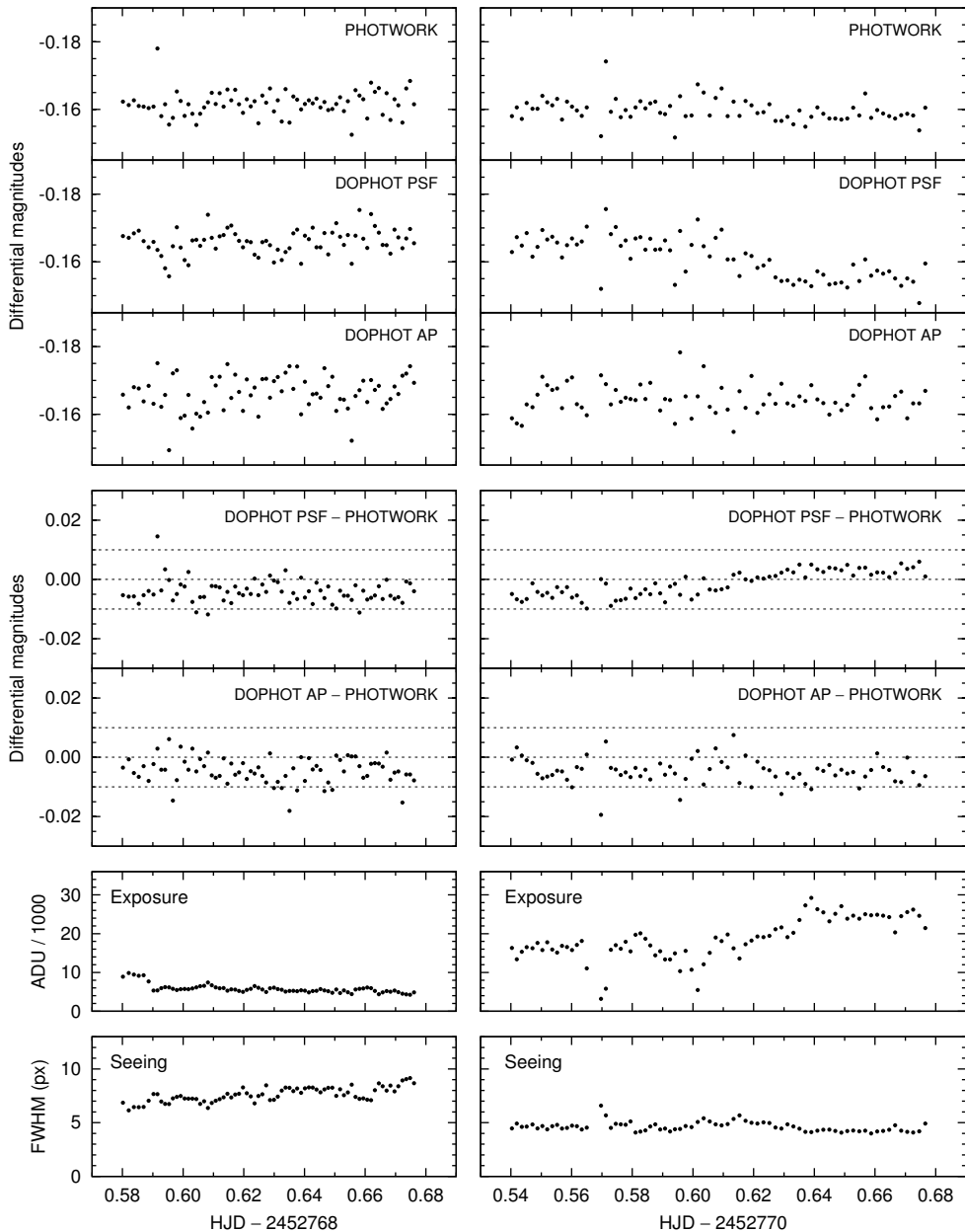


Figure 2.7: Comparison of differential light curves of equally-exposed stars (#23 minus #20). The light curves have been obtained with the PHOTWORK and DOPHOT software (PSF and aperture photometry). Left panels correspond to JD 2452768 and right panels to JD 2452770. The exposure panels give the peak ADU values of star #23 on CCD frames.

is selected afterwards by inspecting differential light curves. However, we comment on a few issues with regard to estimating FWHM.

1. A single FWHM value is ambiguous when stellar images are not round, e.g. in case of tracking errors or defocusing with poorly-collimated optics.
2. When stellar images are not round, PHOTWORK rather overestimates than underestimates FWHM values, as the algorithm fits a two-dimensional Gaussian profile to a stellar image and uses the larger of the widths in X and Y directions.²
3. Gaussian profile might not be a good fit to a real-world stellar image.
4. The FWHM values from MOMF may not be accurate outside of the optimal working range from 3 px to 7 px.
5. The FWHM-estimation algorithms in various software packages are not evident without closer examination of the code.

We find that MOMF and PHOTWORK give comparable differential light curves. Systematic differences between the results from these two software are small for well-exposed stars, but become significant for poorly-exposed stars. No good agreement was found between aperture photometry from PHOTWORK and PSF photometry from either IRAF/DAOPHOT or DoPHOT.

Due to systematic effects in magnitude extraction, light curves should be obtained in a consistent way, preferably using a single software package. Merging light curves from different reductions should be done with care and possible systematic errors should be taken into account.

The tests described above were carried out on isolated stars in sparsely populated or semi-crowded fields. The more a field is crowded, the more favourable PSF photometry becomes.

If photometric accuracy is critical for reaching scientific goals, extensive and quantitative comparisons should be carried out, in order to find optimal data reduction methods.

References

- Becker, A. C., Silvestri, N. M., Owen, R. E., Ivezić, Ž., & Lupton, R. H. 2007, PASP, 119, 1462
- Kjeldsen, H. & Frandsen, S. 1992, PASP, 104, 413
- O'Donoghue, D., Kanaan, A., Kleinman, S. J., Krzesinski, J., & Pritchett, C. 2000, Baltic Astronomy, 9, 375
- Schechter, P. L., Mateo, M., & Saha, A. 1993, PASP, 105, 1342

²This behaviour of PHOTWORK was changed in October 2011. In the newer versions, the mean FWHM of the two axes is used instead of the maximum value.

Part II

Case studies

Chapter 3

Observations of a stellar occultation by Charon

This Chapter is based on the published paper:

Charon's radius and atmospheric constraints from observations of a stellar occultation

A. A. S. Gulbis, J. L. Elliot, M. J. Person, E. R. Adams, B. A. Babcock,
M. Emilio, J. W. Gangestad, S. D. Kern, E. A. Kramer, D. J. Osip,
J. M. Pasachoff, S. P. Souza, and T. Tuvikene,
2006, Nature, 439, 48

3.1 Stellar occultations

A stellar occultation occurs when an object passes in front of a star, temporarily blocking its light as seen from Earth. Observing stellar occultations is used for determining the shapes and probing the atmospheres of planetary satellites and small Solar System bodies, i.e. asteroids and Kuiper Belt objects. This method provides the highest spatial resolution available from Earth-based observing methods.

By registering the start and end time of an occultation, and by using the coordinates of the observer and the orbital parameters of an occulting object, the length along the cross-section of the object – a chord – can be determined. Thus, a single observer can establish a lower limit on the diameter of the object. By observing an occultation from multiple locations on Earth, multiple occultation chords are registered, and the shape of an occulting object can be determined.

Stellar occultations by outer Solar System objects are rare, due to their small angular diameters and slow motion in the sky as seen from Earth. A stellar occultation by Pluto's moon Charon has been observed only once before the present work, in 1980, when a single chord was registered. This observation placed a lower limit of 600 km on Charon's radius (Walker 1980), later refined to 601.5 km (Elliot & Young 1991), and suggested a possible atmosphere. Modelling of the Pluto–Charon mutual occultation

Table 3.1: Observing sites and telescopes, arranged for the Charon occultation on 11 July 2005.

Site	Telescope	Longitude (° ' '')	Latitude (° ' '')	Altitude (m)	Observers
Pico dos Dias	0.6-m Zeiss	45 35 00 W	-22 32 07	1878	JMP, SPS, ME
Cerro Armazones	0.84-m	70 11 46 W	-24 35 52	2763	BAB, MJP, JWG, TT
Las Campanas	2.5-m du Pont	70 42 13 W	-29 00 26	2327	AASG, DJO
	6.5-m Clay	70 41 33 W	-29 00 51	2429	JLE, ERA
Cerro Pachón	8-m Gemini S.	70 43 24 W	-30 13 42	2725	SDK

Observers: JMP – J. M. Pasachoff; SPS – S. P. Souza; ME – M. Emilio; BAB – B. A. Babcock; MJP – M. J. Person; JWG – J. W. Gangestad; TT – T. Tuvikene; AASG – A. A. S. Gulbis; DJO – D. J. Osip; JLE – J. L. Elliott; ERA – E. R. Adams; SDK – S. D. Kern.

events in the 1980s yielded the radius range of 600–650 km, corresponding to a density of $1.56 \pm 0.22 \text{ g cm}^{-3}$ (see the references in Gulbis et al. 2006). The uncertainty in Charon’s density has been mainly due to the uncertainty in its radius, as the radius contributes to the density in the third power.

An occultation by Charon of the star C313.2 (UCAC2 26257135, with the *R*-band magnitude of 14.8) was predicted to occur on 11 July 2005 03:36:57 UT (geocentric mid-time).¹ By the prediction, the distance to Charon at the time of occultation was 30.07 AU and the geocentric shadow velocity was 20.93 km s^{-1} . The occultation was visible from about a 1200-km wide strip in South America, including the locations of large telescopes in Chile.

3.2 Observations

Observations of the Charon occultation were arranged at four sites in Chile and Brazil, using five telescopes, as listed in Table 3.1. Chilean sites included Observatorio Cerro Armazones (OCA), Las Campanas Observatory, and Cerro Pachón (Gemini South). In Brazil, observations were arranged at Observatório Pico dos Dias (OPD).

Owing to the shadow velocity, the spatial resolution with which Charon could be probed, was mainly limited by the time resolution of observations. Thus, cameras capable of fast cadence were required, with intervals between exposure time centres of 0.1–0.5 s.

The instruments used for the observations, except at Gemini South, were POETS (Portable Occultation, Eclipse, and Transit Systems), described by Souza et al. (2006). Each POETS system consisted of a high-speed Andor iXon DV-887-BI camera, an instrument control computer, and a GPS receiver to trigger frames and provide accurate timing. POETS cameras utilise frame-transfer CCDs with 512×512 pixels of $16 \mu\text{m}$, with the frame transfer time of 1.74 ms. Integration times are thus 1.74 ms less than cycle times. The POETS systems were used with no filter.

Gemini South observations were carried out with the Acquisition Camera (frame-transfer CCD with 1024×1024 pixels of $13 \mu\text{m}$), using the R_G0154 filter (wavelength

¹<http://occult.mit.edu/research/occultations/Charon/c313/C313.2-U2.0-2.2.html>

Table 3.2: Observation details.

Telescope	Camera	Filter	Binning	Pixel scale (arcsec)	Data rate (Hz)	Spatial resolution (km)
OPD 0.6-m	POETS	—	2×2	0.88	2	—
OCA 0.84-m	POETS	—	2×2	1.64	2	10.67
2.5-m du Pont	POETS	—	6×6	1.04	5	4.27
6.5-m Clay	POETS	—	4×4	0.18	10	2.13
8-m Gemini South	AcqCam	R	2×2	0.24	~2.24	10.66

interval 610–750 nm). A 128×128 subframe was recorded for these observations. The timings were derived from the Network Time Protocol (NTP). The integration time was 0.3 s, with 0.146 ± 0.001 s required for readout. Observation details are summarised in Table 3.2.

The time resolution of observations varied from 0.1 s (Clay) to 0.5 s (OCA 0.84-m telescope). Corresponding spatial resolutions were between 2.13 and 10.67 km, which ranged from less than two to over eight times the characteristic scale of diffraction effects, i.e., the Fresnel scale ($\sqrt{\lambda D}/2 = 1.27$ km, where wavelength $\lambda = 720$ nm and D is the distance to Charon).

The observations were successful at all sites except Pico dos Dias, where the occultation was not observable due to clouds. Astrometric data were collected about an hour before and after the occultation. High-speed observations were carried out contiguously for 20 minutes, covering the predicted occultation mid-times. For reducing the data, aperture photometry was used with square apertures containing Pluto–Charon and C313.2. Astrometric frames where C313.2 was clearly separated from Pluto–Charon, were used to establish the offset between a reference star and C313.2. Apertures were then centred based on the positions of the reference star, and by applying the offset. The sum of the signal in the aperture, minus the back-

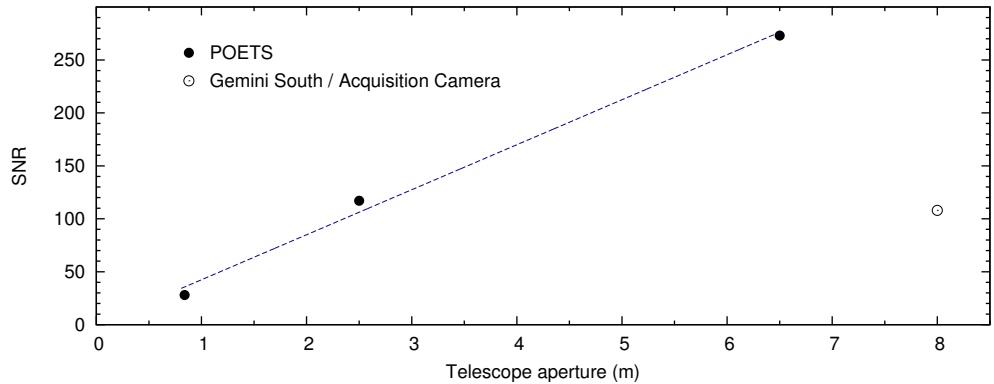


Figure 3.1: Signal-to-noise ratio of data as a function of telescope aperture.

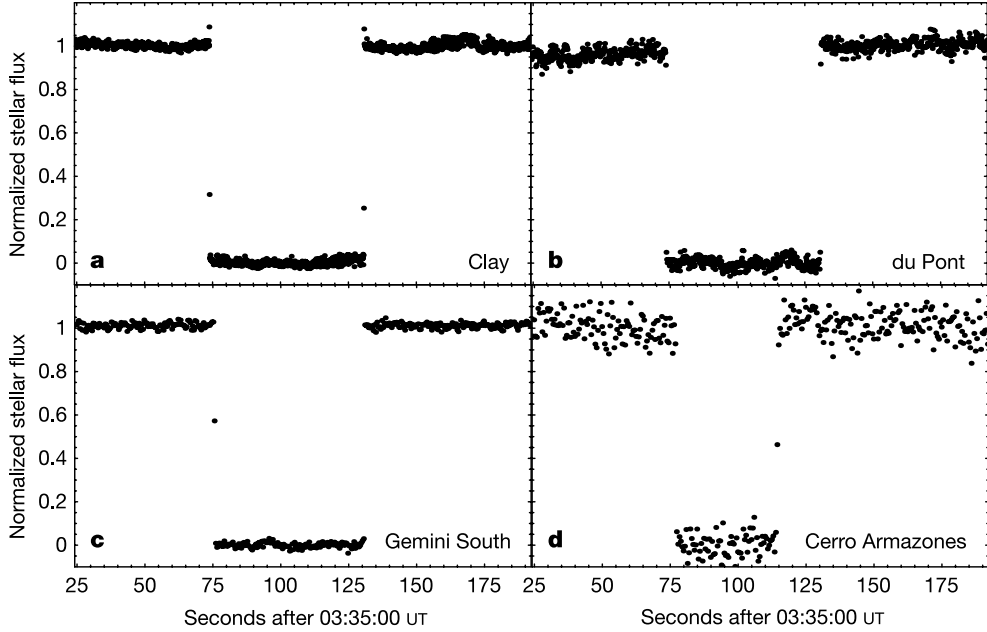


Figure 3.2: Light curves of the stellar occultation by Charon. The high data points just before the immersion and after the emersion in the Clay light curve result from the first diffraction fringe.

ground, was calculated to get light curves. The final aperture size for each data set was selected by maximizing the signal-to-noise ratio (SNR).

Signal-to-noise ratios were calculated on the basis of the residuals from light-curve fits and were normalised to a 1-s cycle time. The SNR as a function of telescope aperture is shown in Fig. 3.1. The correlation between the SNR and telescope size is evident for the three observations that utilised the POETS systems. The relatively small SNR of the Gemini South data is caused by using the *R* passband for observations, as opposed to filterless observations with the POETS systems.

3.3 Light curves and occultation times

Normalised light curves from the four successful observations are shown in Fig. 3.2. Fluxes were normalised so that the combined light from Pluto–Charon and C313.2 was set equal to one, and the light from Pluto–Charon alone (during occultation) was set equal to zero.

The occultation immersion and emersion times were determined separately from light curves by fitting a model of the straight-edge diffraction by a limb, integrated over the exposure time of each frame. The resulting occultation times are given in Table 3.3. Large timing errors of the Gemini South occultation chord are mainly due to CCD readout time between exposures, during which no data were recorded.

Table 3.3: Occultation chords.

Telescope	SNR	Occultation times (s after 03:35:00 UT)	
		Immersion	Emersion
OCA 0.84-m	28	76.99 \pm 0.04	114.28 \pm 0.03
2.5-m du Pont	117	73.792 \pm 0.005	130.609 \pm 0.004
6.5-m Clay	273	73.744 \pm 0.001	130.563 \pm 0.002
8-m Gemini South	108	75.50 \pm 0.15	130.55 \pm 0.15

3.4 Charon's radius and density

Fitting a circular figure to the registered chords, weighted inversely with the squared timing errors, gives the mean radius of 606.015 ± 0.039 km. The mean radius from an elliptical weighted fit is 598 km; however, the fitted ellipticity is not statistically significant. The adopted mean radius of Charon is 606 ± 8 km. The uncertainty is estimated by the difference between the mean radii from circular and elliptical weighted fits.

Assuming that Charon is spherical and has a mass of $(1.60 \pm 0.12) \times 10^{24}$ g, we find its density to be 1.72 ± 0.15 g cm $^{-3}$. For ice density of 1.0 g cm $^{-3}$ and rock density of 3.0 g cm $^{-3}$, the derived rock-mass fraction is 0.63 ± 0.05 . This value is smaller than Pluto's (0.73 ± 0.06), which has its density estimated in the range 1.8–2.1 g cm $^{-3}$ (Olkin et al. 2003).

Person et al. (2006) later combined all available data sets from the 2005 occultation observations, obtained by three separate research groups. Combining all occultation chords allowed them to more accurately determine the mean radius of Charon: 606.0 ± 1.5 km. The improvement in the determination of Charon's radius and density from the 2005 July occultation event is obvious from Table 3.4.

The results can be used to constrain Pluto's radius by fixing Charon's radius in reanalyses of the mutual Pluto–Charon events.

Table 3.4: Determinations of Charon's radius and density.

Reference	Radius (km)	Assumed mass (10^{24} g)	Density (g cm $^{-3}$)
Previous work (refs in Gulbis et al. 2006)	600–650	1.60 \pm 0.12	1.56 \pm 0.22
Gulbis et al. (2006)	606 \pm 8	1.60 \pm 0.12	1.72 \pm 0.15
Sicardy et al. (2006)	603.6 \pm 1.4	1.58 \pm 0.07	1.71 \pm 0.08
Person et al. (2006)	606.0 \pm 1.5	1.520 \pm 0.064	1.63 \pm 0.07

3.5 Related work

The same equipment that was used for the Charon occultation observations at the OCA, was also used for observations of the pulsating star CY Aqr. The very high time resolution of the POETS instrument allowed us to obtain an unprecedented light curve of the star, as reported in Chapter 6.

References

- Elliot, J. L. & Young, L. A. 1991, Icarus, 89, 244
Gulbis, A. A. S., Elliot, J. L., Person, M. J., et al. 2006, Nature, 439, 48
Olkin, C. B., Wasserman, L. H., & Franz, O. G. 2003, Icarus, 164, 254
Person, M. J., Elliot, J. L., Gulbis, A. A. S., et al. 2006, AJ, 132, 1575
Sicardy, B., Bellucci, A., Gendron, E., et al. 2006, Nature, 439, 52
Souza, S. P., Babcock, B. A., Pasachoff, J. M., et al. 2006, PASP, 118, 1550
Walker, A. R. 1980, MNRAS, 192, 47P

Chapter 4

GSC 08613–02122, a new δ Scuti star in Carina

This Chapter was published as

GSC 08613–02122, a new δ Scuti star in Carina

T. Tuvikene and C. Sterken,
2010, JAD, 16, 1

Abstract

We present a collection of more than 4000 *BVRI* and *uvby* differential photometric measurements of the newly-discovered 12th-magnitude southern δ Scuti star GSC 08613–02122. The star has a main pulsation period of about 4 hours with an amplitude of 0^m05 in the V band. The pulsation amplitude is variable, and the $O - C$ diagram reveals the existence of a long $P \sim 29.5$ -day cycle, which possibly results from the beating of the main pulsation frequency with a nearby frequency.

4.1 Introduction

GSC 08613–02122 ($\alpha_{J2000} = 10^{\text{h}}37^{\text{m}}05^{\text{s}}$, $\delta_{J2000} = -58^{\circ}14'03''$) is a 12th-magnitude star in Carina, 10 arcmin East of the core of the open cluster NGC 3293. We found the variability of GSC 08613–02122 from wide-field images of the NGC 3293 field. We consequently carried out dedicated monitoring of the star in multiple photometric bands.

The star is listed in the ASAS-3 Photometric *V*-Band Catalogue¹, but is not classified as variable.

¹<http://www.astroww.edu.pl/asas/?page=catalogues>

4.2 Observations and data reduction

CCD photometry of GSC 08613–02122 was carried out on 18 nights during two observing runs in 2006 and 2007. In addition, the star was observed photoelectrically on 16 nights in 2006–2008. The observations are summarised in Table 4.1.

Table 4.1: Photometric observations of GSC 08613–02122.

Date	JD–2450000	Obs.	Nights	<i>N</i>	Band
2006 Jan	3743.7–3753.9	OCA	10	939	<i>B</i>
2006 Jan	3743.7–3753.9	OCA	10	1775	<i>V</i>
2007 Feb–Mar	4135.5–4170.5	SAAO	8	368	<i>B</i>
2007 Feb–Mar	4135.5–4170.6	SAAO	8	379	<i>V</i>
2007 Feb–Mar	4135.6–4170.6	SAAO	8	361	<i>R</i>
2007 Feb–Mar	4145.5–4170.6	SAAO	7	287	<i>I</i>
2006 Nov	4057.8–4058.8	SAT	2	2	<i>uvby</i>
2007 Jan–Feb	4120.8–4132.8	SAT	6	6	<i>uvby</i>
2007 Dec	4442.8–4448.8	SAT	6	6	<i>uvby</i>
2008 Jan	4478.8–4479.8	SAT	2	2	<i>uvby</i>

4.2.1 CCD photometry

The star was observed in January 2006 with the 41-cm Meade telescope at Observatorio Cerro Armazones (OCA), Chile, using an SBIG STL-6303E CCD camera (3072×2048 pixels, FOV $23.0' \times 15.4'$) and Johnson *B* and *V* filters. GSC 08613–02122 was captured at the edge of the field of view of our main target NGC 3293. From February to March 2007 we used the 1.0-m telescope at SAAO, Sutherland, South Africa, with an STE4 CCD camera (1024×1024 pixels, FOV $5.3' \times 5.3'$) and *BVRI* filters for follow-up monitoring. A sample OCA frame is shown in Fig. 4.1 and an SAAO frame in Fig. 4.2.

Raw frames were calibrated using bias and twilight flat-field frames. For the OCA images, dark frames were used instead of bias frames. Magnitudes were extracted by means of aperture photometry, using the workflow implemented in the PHOTWORK software (see Sections 1.3–1.4 for details). Aperture sizes were scaled with the full width at half maximum (FWHM) of stellar images, and an aperture radius of $2.0 \times \text{FWHM}$ was used throughout the data reduction.

In order to minimise flat-field errors, comparison stars C1 and C2 (see Fig. 4.2) for the SAAO field were chosen from the immediate vicinity of GSC 08613–02122. Since C1 and C2 are fainter than the target star, they induce considerable scatter in the OCA photometry. Hence, for the OCA field we selected brighter comparison stars (C3 and C4 in Fig. 4.1) from NGC 3293. All magnitudes were then shifted to match the mean value of C1 and C2.

Photometric errors were derived on the basis of C1 *minus* C2 for the SAAO data. For the OCA data, errors were derived from light curves of constant stars of similar brightness as the target star (C5 for *B* and C6 for *V* magnitudes). The errors for

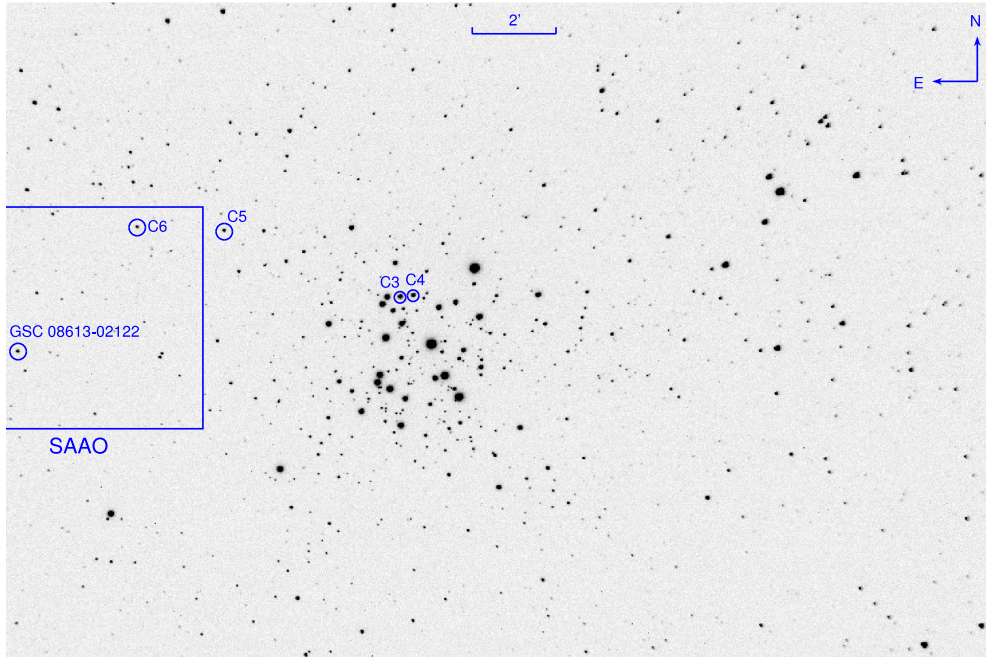


Figure 4.1: OCA V -band frame of NGC 3293 with GSC 08613–02122 marked. The field of view is $23' \times 15'4$. C3, C4, C5 and C6 indicate the comparison stars, and the box represents the SAAO field of view.

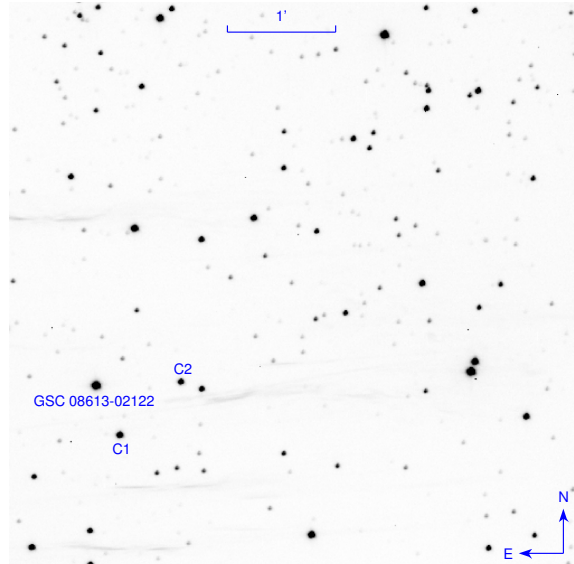


Figure 4.2: SAAO V -band frame of GSC 08613–02122 and the comparison stars (C1, C2). The field of view is $5'3$.

individual nights, as well as for the complete OCA and SAAO data sets are presented in Table 4.2.

For standardisation purposes, the Landolt standard star SA 98 193 and 13 secondary standards in its field (Galadí-Enríquez et al. 2000) were observed during one night with photometric conditions (JD 2454145), and colour transformations were applied for that night only. Standard *BVRI* magnitudes were determined for GSC 08613–02122 and its comparison stars C1 and C2 (Table 4.3).

Table 4.2: Photometric errors of GSC 08613–02122 light curves.

JD	<i>B</i>	<i>V</i>	<i>R</i>	<i>I</i>
53743	0.0259	0.0119	—	—
53745	0.0152	0.0114	—	—
53746	0.0160	0.0137	—	—
53747	0.0158	0.0126	—	—
53748	0.0140	0.0114	—	—
53749	0.0143	0.0127	—	—
53750	0.0138	0.0125	—	—
53751	0.0131	0.0124	—	—
53752	0.0158	0.0125	—	—
53753	0.0125	0.0114	—	—
All OCA	0.0172	0.0131	—	—
54135	0.0049	0.0036	0.0076	—
54139	0.0044	0.0044	0.0042	—
54145	0.0049	0.0038	0.0047	0.0060
54152	0.0047	0.0048	0.0038	0.0062
54167	0.0072	0.0050	0.0059	0.0083
54168	0.0046	0.0052	0.0034	0.0068
54169	0.0048	0.0038	0.0059	0.0046
54170	0.0041	0.0050	0.0061	0.0086
All SAAO	0.0059	0.0052	0.0060	0.0078

4.2.2 Photoelectric photometry

GSC 08613–02122 was observed with the Strömgren Automatic Telescope (SAT) at ESO, La Silla at four occasions in 2006–2007–2008. A diaphragm of 17 arcsec was used. Extinction corrections were derived from standard-star observations, and transformations to the standard *uvby* system were derived as described by Olsen (1994). We stress, though, that no attempt was made to obtain exact colour indices on the *uvby* standard system because that would have required a substantial amount of additional observing time. Nor was any specific comparison star selected and observed. However, star Cl* NGC 3293 FEAS 20 (star 20 in the list of Feast 1958) in NGC 3293, was measured every time before or after GSC 08613–02122 was observed, and the *y* magnitude and Strömgren colour indices were derived relatively to that star. Note

that there is a difference in V of about 4 magnitudes between both stars, and that the δ Scuti variable is much redder than the nearby B1 III star.

4.3 Results

4.3.1 Average magnitudes and colour indices

The mean magnitude and colour indices² of GSC 08613–02122 are: $y = 12.04 \pm 0.01$, $b - y = 0.250 \pm 0.003$, $m_1 = 0.186 \pm 0.005$, $c_1 = 0.780 \pm 0.017$. One additional measurement obtained on 22 January 2010 yields very similar results (12^m01 , 0^m257 , 0^m262 , and 0^m774). Table 4.3 lists the average $BVRI$ magnitudes and colour indices of GSC 08613–02122 and its comparison stars.

Table 4.3: $BVRI$ photometry for GSC 08613–02122 and its comparison stars.

Star	V	$B - V$	$V - R$	$V - I$
GSC 08613–02122 (min)	12.117 ± 0.007	0.429 ± 0.013	0.279 ± 0.009	0.542 ± 0.010
GSC 08613–02122 (max)	11.992 ± 0.005	0.381 ± 0.012	0.252 ± 0.008	0.492 ± 0.009
C1	13.457 ± 0.007	0.459 ± 0.013	0.291 ± 0.010	0.575 ± 0.011
C2	14.070 ± 0.007	0.528 ± 0.015	0.334 ± 0.010	0.656 ± 0.013

4.3.2 Light and colour curves

The BV light curves from OCA are shown in Fig. 4.3, and the $BVRI$ light curves from SAAO are shown in Fig. 4.4. Figure 4.5 displays the overall light curve in V , together with the y magnitudes transformed to the Johnson V scale.

The $B - V$, $V - R$ and $R - I$ colour curves for JD 2454145.5, together with the V light curve, are shown in Fig. 4.6. The colour indices of the star are redder at the phase of light minimum than at maximum.

4.3.3 Frequencies

As Fig. 4.5 clearly shows, the relatively long pulsation period of this star makes it a poor candidate for frequency analysis of data provided by one single observing site: the spectral window displays strong 1 c d^{-1} aliases of any true frequency that is present in the data.

The frequency resolution of our time-series data is $1.5/\Delta T = 0.15\text{ c d}^{-1}$ (where ΔT is the time span of the observations, Loumos & Deeming 1978) for the OCA data, and 0.04 c d^{-1} for the SAAO data. A frequency analysis³ of all combined V data in the frequency range $0\text{--}10\text{ c d}^{-1}$ reveals the highest peak at 6.014 c d^{-1} with an amplitude of 0^m054 , and a nearby peak at 5.986 . The OCA data alone, on the other hand, yield a highest-peak frequency of 4.999 (amplitude 0^m055) and a slightly

² $m_1 = (v - b) - (b - y)$; $c_1 = (u - v) - (v - b)$

³Using PERIOD04 (Lenz & Breger 2005).

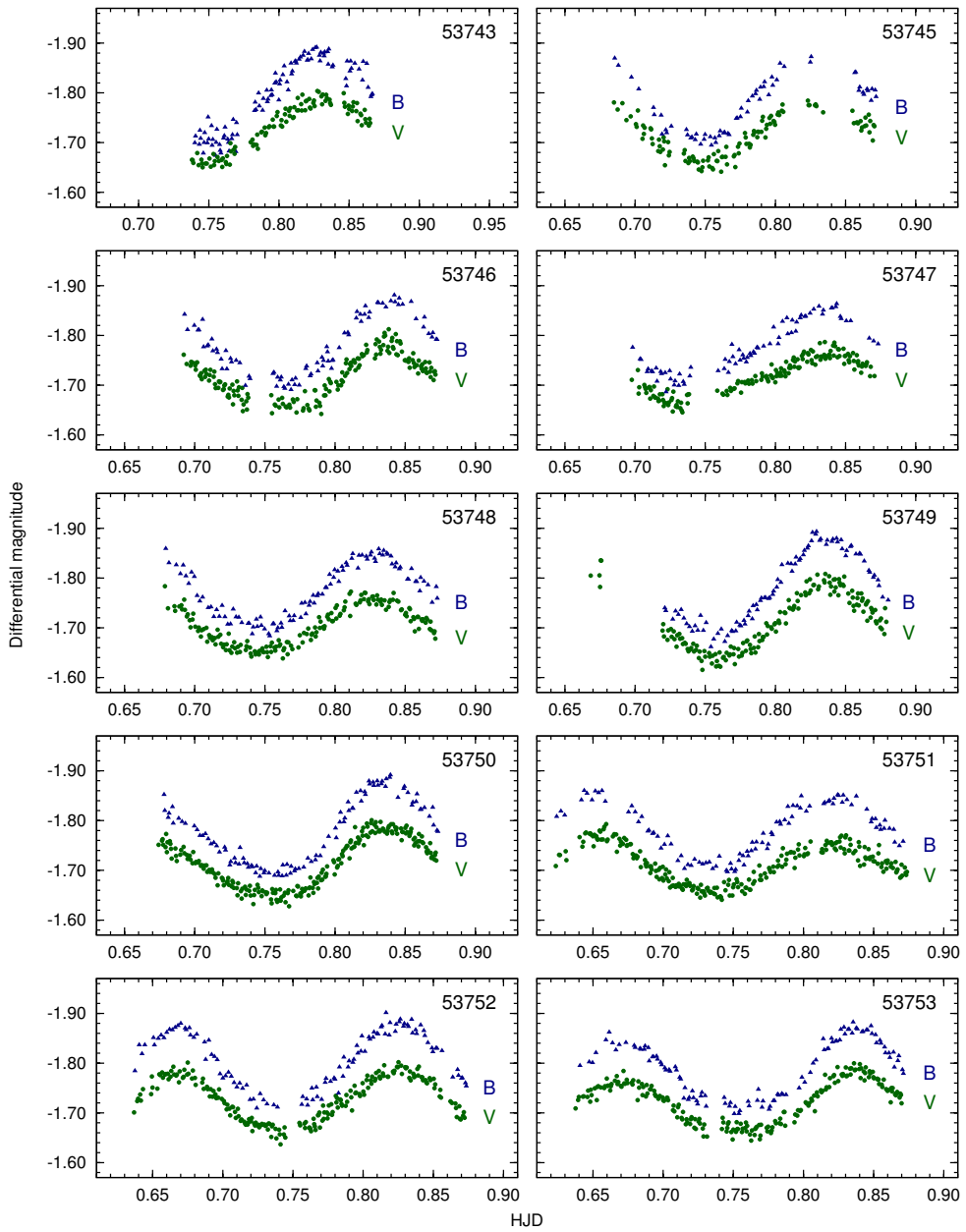


Figure 4.3: OCA differential light curves in *B* and *V* passbands.

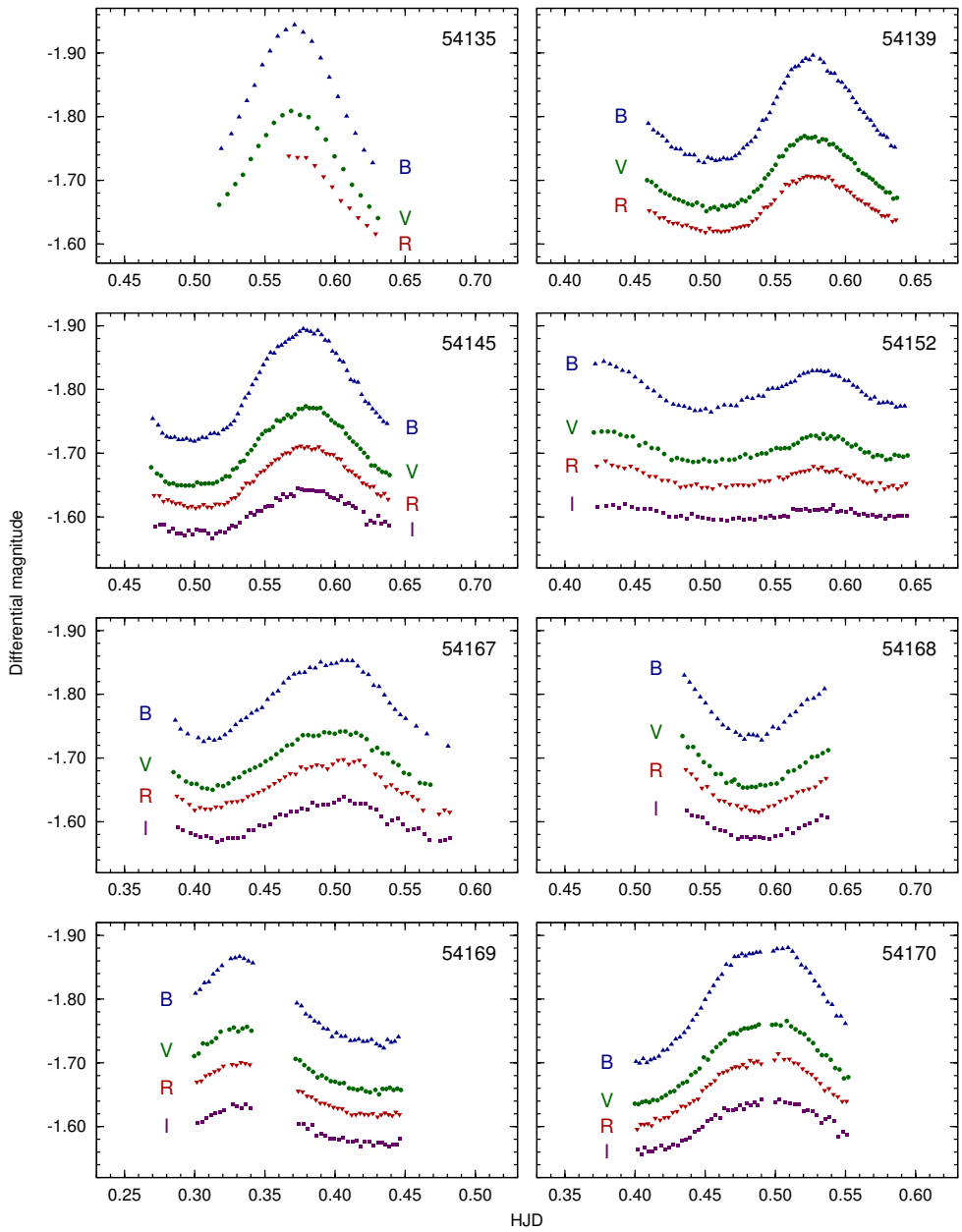


Figure 4.4: SAAO differential light curves in *BVRI*.

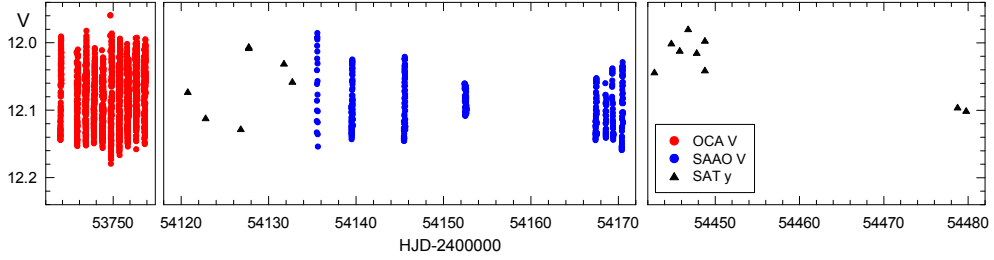


Figure 4.5: Combined V light curve for all seasons.

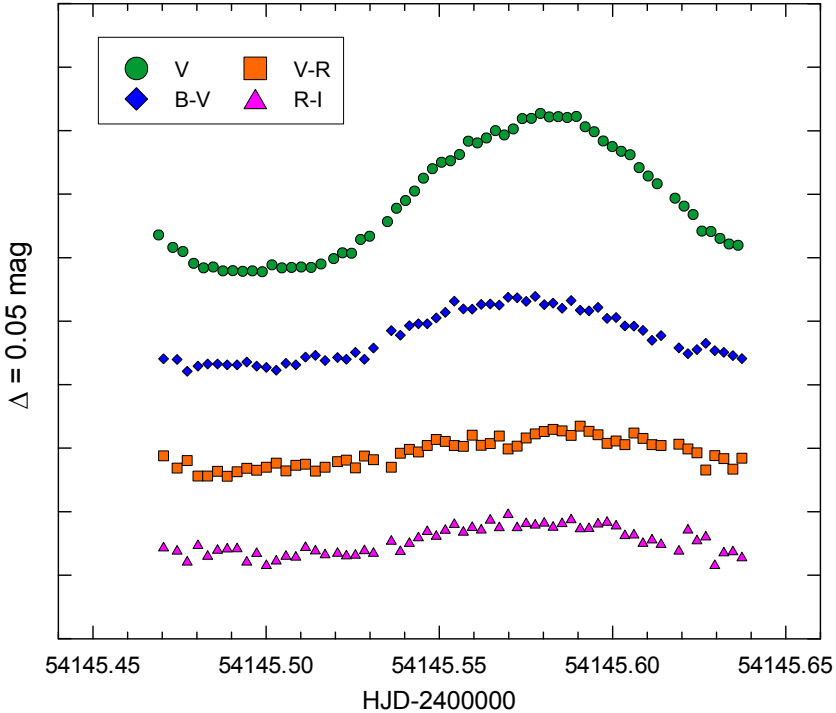


Figure 4.6: V light curve and colour curves (SAAO). Tick marks on the ordinate axis are $0.^m05$ apart on an inverted scale.

lower one at 6.004. The SAAO data (379 data points with standard deviation $0.^m038$) yield a highest peak at 5.982 accompanied by a second peak at 6.186 (see Fig. 4.7). Prewhitenning with both frequencies reduces the residuals to $0.^m013$, but more data are needed to derive additional stable frequencies. Combining the SAAO and SAT V magnitudes makes the peak(s) near 6 c d^{-1} stand out more prominently. A close look at Fig. 4.4 reveals artefacts that cannot be accounted for by adding harmonics, viz. the broad shape of the light curves on JD 2454135, and the flat-topped B light curves on JD 2454167 and 2454170.

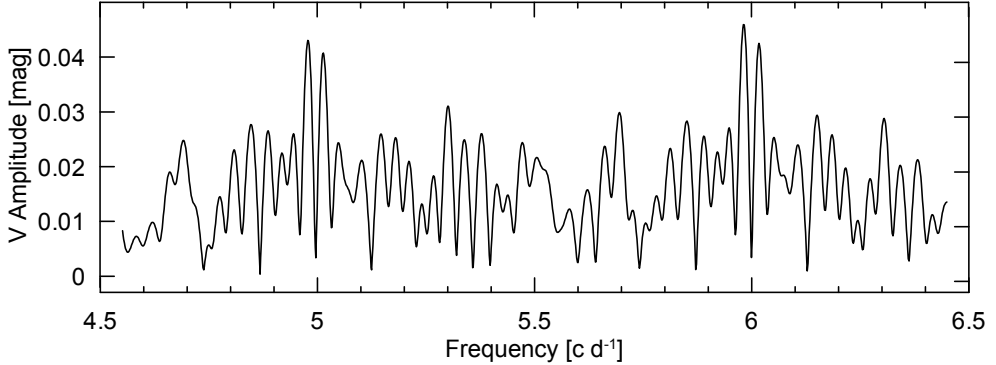


Figure 4.7: Frequency spectrum for the SAAO V data in the $5\text{--}6\text{ c d}^{-1}$ range.

The argument for opting for the $\sim 6\text{ c d}^{-1}$ frequency solution rather than the $\sim 5\text{ c d}^{-1}$ one is based on the light curves in Fig. 4.3: none of the three sets of light curves with two maxima observed on JD24553751–53 at OCA is fully compatible with a $0^{\mathrm{d}}200$ period, while they are all commensurate with a period of about $0^{\mathrm{d}}166$.

To support our argument further, we determined the times of maximum light for all V light curves with a well-defined maximum, see Table 4.4. The cycle number E is derived assuming that the main frequency of variation is close to 6 c d^{-1} . This leads to the following set of ephemeris equations (note that the E schemes for both data sets are independent):

$$\begin{aligned} T_{\max\text{OCA}} &= 2453743.8336 &+& 0.1666 E \\ && \pm 0.0045 & \pm 0.0001 \\ T_{\max\text{SAAO}} &= 2454135.5927 &+& 0.16623 E \\ && \pm 0.0130 & \pm 0.00009 \end{aligned} \quad (4.1)$$

4.3.4 Amplitude variations

V -passband amplitudes were deduced from the V light curves as the difference between maximum and minimum light for each observed pulsation cycle. The amplitudes in each photometric band are shown in Fig. 4.8: the $BVRI$ wide-band amplitudes (i.e. full range between maximum and minimum light) were derived from the SAAO data obtained on JD 2454145.5. The ranges in $uvby$ were derived from all SAT data – note that the u -band range strongly depends on the measured c_1 index, which is very much affected by low photon-noise. This illustration underlines the importance of the photometric bandwidth in discussing the amplitude: whereas the broad V band yields a very similar pulsation amplitude as the narrower y , filter B contains b as well as v . The amplitude in b (as expected on the basis of its effective wavelength being longer) is slightly less than in B , but the v amplitude is substantially higher despite the fact that the corresponding band is completely embedded in broadband B .

Table 4.4: Times of maximum and cycle numbers E for OCA and SAAO light curves.

HJD	E_{OCA}	HJD	E_{SAAO}
3743.8327	0	4135.5708	0
3746.8356	18	4139.5775	24
3747.8372	24	4145.5798	60
3748.8264	30	4152.5826	102
3749.8373	36	4167.4973	192
3750.8367	42	4169.3331	203
3751.8194	48	4170.4952	210
3752.6680	53		
3752.8260	54		
3753.6708	59		
3753.8368	60		

Figure 4.9 shows amplitude as a function of time, and illustrates strong amplitude variations – especially during the SAAO season.

4.3.5 Period and phase variations

Equations 4.1 lead to the $O-C$ diagrams in Fig. 4.10. The OCA data, covering about 60 cycles, do not reveal any trends, though erratic changes up to about 0.1 cycles do occur. The picture for the next season is quite different: up to cycle 100 there is an almost monotonically increasing trend, which is followed by what appears an abrupt reset another 100 cycles later. Unfortunately, no data were taken during that time interval. The shape of the curve suggests a low-frequency modulation, and the data

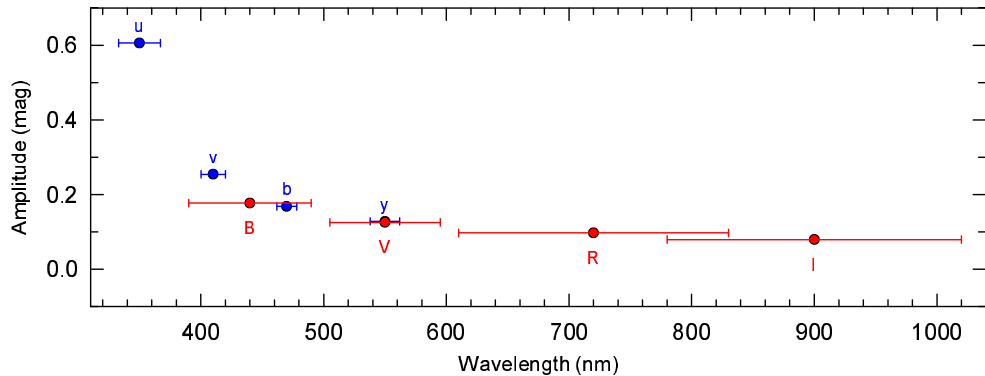


Figure 4.8: Amplitude ranges for combined SAT (2006–2008) and SAAO data (obtained on JD 2454145.5). The horizontal bars outline the photometric bandwidths.

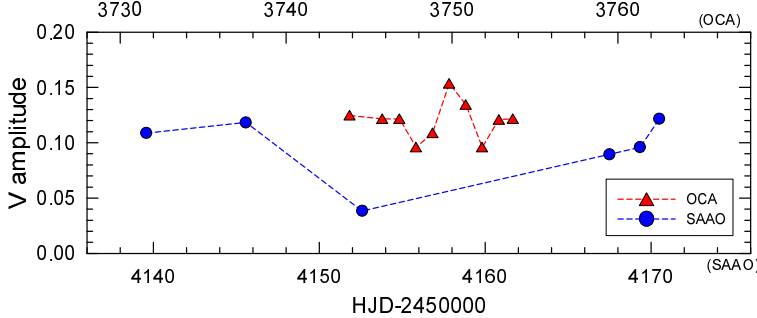


Figure 4.9: Variations in V amplitude as a function of HJD.

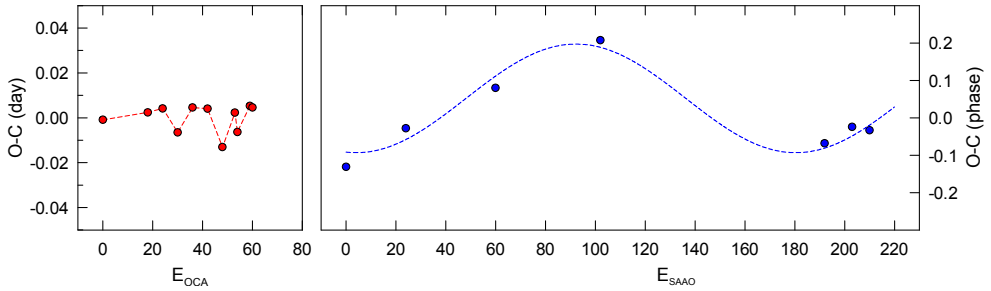


Figure 4.10: $O - C$ diagrams for GSC 08613–02122 according to ephemeris (4.1).

support its period $P \approx 176$ cycles ($29^{d}5$, $f = 0.034 \text{ c d}^{-1}$) and an amplitude (half-range) of a quarter of the pulsation cycle. In other words, period or phase variability up to half a cycle seems to be present. The evidence for this long cycle – which was obtained independently of the Fourier analysis – supports the presence of a second peak 0.034 c d^{-1} away from the main pulsation derived in Eq. 4.1.

4.4 Discussion

4.4.1 Location of GSC 08613–02122 in the spectral-classification diagram

From the $uvby$ photometry of GSC 08613–02122 we calculated the average reddening-free colour indices $[c_1] = c_1 - 0.20(b - y)$ and $[m_1] = m_1 + 0.30(b - y)$ (Crawford 1975), and obtain $[c_1] = 0.730 \pm 0.020$ and $[m_1] = 0.263 \pm 0.006$, which point to a spectral type F3–F5. Figure 4.11 shows the position of the star in Strömgren’s $[m_1], [c_1]$ spectral-classification diagram (Strömgren 1966), together with the locations of δ Scuti, 4 CVn, GSC 04778-00152 (Chapter 5), the δ Scuti stars from the catalog of Rodríguez et al.

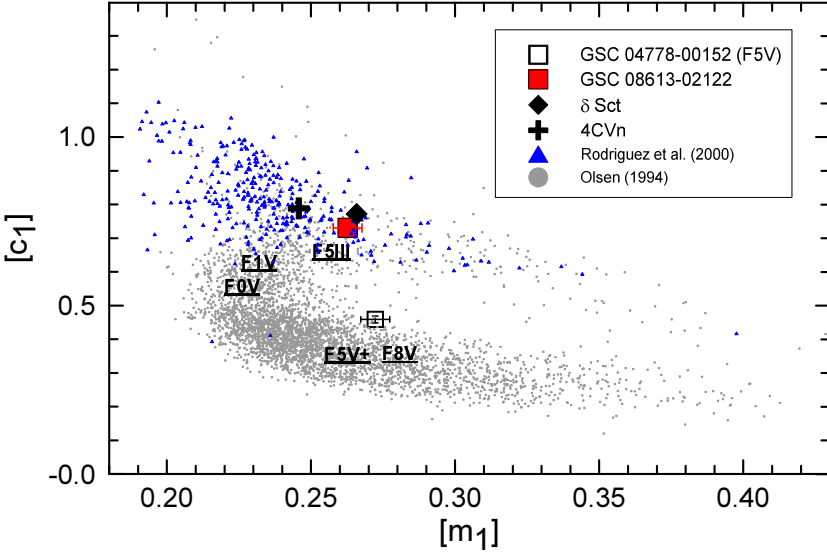


Figure 4.11: Reddening-free Strömgren $[m_1]$, $[c_1]$ diagram for F-stars from the list of Olsen (1994) (grey dots) with the positions of GSC 08613–02122, δ Scuti and 4 CVn. The spectral types of a couple of bright F stars from Cowley (1976) are indicated, as well as the position of GSC 04778–00152 (Chapter 5).

(2000), and the F stars from the catalogue of Olsen (1994).

4.4.2 Nature of the erratic variations

The amplitude and phase shifts suggest beating of two close frequencies of similar amplitude, though the very different behaviour during two consecutive years somehow excludes this interpretation. An alternative mechanism to produce the observed effects is decay of a second pulsation mode followed by its re-excitation at a later moment at a different phase.

Similar amplitude variations as shown in Fig. 4.9 have notably been seen in 4 CVn, the best-studied cool, evolved δ Scuti star so far (Breger 2000, and references therein): in neighboring years the amplitudes usually are similar, but annual variability over longer time scales is also present. Breger & Bischof (2002) also draw attention to the strange case of 4 CVn, with its phase shift of up to half a cycle near minimum amplitude, which is interpreted not as a double mode, but as re-excited single mode. These authors also examined whether close pulsation frequencies exist in δ Scuti stars, and they emphasise that the presence of double peaks does not necessarily mean that there really exist two pulsation modes with close frequencies by listing the following possible problems:

- frequency resolution,
- prewhitening with an incorrect frequency producing a spurious peak in the fre-

quency spectrum,

- amplitude variability of a single mode,
- systematic time errors in the used HJD,
- photometric passband incompatibilities, and
- effects of aliasing.

We are aware that the frequency resolution of our dataset is not optimal, but there should be no adverse effects in the timestamp, since the computer clock was synchronised with time servers at the beginning of each night. Moreover, the issue of passband mismatches can be neglected since the V filters – even the y band – are quite compatible for measuring stars of this type, as is also substantiated by the similar amplitudes as shown in Fig. 4.9.

4.5 Conclusions

Photometric $BVRI$ and $uvby$ differential measurements collected at Observatorio Cerro Armazones (Chile), ESO (La Silla, Chile), and SAAO (Sutherland, South Africa) reveal that the 12th-magnitude star GSC 08613–02122 is a δ Scuti star with a main pulsation period of about four hours with an amplitude of $0.^m05$ in the V passband. The pulsation amplitude is variable, and the $O - C$ diagram of the 2007 season reveals the existence of a long $P \sim 29.^d5$ cycle resulting from the beating of the main pulsation frequency with a nearby frequency. The photometric behaviour of the star is akin to 4 CVn.

References

- Breger, M. 2000, in Astronomical Society of the Pacific Conference Series, Vol. 210, *Delta Scuti and Related Stars*, ed. M. Breger & M. Montgomery, p. 3
- Breger, M. & Bischof, K. M. 2002, A&A, 385, 537
- Cowley, A. P. 1976, PASP, 88, 95
- Crawford, D. L. 1975, PASP, 87, 481
- Feast, M. W. 1958, MNRAS, 118, 618
- Galadí-Enríquez, D., Trullols, E., & Jordi, C. 2000, A&AS, 146, 169
- Lenz, P. & Breger, M. 2005, Communications in Asteroseismology, 146, 53
- Loumos, G. L. & Deeming, T. J. 1978, Ap&SS, 56, 285
- Olsen, E. H. 1994, A&AS, 106, 257
- Rodríguez, E., López-González, M. J., & López de Coca, P. 2000, A&AS, 144, 469
- Strömgren, B. 1966, ARA&A, 4, 433

Chapter 5

GSC 04778–00152, a contact binary with a visual companion

This Chapter is based on the following published papers:

The contact binary GSC 04778–00152 with a visual companion

T. Tuvikene, T. Eenmäe, C. Sterken, and E. Brogt,
2008, Baltic Astronomy, 17, 79 (Paper I)

Photometry and spectroscopy of the contact binary GSC 04778–00152

T. Tuvikene, C. Sterken, T. Eenmäe, R. Hinojosa-Goñi, E. Brogt, P. Longa Peña,
T. Liimets, M. Ahumada, P. Troncoso, and N. Vogt,
2008, JAD, 14, 1 (Paper II)

Abstract

Photometric and spectroscopic observations of the unstudied 12th-magnitude eclipsing binary GSC 04778–00152 are presented. We report the discovery of a visual companion about 1 mag fainter and 2 arcsec away from the binary. By subtracting the light contribution of the visual companion, we obtain the *UBVRI* light curves of the binary system alone. The shape of the light curve indicates that GSC 04778–00152 is an A-type W UMa contact binary. From light-curve modelling, we derive parameters of the binary system.

5.1 Introduction

The variable star GSC 04778–00152 ($\alpha_{J2000} = 05^{\text{h}}31^{\text{m}}21^{\text{s}}$, $\delta_{J2000} = -7^{\circ}23'42''$, see Fig. 5.1) was discovered by the All Sky Automated Survey (ASAS) and classified as a contact or semi-detached binary with the period of 0.51746 days (Pojmanski 2002).

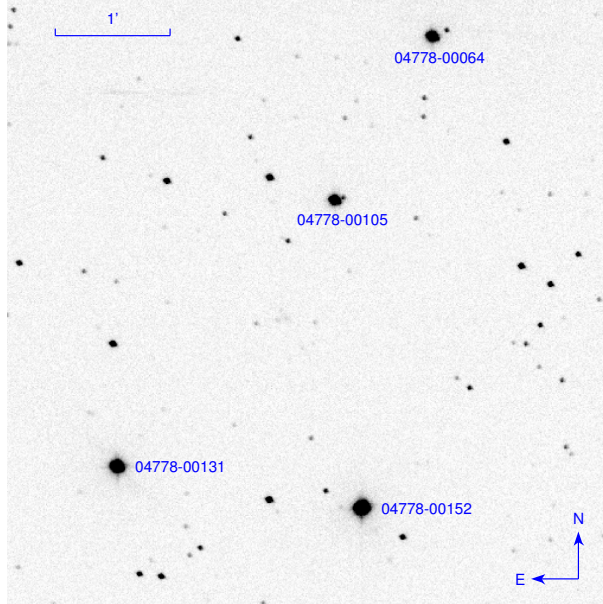


Figure 5.1: SAAO V -band frame of GSC 04778–00152 and associated comparison stars. The field of view is $5\text{'}3$.

The reported V -magnitude at maximum brightness was 11.95 and the amplitude of variation in V was 0.29 mag.

We detected the variability of GSC 04778–00152 from wide-field images of the region around the δ Sct star V1162 Ori in January 2006. Later we conducted follow-up observations, collecting photometric data in multiple passbands, and additional spectra.

5.2 Observations and data reduction

5.2.1 CCD photometry

CCD photometry of GSC 04778–00152 was carried out on 54 nights during 9 observing runs, see the log of observations in Table 5.1.

In January 2006 the observations were made with the 41-cm Meade telescope at Observatorio Cerro Armazones (OCA), Chile, using an SBIG STL-6303E CCD camera (3072×2048 pixels, FOV $23\text{'}0 \times 15\text{'}4$) and Johnson V filter. As the main target was V1162 Ori, the observations were not optimised for GSC 04778–00152: the binary star was recorded at the edge of the wide field where the image quality was rather poor due to optical aberrations.

On 3 nights in December 2006 and on 2 nights in October 2007 we used the 2.4-m Hiltner telescope at the MDM Observatory, Arizona, USA, equipped with the $8\text{k} \times 8\text{k}$ Mosaic imager (FOV $23\text{'}6 \times 23\text{'}6$).

Table 5.1: Journal of photometric observations of GSC 04778–00152.

Date	JD–2450000	Obs.	Nights	band	Observers
2006 Jan	3744–3753	OCA	9	V	TT
2006 Dec	4078–4081	MDM	3	V	EB
2006 Dec	4085–4091	OCA	6	–	RH
2006 Dec–2007 Jan	4095–4126	Tartu	7	V	TE, TL
2007 Jan	4118–4125	OCA	4	–	MA, PT, PLP
2007 Jan–Mar	4132–4172	SAAO	17	UBVRI	TT
2007 Oct	4390–4391	MDM	2	V	EB
2006 Nov	4057–4058	SAT	2	uvby	CS
2007 Jan	4120–4122	SAT	2	uvby	CS

Table 5.2: CCD photometric observations of GSC 04778–00152. N is the number of individual magnitudes obtained during each night in the indicated passband, and r is the aperture-radius factor used for the magnitude extraction.

JD–2450000	Obs.	N	band	r
3745.6–3753.6	OCA	755	V	2.5
4078.9–4081.9	MDM	88	V	3.0
4085.7–4091.8	OCA	2304	–	2.0
4095.4–4126.4	Tartu	265	V	2.0
4118.5–4125.7	OCA	984	–	2.0
4134.4–4170.3	SAAO	69	U	3.0
4132.4–4172.3	SAAO	149	B	3.0
4132.4–4172.3	SAAO	395	V	3.0
4132.4–4170.3	SAAO	123	R	3.0
4132.4–4170.3	SAAO	123	I	3.0
4391.0–4392.0	MDM	26	V	3.0

In December 2006 and January 2007, we also used the 41-cm Meade telescope at OCA, using an SBIG ST-7XME CCD camera (FOV $5.9' \times 3.9'$) with no filter.

At the Tartu Observatory the observations were carried out in December 2006 and January 2007, using the 60-cm telescope with a SpectraSource Instruments HPC-1 camera (1024×1024 pixels, FOV $11.2' \times 11.2'$) and V filter.

From January to March 2007 the system was observed using the 1.0-m telescope at SAAO, Sutherland, South Africa with an STE4 CCD camera (1024×1024 pixels, FOV $5.3' \times 5.3'$) and $UBVRI$ filters.

The frames were calibrated by subtracting bias and through dividing by twilight-sky flat fields. For the Tartu data, dark frames were subtracted instead of bias frames. Magnitudes were extracted by using aperture photometry with the PHOTWORK software in a workflow described in Chapter 1. Apertures were scaled by the average FWHM of stellar images on the frames; aperture radii between 2.0 and $3.0 \times \text{FWHM}$ were used (the aperture-radius factors r are listed in Table 5.2).

The CCD images from the MDM Observatory revealed a slightly fainter visual

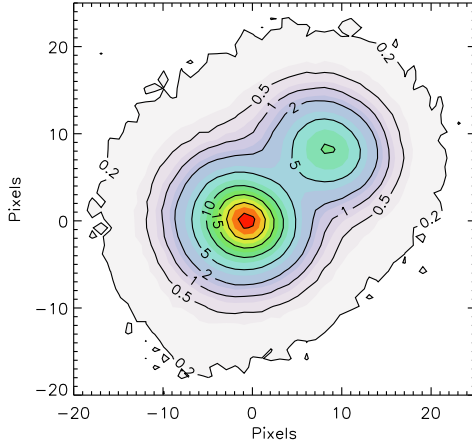


Figure 5.2: The GSC 04778–00152 system: the binary (star A, lower-left) and its fainter visual companion (star B, upper-right). North is up and east is left. The contours correspond to constant flux in the V -band CCD image (values in $1000 \times \text{ADU}$). The image scale is $0''.173 \text{ px}^{-1}$.

companion (hereafter star B) about 2 arcsec away from the eclipsing binary (star A). The stars A and B are indicated in Fig. 5.2.

Aperture photometry was used to measure the total brightness of the stars A and B together. In order to extract the magnitudes of stars A and B separately, we analysed a subset of CCD frames with PSF photometry, using DAOPHOT routines in ESO-MIDAS.

On the basis of four nights over a 90-day time interval, the visual companion B did not show any variability. This allowed us to subtract the contribution of star B from the composite light curves acquired with aperture photometry.

The Landolt standard star SA 98 193 and about 15 surrounding secondary standards were observed on a photometric night (JD 2454145). These observations, together with the published data from Galadí-Enríquez et al. (2000), were used to establish the transformation of the magnitudes to the standard $UBVRI$ system. The standard magnitudes and colours of stars in the GSC 04778–00152 field are presented in Table 5.3.

The constant star GSC 04778–00131 of similar brightness and colours as GSC 04778–02122, was used as the comparison star for the binary in order to construct differential light curves.

5.2.2 Photoelectric photometry

The system was observed with the Strömgren Automatic Telescope (SAT) at ESO, La Silla at three occasions in November 2006 and January 2007. A diaphragm of 17 arcsec was used. Extinction corrections were derived from standard-star observations, and transformations to the standard $uvby$ system were based on the methods described

Table 5.3: *UBVRI* photometry for stars in the GSC 04778–00152 field.

Star	<i>V</i>	<i>B</i> – <i>V</i>	<i>U</i> – <i>B</i>	<i>V</i> – <i>R</i>	<i>V</i> – <i>I</i>
A (min II)	12.524 (0.009)	0.504 (0.010)	0.088 (0.012)	0.298 (0.011)	0.570 (0.011)
A (min II) + B	12.078 (0.009)	0.584 (0.010)	0.140 (0.010)	0.326 (0.011)	0.647 (0.011)
B	13.264 (0.013)	0.757 (0.017)	0.271 (0.036)	0.387 (0.021)	0.792 (0.017)
GSC 04778–00131	12.501 (0.009)	0.549 (0.010)	0.052 (0.008)	0.334 (0.011)	0.646 (0.011)
GSC 04778–00064	13.322 (0.010)	0.642 (0.011)	0.101 (0.007)	0.385 (0.011)	0.741 (0.012)
GSC 04778–00105	13.657 (0.012)	0.687 (0.013)	0.095 (0.015)	0.422 (0.017)	0.815 (0.016)

 Table 5.4: Photoelectric *uvby* observations of GSC 04778–00152.

JD–2400000	Phase	<i>y</i>	<i>b</i> – <i>y</i>	<i>m</i> ₁	<i>c</i> ₁
54057.73606	0.258	11.953	0.361	0.174	0.517
54057.81083	0.402	12.027	0.369	0.163	0.548
54058.82131	0.355	11.948	0.387	0.147	0.558
54120.68043	0.900	12.016	0.388	0.148	0.562
54122.67954	0.763	11.920	0.368	0.164	0.511

by Olsen (1994). The *uvby* observations are summarised in Table 5.4. The averaged indices at phases 0.35 and 0.70 are: $V = 11.93 \pm 0.01$, $b - y = 0.377 \pm 0.009$, $m_1 = 0.055 \pm 0.008$, $c_1 = 0.534 \pm 0.023$. Figure 5.5a shows the *y* magnitudes transformed to the Johnson *V* scale.¹ There is a systematic difference of $0^m 02 \pm 0^m 006$ between the photoelectrically determined *V* and the result from CCD imaging. We attribute this difference to the selection of standard stars, and to different detector and filter characteristics.

5.2.3 Spectroscopy

Spectroscopic observations were carried out at the Tartu Observatory, Estonia, using the 1.5-m telescope with the Cassegrain spectrograph ASP-32 and an Andor Newton CCD camera. The spectrograph was used in low- and moderate-resolution modes with the gratings of 600 and 1200 lines mm⁻¹. We observed GSC 04778–00152 in four wavelength regions that are presented in Table 5.5. Spectral resolution was determined either using very narrow (OI) telluric emission lines in red regions or narrow lines from a ThAr spectral lamp in blue regions.

Three spectra in the red and one in the near-infrared region were obtained in January and February 2007. The integration time was 50 min for all spectra. The blue region was covered in October and November 2007, with integration times of 50 and 90 min. Due to the average seeing of 4 arcsec and the 2-arcsec-wide slit that was oriented in the north-south direction, we also recorded the contribution of the fainter companion, which affects the spectrum in the red region, while in the blue region the contamination is not noticeable.

¹The Strömgren *uvby* system, by definition, only comprises colour indices $b - y$, $m_1 = (v - b) - (b - y)$ and $c_1 = (u - v) - (v - b)$. For normal stars, there is a linear relation between *y* and Johnson *V*.

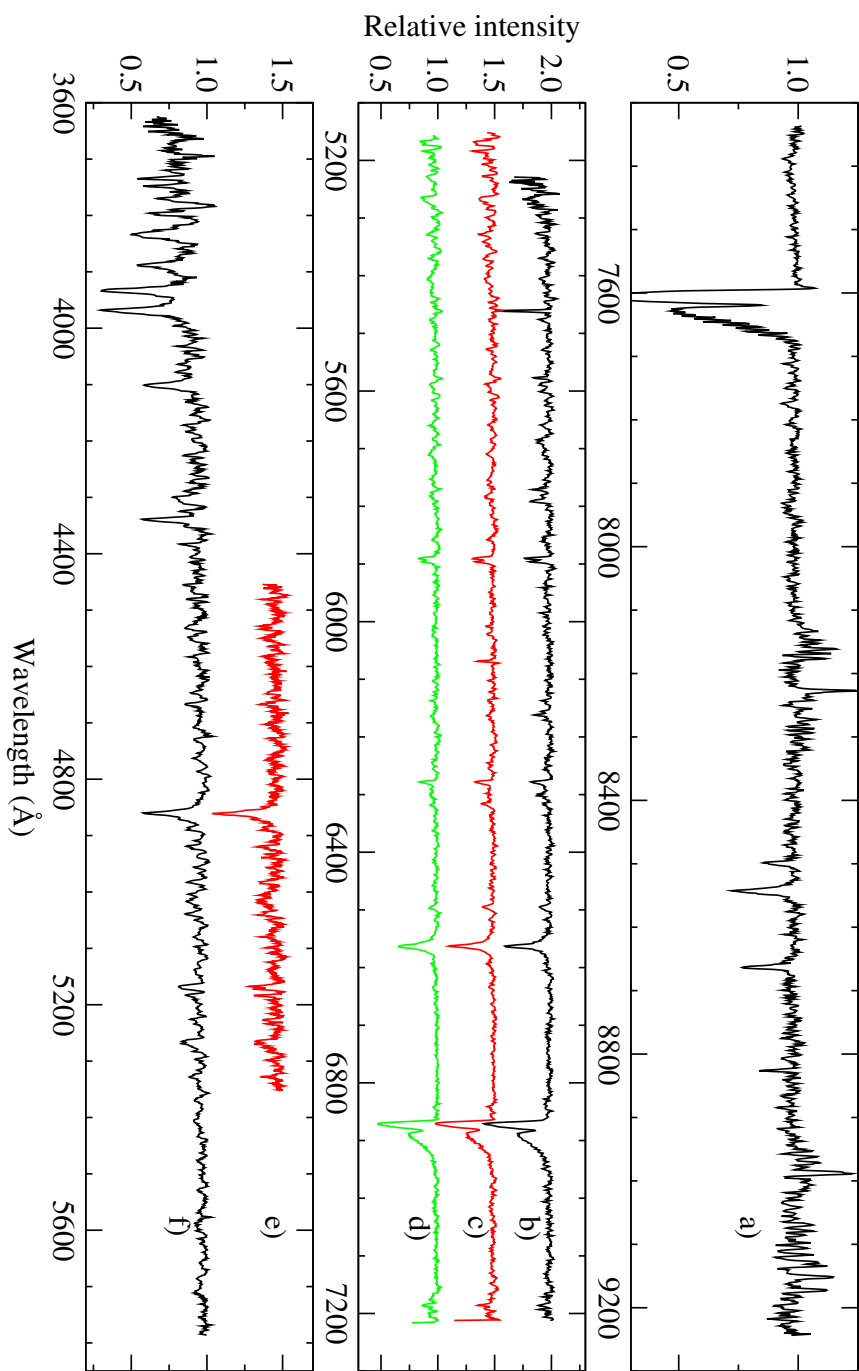


Figure 5.3: Low and medium resolution normalised spectra of GSC 04778-00152, see Table 5.5 for details.

Table 5.5: Journal of spectroscopic observations. Label refers to Fig. 5.3.

Date	HJD	Phase	Exposure (s)	Region (Å)	Resol.	Disp. (Å/px)	Label
2007 Feb 23	54155.27147	0.748	3000	7340–9240	3360	1.19	a
2007 Jan 24	54125.41918	0.058	3600	5152–7250	2600	1.29	b
2007 Feb 10	54142.21358	0.514	3000	5152–7250	2600	1.29	c
2007 Feb 10	54142.33403	0.756	3000	5152–7250	2600	1.29	d
2007 Nov 10	54415.55488	0.755	3000	4454–5352	4340	0.53	e
2007 Oct 31	54405.46060	0.247	5400	3625–5785	2025	1.35	f

Data reduction was carried out using IRAF. The stellar signal was extracted from CCD frames and the wavelength scale was determined using comparison spectra of a ThAr lamp. One-dimensional spectra were rebinned with a step of 1.0 \AA for spectra obtained with the 600 lines mm^{-1} grating, and 0.5 \AA for higher-resolution spectra. The signal-to-noise ratio (SNR) for all spectra was between 50 and 80, depending on wavelength. The spectra were normalised and analysed using routines in the ESO-MIDAS software. We did not correct our spectra for heliocentric velocity.

For the near-infrared spectrum (a in Table 5.5 and on Fig. 5.3), fringing correction was made before extraction, using a $\text{SNR} \sim 500$ spectrum that was practically free of stellar lines (the spectrum of the rapidly rotating O-class star 68 Cygni).

The low-resolution spectrum of the blue region, obtained on 2007 October 31 / November 1, was used to derive the β index of GSC 04778–00152. The normalised spectrum was convolved with the response curves of the H β wide and narrow filters of the SAT photometer. The instrumental β index was then transformed to the standard system, using observations of 7 standard stars from Olsen (1983), yielding $\beta = 2.658 \pm 0.025$.

5.3 Results

5.3.1 CCD astrometry

Astrometric measurements of stars A and B were performed on the basis of CCD frames from the MDM Observatory. The seeing in these frames varied between 1.4 and 1.8 arcsec. The stellar images were fitted with PSF, using DAOPHOT software. The PSF was constructed from the Moffat function on which empirical corrections were applied.

In order to determine the pixel scale and the orientation of the detector, we observed 13 astrometric standard stars in the open cluster NGC 1647. The coordinates and proper motions of the stars were taken from Geffert et al. (1996).

The measurements of star B relative to star A are presented in Table 5.6. The columns list the epoch of the measurement, the number of CCD frames (N), the angular separation with standard error (ρ, σ_ρ), and the position angle, measured from north to east, with standard error (θ, σ_θ). The position of star B in October

Table 5.6: Astrometric measurements of star B relative to star A.

Epoch (Julian year)	N	ρ ["]	σ_ρ ["]	θ [°]	σ_θ [°]
2006.9429	21	2.131	0.002	311.67	0.08
2007.7947	11	2.133	0.002	311.76	0.10

Table 5.7: Heliocentric Julian dates of minima. The error column gives the error as computed with the Kwee–van Woerden procedure.

HJD–240000	Error	E	$O - C$	Source
53746.61205	0.00022	0	0.00006	Paper I (OCA)
54080.88796	0.00014	646	-0.00015	Paper I (MDM)
54089.68549	0.00014	663	0.00064	Paper II (OCA)
54091.75229	0.00015	667	-0.00237	Paper II (OCA)
54104.43254	0.00099	691.5	0.00022	Paper II (Tartu)
54118.66246	0.00009	719	0.00012	Paper II (OCA)
54125.64792	0.00025	732.5	-0.00007	Paper II (OCA)
54139.36075	0.00020	759	0.00020	Paper I (SAAO)
54167.30315	0.00010	813	0.00001	Paper I (SAAO)
54168.33783	0.00033	815	-0.00022	Paper II (SAAO)

2007 coincides, within the errors, with the position measured in December 2006.

5.3.2 Primary and secondary minima

Our V -band photometry (Paper I) covers 4 primary minima that were used for period analysis. Additional photometry from Paper II adds 4 primary and 2 secondary minima. The times of minimum were determined with the Kwee–van Woerden method (Kwee & van Woerden 1956) and are listed in Table 5.7. Figure 5.4 shows the corresponding $O - C$ diagram. It is evident that some of the times of minimum from Paper II display a larger scatter in the $O - C$ graph, evidently the symptom of an unstable observatory clock.

Using a linear weighted least-squares fit, we obtain the following ephemeris for the primary minima:

$$\begin{aligned} \text{HJD (Min I)} = 2453746.61199 + & 0.5174553 E \\ & \pm 0.00021 \quad \pm 0.0000003 \end{aligned} \quad (5.1)$$

5.3.3 Phase diagrams

The differential $UBVRI$ and filterless light curves, phased with the derived period (5.1), are plotted in Fig. 5.5. The shape of the light curve is typical of W UMa type systems. It can be seen that the eclipses have unequal depths and that the secondary minimum displays an interval of constant brightness, indicating total occultation.

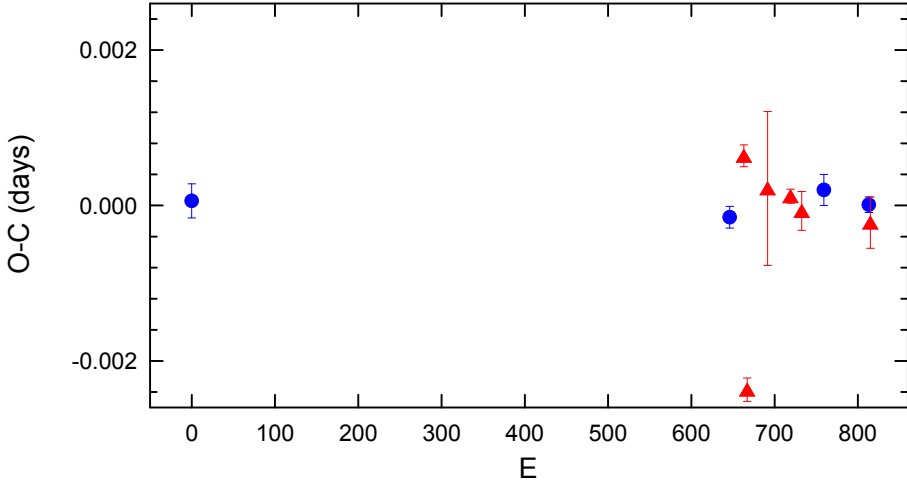


Figure 5.4: $O - C$ diagram for GSC 04778–00152 constructed with ephemeris (5.1). ●: data from Paper I, ▲: data from Paper II.

tion. Star A is therefore an A-type W UMa star where the more massive component has the greater surface brightness.

5.3.4 Peculiarities

The phase diagram in Fig. 5.5a displays an intriguing coincidence of one outlying SAT y and Tartu V magnitude around phase 0.25 and (to a lesser extent) around phase 0.75. In order to check whether this is a systematic effect, or whether this is mere coincidence, we have inspected all V and filterless light curves discussed before. No such events were observed around JD 2453748.554 nor on JD 2453750.61935 (OCA V , phase ~ 0.75). Also the SAAO V light curves at JD 2454133.28405 ($\phi = 0.257$), JD 2454136.38388 ($\phi = 0.247$) and JD 2454145.44 ($\phi = 0.749$)² do not reveal any such deviations. Figure 5.6 shows the two outliers observed at Tartu.

It is not unambiguously clear whether these drops in light (of a typical duration of about 7 minutes) are systematically linked to these two phases of maximum. Note that the SAT data were obtained in a non-differential way.

5.4 Analysis

5.4.1 Spectral type

From the photoelectric photometry of GSC 04778–00152 (including star B) we derived the reddening-free colour indices $[c_1]$ and $[m_1]$ (Strömgren 1966), which point to a spectral type of F3–F5 for the binary.

²Note that the time resolution of the SAAO data is substantially lower because of the cycle time needed to observe in 5 passbands.

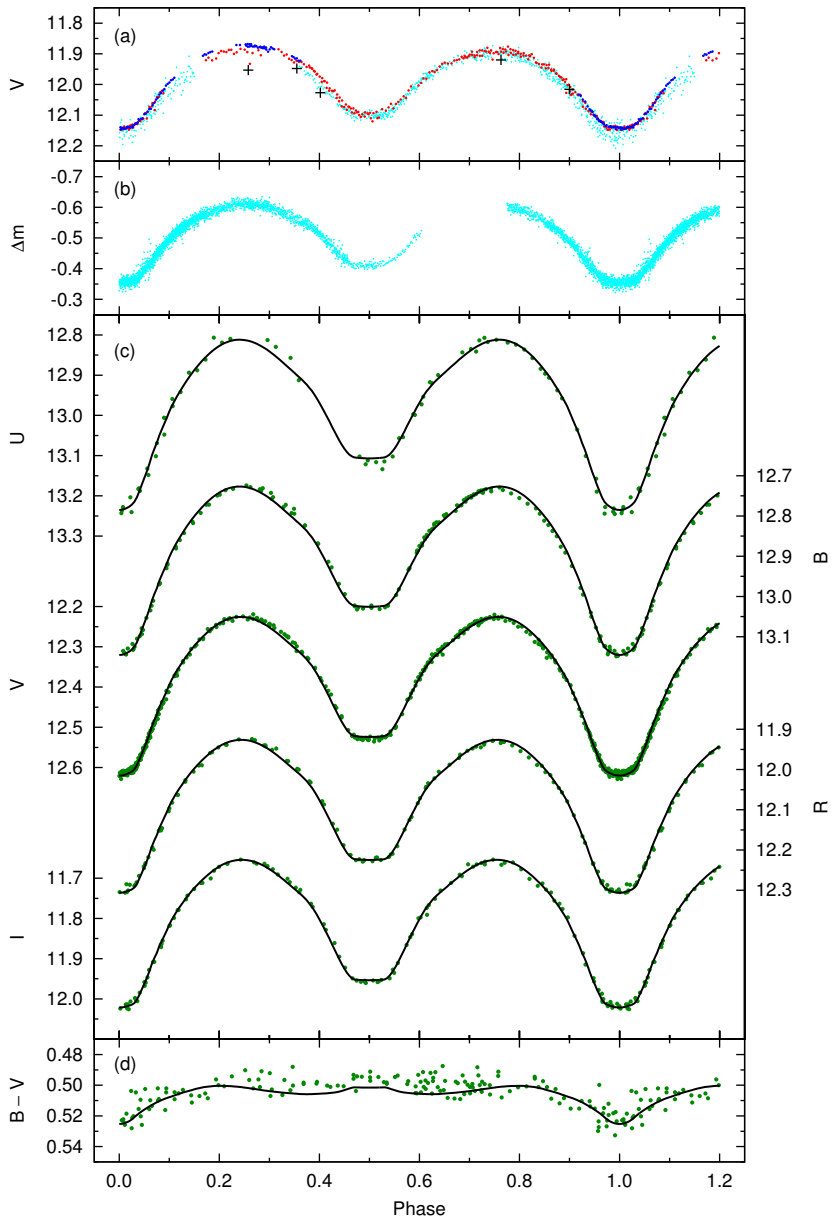


Figure 5.5: Phase diagrams of GSC 04778-00152. (a) Differential V light curve including the contribution of star B. Cyan dots refer to the OCA data, red dots to the Tartu data, blue dots to the MDM data, and plusses denote the SAT y magnitudes transformed to the Johnson V scale. (b) OCA filterless differential light curve. (c) Phase diagram of the binary star A, with the light of star B subtracted (SAAO data). The light curve solution is shown with a continuous line. (d) $B - V$ colour curve of star A (points), together with the synthetic curve (solid line).

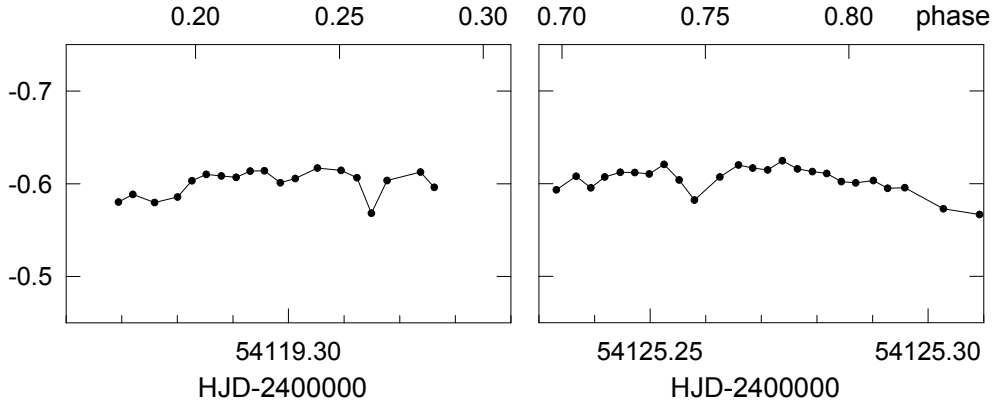


Figure 5.6: Detail of V light curves with the two outlier V observations detected around phases 0.25 and 0.75.

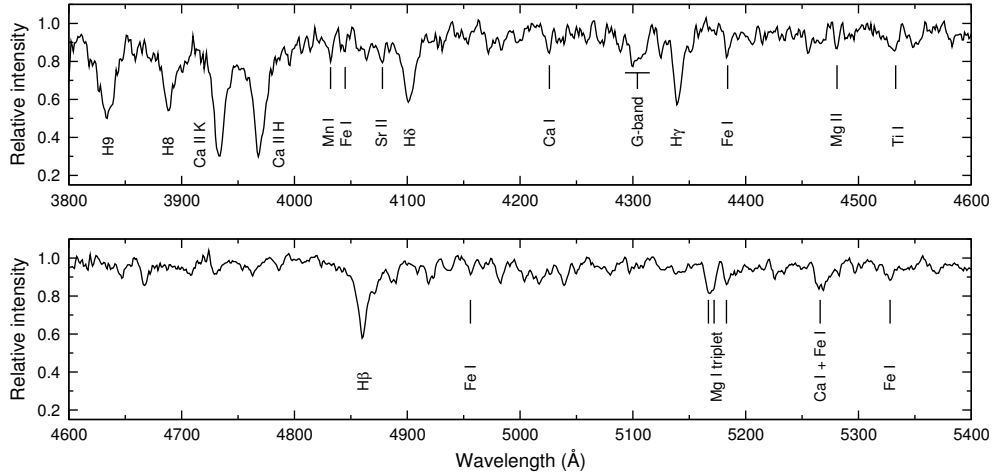


Figure 5.7: The spectrum of GSC 04778–00152 obtained on 2007 October 31 / November 1, at phase 0.25.

Using the Digital Spectral Classification Atlas³, we analysed the spectrum obtained on 2007 October 31 / November 1 (Fig. 5.7). The strength of the G-band relative to $H\gamma$ and the strengths of Ca II K and H lines lead to a spectral type around F5. The widths of the hydrogen lines and their strengths compared to metallic lines also refer to F5. Comparing the G-band strength of GSC 04778–00152 with the observed $H\beta$ standards of spectral classes F4V and F6V, places our target in between them. There is no evidence that luminosity class is above IV, the luminosity-sensitive lines are more similar to those in dwarfs.

We conclude that the spectral class of star A at phase 0.25 is F5V. The uncertainty

³http://nedwww.ipac.caltech.edu/level5/Gray/Gray_contents.html

of our estimation does not exceed one subclass. As can be seen from the $B - V$ curve (Fig. 5.5d), the system colour does not change between phase 0.25 and the secondary minimum, where we see only the hotter binary component. Therefore the estimated spectral class corresponds mainly to the primary star of the binary.

5.4.2 Stellar parameters

The *uvby* indices from Section 5.2.2, together with the β index from Section 5.2.3 enable us to determine approximate stellar parameters. Applying the Vienna TempLogG v2 web interface⁴, we obtain $E_{b-y} = 0.112 \pm 0.060$, $M_V = 2.7 \pm 0.5$, $T_{\text{eff}} = 6500 \pm 300$ K, and $\log g = 4.0 \pm 0.4$. The system is at a distance $d = 560 \pm 180$ pc. Note that these parameters apply to the composite system A + B.

The absolute magnitude and distance may also be derived from the luminosity calibration of contact binaries (Rucinski & Duerbeck 1997). By using the intrinsic colour index, which corresponds to the F5V spectral type, $(B - V)_0 = 0.44$ (Straižys 1992), and the period value (Eq. 5.1), we get $M_V = 2.7 \pm 0.4$ and $d = 740^{+170}_{-110}$ pc.

5.4.3 Light-curve solution

The *BVRI* light curves of star A were solved simultaneously with the binary star modelling package PHOEBE, version 0.29d (Prša & Zwitter 2005), which uses the Wilson-Devinney code as back-end. Curve-dependent weights were applied, according to the photometric errors in separate passbands. The program was run in the mode “overcontact binary not in thermal contact”.

Assuming a spectral type of F5V and using the effective temperature calibration from Gray et al. (2003), we fixed $T_{\text{eff},1} = 6530$ K for the primary component. We also adopted the gravity darkening coefficients, $g_1 = g_2 = 0.32$, and the albedo values, $A_1 = A_2 = 0.5$, for the modelling. Subscripts refer to the binary components. A logarithmic limb-darkening law was chosen, as suggested by van Hamme (1993). The fitted parameters were the mass ratio, $q = m_2/m_1$, the orbital inclination, i , the effective temperature of the secondary, $T_{\text{eff},2}$, the surface potential, $\Omega_1 = \Omega_2$, and the luminosities of the primary star. The luminosity in *U* was fitted separately, using the *U*-band light curve alone and fixing all the parameters from the *BVRI* solution.

For error evaluation we carried out a data-resampling experiment, similar to the one described in Maceroni & Rucinski (1997). Half of the *BVRI* data points were randomly selected and the resampled light curves were simultaneously solved with the program PHOEBE, using the complete light-curve solution as a starting point. The procedure was repeated 100 times.

The derived binary system parameters are listed in Table 5.8. We give both sets of estimates, the complete light-curve solution with standard errors from PHOEBE, and the median values of the parameters with uncertainties at 68 percent confidence level from the resampling experiment. The synthetic light and colour curves are plotted in Fig. 5.5.

⁴<http://ams.astro.univie.ac.at/templogg/>

Table 5.8: System parameters from the light-curve solution of star A. Subscripts refer to the binary components.

Parameter	Solution	Resampling	Parameter	Solution	Resampling
$q = m_2/m_1$	0.1822(7)	0.1819(13)	Ω_{in}	2.1878	
$i [^\circ]$	78.07(17)	78.13(27)	Ω_{out}	2.0711	
$T_{\text{eff},1}$ (fixed) [K]	6530		Fill-out	0.303(24)	
$T_{\text{eff},2}$ [K]	6039(7)	6041(10)	r_1/a (pole)	0.5026	0.5028(10)
$\Omega_1 = \Omega_2$	2.1524(28)	2.1516(50)	r_1/a (side)	0.5516	0.5519(14)
$[L_1/(L_1 + L_2)]_U$	0.8725(17)		r_1/a (back)	0.5762	0.5764(16)
$[L_1/(L_1 + L_2)]_B$	0.8711(14)	0.8711(16)	r_2/a (pole)	0.2365	0.2365(6)
$[L_1/(L_1 + L_2)]_V$	0.8623(11)	0.8623(11)	r_2/a (side)	0.2473	0.2474(7)
$[L_1/(L_1 + L_2)]_R$	0.8567(10)	0.8567(13)	r_2/a (back)	0.2897	0.2900(15)
$[L_1/(L_1 + L_2)]_I$	0.8511(9)	0.8511(14)			

5.5 Conclusions

GSC 04778–00152 is a slightly-reddened eclipsing contact binary with a visual companion. Companion B is redder and about 1 mag fainter than binary A. The stars have an angular separation of 2.132 ± 0.002 arcsec which, at the derived distance of 600–800 pc, would mean a physical separation of more than 1000 AU.

Our spectra indicate that the spectral type of star A at phase 0.25 is F5V, which is mainly attributed to the primary component. The corresponding effective temperature is 6530 K. From the light-curve solution we get that the secondary component has 18 percent of the mass of the primary and is about 500 K cooler.

References

- Galadí-Enríquez, D., Trullols, E., & Jordi, C. 2000, A&AS, 146, 169
 Geffert, M., Bonnefond, P., Maintz, G., & Guibert, J. 1996, A&AS, 118, 277
 Gray, R. O., Corbally, C. J., Garrison, R. F., McFadden, M. T., & Robinson, P. E. 2003, AJ, 126, 2048
 Kwee, K. K. & van Woerden, H. 1956, Bull. Astron. Inst. Netherlands, 12, 327
 Maceroni, C. & Rucinski, S. M. 1997, PASP, 109, 782
 Olsen, E. H. 1983, A&AS, 54, 55
 Olsen, E. H. 1994, A&AS, 106, 257
 Pojmanski, G. 2002, Acta Astronomica, 52, 397
 Prša, A. & Zwitter, T. 2005, ApJ, 628, 426
 Rucinski, S. M. & Duerbeck, H. W. 1997, PASP, 109, 1340

Straizys, V. 1992, in *Multicolor Stellar Photometry* (Pachart Publishing House, Tucson, Arizona)

Strömgren, B. 1966, ARA&A, 4, 433

van Hamme, W. 1993, AJ, 106, 2096

Chapter 6

On the light variability of CY Aquarii

This Chapter is based on the following published papers:

New times of maximum of CY Aquarii

T. Tuvikene, C. Sterken, E. Brogt, D. Cont, A. Henden, C. Papadaki,
I. Volkov, and C. Wiedemair,
2010, JAD, 16, 2

Times of maximum of CY Aquarii: the 2010 season

C. Sterken, C. Wiedemair, T. Tuvikene, J. Rigo, T. Munaro,
M. Untergassmair, and D. Rainer,
2011, JAD, 17, 2

Multiband photometry of CY Aquarii: the 2011 season

C. Sterken, C. Wiedemair, T. Munaro, J. Rigo, J. Durnwalder, A. Kirchler,
J. Damini Hofer, F. Schraffl, E. H. Olsen, and T. Tuvikene,
2012, JAD, 18, 2

Abstract

We present a collection of 155 new times of maximum of the SX Phoenicis star CY Aquarii. 102 timings, together with 20 times of maximum taken from the literature, lead to a new local linear ephemeris for 2003–2009 with a formally slightly shorter period than the one for 1996–2002. Additional 24 times of maximum from the 2010 season and 29 timings from the 2011 season lead to slightly more precise local linear ephemerides for 2003–2010 and 2003–2011. In addition, we present *uvwby* light curves for CY Aqr. Our data from the 2011 season display the smallest residual spread compared to any other substantial dataset published during the last decade. It will

require at least another half decade of additional monitoring before any significant update to any model can be considered. Such monitoring should preferably occur at regular intervals, be done in a consistent photometric band, and at high time resolution.

6.1 Introduction

CY Aquarii (BD +0°4900) is a short-period (87.9 min) large-amplitude (0^m71 in V) SX Phoenicis star. Since the discovery of its variability in 1934, this pulsating star has been extensively observed, and several investigations of its changing pulsation period using the $O - C$ diagram have been published. The latest substantial study of the long-term period change of CY Aqr (Fu & Sterken 2003) listed 23 new times of maximum (hereafter denoted as T_{\max}), and from an analysis of the $O - C$ diagram of all available T_{\max} , these authors derived an updated value of the pulsation period of $0^d061038394 \pm 0^d000000006$. A linear period change combined with the light-time effect in a highly-eccentric orbit led them to a possible solution involving a highly-eccentric ($e = 0.77 \pm 0.01$) orbit with period $P_{\text{orb}} = 52^{\text{d}}5 \pm 0^{\text{d}}3$. Their Fig. 3 indicates that by the end of 2002, the $O - C$ curve was approaching a maximum, so that the subsequent decade could possibly confirm the binary model.

We present a collection of T_{\max} obtained since the last maximum used by Fu & Sterken (2003), in addition to 6 timings obtained in 1998–2000. These times were

Table 6.1: Journal of photometric observations: JD, observatory site, number of nights with at least one T_{\max} , photometric band and number of measurements. “Red.” refers to the initials of the author who carried out the data reduction.

JD–2400000	Site	N	Band	Data	Observer	Red.
51107.62–51195.60	USNO	4	UVI_c	290	AH	AH
51806.74–51806.82	TASS	1	VI_c	82	AH	AH
53249.50–53250.58	SKO	2	—	794	CP	TT
53286.47–53292.46	OHL	4	—	806	CP	TT
53304.27–53306.27	MLO	3	V	278	CS	CS
53304.27–53311.40	SAI	6	—	911	IV	TT
53556.79–53565.93	OCA	6	B	1910	TT	TT
53561.73–53561.84	OCA	1	—	16057	TT	TT
53612.92–53613.78	MDM	2	B	84	EB	TT
53682.34–53689.34	SAAO	4	V	322	TT	TT
54729.29–54829.27	RGB	9	—	4972	DC, CW	TT
55460.35–55547.29	RGB	12	—	2346	CW+	TT
55826.31–55923.30	RGB	12	—	3466	CW+	TT
55886.53–55889.60	SAT	3	$uvby$	195	CS	EHO

Observer code: EB = E. Brogt; DC = D. Cont; AH = A. Henden;
 CP = C. Papadaki; CS = C. Sterken; TT = T. Tuvikene; IV = I. Volkov;
 CW = C. Wiedemair; EHO = E. H. Olsen.

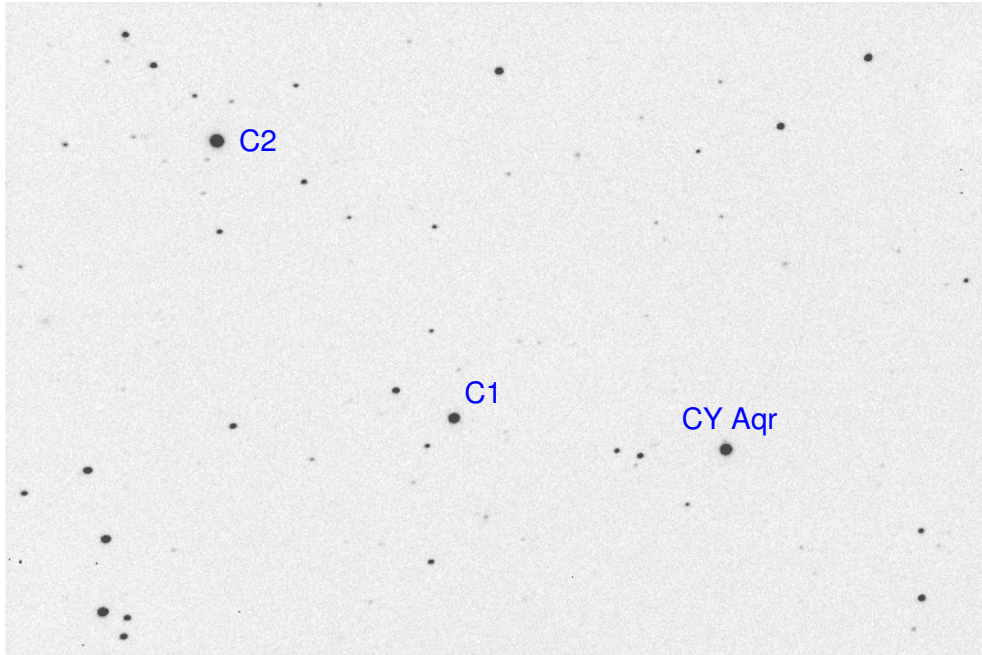


Figure 6.1: CY Aqr CCD frame of 11 October 2010. North is up and East is left, field of view is $18' \times 12'$. CY Aqr and the comparison stars $C_1 = \text{GSC } 00567-01826$ and $C_2 = \text{GSC } 00567-02036$ are marked.

derived from new photometric observations as described in Section 6.2, together with some T_{\max} taken directly from the literature.

6.2 Observations and data reduction

The bulk of the data discussed in this Section were obtained through CCD imaging at more than half a dozen observatories worldwide. Some light curves were also acquired through differential photomultiplier-based photometry. Table 6.1 gives the journal of observations.

Except when stated otherwise, CCD magnitudes were extracted by means of aperture photometry, using the PHOTWORK software in a workflow as described in Chapter 1. Aperture sizes were scaled with the full width at half maximum (FWHM) of star images, and an aperture radius of $(1.6, 2.0, \text{ or } 2.5) \times \text{FWHM}$ was used throughout each data set. Exceptions to this rule are those data sets where we used the magnitudes extracted by the cited authors. Deviations from the above-mentioned procedures are indicated in the following subsections.

Differential light curves of CY Aqr were obtained by using $C_1 = \text{GSC } 00567-01826$ as a comparison star, see Fig. 6.1 for a finding chart.

6.2.1 USNO

CCD frames were acquired with the USNO-Flagstaff 1.0-m telescope on October 21 and 29, 1998 (V and I_c band, respectively) and on December 15, 1998 and January 17, 1999 (U band). The field of view was $11'.3 \times 11'.3$, with pixel scale of $0''.6763 \text{ pixel}^{-1}$ using a SITe/Tektronix thinned, back-illuminated 1024×1024 CCD. Aperture photometry was used with aperture diameter of 14 arcsec.

6.2.2 TASS

This is a simultaneous V/I_c set from September 19, 2000, using the USNO TASS Sky Survey camera. TASS uses dual 10-cm telescope apertures, with a Loral front-illuminated $2k \times 2k$ CCD for each telescope. The final image scale is $7''.5 \text{ pixel}^{-1}$. Each exposure is 120 seconds long, and the resultant images were dark-subtracted and flat-fielded. Aperture photometry was used, with an aperture set to 30 arcsec diameter to match the pixel scale and seeing with the system.

6.2.3 Skinakas Observatory

Observations with the 1.3-m Ritchey-Chrétien telescope were made at Skinakas Observatory (SKO, Greece) on August 31 and September 1, 2004. The field of view (FOV) was $8'.5 \times 8'.5$ on a 1024×1024 pixel SITe CCD camera.

6.2.4 Observatorium Hoher List

On October 7–13, 2004, CCD frames were acquired at Observatorium Hoher List (OHL) in Germany, using the 1-m Cassegrain-Nasmyth telescope with the 2048×2048 , $15\text{-}\mu\text{m}$ pixel HoLiCam CCD camera with a two-sided read-out. The focal reducer was used, the effective FOV was $14'.1 \times 14'.1$.

6.2.5 Mount Laguna Observatory

In September 2004 the Smith 24-inch telescope at Mount Laguna Observatory (MLO, San Diego State University, CA) was used. The telescope is an $f/20$ Cassegrain reflector equipped with a pulse-counting photoelectric photometer employing a thermoelectrically cooled Hamamatsu R943-02 GaAs photomultiplier tube.

The observations were carried out in a continuous sequence $C, P, S, C, P, S, C, \dots$, where P is CY Aqr, S the sky background, and C is the $V \approx 11.7$ comparison star about 5 arcmin East of P (see Fig. 6.1). As a rule, each observation consisted of at least five 10-s integrations, but during the phase of maximum light, P consisted of 2–3 series of such integrations. All measurements were taken through a standard Johnson V filter. The counts were corrected for dead time and for sky-background contribution, the resulting instrumental magnitudes were corrected for atmospheric extinction, and then differential magnitudes with respect to C were formed. No transformation to the standard Johnson system was attempted.

Sky conditions were photometric. The combination of manual operation and small aperture yielded a data density of 5–7 measurements during a time interval of 15

minutes centred on the time of maximum, which is close to the lower limit for a reliable determination of T_{\max} .

6.2.6 Crimean Laboratory of the Sternberg Astronomical Institute

In October–November 2004 observations were made at the Sternberg Astronomical Institute Crimean Station (SAI). The following setups were used: on October 25 the Zeiss 60-cm Cassegrain telescope equipped with an Apogee-7 camera, and on October 27–30 and November 1, the Maksutov 50-cm telescope with a Pictor 416 CCD camera. Some nights were partially clouded. No adequate flat-field exposures could be collected, hence all magnitudes were obtained from frames that were only corrected for dark.

6.2.7 Observatorio Cerro Armazones

The star was intensely observed with the 84-cm telescope at Observatorio Cerro Armazones (OCA), Chile during 6 nights in July 2005. An SBIG ST-9E CCD-camera with a 512×512 KAF 0261E chip with a field of view of 11'.6 was used. Raw frames were calibrated using dark frames and twilight flat-field frames. Figure 6.2 shows a sample of light curves collected at OCA on JD 2453565.

In addition, on July 10, 2005, the 84-cm OCA telescope was used with the “Portable Occultation, Eclipse, and Transit Systems” (POETS) instrument, see Souza et al. (2006) and Gulbis et al. (2006). The same instrumentation was used for observations of a stellar occultation by Charon (Chapter 3). The system consisted of a high-speed Andor Ixon camera (512×512 pixels), instrument control computer, and a GPS receiver that provided accurate timing and triggered the exposures. Integration

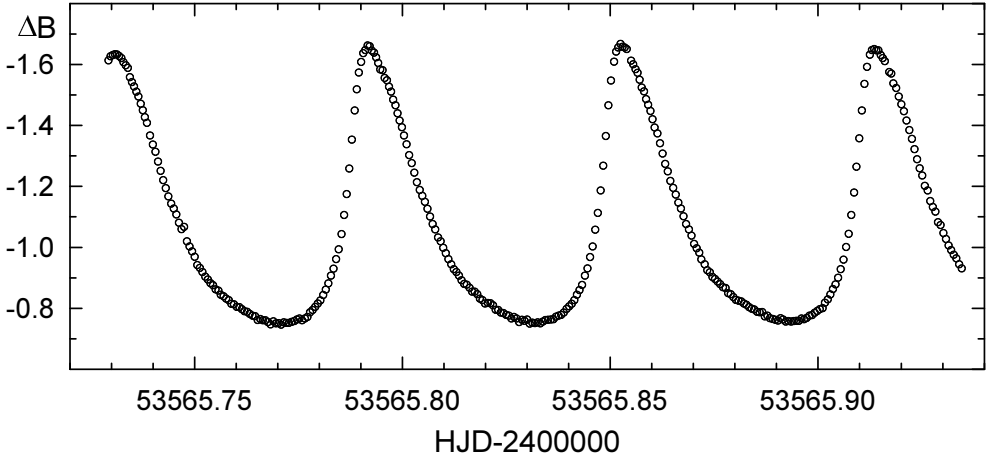


Figure 6.2: Sample of OCA B light curves.

times were 1.74 ms less than the cycle time (0.5 s). A binning of 2×2 was used, resulting in a pixel scale of $2''.8$. No flat field nor bias frames were acquired, hence the resulting light curves were extracted from uncalibrated white-light CCD frames.

Figure 6.3 shows the differential magnitude of CY Aqr minus the comparison star,

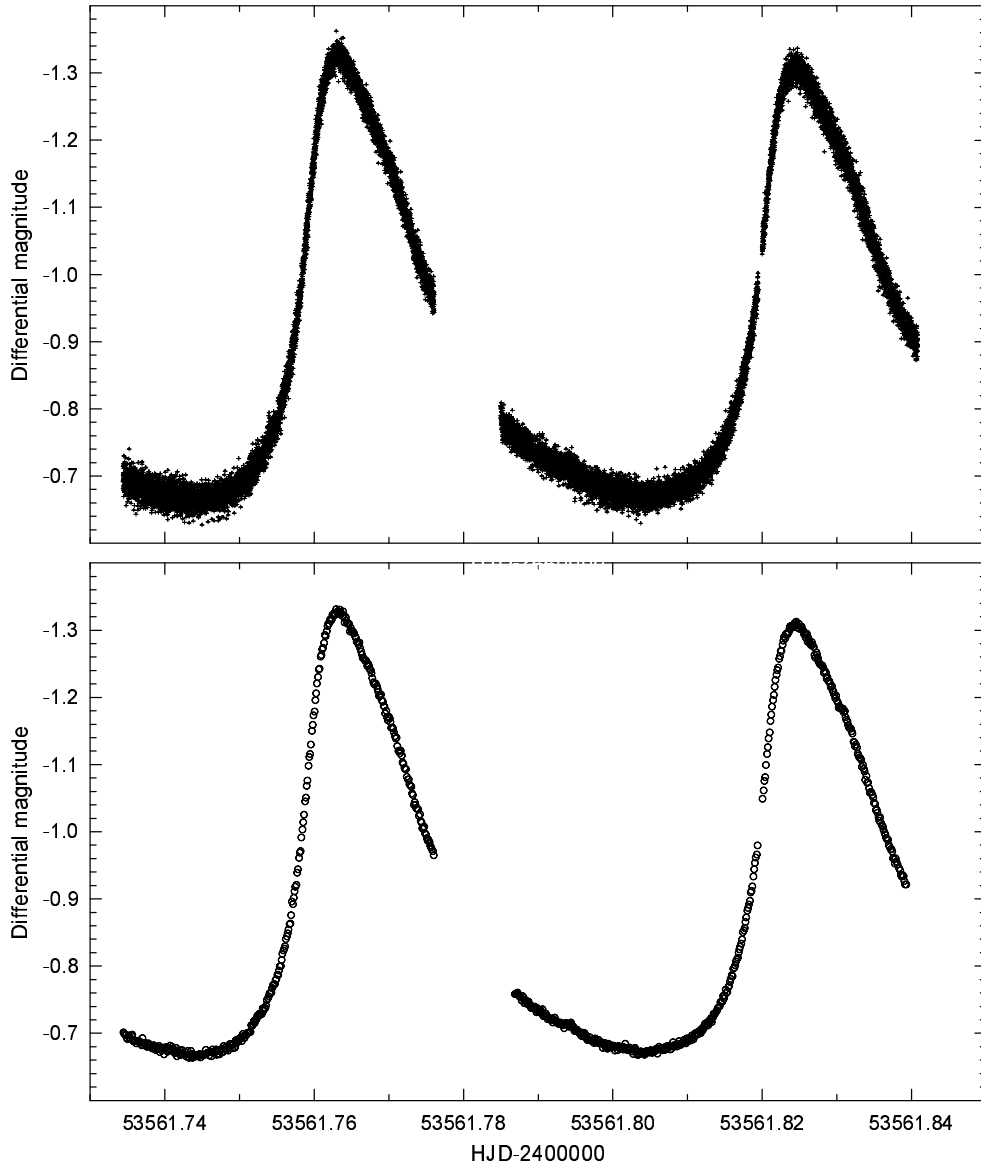


Figure 6.3: OCA high-resolution light curve, see Section 6.2.7. *Top:* raw light curve; *Bottom:* light curve binned in 10-second bins.

and also a binned light curve (bin width of 10 seconds, covering 20 frames). The light curves are quite regular, and are the best-covered light curves presented since the beginning of this star's observational history.

6.2.8 MDM Observatory

On October 30 and 31, 2007, the 2.4-m Hiltner telescope at the MDM Observatory, Arizona, USA, equipped with the 8k \times 8k Mosaic imager (FOV 23'.6 \times 23'.6) was used.

6.2.9 South African Astronomical Observatory

In November 2005 the 1.0-m telescope at the South African Astronomical Observatory (SAAO), Sutherland, South Africa (STE4 CCD camera with 1024 \times 1024 pixels, field of view 5'.3 \times 5'.3, with V filter) was used. Raw frames were calibrated using bias and twilight flat-field frames.

6.2.10 Realgymnasium Bruneck

From September 19 to December 28, 2008, 14 partial nights of observations were obtained by a team of students from the Realgymnasium Bruneck (RGB, Südtirol, Italy) under the supervision of C. Wiedemair. A 10-inch Meade LX200 telescope with an SBIG ST8-XME CCD camera was used on the college roof. Typical exposure time was 20 s, with 2 \times 2 binning. The technical limitations of this rooftop equipment

Table 6.2: Journal of photometric observations in the 2010 and 2011 seasons: JD, number of CCD frames, average differential magnitude between comparison stars, and standard deviation σ for each nightly sequence.

JD–2400000	Data	$C_1 - C_2$	σ	JD–2400000	Data	$C_1 - C_2$	σ
55460.35 – .44	123	–1.012	0.008	55826.31 – .43	266	–1.028	0.006
55469.29 – .41	166	–1.013	0.006	55839.29 – .43	288	–1.029	0.007
55481.28 – .37	143	–1.012	0.008	55838.28 – .39	229	–1.026	0.008
55484.28 – .43	298	–1.015	0.007	55849.27 – .38	248	–1.028	0.007
55490.31 – .35	99	–1.031	0.007	55853.28 – .40	259	–1.029	0.007
55496.28 – .39	216	–1.039	0.011	55865.29 – .43	296	–1.029	0.008
55498.26 – .41	263	–1.025	0.008	55868.26 – .42	357	–1.030	0.007
55506.25 – .40	288	–1.023	0.006	55875.22 – .38	356	–1.031	0.010
55530.21 – .31	162	–1.022	0.007	55882.24 – .40	346	–1.027	0.012
55535.20 – .35	324	–1.023	0.007	55889.20 – .37	357	–1.026	0.007
55544.21 – .28	143	–1.019	0.011	55915.20 – .31	236	–1.030	0.011
55547.19 – .29	121	–1.020	0.010	55923.19 – .30	228	–1.026	0.019
Total (2010)	2346	–1.021		Total (2011)	3466	–1.028	

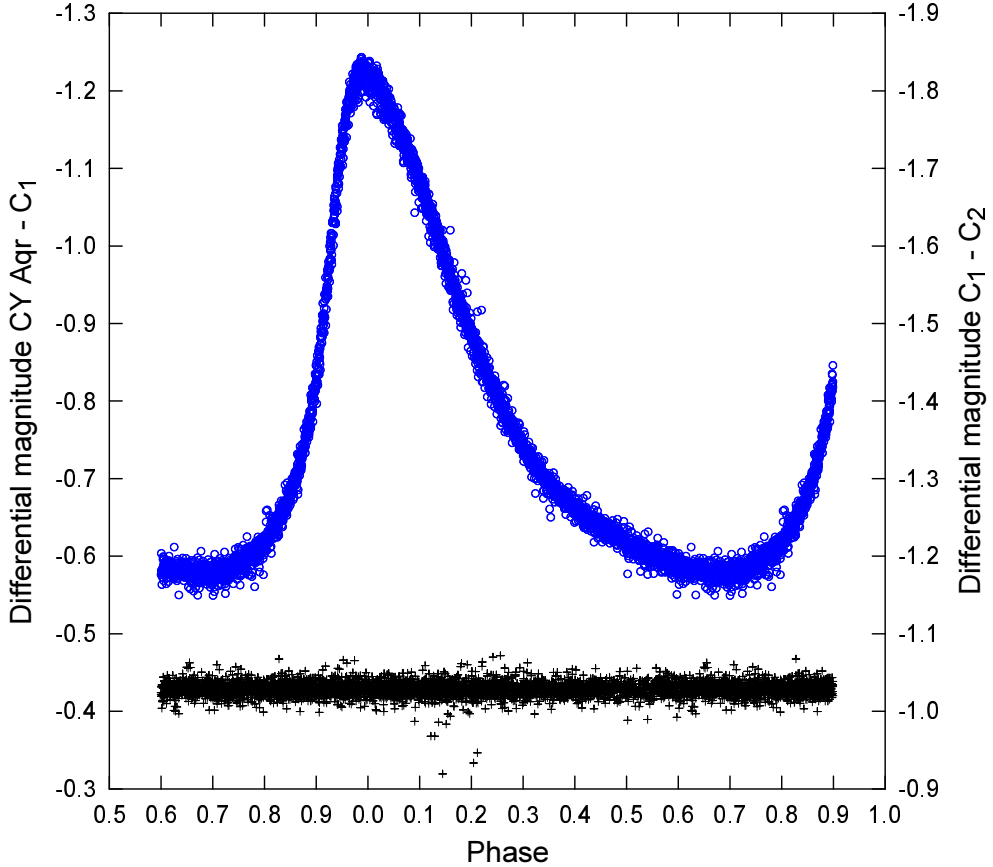


Figure 6.4: Phase diagram of the 2011 Bruneck data, constructed with Eq. 6.3. \circ : differential magnitude of CY Aqr, $+$: difference between comparison star magnitudes.

prevented the acquisition of valid flat-field frames, hence these CCD frames were dark-corrected only.

The 2010 season data were obtained during 12 partial nights in September–December 2010 from the same location and using the same equipment as in 2008. Typical exposure time was 35–50 s, with 2×2 binning, and no filter was used. The CCD frames were dark-corrected only. An aperture radius of $1.6 \times \text{FWHM}$ was used for all the frames from this season.

The 2011 season CCD data were obtained through imaging during 12 partial nights in September–December 2011 from the same location and using the same instruments as in 2008 and 2010. The observations were obtained by C. Wiedemair and a team of students. Exposure time was 35 s, with 2×2 binning, and no filter was used. Flat-field frames were obtained by taking 7-second exposures of a light foil placed in front of the telescope aperture. Data frames were calibrated with nightly-averaged master darks and flats. Table 6.2 gives the journal of observations for the 2010 and 2011 seasons.

Differential light curves of CY Aqr were obtained relative to $C_1 = \text{GSC}00567-01826$ as comparison star. Magnitudes of $C_2 = \text{GSC}00567-02036$ were derived to assess the observational precision of our data. The average differential magnitude of the comparison stars given in Table 6.2 reveals a slight shift in zeropoint of our magnitude scale: whereas $(\overline{C_1 - C_2})_{2010} = -1.021 \pm 0.002$, the 2011 data yield $(\overline{C_1 - C_2})_{2011} = -1.028 \pm 0.001$. Whether this $0.^m007$ difference is due to a change in one or in both comparison stars, or whether it is due to an artefact in the reduction workflow, cannot be decided with the data that are available at this moment. Figure 6.4 shows the phase diagram for the 2011 CCD data.

6.2.11 Strömgren Automatic Telescope

CY Aqr was observed with the Strömgren Automatic Telescope (SAT) at ESO, La Silla by C. Sterken during three partial nights in November 2011. A diaphragm of 17 arcsec was used. Table 6.3 gives the journal of observations. Despite the fact that optimal photon statistics would require an integration time of at least 3 to 4 minutes, an integration time of 60 seconds was chosen to allow for adequate time resolution during the steep rise to maximum light. After every integration, the star was re-centred in the diaphragm. A 60-second sky background integration was secured every ten to fifteen minutes. In addition, some measurements of comparison star $C_1 = \text{GSC}00567-01826$ were made, as well as one measurement of BD+00°4902 (GSC 00567-00884), the comparison star used by Hardie & Tolbert (1961), who give $V = 9.72$, $B - V = +0.76$, $U - B = +0.38$.

Extinction corrections were derived from constant-star observations obtained during the same nights. Differential magnitudes and colour indices of CY Aqr relative to $C_1 = \text{GSC}00567-01826$ were calculated, and these instrumental magnitudes were then transformed into quasi-standard *uvby* photometry, using average transformation coefficients obtained from other nights with well-determined transformation equations. This led to quasi-standard Strömgren photometric indices for BD+00°4902 as given in Table 6.3. The resulting differential magnitudes were constructed by subtracting the average magnitude of $C_1 = \text{GSC}00567-01826$, and by adding the photometric parameters of BD+00°4902. Figure 6.5 shows the phase diagrams of all *uvby* data.

Table 6.3: Journal of photoelectric *uvby* observations from 2011: JD range, number of integrations, and average photometric parameters with associated mean errors in millimagnitudes. By definition, $m_1 = (v - b) - (b - y)$ and $c_1 = (u - v) - (v - b)$.

Star	JD-2400000	Data	<i>V</i>	<i>b - y</i>	m_1	c_1
CY Aqr	55886.53 – .60	96				
CY Aqr	55887.53 – .59	67				
CY Aqr	55889.56 – .60	32				
C_1	55890.54	8	11.904(5)	0.309(6)	0.246(8)	0.470(10)
BD+00°4902	55890.54	2	9.875(6)	0.439(3)	0.396(1)	0.362(10)

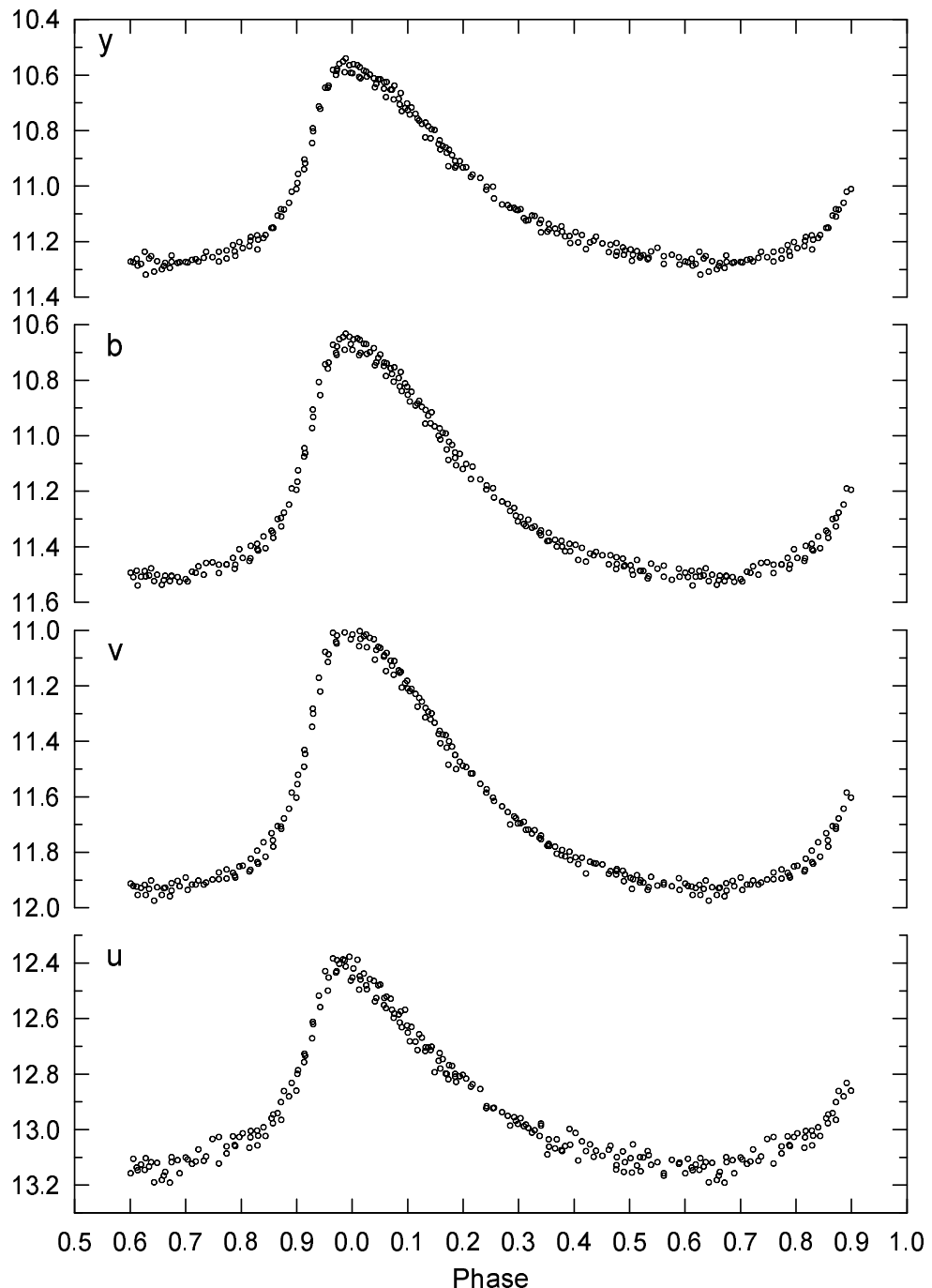


Figure 6.5: Phase diagrams of all $uvby$ data.

6.2.12 Miscellaneous sources

Published light curves and/or T_{\max} were collected from various sources, viz.:

1. The American Association of Variable Star Observers (AAVSO) data archives contains visual estimates since September 1968. From 2003 on, photoelectric observations of a dozen well-covered maxima have been added. The following light-curve data were used in this study (JD–2 400 000 followed by AAVSO observer code): 52931 (OAR), 53605 (ZRE), 53989 (PWM), 54008 (DKS), 54032 (DKS), 54734 (ATE), 54736 (ATE), 54738 (ATE), 54739 (ATE), 55085 (SJAR), 55114 (SJAR), and 55157 (SJAR).
2. One light curve was acquired by L. Barrera on July 1, 2003 at OCA with a 41-cm telescope, and its resulting $T_{\max} = 2452821.9182$ was published by Fu et al. (2004).
3. Derekas et al. (2009), in a study of binarity and multiperiodicity in high-amplitude δ Scuti stars, list 11 new T_{\max} obtained from V and I photometry.
4. Some isolated times of maximum are also listed by Hubscher et al. (2005), Biro et al. (2006), Paschke (2007) and Paschke (2009).
5. Two new T_{\max} , viz. 2453647.0339 and 2454007.0997 were acquired by Li et al. (2007). Three additional new maxima were given by these authors: one T_{\max} derived from Fig. 2 of Chen et al. (2003), and two maxima from the AAVSO data. We have not retained the former maximum because the shape of the light curve in Fig. 2 of Chen et al. (2003) has a very irregular and atypical minimum and maximum, quite unlike Fig. 6.3. Moreover, these data are not of optimal quality because they were derived from square-aperture photometry in a very early version of the data-reduction pipeline software (Chen 2010). We have not used the AAVSO-based T_{\max} listed in Table 2 of Li et al. (2007), viz. 2454032.4915 and 2454032.5521, but we derived the T_{\max} from the original data, as explained in Section 6.3.1, and we added the heliocentric correction.¹
6. Two times of maximum were published by Hubscher (2011) and by Hubscher & Monninger (2011).
7. The most recent set of times of maximum was released by Hojjatpanah et al. (2011). These T_{\max} and accompanying light curves are analysed in Section 6.3.3.

6.3 Times of maximum, new ephemeris and $O - C$ diagram

6.3.1 Times of maximum light

Times of maximum light were derived from visual inspection of the light curves with underlying running averages covering a time interval of ± 0.1 phase bins from the time of maximum. Since the set of light curves is quite heterogeneous with respect to data

¹The AAVSO database lists non-heliocentric JD.

Table 6.4: Relative weights assigned to the T_{\max} derived in this work.

Weight	Data density	Shape of maximum	Comment
1	very low	(ir)regular	
2	medium	+	irregular
3	high	+	irregular
4	medium	+	regular
5	high	+	regular
			smooth light curve

density and shape of the local maximum, we have established a scheme of weights (1–5) according to the criteria given in Table 6.4, in addition to applying a weight decrease by one unit whenever three estimates of the same maximum time based on the same data differed by more than $0^d 002$. No weights were assigned to published T_{\max} , except for FSB2004 and L2007 for which light curves were available. All 175 T_{\max} are listed in Table 6.5. From comparison of derived maximum times in different photometric bands, we estimate that the mean error on one T_{\max} is $\leq 0^d 0003$. Cycle numbers E were calculated using the ephemeris given by Fu et al. (2004).

 Table 6.5: Times of maximum light (HJD–2400000) of CY Aqr, weight W (from Table 6.4), cycle number E , and photometric passband. Source refers to this Chapter and to references in the literature, viz. DKB2009: Derekas et al. (2009); FSB2004: Fu et al. (2004); HPW2005: Hubscher et al. (2005); BBC2006: Biro et al. (2006); LFZ2007: Li et al. (2007); P2007: Paschke (2007); P2009: Paschke (2009).

T_{\max}	W	E	Source	Band	T_{\max}	W	E	Source	Band
51107.6543	5	408729	Sect. 6.2.1	V	53307.2334	4	444765	Sect. 6.2.6	V
51115.5893	5	408859	Sect. 6.2.1	I	53307.2936	1	444766	Sect. 6.2.6	V
51115.6503	4	408860	Sect. 6.2.1	I	53307.3556	4	444767	Sect. 6.2.6	V
51162.6502	1	409630	Sect. 6.2.1	U	53307.4163	1	444768	Sect. 6.2.6	V
51806.7891	1	420183	Sect. 6.2.2	I	53309.3698	4	444800	Sect. 6.2.6	V
51806.7892	1	420183	Sect. 6.2.2	V	53311.3842	4	444833	Sect. 6.2.6	V
52821.9182	3	436814	FSB2004	V	53334.9453	—	445219	DKB2009	I
52903.4032	2	438149	Sect. 6.2.12	V	53336.9592	—	445252	DKB2009	I
52920.9223	—	438436	DKB2009	V	53337.9357	—	445268	DKB2009	I
52920.9827	—	438437	DKB2009	V	53556.8802	4	448855	Sect. 6.2.7	B
52921.0439	—	438438	DKB2009	V	53556.9409	4	448856	Sect. 6.2.7	B
52923.0587	—	438471	DKB2009	V	53557.7959	5	448870	Sect. 6.2.7	B
52926.9643	—	438535	DKB2009	V	53557.8567	5	448871	Sect. 6.2.7	B
52927.0258	—	438536	DKB2009	V	53557.9178	5	448872	Sect. 6.2.7	B
52930.3215	4	438590	Sect. 6.2.12	V	53558.7723	5	448886	Sect. 6.2.7	B
52931.2981	4	438606	Sect. 6.2.12	V	53558.8336	5	448887	Sect. 6.2.7	B
52931.3595	4	438607	Sect. 6.2.12	V	53558.8945	5	448888	Sect. 6.2.7	B
53249.5522	5	443820	Sect. 6.2.3	—	53559.7489	5	448902	Sect. 6.2.7	B
53250.5287	5	443836	Sect. 6.2.3	—	53559.8101	5	448903	Sect. 6.2.7	B
53254.9840	1	443909	Sect. 6.2.5	V	53559.8709	5	448904	Sect. 6.2.7	B
53256.3278	—	443931	HPW2005	V	53559.9320	5	448905	Sect. 6.2.7	B
53256.3883	—	443932	HPW2005	V	53561.7632	5	448935	Sect. 6.2.7	—
53256.8758	1	443940	Sect. 6.2.5	V	53561.8244	5	448936	Sect. 6.2.7	B
53256.9374	1	443941	Sect. 6.2.5	V	53563.7774	5	448968	Sect. 6.2.7	B
53286.4191	5	444424	Sect. 6.2.4	—	53563.8387	5	448969	Sect. 6.2.7	B
53289.2884	2	444471	Sect. 6.2.4	—	53563.8997	5	448970	Sect. 6.2.7	B
53289.4099	5	444473	Sect. 6.2.4	—	53565.7310	4	449000	Sect. 6.2.7	B
53292.4012	3	444522	Sect. 6.2.4	—	53565.7919	5	449001	Sect. 6.2.7	B
53304.3034	5	444717	Sect. 6.2.6	V	53565.8526	4	449002	Sect. 6.2.7	B
53304.3649	4	444718	Sect. 6.2.6	V	53565.9138	5	449003	Sect. 6.2.7	B
53306.3184	4	444750	Sect. 6.2.6	V	53566.5233	—	449013	BBC2006	V

Table 6.5 – continued.

T_{\max}	W	E	Source	Band	T_{\max}	W	E	Source	Band
53605.7721	4	449656	Sect. 6.2.12	<i>V</i>	55157.2436	1	475074	Sect. 6.2.12	<i>B</i>
53613.7080	1	449786	Sect. 6.2.8	<i>B</i>	55157.2449	2	475074	Sect. 6.2.12	<i>V</i>
53613.7678	2	449787	Sect. 6.2.8	<i>B</i>	55157.2452	1	475074	Sect. 6.2.12	<i>R</i>
53647.0339	5	450332	LFZ2007	<i>V</i>	55460.3611	5	480040	Sect. 6.2.10	—
53682.3752	4	450911	Sect. 6.2.9	<i>V</i>	55460.4222	5	480041	Sect. 6.2.10	—
53683.2906	5	450926	Sect. 6.2.9	<i>V</i>	55469.3340	5	480187	Sect. 6.2.10	—
53683.3517	5	450927	Sect. 6.2.9	<i>V</i>	55469.3948	5	480188	Sect. 6.2.10	—
53684.3285	5	450943	Sect. 6.2.9	<i>V</i>	55481.2973	5	480383	Sect. 6.2.10	—
53688.3568	4	451009	Sect. 6.2.9	<i>V</i>	55481.3584	4	480384	Sect. 6.2.10	—
53689.3337	4	451025	Sect. 6.2.9	<i>V</i>	55484.2878	5	480432	Sect. 6.2.10	—
53989.3372	4	455940	Sect. 6.2.12	<i>V</i>	55484.3493	4	480433	Sect. 6.2.10	—
53989.3980	3	455941	Sect. 6.2.12	<i>V</i>	55484.4102	5	480434	Sect. 6.2.10	—
54007.0997	3	456231	LFZ2007	—	55490.3309	5	480531	Sect. 6.2.10	—
54008.7473	4	456258	Sect. 6.2.12	<i>V</i>	55496.3128	3	480629	Sect. 6.2.10	—
54032.4907	5	456647	Sect. 6.2.12	<i>V</i>	55496.3744	4	480630	Sect. 6.2.10	—
54032.5523	5	456648	Sect. 6.2.12	<i>V</i>	55498.2662	5	480661	Sect. 6.2.10	—
54092.2510	—	457626	P2007	<i>V</i>	55498.3270	4	480662	Sect. 6.2.10	—
54092.3110	—	457627	P2007	<i>V</i>	55498.3883	5	480663	Sect. 6.2.10	—
54307.5293	—	461153	DKB2009	<i>I</i>	55506.2618	5	480792	Sect. 6.2.10	—
54308.5073	—	461169	DKB2009	<i>I</i>	55506.3225	5	480793	Sect. 6.2.10	—
54410.5627	1	462841	Sect. 6.2.9	<i>V</i>	55506.3837	5	480794	Sect. 6.2.10	—
54671.5630	—	467117	P2009	<i>V</i>	55530.2500	5	481185	Sect. 6.2.10	—
54709.4677	3	467738	Sect. 6.2.9	<i>V</i>	55535.2553	5	481267	Sect. 6.2.10	—
54729.3056	3	468063	Sect. 6.2.10	—	55535.3163	4	481268	Sect. 6.2.10	—
54729.3665	3	468064	Sect. 6.2.10	—	55544.2280	3	481414	Sect. 6.2.10	—
54729.4272	4	468065	Sect. 6.2.10	—	55547.2188	5	481463	Sect. 6.2.10	—
54730.2815	3	468079	Sect. 6.2.10	—	55547.2800	3	481464	Sect. 6.2.10	—
54730.3428	4	468080	Sect. 6.2.10	—	55826.3469	5	486036	Sect. 6.2.10	—
54730.4039	3	468081	Sect. 6.2.10	—	55826.4079	5	486037	Sect. 6.2.10	—
54730.4647	4	468082	Sect. 6.2.10	—	55831.3520	5	486118	Sect. 6.2.10	—
54734.3710	3	468146	Sect. 6.2.12	<i>V</i>	55831.4132	5	486119	Sect. 6.2.10	—
54734.4318	4	468147	Sect. 6.2.12	<i>V</i>	55838.3103	3	486232	Sect. 6.2.10	—
54736.3854	5	468179	Sect. 6.2.12	<i>V</i>	55838.3718	5	486233	Sect. 6.2.10	—
54738.3388	5	468211	Sect. 6.2.10	—	55849.2971	3	486412	Sect. 6.2.10	—
54738.3993	4	468212	Sect. 6.2.12	<i>V</i>	55849.3585	5	486413	Sect. 6.2.10	—
54738.3999	5	468212	Sect. 6.2.10	—	55853.3258	3	486478	Sect. 6.2.10	—
54739.3754	5	468228	Sect. 6.2.12	<i>V</i>	55853.3867	3	486479	Sect. 6.2.10	—
54749.3254	3	468391	Sect. 6.2.10	—	55865.3505	5	486675	Sect. 6.2.10	—
54749.3867	4	468392	Sect. 6.2.10	—	55865.4115	3	486676	Sect. 6.2.10	—
54757.2605	5	468521	Sect. 6.2.10	—	55868.2802	3	486723	Sect. 6.2.10	—
54757.3214	4	468522	Sect. 6.2.10	—	55868.3414	3	486724	Sect. 6.2.10	—
54757.3825	5	468523	Sect. 6.2.10	—	55875.2385	2	486837	Sect. 6.2.10	—
54761.2892	5	468587	Sect. 6.2.10	<i>V</i>	55875.2999	3	486838	Sect. 6.2.10	—
54761.3503	5	468588	Sect. 6.2.10	<i>V</i>	55882.2581	3	486952	Sect. 6.2.10	—
54781.2485	3	468914	Sect. 6.2.10	<i>V</i>	55882.3189	5	486953	Sect. 6.2.10	—
54781.3091	2	468915	Sect. 6.2.10	<i>V</i>	55889.2167	5	487066	Sect. 6.2.10	—
54796.2637	5	469160	Sect. 6.2.10	<i>V</i>	55889.2774	5	487067	Sect. 6.2.10	—
54796.3253	5	469161	Sect. 6.2.10	<i>V</i>	55889.3388	3	487068	Sect. 6.2.10	—
54809.2041	5	469372	Sect. 6.2.10	<i>V</i>	55915.2189	3	487492	Sect. 6.2.10	—
54809.2648	5	469373	Sect. 6.2.10	<i>V</i>	55915.2800	3	487493	Sect. 6.2.10	—
54827.2105	4	469667	Sect. 6.2.10	<i>V</i>	55923.2146	3	487623	Sect. 6.2.10	—
55085.4631	1	473898	Sect. 6.2.12	<i>R</i>	55923.2760	2	487624	Sect. 6.2.10	—
55085.4633	1	473898	Sect. 6.2.12	<i>V</i>	55886.5307	1	487022	Sect. 6.2.11	<i>uvby</i>
55085.4641	1	473898	Sect. 6.2.12	<i>B</i>	55886.5916	4	487023	Sect. 6.2.11	<i>uvby</i>
55114.3956	1	474372	Sect. 6.2.12	<i>V</i>	55887.5682	2	487039	Sect. 6.2.11	<i>uvby</i>
55114.3957	1	474372	Sect. 6.2.12	<i>R</i>	55889.5828	4	487072	Sect. 6.2.11	<i>uvby</i>
55114.3964	1	474372	Sect. 6.2.12	<i>B</i>					

6.3.2 Ephemeris and resulting $O - C$ diagrams

A linear least-squares fit of the 116 times of maximum in Table 6.5 obtained after the last T_{\max} published by Fu & Sterken (2003) and up to the 2009 season, results in

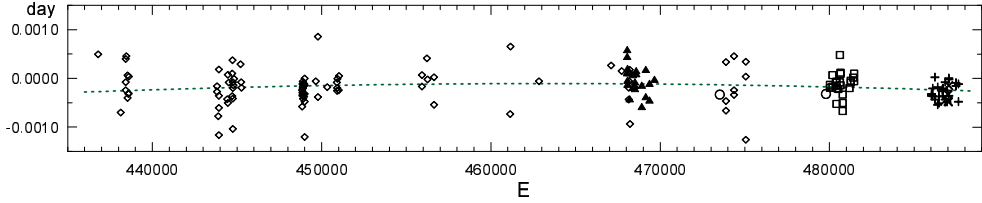


Figure 6.6: $O - C$ curve with respect to ephemeris (6.3). The dashed line is the parabolic fit; \times : the four maxima obtained with the SAT (Section 6.2.11); $+$: the Bruneck data from the 2011 season; \square : the Bruneck data from the 2010 season; \blacktriangle : the Bruneck CCD maxima from 2008; \diamond : data from other sources listed in Table 6.5; \circ : the two maxima from Hubscher (2011) and Hubscher & Monninger (2011).

$P = 0^d 061038350 \pm 0^d 000000004$. Removing two outlying points with $O - C \approx 0^d 008$ (i.e. of the order of the heliocentric correction for the maxima labeled P2007) leads to essentially the same result, though with improved accuracy. The 114 times of maximum provide a local linear ephemeris for 2003–2009:

$$T_{\max} = 2426159.512 + 0.061038349 \times E. \quad (6.1)$$

$$\pm 0.001 \quad \pm 0.000000002$$

A linear least-squares fit of the 24 times of maximum from the 2010 season results in $P = 0^d 061038350 \pm 0^d 000000004$. The previously mentioned 114 T_{\max} from 2003–2009 together with the 24 new timings from 2010 provide the local linear ephemeris for 2003–2010:

$$T_{\max} = 2426159.5122 + 0.061038349 \times E. \quad (6.2)$$

$$\pm 0.0005 \quad \pm 0.000000001$$

Adding the 29 new times of maximum from the 2011 season – i.e. using all timings since $E = 436814$ (HJD 2452821.9182), with exclusion of two outliers – leads to a linear ephemeris for 2003–2011:

$$T_{\max} = 2426159.5132 + 0.0610383466 \times E. \quad (6.3)$$

$$\pm 0.0001 \quad \pm 0.0000000003$$

Figure 6.6 shows the resulting $O - C$ curve with respect to ephemeris (6.3). These 167 times of maximum yield residuals with a standard deviation of $0^d 0003$.

The dashed curve is the parabolic fit, which seems to suggest a very subtle period shortening of $\dot{P} = -0.02 \pm 0.01$ seconds per century. The question, of course, is whether this result is reliable, i.e., whether the quadratic term in the fit is significant. From the variance of the linear and parabolic fits, we find Pringle’s (1975) statistical parameter

$$\lambda = \frac{\sigma_1^2 - \sigma_2^2}{\sigma_2^2} \cdot (n - 3) = 6.96 \quad (6.4)$$

that leads to a probability of 99% for the significance of the quadratic term,² which is equivalent to only 2.55σ on a normal distribution.

²The confidence level at which we can rule out the null hypothesis that the parabolic term is zero is given by $\lambda = F(1, n - 3)$ where n is the number of data, and F is Fisher’s F distribution.

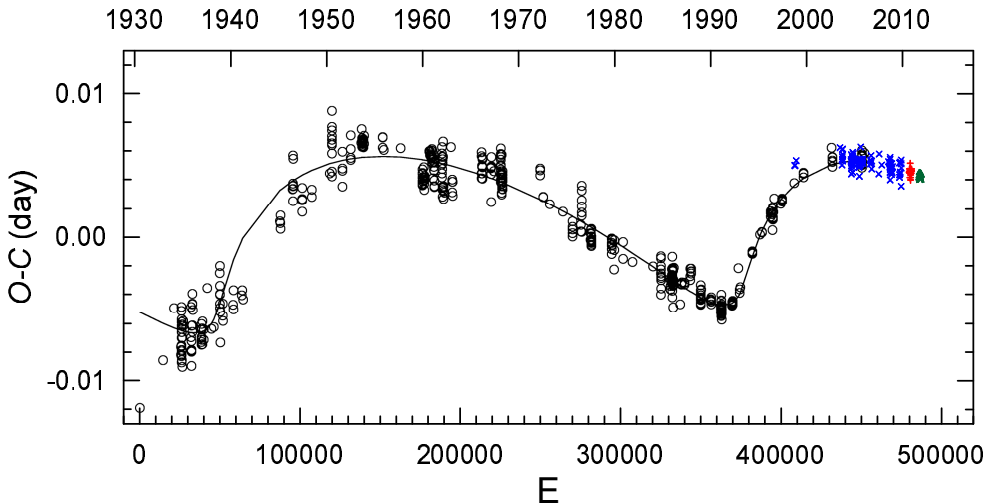


Figure 6.7: Complete $O - C$ curve with respect to ephemeris (1) of Fu & Sterken (2003). Full line and \circ : light-time orbit solution and data from Fu & Sterken (2003); \times : the 120 T_{\max} until 2009 from Table 6.5, without two outliers; $+$: all T_{\max} from the 2010 season; \triangle : 29 maxima from the 2011 season.

Figure 6.7 shows the new $O - C$ points overplotted in Fig. 3 of Fu & Sterken (2003) (ephemeris $T_{\max} = 2426159.4967 + 0.0610383716E$). The graph clearly illustrates two points, viz.,

1. the internal scatter of our times of maximum from the 2011 season is about the lowest reported during the last decade, and
2. though the parabolic fit for the 2003–2011 time interval is not significant on a 3σ level, the graph supports the presence of a linear period decrease over the last decade.

6.3.3 Additional times of maximum from the literature

As mentioned in Section 6.2.12, two times of maximum were published by Hubscher (2011) and by Hubscher & Monninger (2011). These single maxima fit quite well in the picture (see \circ in Fig. 6.6), but these data have not been used for the determination of the linear ephemeris.

The 10 maxima reported by Hojjatpanah et al. (2011), though, pose a serious problem: the maxima come, in average, 0.17 cycles (about 15 minutes) early, and would lead to $\overline{O - C} = -0^{\text{d}}.01$. In addition, the light curve of the second night (JD 55801.19–.51) is shifted by about half of this amount with respect to the light curve of the previous night (JD 55800.23–.53). To clarify this divergence, we first determined the times of maximum from the light curve data in the same way as we did for our own data. This led to 9 results (we omitted the maximum near 2455800.519 because it was insufficiently covered by the data), which yielded a normal point for each

Table 6.6: Times of maximum light (HJD–2400000) of CY Aqr, weight W (see Table 6.4), and cycle number E , independently derived from the data of Hojjatpanah et al. (2011).

$T_{\max} (V)$	W	E
55800.2847	3	485609
55800.3452	3	485610
55800.4066	1	485611
55800.4667	3	485612
55801.2607	3	485625
55801.3220	3	485626
55801.3828	3	485627
55801.4439	5	485628
55801.5050	3	485629

nightly set of maxima, viz., JD 55800.2728 ± 0.0002 and 55800.2671 ± 0.0001 . The difference between those timings was thus $0^d 0057 \pm 0.0002$, which corresponds to the heliocentric correction ($HC = 0.0057$) for that date. We can thus assume that for the first night the heliocentric correction was applied with the wrong sign, and that for the second night, HC was subtracted twice. Hence, all given times in file 6099-t6 in Hojjatpanah et al. (2011) had to be corrected by $+2 \times 0^d 0057$ for the first night, and by $+3 \times 0^d 0057$ for the second night. The newly-derived maxima are given in Table 6.6 with corresponding E and W values, and lead to $\overline{O - C} = +0^d 0006 \pm 0^d 0001$ for linear ephemeris formula (6.3), a deviation from our own $\overline{O - C} = -0^d 00028 \pm 0^d 00003$ by more than one minute. The origin of this discrepancy can be attributed to

1. the standard error of ~ 25 seconds on our estimate of HC , and/or
2. a possible 15 or 30 seconds depending whether the times recorded deviate from the time of mid-exposure, and/or
3. an offset in the time recording system.

Figure 6.8 shows the resulting phase diagrams of all V data (\diamond) discussed above, together with the phase diagram shown in Fig. 6.4. Although both datasets were acquired with instruments of very similar aperture, the difference in spread is substantial. The larger scatter of the V -band data can be attributed to the data-reduction procedure, including the various irregularities (jumps) in the light curves. The range between minimum and maximum of the V data is about $0^m 1$ larger than for the unfiltered data: this difference is also a combination of hardware (broadband V and filterless detector) and of data-reduction procedure.

6.4 Conclusions

The pulsation period in Eq. 6.1 is formally shorter than the one quoted in Table 3 of Fu & Sterken (2003) for 1996–2002 ($P = 0^d 061038394 \pm 0^d 000000006$), which does

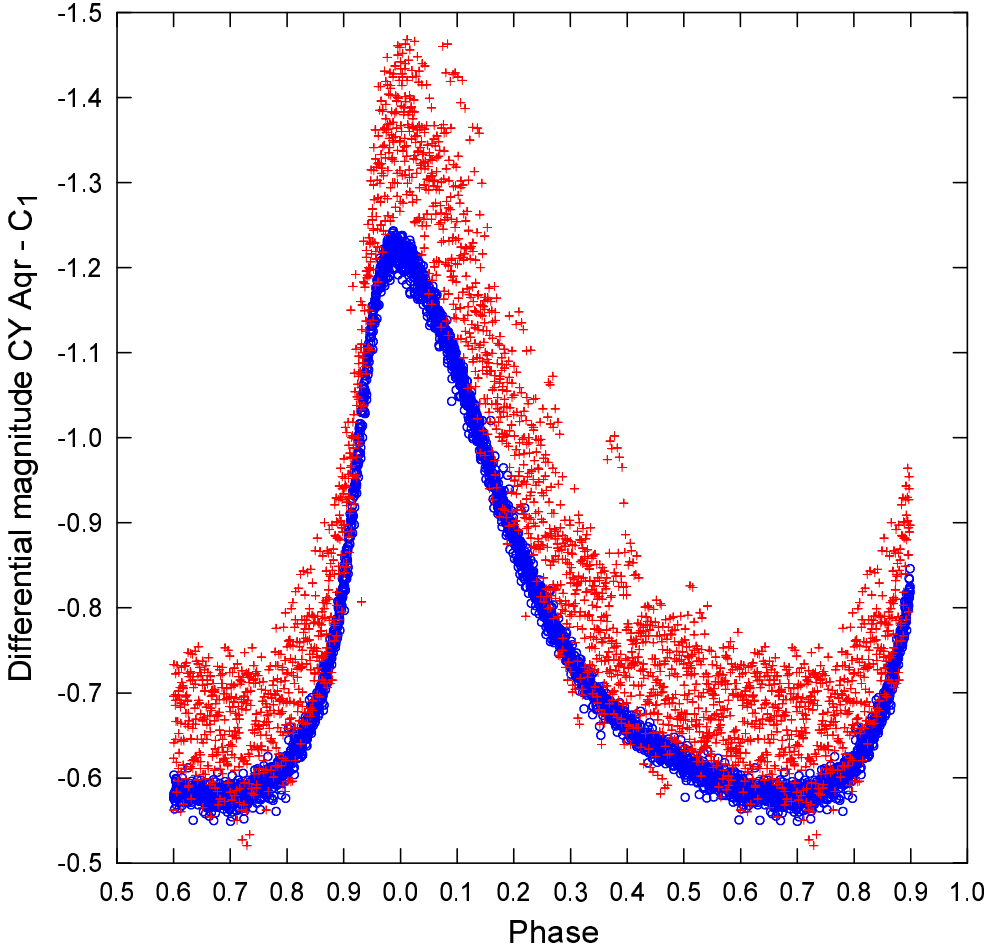


Figure 6.8: Phase diagram, constructed with Eq. (6.3), of the differential magnitudes (+, V) from Hojjatpanah et al. (2011) and the differential (\circ , filterless) magnitudes from the 2011 Bruneck data.

not mean that this result provides any evidence supporting the piecewise linear $O - C$ trend model.

The pulsation periods in Eqs. 6.1 and 6.2 are formally identical, though the new data provide a better accuracy on the period as well as on the initial epoch. The accuracy is further improved in Eq. 6.3, by including data from the 2011 season.

It will require at least another half decade of additional monitoring before any significant update to the presented model can be considered. Such monitoring should preferably occur at regular intervals (at least at the beginning and end of each observing season), be done in a consistent photometric band (preferably Johnson V) and at high time resolution in order to achieve data of high weight (4 or 5 in the scheme presented in Table 6.4).

Table 6.7: Overview of most recently published linear ephemeris formulae for CY Aqr. Note that the mean errors for the interval 1930–2002 were not taken from the reference, but were calculated from the 544 maxima. The error in P is illusory because of the long-term wave.

Time base	T_0 (HJD)	\pm	P (days)	\pm	Reference
1930–2002	2426159.4967	0.0004	0.06103837	0.000000002	Fu & Sterken (2003)
2003–2009	2426159.512	0.001	0.061038349	0.0000000002	Eq. 6.1
2003–2010	2426159.5122	0.0005	0.061038349	0.0000000001	Eq. 6.2
2003–2011	2426159.5132	0.0001	0.0610383466	0.00000000003	Eq. 6.3

Table 6.7 gives an overview of the most recent linear ephemeris formulae for CY Aqr. Our data show that modest equipment supported by adequate training and tutoring – when sustained for at least 5 to 10 years – will provide enough evidence to conclude whether the binary model can fully account for all the period variability observed in this star. The decreasing internal variance of our $O - C$ residuals (see Fig. 6.9) shows that a systematic and careful approach in observing as well as in data reduction yields its fruits.

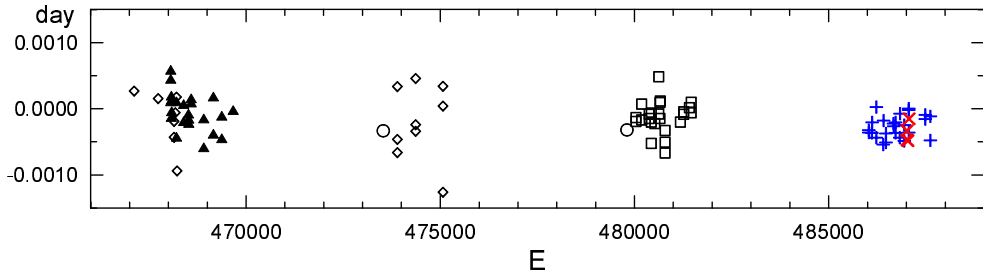


Figure 6.9: Detail of the $O - C$ curve of Fig. 6.6. \times : the four maxima obtained with the SAT (Section 6.2.11); $+$: the 2011 Bruneck maxima; \square : the 2010 Bruneck data; \blacktriangle : the 2008 Bruneck CCD maxima; \diamond : data from other sources listed in Table 6.5; \circ : the two maxima from Hubscher (2011) and Hubscher & Monninger (2011).

References

- Biro, I. B., Borkovits, T., Csizmadia, S., et al. 2006, IBVS, 5684
 Chen, W. P. 2010, personal communication
 Chen, W. P., Zhang, Z. W., King, S. K., et al. 2003, Baltic Astronomy, 12, 568
 Derekas, A., Kiss, L. L., Bedding, T. R., et al. 2009, MNRAS, 394, 995
 Fu, J. N. & Sterken, C. 2003, A&A, 405, 685

- Fu, J. N., Sterken, C., & Barrera, L. 2004, in ASP Conference Series, Vol. 318, *Spectroscopically and Spatially Resolving the Components of the Close Binary Stars*, ed. R. W. Hilditch, H. Hensberge, & K. Pavlovski, p. 346
- Gulbis, A. A. S., Elliot, J. L., Person, M. J., et al. 2006, Nature, 439, 48
- Hardie, R. H. & Tolbert, C. R. 1961, ApJ, 134, 581
- Hojjatpanah, S., Zangi, P., Khazraei, M., & Riazi, N. 2011, Information Bulletin on Variable Stars, 6099, 3
- Hubscher, J. 2011, Information Bulletin on Variable Stars, 5984, 1
- Hubscher, J. & Monninger, G. 2011, Information Bulletin on Variable Stars, 5959, 1
- Hubscher, J., Paschke, A., & Walter, F. 2005, IBVS, 5657
- Li, C., Fu, J.-N., Zhang, Y.-P., & Jiang, S.-Y. 2007, J. Beijing Normal University, 43, 621
- Paschke, A. 2007, Open European Journal on Variable Stars, 73
- Paschke, A. 2009, Open European Journal on Variable Stars, 116
- Pringle, J. E. 1975, MNRAS, 170, 633
- Souza, S. P., Babcock, B. A., Pasachoff, J. M., et al. 2006, PASP, 118, 1550

Chapter 7

Photometric monitoring of the open cluster NGC 3293

7.1 Stellar identifications

Several numbering systems have been used for the stars in the NGC 3293 region. Feast (1958) introduced numbers 1–35 for cluster stars and 36–51 for field stars. Turner et al. (1980) numbered additional 63 stars in the range of 52–133, skipping 19 numbers. Herbst & Miller (1982) extended the numbering system with stars 134–497, thus completing the system that is denoted as FEAS in the SIMBAD database.

Alternatively, Feinstein & Marraco (1980) added 7 stars (numbers 52–58) to the original numbering by Feast (1958). Shobbrook (1983), on the other hand, extended the system of Turner et al. (1980) by 6 stars (numbers 134–139). Balona (1994) based his identifications on Turner et al. (1980) and Shobbrook (1983), adding numbers 140–236.

Evans et al. (2005) introduced a spectroscopic survey of massive stars, including a stellar field centred on NGC 3293. They numbered 126 stars in a 25-arcmin diameter field of view. The system is denoted as ESL and the order follows V -magnitudes of stars.

Throughout this work we use the star numbering introduced by Baume et al. (2003) and denoted as BVC. The numbers are sorted by V -magnitudes, BVC 1 being the brightest and BVC 1690 the faintest.

The finding chart of NGC 3293 is presented in Fig. 7.1 and shows the stars BVC 1–100. Table 7.1 gives cross-identifications for BVC 1–100 and a few other stars of interest.

Star No. 69 from the list of Turner et al. (1980) was incorrectly marked in their Fig. 1. Herbst & Miller (1982) clarifies this by including No. 69 correctly in their finding chart. Balona (1994), however, uses No. 69 for FEAS 496 (=BVC 160) and No. 228 for FEAS 69 (=BVC 112).

The identification of star No. 51 by Feinstein & Marraco (1980) is ambiguous. In the finding chart they have marked two stars with this number, FEAS 51 and FEAS 86

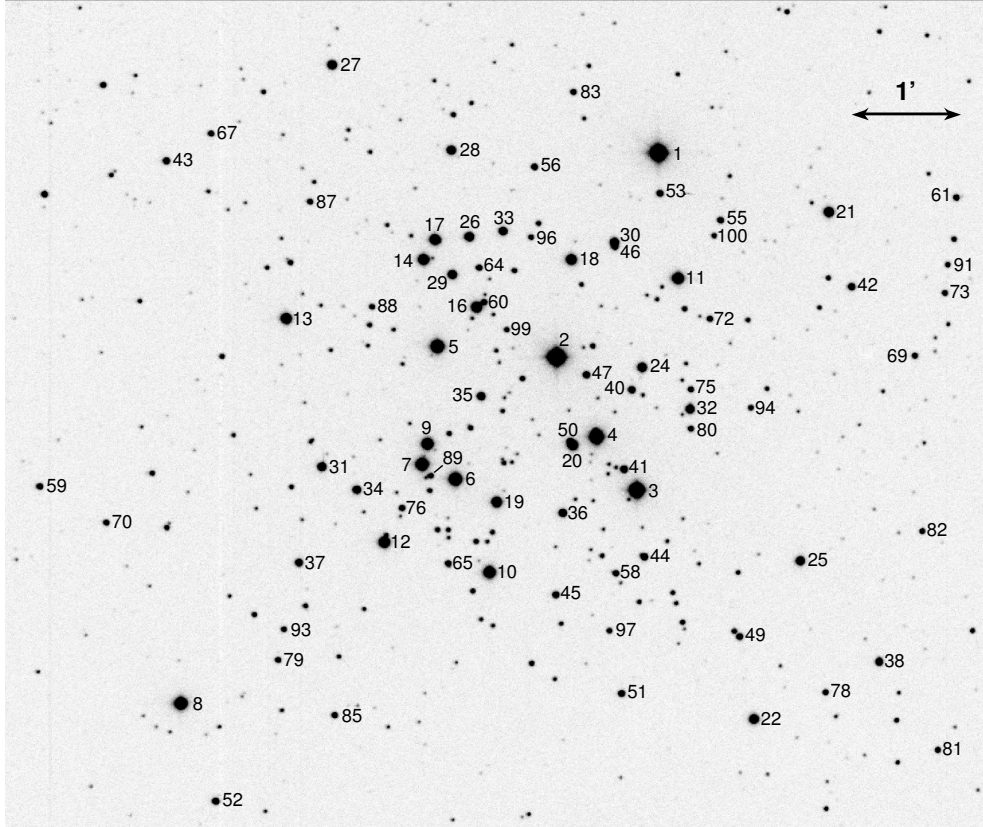


Figure 7.1: Finding chart for the NGC 3293 field. North is up and east is left. Numbers are placed to the right of the stars, except for #7, 14, 16, 29, 35, 40, 61, 69 (left), #2, 17, 26, 33 (up), and #20 (below). Star #86 is located very close to #17 and is not labeled.

(=BVC 36). The reported *UBV* magnitudes, however, match the photometry of BVC 36 (Baume et al. 2003).

Baume et al. (2003) also gives cross-identifications for stars in their Table 1. Here we attempt to clarify a few ambiguities: BVC 38 is erroneously referred to as Feast 41 (= HD 303073 = CPD-57°3457 = TYC 8613-2306-1), whereas BVC 38 = FEAS 126 and is not listed by Feast (1958); BVC 7 = FEAS 6 = CPD-57°3526B (no HD entry); BVC 9 = FEAS 26 = CPD-57°3526 (no HD entry); BVC 12 = FEAS 27 = HD 92007 = CPD-57°3527.

Table 7.1: Cross-identification of stars in the NGC 3293 field.

#	#B	#F	#E	GCVS	NSV	HD	CPD-57°	Remarks
1	3	3	2	V513 Car	—	91943	3499	HIP 51857
2	4	4	1	—	18454	91969	3508	HIP 51866
3	21	21	—	V361 Car	—	—	3502	IRAS 10338-5756
4	22	22	3	—	—	—	3506A	—

Table 7.1 – continued.

#	#B	#F	#E	GCVS	NSV	HD	CPD–57°	Remarks
5	20	20	4	—	—	—	3523	—
6	25	25	5	—	—	—	3521	—
7	6	6	6	—	—	—	3526B	—
8	—	8	7	—	—	92044	3540	—
9	26	26	11	V379 Car	—	—	3526	λ Eri ⁽⁴⁾ , Be ⁽⁵⁾
10	7	7	8	—	—	91983	3516	—
11	16	16	10	V403 Car	—	—	3500	β Cep ⁽²⁾
12	27	27	12	V380 Car	—	92007	3527	β Cep ⁽²⁾
13	5	5	13	V381 Car	—	92024	3533	EB ⁽³⁾ , β Cep ⁽²⁾
14	19	19	14	—	—	—	3524A	Be ⁽⁸⁾
15	—	2	—	—	—	91850	3468	—
16	133	133	15	V440 Car	—	—	3515	β Cep ⁽⁴⁾
17	18	18	18	V406 Car	—	—	3524B	β Cep ⁽²⁾
18	14	14	19	V405 Car	—	—	3507	β Cep ⁽²⁾
19	24	24	17	V378 Car	—	—	3517	β Cep ⁽²⁾
20	23	23	—	V404 Car	—	—	3506B	β Cep ⁽²⁾
21	10	10	20	V401 Car	—	303067	3486	β Cep ⁽²⁾
22	—	43	—	—	—	303076	3491	—
23	—	42	—	—	—	303074	3461	—
24	65	65	21	V412 Car	—	—	3503	β Cep ⁽²⁾
25	—	12	22	V402 Car	—	303075	3490	Be ⁽¹⁾
26	131	131	23	—	—	—	3519	—
27	—	9	24	—	—	303065	3530	—
28	—	13	26	—	—	—	3522	—
29	132	132	28	—	—	—	3520	—
30	15	15	25	—	—	—	3504	—
31	28	28	29	—	18457	—	3531	variable ⁽²⁾
32	79	79	27	—	18449	—	3497	variable ⁽⁴⁾ , Be ⁽⁵⁾
33	17	17	30	—	—	—	3514	—
34	33	33	31	—	—	—	3528	—
35	29	29	32	—	18455	—	3518	variable ⁽²⁾
36	86	86	34	—	—	—	3509	—
37	89	89	37	—	—	—	3532	—
38	—	126	—	—	—	—	—	—
39	—	—	—	—	—	—	3470	—
40	63	63	40	—	18451	—	—	variable ⁽⁴⁾ , Be ⁽⁵⁾
41	87	87	41	V438 Car	—	—	—	variable ⁽⁴⁾
42	92	92	43	—	—	—	3485	—
43	—	116	—	—	—	—	—	—
44	83	83	—	—	—	—	3501	—
45	85	85	—	—	—	—	3510	—
46	231	—	—	—	—	—	—	—
47	31	31	—	—	18453	—	—	—
48	—	—	38	—	—	—	3474	—
49	—	322	47	—	—	—	3492	—
50	198	—	16	—	—	—	—	—
51	137	292	48	—	—	—	3505	—
52	—	—	45	—	—	—	3538	—
53	75	75	50	—	18450	—	—	variable ⁽⁴⁾
54	—	459	52	—	—	—	3487	—
55	73	73	—	—	—	—	3494	—
56	—	130	53	—	—	—	3512	—
57	—	—	56	—	—	—	3476	—

Table 7.1 – continued.

#	#B	#F	#E	GCVS	NSV	HD	CPD–57°	Remarks
58	84	84	57	—	—	—	—	—
59	—	122	54	—	—	—	—	—
60	225	—	64	—	—	—	—	—
61	—	431	60	—	—	—	—	—
62	—	—	—	—	—	—	—	—
63	—	277	59	—	—	—	—	—
64	52	52	61	—	—	—	—	—
65	90	90	66	—	—	—	—	—
66	—	—	—	—	—	—	—	—
67	—	117	67	—	—	—	—	—
68	—	408	72	—	—	—	—	—
69	—	393	69	—	—	—	—	—
70	—	123	—	—	—	—	—	—
71	—	—	71	—	—	—	—	—
72	222	—	73	—	18448	—	—	variable ⁽⁴⁾
73	—	403	74	—	—	—	—	—
74	—	—	76	—	—	—	—	—
75	78	78	—	—	—	—	—	—
76	178	—	—	—	—	—	—	—
77	—	—	77	—	—	—	—	—
78	—	307	—	—	—	—	—	—
79	—	255	—	—	—	—	—	—
80	80	80	—	—	—	—	—	—
81	—	299	75	—	—	—	—	—
82	—	352	79	—	—	—	—	—
83	—	446	—	—	—	—	—	—
84	—	—	—	—	—	—	—	—
85	—	264	62	—	—	—	—	EB ⁽⁷⁾
86	—	—	—	—	—	—	—	—
87	—	184	—	—	—	—	—	—
88	93	93	84	—	18456	—	—	variable ⁽⁴⁾
89	184	—	—	—	—	—	—	—
90	—	—	87	—	—	—	—	—
91	—	401	88	—	—	—	—	—
92	—	—	—	—	—	—	—	—
93	—	246	—	—	—	—	—	—
94	81	81	93	—	—	—	—	—
95	—	—	96	—	—	—	—	—
96	30	30	—	—	—	—	—	—
97	104	104	90	—	—	—	—	—
98	140	289	—	—	—	—	—	—
99	55	55	98	—	—	—	—	—
100	72	72	—	—	—	—	—	Be ⁽⁸⁾
112	228	69	104	—	—	—	—	—
156	194	227	—	V441 Car	—	—	—	variable ⁽⁴⁾
160	69	496	—	—	—	—	—	—
168	60	60	—	V439 Car	—	—	—	probable λ Eri ⁽⁴⁾
183	—	187	—	—	—	—	—	δ Sct ⁽⁶⁾
363	208	—	—	—	—	—	—	δ Sct ⁽⁶⁾
—	—	11	—	V400 Car	—	303068	3464	β Cep ⁽²⁾

Notes: # – identification number (BVC) from Baume et al. (2003), #B – Balona (1994), #F – FEAS, #E – ESL (Evans et al. 2005).

References: (1) Schild (1970); (2) Balona & Engelbrecht (1981, 1983); (3) Engelbrecht (1986); (4) Balona (1994); (5) Evans et al. (2005); (6) Handler et al. (2007); (7) Handler et al. (2008); (8) McSwain et al. (2009).

7.2 Telescopes and instruments

The observations of NGC 3293 were carried out with 5 telescopes at 3 observatories in Chile and South Africa. The observatory sites with their geographical coordinates are summarised in Table 7.2.

ESO–La Silla Observatory is located on a mountain-top 160 km north of La Serena, Chile. The 0.91-m Dutch telescope with CCD-camera and Strömgren *by* filters was used during several observing runs in 1997–1999. Observations with the Danish 1.54-m telescope and DFOSC instrument were made in 2000, 2001, 2002, and 2006. Strömgren *uvby* filters were used in 2000–2002, whereas in 2006 the cluster was observed through Strömgren *y* and Johnson *U* filters.

Observatorio Cerro Armazones (OCA) is operated by Instituto de Astronomía of Universidad Católica del Norte in Antofagasta, Chile. The observatory is situated in the Atacama desert, 105 km south of Antofagasta, below the Cerro Armazones mountain-top. We used the 16-inch (0.41-m) Meade LX200 Schmidt-Cassegrain telescope with the SBIG STL-6303E camera and *BV* filters.

The South African Astronomical Observatory (SAAO) has an observatory site near Sutherland, South Africa, 280 km north-east of Cape Town. The observations with the 1.0-m telescope and STE4 CCD-camera were carried out in 2001, 2005, 2006, and 2007. The following filters were used: *uvby* in 2001, *by* in 2005, *UBV* in 2006, and *UBVR* in 2007. The 1.9-m telescope with the same camera and *UBV* filters was used during one night in 2007.

Table 7.3 summarises the telescopes and instruments with their field of view and pixel scale.

Table 7.2: Observatory sites.

Observatory	Site	Latitude	Longitude	Altitude
ESO	La Silla, Chile	29° 15' S	70° 44' W	2340 m
OCA	Cerro Armazones, Chile	24° 36' S	70° 12' W	2763 m
SAAO	Sutherland, South Africa	32° 23' S	20° 49' E	1760 m

Table 7.3: Telescopes and instruments.

Telescope	Instrument	Pixel scale	Pixels	FOV
Dutch 0.91 m	ESO #33 CCD	0''.442	512×512	3.77×3.77
Danish 1.54 m	DFOSC	0''.39	2048×2048	13.7×13.7
OCA 0.41 m	SBIG STL-6303E	0''.463	3072×2048	23.0×15.4
SAAO 1.0 m	STE4 CCD	0''.31	1024×1024	5.3×5.3
SAAO 1.9 m	STE4 CCD	0''.144	1024×1024	2.5×2.5

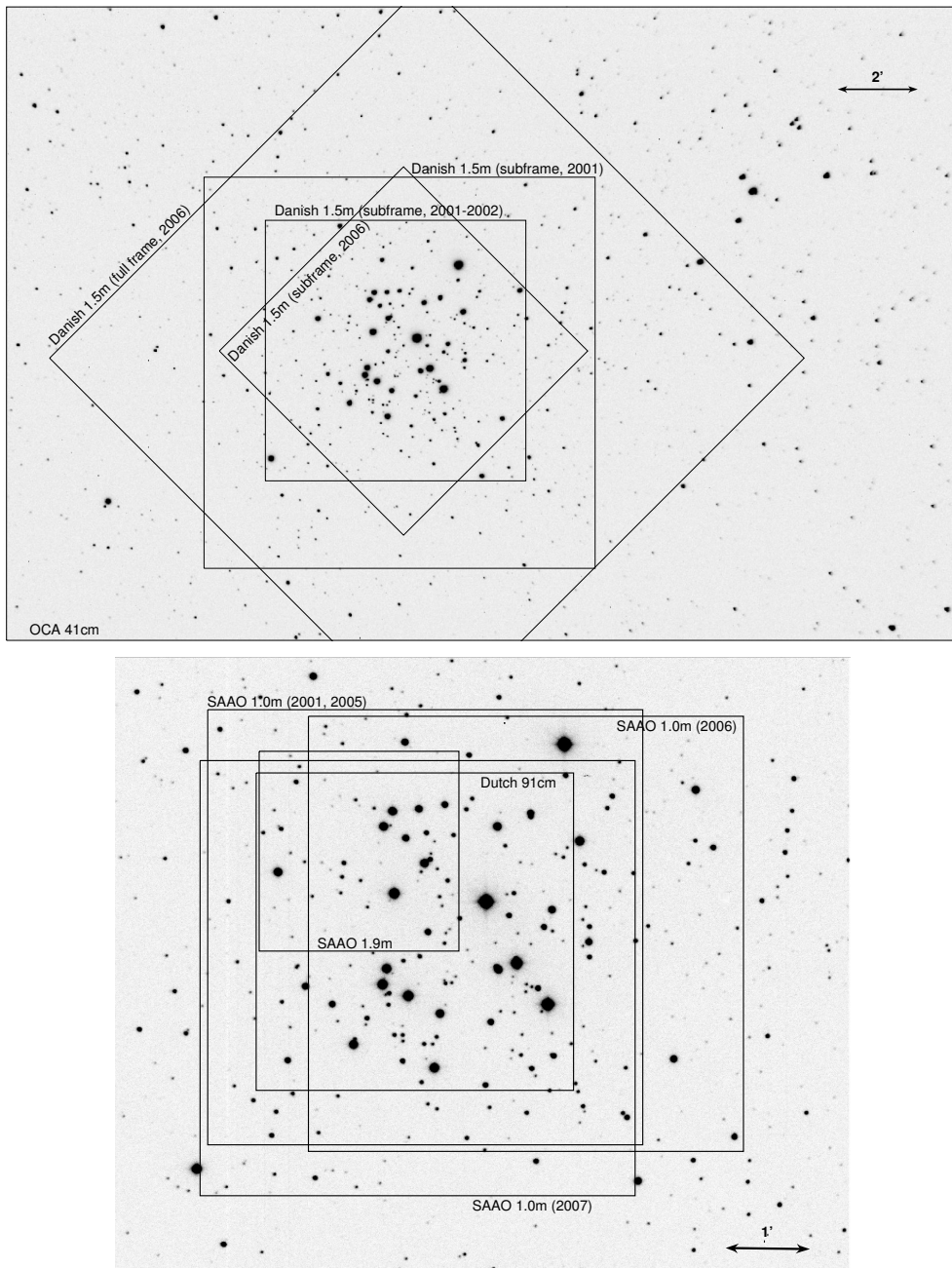


Figure 7.2: NGC 3293 field as observed with different telescopes. Top: full CCD frame obtained with the OCA 0.41-m telescope. The field-of-view of the Danish 1.54-m telescope is superimposed. Bottom: the rectangles correspond to the SAAO 1.0-m, 1.9-m, and the Dutch 0.91-m telescope fields.

The NGC 3293 field is illustrated in Fig. 7.2. The boundaries that correspond to the field of view of a given telescope, camera, subframe, and pointing, are shown.

7.3 Contribution to a multi-site campaign

A massive CCD photometry campaign of NGC 3293 was set up by Gerald Handler from January to May, 2006, involving six observing sites in the Southern Hemisphere. The campaign resulted in more than 700 hours of high-quality *UBV* photometry (Handler et al. 2007, 2008).

We contributed to the campaign with three observing runs: January 7–17 (OCA 0.41-m telescope), February 14–18 (Danish 1.54 m), and March 14–27 (SAAO 1.0 m), see Table 7.5 for details.

7.4 Observing strategy

The strategy for observing NGC 3293 has been the following:

1. include BVC 13 (= HD 92024), BVC 5 and the core of NGC 3293 on each CCD frame;
2. not to overexpose BVC 5;
3. obtain time-resolved photometry in at least two passbands (Strömgren *by* or Johnson *BV*);
4. obtain twilight flat field frames on as many nights as possible.

The strategy during the 2006 campaign was to include as many β Cep stars on CCD frames as possible and optimise integration time according to the brightest β Cep star

Table 7.4: Logbook of CCD frames.

Seq.	Filename	Date	Time	HJD	Exp.	X	F	Dimensions
1	50451_2958	1997-01-03	07:05:59	50451.79555	2.0	1.180	<i>y</i>	506×508
2	50451_2973	1997-01-03	07:08:11	50451.79708	2.0	1.178	<i>b</i>	506×508
3	50451_2986	1997-01-03	07:10:06	50451.79841	2.0	1.177	<i>y</i>	506×508
4	50451_2991	1997-01-03	07:10:45	50451.79887	3.0	1.176	<i>b</i>	506×508
5	50451_3341	1997-01-03	08:01:10	50451.83388	2.0	1.146	<i>y</i>	506×508
⋮	⋮	⋮	⋮	⋮	⋮	⋮	⋮	⋮
12278	ngc3293.01001.V.f	2006-01-08	05:42:39	53743.73801	15.0	1.346	<i>V</i>	3072×2048
12279	ngc3293.01002.V.f	2006-01-08	05:43:20	53743.73848	15.0	1.344	<i>V</i>	3072×2048
12280	ngc3293.01003.V.f	2006-01-08	05:44:02	53743.73897	15.0	1.343	<i>V</i>	3072×2048
12281	ngc3293.01005.B.f	2006-01-08	05:45:33	53743.74005	20.0	1.339	<i>B</i>	3072×2048
12282	ngc3293.01006.B.f	2006-01-08	05:46:19	53743.74058	20.0	1.338	<i>B</i>	3072×2048
⋮	⋮	⋮	⋮	⋮	⋮	⋮	⋮	⋮
22674	a6564621f	2007-03-14	00:16:12	54173.51404	18.0	1.235	<i>B</i>	1024×1024
22675	a6564622f	2007-03-14	00:17:28	54173.51488	12.0	1.237	<i>V</i>	1024×1024
22676	a6564623f	2007-03-14	00:18:38	54173.51573	18.0	1.239	<i>B</i>	1024×1024
22677	a6564624f	2007-03-14	00:19:54	54173.51657	12.0	1.241	<i>V</i>	1024×1024

Note: The complete Table is available from the author. Only a small excerpt is shown here.

in the field of view. It meant overexposing several bright stars in the cluster, including BVC 5.

7.5 Observing logs and statistics

NGC 3293 has been observed on 203 nights from January 1997 to March 2007. In total, 22677 CCD frames have been obtained.

Table 7.4 lists all the CCD frames with each row corresponding to a single image. The filename, date and time (UT) of the start of the exposure, HJD of mid-exposure, integration time in seconds, air mass at mid-exposure, passband, and frame size (in pixels) are given.

The observing nights are summarised in Table 7.5. Table rows represent the individual nights, while columns give the date, Julian day number, telescope, number of frames in *uvby* and *UBVR* passbands, time (in hours) spent for observing, and observer's name.

Table 7.5: Journal of observations. LJD is the Local Julian Day *minus* 2 400 000. Number of CCD frames in *uvby* and *UBVR* passbands are presented in columns 4–11.

Date	LJD	Telescope	<i>u</i>	<i>v</i>	<i>b</i>	<i>y</i>	<i>U</i>	<i>B</i>	<i>V</i>	<i>R</i>	Hours	Observer
1997-01-02	50451	Dutch 0.91 m	—	—	9	9	—	—	—	—	1.5	Sterken
1997-01-03	50452	Dutch 0.91 m	—	—	11	11	—	—	—	—	3.2	Sterken
1997-01-04	50453	Dutch 0.91 m	—	—	70	72	—	—	—	—	2.8	Sterken
1997-01-05	50454	Dutch 0.91 m	—	—	137	139	—	—	—	—	4.1	Sterken
1997-01-06	50455	Dutch 0.91 m	—	—	39	39	—	—	—	—	1.2	Sterken
1997-01-07	50456	Dutch 0.91 m	—	—	61	62	—	—	—	—	1.9	Sterken
1997-01-08	50457	Dutch 0.91 m	—	—	156	158	—	—	—	—	5.4	Sterken
1997-01-09	50458	Dutch 0.91 m	—	—	112	112	—	—	—	—	4.7	Sterken
1997-01-31	50480	Dutch 0.91 m	—	—	79	80	—	—	—	—	2.9	Sterken
1997-02-01	50481	Dutch 0.91 m	—	—	87	88	—	—	—	—	3.1	Sterken
1997-02-02	50482	Dutch 0.91 m	—	—	85	85	—	—	—	—	5.8	Sterken
1997-02-03	50483	Dutch 0.91 m	—	—	61	61	—	—	—	—	8.3	Sterken
1997-02-04	50484	Dutch 0.91 m	—	—	17	17	—	—	—	—	3.2	Sterken
1997-02-05	50485	Dutch 0.91 m	—	—	131	132	—	—	—	—	7.6	Sterken
1997-02-06	50486	Dutch 0.91 m	—	—	177	178	—	—	—	—	7.6	Sterken
1997-02-07	50487	Dutch 0.91 m	—	—	154	154	—	—	—	—	7.8	Sterken
1997-05-13	50582	Dutch 0.91 m	—	—	120	118	—	—	—	—	5.8	Sterken
1997-05-14	50583	Dutch 0.91 m	—	—	137	144	—	—	—	—	5.8	Sterken
1997-05-15	50584	Dutch 0.91 m	—	—	7	11	—	—	—	—	3.4	Sterken
1997-05-16	50585	Dutch 0.91 m	—	—	88	92	—	—	—	—	3.9	Sterken
1997-05-19	50588	Dutch 0.91 m	—	—	72	75	—	—	—	—	4.7	Sterken
1997-05-20	50589	Dutch 0.91 m	—	—	98	101	—	—	—	—	5.6	Sterken
1997-05-21	50590	Dutch 0.91 m	—	—	132	138	—	—	—	—	6.0	Sterken
1997-07-15	50645	Dutch 0.91 m	—	—	13	16	—	—	—	—	2.0	Arentoft
1997-07-16	50646	Dutch 0.91 m	—	—	13	16	—	—	—	—	1.5	Arentoft
1997-07-17	50647	Dutch 0.91 m	—	—	15	19	—	—	—	—	1.5	Arentoft
1997-07-18	50648	Dutch 0.91 m	—	—	17	23	—	—	—	—	1.9	Arentoft
1997-07-19	50649	Dutch 0.91 m	—	—	17	24	—	—	—	—	1.7	Arentoft
1997-07-20	50650	Dutch 0.91 m	—	—	16	18	—	—	—	—	1.8	Arentoft
1997-07-21	50651	Dutch 0.91 m	—	—	12	17	—	—	—	—	1.4	Arentoft
1997-07-22	50652	Dutch 0.91 m	—	—	6	13	—	—	—	—	0.7	Arentoft
1998-01-04	50818	Dutch 0.91 m	—	—	30	34	—	—	—	—	4.2	Sterken
1998-01-05	50819	Dutch 0.91 m	—	—	11	11	—	—	—	—	4.2	Sterken
1998-01-06	50820	Dutch 0.91 m	—	—	4	4	—	—	—	—	3.8	Sterken
1998-01-07	50821	Dutch 0.91 m	—	—	12	16	—	—	—	—	4.3	Sterken
1998-01-08	50822	Dutch 0.91 m	—	—	34	32	—	—	—	—	3.1	Sterken
1998-01-09	50823	Dutch 0.91 m	—	—	1	1	—	—	—	—	0.0	Sterken
1998-01-10	50824	Dutch 0.91 m	—	—	9	8	—	—	—	—	3.5	Sterken
1998-01-11	50825	Dutch 0.91 m	—	—	15	16	—	—	—	—	1.2	Sterken

Table 7.5 – continued.

Date	LJD	Telescope	<i>u</i>	<i>v</i>	<i>b</i>	<i>y</i>	<i>U</i>	<i>B</i>	<i>V</i>	<i>R</i>	Hours	Observer
1998-01-12	50826	Dutch 0.91 m	–	–	4	4	–	–	–	–	4.0	Sterken
1998-01-13	50827	Dutch 0.91 m	–	–	17	19	–	–	–	–	1.2	Sterken
1998-01-14	50828	Dutch 0.91 m	–	–	32	34	–	–	–	–	2.3	Arentoft
1998-01-15	50829	Dutch 0.91 m	–	–	20	21	–	–	–	–	0.5	Arentoft
1998-01-16	50830	Dutch 0.91 m	–	–	28	30	–	–	–	–	0.7	Arentoft
1998-01-17	50831	Dutch 0.91 m	–	–	2	2	–	–	–	–	0.0	Arentoft
1998-01-18	50832	Dutch 0.91 m	–	–	4	8	–	–	–	–	0.2	Arentoft
1998-01-19	50833	Dutch 0.91 m	–	–	8	8	–	–	–	–	0.2	Arentoft
1998-01-20	50834	Dutch 0.91 m	–	–	21	22	–	–	–	–	0.5	Arentoft
1998-01-21	50835	Dutch 0.91 m	–	–	21	23	–	–	–	–	1.8	Arentoft
1998-01-22	50836	Dutch 0.91 m	–	–	10	12	–	–	–	–	2.4	Arentoft
1998-01-24	50838	Dutch 0.91 m	–	–	6	6	–	–	–	–	0.1	Arentoft
1998-01-25	50839	Dutch 0.91 m	–	–	8	8	–	–	–	–	0.2	Arentoft
1998-01-26	50840	Dutch 0.91 m	–	–	10	11	–	–	–	–	0.2	Arentoft
1998-01-27	50841	Dutch 0.91 m	–	–	7	8	–	–	–	–	0.2	Arentoft
1998-01-28	50842	Dutch 0.91 m	–	–	6	7	–	–	–	–	0.2	Arentoft
1998-01-29	50843	Dutch 0.91 m	–	–	4	4	–	–	–	–	0.1	Arentoft
1998-02-04	50849	Dutch 0.91 m	–	–	4	4	–	–	–	–	1.5	Sterken
1998-02-05	50850	Dutch 0.91 m	–	–	4	4	–	–	–	–	4.5	Sterken
1998-02-06	50851	Dutch 0.91 m	–	–	8	8	–	–	–	–	4.4	Sterken
1998-02-09	50854	Dutch 0.91 m	–	–	104	105	–	–	–	–	3.7	Sterken
1998-03-14	50887	Dutch 0.91 m	–	–	30	28	–	–	–	–	2.6	Sterken
1998-03-17	50890	Dutch 0.91 m	–	–	5	5	–	–	–	–	4.7	Sterken
1998-03-18	50891	Dutch 0.91 m	–	–	3	3	–	–	–	–	0.1	Sterken
1998-03-19	50892	Dutch 0.91 m	–	–	40	40	–	–	–	–	1.5	Sterken
1998-04-14	50918	Dutch 0.91 m	–	–	3	4	–	–	–	–	0.1	Arentoft
1998-04-16	50920	Dutch 0.91 m	–	–	10	11	–	–	–	–	0.3	Arentoft
1998-04-17	50921	Dutch 0.91 m	–	–	5	6	–	–	–	–	0.1	Arentoft
1998-04-18	50922	Dutch 0.91 m	–	–	6	7	–	–	–	–	0.2	Arentoft
1998-12-31	51179	Dutch 0.91 m	–	–	13	14	–	–	–	–	0.4	Arentoft
1999-01-02	51181	Dutch 0.91 m	–	–	15	18	–	–	–	–	2.3	Arentoft
1999-01-03	51182	Dutch 0.91 m	–	–	7	9	–	–	–	–	2.8	Arentoft
1999-01-04	51183	Dutch 0.91 m	–	–	118	119	–	–	–	–	3.0	Arentoft
1999-01-05	51184	Dutch 0.91 m	–	–	7	7	–	–	–	–	3.4	Arentoft
1999-01-06	51185	Dutch 0.91 m	–	–	17	17	–	–	–	–	1.6	Arentoft
1999-01-07	51186	Dutch 0.91 m	–	–	10	10	–	–	–	–	1.6	Arentoft
1999-01-08	51187	Dutch 0.91 m	–	–	11	11	–	–	–	–	1.4	Arentoft
1999-01-19	51198	Dutch 0.91 m	–	–	12	12	–	–	–	–	7.2	Sterken
1999-01-20	51199	Dutch 0.91 m	–	–	5	5	–	–	–	–	2.9	Sterken
1999-01-21	51200	Dutch 0.91 m	–	–	2	2	–	–	–	–	0.0	Sterken
1999-01-22	51201	Dutch 0.91 m	–	–	2	2	–	–	–	–	0.0	Sterken
1999-01-23	51202	Dutch 0.91 m	–	–	2	3	–	–	–	–	0.1	Sterken
1999-01-24	51203	Dutch 0.91 m	–	–	2	2	–	–	–	–	0.0	Sterken
1999-01-25	51204	Dutch 0.91 m	–	–	2	2	–	–	–	–	0.0	Sterken
1999-01-26	51205	Dutch 0.91 m	–	–	2	2	–	–	–	–	0.0	Sterken
1999-01-27	51206	Dutch 0.91 m	–	–	2	2	–	–	–	–	0.1	Sterken
1999-01-28	51207	Dutch 0.91 m	–	–	105	105	–	–	–	–	3.3	Sterken
1999-01-29	51208	Dutch 0.91 m	–	–	144	144	–	–	–	–	4.4	Sterken
1999-01-30	51209	Dutch 0.91 m	–	–	129	129	–	–	–	–	6.2	Sterken
1999-03-23	51261	Dutch 0.91 m	–	–	7	8	–	–	–	–	6.1	Sterken
1999-03-24	51262	Dutch 0.91 m	–	–	11	11	–	–	–	–	2.0	Sterken
1999-03-25	51263	Dutch 0.91 m	–	–	25	26	–	–	–	–	4.1	Sterken
1999-03-26	51264	Dutch 0.91 m	–	–	64	64	–	–	–	–	5.8	Sterken
1999-03-27	51265	Dutch 0.91 m	–	–	65	66	–	–	–	–	5.0	Sterken
1999-03-28	51266	Dutch 0.91 m	–	–	53	53	–	–	–	–	4.2	Sterken
1999-03-29	51267	Dutch 0.91 m	–	–	150	151	–	–	–	–	3.8	Sterken
1999-03-30	51268	Dutch 0.91 m	–	–	38	37	–	–	–	–	2.8	Sterken
1999-03-31	51269	Dutch 0.91 m	–	–	35	36	–	–	–	–	1.8	Sterken
2000-02-17	51592	Danish 1.54 m	–	2	–	2	–	–	–	–	0.1	Sterken
2000-02-19	51594	Danish 1.54 m	–	3	–	3	–	–	–	–	0.1	Sterken
2001-01-01	51911	SAAO 1.0 m	10	10	10	10	–	–	–	–	2.2	Knudsen
2001-01-02	51912	SAAO 1.0 m	27	27	26	26	–	–	–	–	3.0	Knudsen
2001-01-03	51913	SAAO 1.0 m	4	4	56	56	–	–	–	–	3.1	Knudsen
2001-01-04	51914	SAAO 1.0 m	–	–	65	63	–	–	–	–	3.3	Knudsen
2001-01-05	51915	SAAO 1.0 m	–	–	80	80	–	–	–	–	3.8	Knudsen

Table 7.5 – continued.

Date	LJD	Telescope	<i>u</i>	<i>v</i>	<i>b</i>	<i>y</i>	<i>U</i>	<i>B</i>	<i>V</i>	<i>R</i>	Hours	Observer
2001-01-06	51916	SAAO 1.0 m	–	–	69	68	–	–	–	–	3.3	Knudsen
2001-01-07	51917	SAAO 1.0 m	–	–	65	64	–	–	–	–	3.6	Knudsen
2001-01-08	51918	SAAO 1.0 m	–	–	65	65	–	–	–	–	4.1	Knudsen
2001-01-09	51919	SAAO 1.0 m	2	1	69	66	–	–	–	–	4.4	Knudsen
2001-01-10	51920	SAAO 1.0 m	1	1	55	54	–	–	–	–	3.2	Knudsen
2001-01-11	51921	SAAO 1.0 m	1	1	79	78	–	–	–	–	4.7	Knudsen
2001-01-14	51924	SAAO 1.0 m	–	–	62	62	–	–	–	–	3.0	Knudsen
2001-01-15	51925	SAAO 1.0 m	1	1	53	52	–	–	–	–	2.6	Knudsen
2001-03-06	51975	Danish 1.54 m	–	7	9	9	–	–	–	–	0.7	Knudsen, Nuspl
2001-03-07	51976	Danish 1.54 m	–	14	14	14	–	–	–	–	1.3	Knudsen, Nuspl
2001-03-08	51977	Danish 1.54 m	–	14	14	15	–	–	–	–	1.8	Knudsen, Nuspl
2001-03-09	51978	Danish 1.54 m	–	2	28	28	–	–	–	–	1.3	Knudsen, Nuspl
2001-03-10	51979	Danish 1.54 m	–	–	125	124	–	–	–	–	4.5	Knudsen, Nuspl
2001-03-11	51980	Danish 1.54 m	–	–	43	43	–	–	–	–	1.4	Knudsen, Nuspl
2001-03-12	51981	Danish 1.54 m	–	–	122	122	–	–	–	–	4.4	Knudsen, Nuspl
2001-03-13	51982	Danish 1.54 m	–	–	81	81	–	–	–	–	2.5	Knudsen, Nuspl
2001-04-09	52009	Danish 1.54 m	–	–	44	44	–	–	–	–	2.0	Freyhammer
2001-04-10	52010	Danish 1.54 m	–	–	43	41	–	–	–	–	1.9	Freyhammer
2001-04-11	52011	Danish 1.54 m	–	–	48	54	–	–	–	–	4.5	Freyhammer
2001-11-24	52238	Danish 1.54 m	–	–	5	6	–	–	–	–	0.2	Sterken
2001-11-25	52239	Danish 1.54 m	–	–	9	9	–	–	–	–	1.0	Sterken
2001-11-26	52240	Danish 1.54 m	–	–	6	6	–	–	–	–	0.1	Sterken
2001-11-27	52241	Danish 1.54 m	4	5	5	6	–	–	–	–	0.5	Sterken
2002-01-10	52285	Danish 1.54 m	1	1	3	3	–	–	–	–	0.1	Sterken
2002-01-11	52286	Danish 1.54 m	–	–	3	3	–	–	–	–	0.1	Sterken
2002-01-12	52287	Danish 1.54 m	–	–	2	2	–	–	–	–	0.0	Sterken
2002-02-01	52307	Danish 1.54 m	7	7	8	8	–	–	–	–	1.0	Sterken
2002-02-02	52308	Danish 1.54 m	4	6	4	4	–	–	–	–	0.2	Sterken
2002-02-03	52309	Danish 1.54 m	4	4	4	6	–	–	–	–	0.3	Sterken
2002-03-30	52364	Danish 1.54 m	7	10	12	14	–	–	–	–	2.9	Sterken
2002-03-31	52365	Danish 1.54 m	8	9	11	12	–	–	–	–	2.7	Sterken
2002-04-01	52366	Danish 1.54 m	8	11	13	18	–	–	–	–	5.3	Sterken
2002-09-19	52537	Danish 1.54 m	3	4	3	4	–	–	–	–	0.2	Sterken
2002-12-13	52622	Danish 1.54 m	23	23	23	24	–	–	–	–	2.8	Sterken
2002-12-14	52623	Danish 1.54 m	14	14	14	17	–	–	–	–	2.0	Sterken
2002-12-15	52624	Danish 1.54 m	28	28	28	28	–	–	–	–	1.7	Sterken
2002-12-18	52627	Danish 1.54 m	27	27	27	28	–	–	–	–	1.6	Sterken
2002-12-19	52628	Danish 1.54 m	25	26	26	27	–	–	–	–	1.5	Sterken
2002-12-20	52629	Danish 1.54 m	26	26	26	26	–	–	–	–	1.5	Sterken
2002-12-21	52630	Danish 1.54 m	20	20	20	20	–	–	–	–	1.2	Sterken
2002-12-22	52631	Danish 1.54 m	36	36	36	36	–	–	–	–	2.1	Sterken
2005-04-08	53469	SAAO 1.0 m	–	–	41	45	–	–	–	–	2.1	Tuvikene
2005-04-09	53470	SAAO 1.0 m	–	–	54	53	–	–	–	–	2.6	Tuvikene
2005-04-13	53474	SAAO 1.0 m	–	–	41	44	–	–	–	–	2.7	Tuvikene
2005-04-14	53475	SAAO 1.0 m	–	–	69	72	–	–	–	–	3.7	Tuvikene
2005-04-15	53476	SAAO 1.0 m	–	–	65	67	–	–	–	–	3.3	Tuvikene
2005-04-16	53477	SAAO 1.0 m	–	–	39	41	–	–	–	–	3.0	Tuvikene
2005-04-17	53478	SAAO 1.0 m	–	–	43	51	–	–	–	–	3.5	Tuvikene
2005-04-18	53479	SAAO 1.0 m	–	–	29	31	–	–	–	–	1.8	Tuvikene
2006-01-07	53743	OCA 0.41 m	–	–	–	–	–	98	107	–	3.1	Tuvikene
2006-01-08	53744	OCA 0.41 m	–	–	–	–	–	92	95	–	3.1	Tuvikene
2006-01-09	53745	OCA 0.41 m	–	–	–	–	–	63	117	–	4.5	Tuvikene
2006-01-10	53746	OCA 0.41 m	–	–	–	–	–	89	178	–	4.4	Tuvikene
2006-01-11	53747	OCA 0.41 m	–	–	–	–	–	86	169	–	4.2	Tuvikene
2006-01-12	53748	OCA 0.41 m	–	–	–	–	–	109	171	–	4.7	Tuvikene
2006-01-13	53749	OCA 0.41 m	–	–	–	–	–	88	162	–	5.1	Tuvikene
2006-01-14	53750	OCA 0.41 m	–	–	–	–	–	111	228	–	4.8	Tuvikene
2006-01-15	53751	OCA 0.41 m	–	–	–	–	–	109	244	–	6.0	Tuvikene
2006-01-16	53752	OCA 0.41 m	–	–	–	–	–	112	212	–	5.7	Tuvikene
2006-01-17	53753	OCA 0.41 m	–	–	–	–	–	115	220	–	5.6	Tuvikene
2006-02-14	53781	Danish 1.54 m	–	–	–	79	–	–	–	–	1.3	Sterken
2006-02-15	53782	Danish 1.54 m	–	–	–	80	80	–	–	–	4.9	Sterken
2006-02-16	53783	Danish 1.54 m	–	–	–	–	238	–	–	–	5.1	Sterken
2006-02-17	53784	Danish 1.54 m	–	–	–	–	324	–	–	–	5.5	Sterken
2006-02-18	53785	Danish 1.54 m	–	–	–	–	457	–	–	–	6.1	Sterken

Table 7.5 – continued.

Date	LJD	Telescope	<i>u</i>	<i>v</i>	<i>b</i>	<i>y</i>	<i>U</i>	<i>B</i>	<i>V</i>	<i>R</i>	Hours	Observer
2006-03-14	53809	SAAO 1.0 m	–	–	–	–	46	108	158	–	8.3	Tuvikene
2006-03-15	53810	SAAO 1.0 m	–	–	–	–	57	114	181	–	8.8	Tuvikene
2006-03-16	53811	SAAO 1.0 m	–	–	–	–	16	30	53	–	4.2	Tuvikene
2006-03-17	53812	SAAO 1.0 m	–	–	–	–	36	73	120	–	6.3	Tuvikene
2006-03-18	53813	SAAO 1.0 m	–	–	–	–	48	104	163	–	8.2	Tuvikene
2006-03-19	53814	SAAO 1.0 m	–	–	–	–	42	85	134	–	7.3	Tuvikene
2006-03-20	53815	SAAO 1.0 m	–	–	–	–	17	38	64	–	5.2	Tuvikene
2006-03-21	53816	SAAO 1.0 m	–	–	–	–	48	99	150	–	7.9	Tuvikene
2006-03-22	53817	SAAO 1.0 m	–	–	–	–	5	12	22	–	1.0	Tuvikene
2006-03-23	53818	SAAO 1.0 m	–	–	–	–	6	18	28	–	1.2	Tuvikene
2006-03-24	53819	SAAO 1.0 m	–	–	–	–	47	57	78	–	8.5	Tuvikene
2006-03-25	53820	SAAO 1.0 m	–	–	–	–	16	16	17	–	1.2	Tuvikene
2006-03-26	53821	SAAO 1.0 m	–	–	–	–	22	49	72	–	3.6	Tuvikene
2006-03-27	53822	SAAO 1.0 m	–	–	–	–	6	12	24	–	1.2	Tuvikene
2007-01-31	54132	SAAO 1.0 m	–	–	–	–	29	30	30	–	2.6	Tuvikene
2007-02-01	54133	SAAO 1.0 m	–	–	–	–	–	65	66	–	3.0	Tuvikene
2007-02-02	54134	SAAO 1.0 m	–	–	–	–	–	99	100	–	3.8	Tuvikene
2007-02-03	54135	SAAO 1.0 m	–	–	–	–	6	7	7	–	0.5	Tuvikene
2007-02-04	54136	SAAO 1.0 m	–	–	–	–	18	71	73	–	4.0	Tuvikene
2007-02-05	54137	SAAO 1.0 m	–	–	–	–	5	98	98	92	5.8	Tuvikene
2007-02-06	54138	SAAO 1.0 m	–	–	–	–	14	46	47	19	2.9	Tuvikene
2007-02-08	54140	SAAO 1.0 m	–	–	–	–	61	78	79	–	6.8	Tuvikene
2007-02-12	54144	SAAO 1.0 m	–	–	–	–	40	40	41	16	3.4	Tuvikene
2007-02-19	54151	SAAO 1.9 m	–	–	–	–	17	135	139	–	7.4	Tuvikene
2007-02-28	54160	SAAO 1.0 m	–	–	–	–	–	139	139	–	5.6	Tuvikene
2007-03-01	54161	SAAO 1.0 m	–	–	–	–	–	89	90	–	3.6	Tuvikene
2007-03-05	54165	SAAO 1.0 m	–	–	–	–	–	101	104	–	8.5	Tuvikene
2007-03-07	54167	SAAO 1.0 m	–	–	–	–	–	84	85	–	1.3	Tuvikene
2007-03-08	54168	SAAO 1.0 m	–	–	–	–	–	83	83	–	3.1	Tuvikene
2007-03-09	54169	SAAO 1.0 m	–	–	–	–	–	117	117	–	4.4	Tuvikene
2007-03-10	54170	SAAO 1.0 m	–	–	–	–	–	37	37	4	1.6	Tuvikene
2007-03-11	54171	SAAO 1.0 m	–	–	–	–	35	47	47	–	3.8	Tuvikene
2007-03-12	54172	SAAO 1.0 m	–	–	–	–	–	175	176	–	6.8	Tuvikene
2007-03-13	54173	SAAO 1.0 m	–	–	–	–	–	110	111	–	4.3	Tuvikene

Our dataset comprises 22677 CCD frames in total, of which 12436 have been obtained in Strömgren *uvby* and 10241 in Johnson-Cousins *UBVR* passbands.

Fig. 7.3 presents the timeline of observations. In the top panel, individual observing nights and their duration can be seen. The cumulative number of CCD frames is plotted in the lower panel. The biggest contributions to the dataset come from the years 1997, 2001, 2006, and 2007.

NGC 3293 has been observed on 203 nights with 611 hours in total being spent. The observed sequences vary in length from a snapshot to 8.8 hours (see histogram in Fig. 7.4).

The histogram of air masses is shown in Fig. 7.5. The majority of the CCD frames has been obtained at low air masses: 11794 ($1.1 < X < 1.2$), 6089 ($1.2 < X < 1.3$), and 4794 ($X > 1.3$).

7.6 Atmospheric extinction, seeing

Atmospheric extinction refers to the absorption and scattering of stellar radiation by the Earth's atmosphere. In the monochromatic case, the magnitude $m(X)$ at air mass

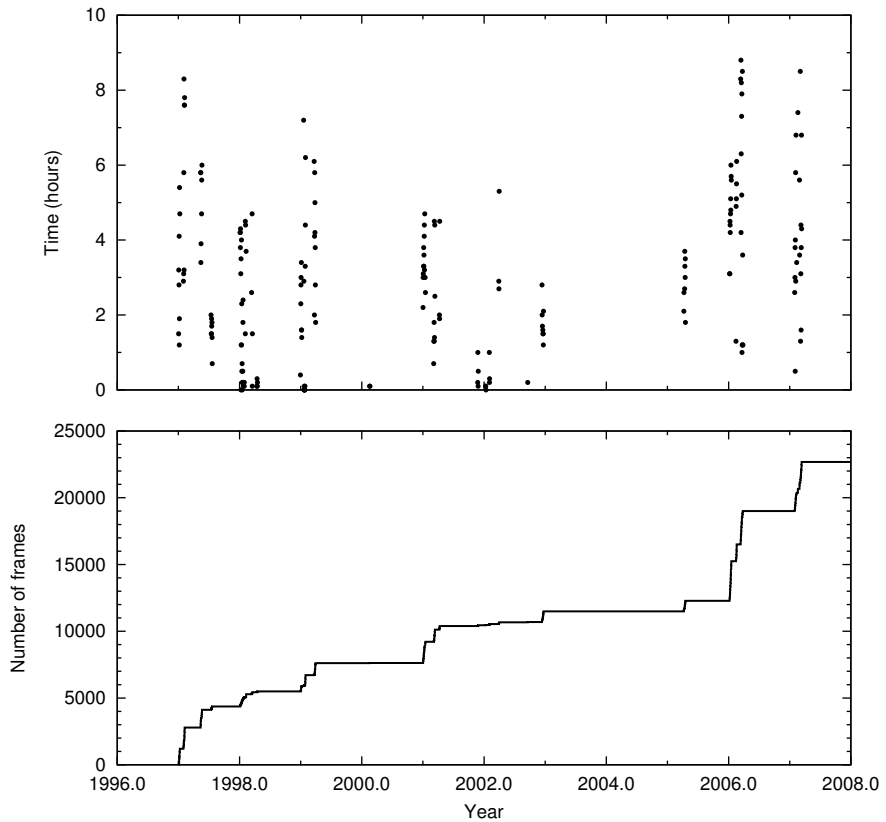


Figure 7.3: Timeline of observations. *Top:* number of observing hours per night as a function of time. *Bottom:* cumulative number of CCD frames.

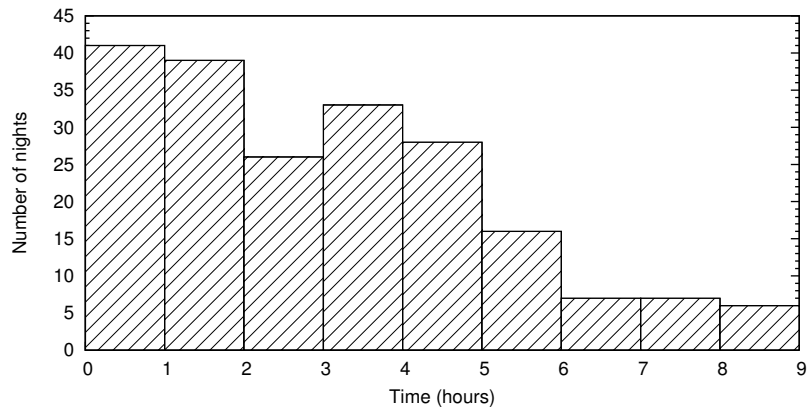


Figure 7.4: Histogram of time per night dedicated to NGC 3293 observations.

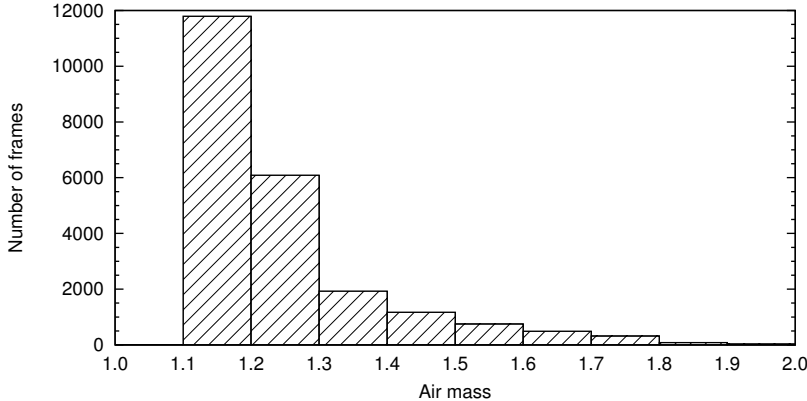


Figure 7.5: Histogram of air masses. The vertical scale gives the number of CCD frames obtained in each air-mass interval.

X follows Bouguer's law (Sterken & Manfroid 1992):

$$m(X) = m_0 + k(\lambda)X, \quad (7.1)$$

where m_0 is the magnitude outside the atmosphere and $k(\lambda)$ is the extinction coefficient at wavelength λ .

We determined atmospheric extinction with Bouguer's method by plotting the magnitudes of a constant star as a function of air mass. The Bouguer plots of every night were visually checked, not only for extinction measurements, but also for identification of any technical issues.

Table 7.6 lists all the nights with NGC 3293 observations. The columns give the date, LJD number, the minimum and maximum air masses, the air-mass range and coverage, classification of atmospheric extinction, and the minimum, median and maximum seeing values. The seeing values reflect only observations made with the Strömgren y or the Johnson V filter.

Table 7.6: Atmospheric conditions during the NGC 3293 observations. LJD is the Local Julian Day minus 2 400 000. Air-mass coverage is either continuous (cont.), discontinuous (discont.), or consisting of two snapshots (2 snaps.). Extinction is classified as constant (const.), variable (var.), or variable due to passing clouds. Extinction classes separated by a slash refer to the east and west side of the meridian.

Date	LJD	Air mass				Extinction	Seeing [arcsec]		
		Min.	Max.	Range	Coverage		Min.	Median	Max.
1997-01-02	50451	1.14	1.18	0.04	—	—	1.23	1.42	1.57
1997-01-03	50452	1.14	1.32	0.17	—	—	1.70	2.01	2.74
1997-01-04	50453	1.14	1.31	0.17	—	—	1.07	1.29	1.71
1997-01-05	50454	1.14	1.59	0.45	cont.	clouds	1.12	1.32	1.74
1997-01-06	50455	1.17	1.26	0.09	—	—	1.13	1.30	1.83
1997-01-07	50456	1.14	1.16	0.02	—	—	1.15	1.95	3.26
1997-01-08	50457	1.14	1.74	0.59	cont.	var.	1.06	1.31	1.75
1997-01-09	50458	1.14	1.54	0.40	cont.	var.	1.11	1.39	1.97

Table 7.6 – continued.

Date	LJD	Air mass			Extinction	Seeing [arcsec]			
		Min.	Max.	Range		Coverage	Min.	Median	
1997-01-31	50480	1.14	1.23	0.08	–	–	1.11	1.34	1.68
1997-02-01	50481	1.14	1.29	0.15	–	–	1.21	1.46	1.83
1997-02-02	50482	1.14	1.38	0.24	–	–	1.06	1.35	2.17
1997-02-03	50483	1.14	1.91	0.77	discont.	const./var.	1.25	1.51	2.18
1997-02-04	50484	1.17	1.63	0.46	discont.	const.	1.38	1.56	2.40
1997-02-05	50485	1.14	1.81	0.66	discont.	var.	1.09	1.41	2.15
1997-02-06	50486	1.14	1.70	0.56	cont.	var.	1.14	1.43	1.84
1997-02-07	50487	1.14	1.58	0.44	cont.	const./var.	1.10	1.42	1.98
1997-05-13	50582	1.14	1.90	0.75	cont.	var.	1.14	1.69	2.85
1997-05-14	50583	1.14	1.77	0.62	cont.	clouds/const.	1.35	1.62	2.16
1997-05-15	50584	1.15	1.24	0.09	–	–	2.41	2.79	3.51
1997-05-16	50585	1.14	1.36	0.21	–	–	1.68	2.68	5.53
1997-05-19	50588	1.15	1.65	0.51	cont.	var.	1.61	1.95	2.40
1997-05-20	50589	1.14	1.82	0.68	discont.	clouds	1.47	1.71	2.36
1997-05-21	50590	1.14	2.00	0.86	cont.	–/const.	1.64	2.35	3.53
1997-07-15	50645	1.37	1.94	0.57	discont.	clouds	1.42	1.61	1.89
1997-07-16	50646	1.37	1.73	0.36	discont.	const.	1.56	1.75	2.29
1997-07-17	50647	1.36	1.73	0.37	discont.	var.	1.62	1.81	3.20
1997-07-18	50648	1.36	1.87	0.51	discont.	const.	1.51	2.07	2.48
1997-07-19	50649	1.39	1.85	0.46	discont.	var.	1.47	1.76	3.14
1997-07-20	50650	1.38	1.86	0.47	discont.	clouds	1.34	1.65	2.37
1997-07-21	50651	1.40	1.75	0.35	discont.	clouds	1.34	1.53	2.28
1997-07-22	50652	1.53	1.74	0.21	–	–	1.49	1.87	2.14
1998-01-04	50818	1.14	1.46	0.31	discont.	var.	1.10	1.40	1.77
1998-01-05	50819	1.15	1.43	0.28	–	–	1.27	1.60	1.78
1998-01-06	50820	1.14	1.43	0.28	–	–	1.18	1.31	1.56
1998-01-07	50821	1.15	1.39	0.24	–	–	1.21	1.35	1.83
1998-01-08	50822	1.14	1.27	0.13	–	–	1.12	1.51	1.92
1998-01-09	50823	1.14	1.14	0.00	–	–	1.27	1.27	1.27
1998-01-10	50824	1.16	1.24	0.08	–	–	1.41	1.57	1.93
1998-01-11	50825	1.14	1.18	0.04	–	–	1.25	1.39	1.65
1998-01-12	50826	1.15	1.40	0.25	–	–	1.20	1.67	1.85
1998-01-13	50827	1.14	1.18	0.04	–	–	1.24	1.33	1.55
1998-01-14	50828	1.14	1.21	0.07	–	–	1.05	1.16	1.51
1998-01-15	50829	1.17	1.20	0.03	–	–	1.32	1.52	2.12
1998-01-16	50830	1.17	1.21	0.05	–	–	1.15	1.22	1.33
1998-01-17	50831	1.15	1.15	0.00	–	–	1.68	2.22	2.22
1998-01-18	50832	1.14	1.14	0.00	–	–	1.14	1.27	2.74
1998-01-19	50833	1.21	1.23	0.02	–	–	1.30	1.39	1.47
1998-01-20	50834	1.18	1.22	0.04	–	–	1.11	1.46	1.81
1998-01-21	50835	1.14	1.24	0.09	–	–	1.35	1.49	1.68
1998-01-22	50836	1.14	1.25	0.10	–	–	1.21	1.54	1.71
1998-01-24	50838	1.24	1.26	0.01	–	–	1.63	1.96	1.98
1998-01-25	50839	1.24	1.26	0.02	–	–	1.50	1.62	1.70
1998-01-26	50840	1.25	1.28	0.03	–	–	1.28	1.32	1.42
1998-01-27	50841	1.27	1.29	0.02	–	–	1.39	1.46	1.67
1998-01-28	50842	1.28	1.30	0.02	–	–	1.47	1.50	1.59
1998-01-29	50843	1.30	1.31	0.01	–	–	1.65	1.83	2.02
1998-02-04	50849	1.15	1.16	0.01	–	–	1.71	1.96	1.97
1998-02-05	50850	1.16	1.44	0.27	–	–	1.58	1.74	1.88
1998-02-06	50851	1.16	1.45	0.30	–	–	1.20	1.29	1.43
1998-02-09	50854	1.14	1.52	0.37	cont.	var.	1.27	1.66	2.07
1998-03-14	50887	1.24	1.75	0.51	discont.	var.	1.16	1.45	2.01

Table 7.6 – continued.

Date	LJD	Air mass			Extinction	Seeing [arcsec]			
		Min.	Max.	Range		Coverage	Min.	Median	
1998-03-17	50890	1.14	1.78	0.64	2 snaps.	–	1.47	1.62	2.83
1998-03-18	50891	1.25	1.25	0.01	–	–	1.41	1.43	1.55
1998-03-19	50892	1.19	1.34	0.16	–	–	1.23	1.39	1.55
1998-04-14	50918	1.54	1.56	0.02	–	–	1.61	1.86	1.90
1998-04-16	50920	1.18	1.20	0.02	–	–	2.62	3.00	4.76
1998-04-17	50921	1.41	1.44	0.03	–	–	1.73	1.91	2.49
1998-04-18	50922	1.31	1.34	0.03	–	–	1.55	1.83	2.18
1998-12-31	51179	1.14	1.14	0.00	–	–	1.21	1.38	1.58
1999-01-02	51181	1.14	1.27	0.13	–	–	1.12	1.20	1.74
1999-01-03	51182	1.18	1.56	0.38	2 snaps.	–	1.15	1.39	1.48
1999-01-04	51183	1.16	1.54	0.38	cont.	var.	1.10	1.46	3.06
1999-01-05	51184	1.17	1.67	0.51	2 snaps.	–	1.32	1.61	1.94
1999-01-06	51185	1.15	1.16	0.01	–	–	1.16	1.40	1.61
1999-01-07	51186	1.15	1.16	0.01	–	–	1.23	1.33	1.59
1999-01-08	51187	1.15	1.16	0.01	–	–	1.12	1.31	1.45
1999-01-19	51198	1.14	2.01	0.86	discont.	var.	1.56	1.77	2.50
1999-01-20	51199	1.15	1.25	0.10	–	–	1.38	1.71	2.37
1999-01-21	51200	1.18	1.18	0.00	–	–	2.19	2.28	2.28
1999-01-22	51201	1.23	1.23	0.00	–	–	1.17	1.76	1.76
1999-01-23	51202	1.14	1.15	0.00	–	–	1.30	1.35	1.35
1999-01-24	51203	1.15	1.15	0.00	–	–	1.42	1.48	1.48
1999-01-25	51204	1.21	1.21	0.00	–	–	1.46	1.75	1.75
1999-01-26	51205	1.16	1.16	0.00	–	–	1.56	1.70	1.70
1999-01-27	51206	1.17	1.17	0.01	–	–	1.45	1.64	1.64
1999-01-28	51207	1.14	1.23	0.09	–	–	1.09	1.28	1.84
1999-01-29	51208	1.14	1.26	0.12	–	–	1.06	1.32	1.83
1999-01-30	51209	1.14	1.39	0.25	–	–	1.10	1.28	2.60
1999-03-23	51261	1.15	2.02	0.87	discont.	var.	1.25	1.60	1.80
1999-03-24	51262	1.17	1.39	0.22	–	–	1.35	1.51	1.75
1999-03-25	51263	1.17	2.03	0.86	discont.	var.	1.37	1.96	2.16
1999-03-26	51264	1.14	1.75	0.61	cont.	var.	1.24	1.67	2.33
1999-03-27	51265	1.14	1.81	0.67	cont.	const.	1.12	1.50	2.12
1999-03-28	51266	1.15	1.78	0.63	cont.	var.	1.25	1.44	1.87
1999-03-29	51267	1.15	1.71	0.55	cont.	var.	1.16	1.46	1.81
1999-03-30	51268	1.22	1.73	0.52	cont.	var.	1.37	1.63	2.04
1999-03-31	51269	1.27	1.62	0.34	cont.	var.	1.40	1.74	2.33
2000-02-17	51592	1.19	1.20	0.01	–	–	3.66	3.70	3.70
2000-02-19	51594	1.47	1.48	0.02	–	–	2.77	2.78	2.83
2001-01-01	51911	1.11	1.21	0.10	–	–	2.40	3.96	5.74
2001-01-02	51912	1.11	1.25	0.14	–	–	1.52	1.85	3.34
2001-01-03	51913	1.11	1.24	0.13	–	–	1.58	2.15	2.88
2001-01-04	51914	1.11	1.25	0.14	–	–	1.56	1.93	2.85
2001-01-05	51915	1.11	1.31	0.20	–	–	1.38	2.04	2.82
2001-01-06	51916	1.11	1.23	0.12	–	–	1.57	2.20	3.22
2001-01-07	51917	1.11	1.26	0.14	–	–	2.07	2.77	4.90
2001-01-08	51918	1.11	1.29	0.18	–	–	1.70	2.16	3.04
2001-01-09	51919	1.11	1.31	0.20	–	–	1.59	2.37	3.25
2001-01-10	51920	1.11	1.18	0.07	–	–	1.61	2.14	3.44
2001-01-11	51921	1.11	1.32	0.21	–	–	1.81	2.18	2.59
2001-01-14	51924	1.11	1.18	0.07	–	–	1.42	2.32	3.78
2001-01-15	51925	1.11	1.18	0.07	–	–	1.72	2.28	3.30
2001-03-06	51975	1.14	1.16	0.01	–	–	3.19	3.29	3.41
2001-03-07	51976	1.14	1.17	0.03	–	–	2.16	2.37	2.55

Table 7.6 – continued.

Date	LJD	Air mass			Extinction	Seeing [arcsec]		
		Min.	Max.	Range		Coverage	Min.	Median
2001-03-08	51977	1.14	1.20	0.06	–	–	2.56	2.95
2001-03-09	51978	1.15	1.21	0.06	–	–	1.15	1.95
2001-03-10	51979	1.14	1.64	0.50	cont.	const.	1.31	1.93
2001-03-11	51980	1.14	1.17	0.02	–	–	1.37	1.70
2001-03-12	51981	1.14	1.57	0.43	cont.	var.	1.36	1.85
2001-03-13	51982	1.14	1.25	0.10	–	–	1.28	1.80
2001-04-09	52009	1.14	1.24	0.09	–	–	1.17	1.88
2001-04-10	52010	1.16	1.30	0.15	–	–	1.62	2.20
2001-04-11	52011	1.15	1.91	0.76	discont.	clouds	1.01	2.17
2001-11-24	52238	1.46	1.50	0.05	–	–	1.02	1.08
2001-11-25	52239	1.25	1.40	0.15	–	–	2.10	2.43
2001-11-26	52240	1.32	1.35	0.02	–	–	2.06	2.24
2001-11-27	52241	1.24	1.30	0.06	–	–	1.84	1.90
2002-01-10	52285	1.19	1.20	0.01	–	–	2.26	2.28
2002-01-11	52286	1.15	1.15	0.00	–	–	1.74	1.76
2002-01-12	52287	1.14	1.14	0.00	–	–	2.28	2.30
2002-02-01	52307	1.14	1.17	0.03	–	–	1.68	1.78
2002-02-02	52308	1.14	1.14	0.00	–	–	1.70	1.73
2002-02-03	52309	1.14	1.14	0.00	–	–	0.91	1.07
2002-03-30	52364	1.17	1.59	0.41	discont.	var.	1.63	2.17
2002-03-31	52365	1.17	1.53	0.35	2 snaps.	–	1.00	1.48
2002-04-01	52366	1.14	1.95	0.81	discont.	const.	1.25	1.73
2002-09-19	52537	2.10	2.21	0.11	–	–	2.05	2.11
2002-12-13	52622	1.17	1.56	0.39	discont.	–	1.78	1.94
2002-12-14	52623	1.16	1.33	0.17	–	–	1.14	1.67
2002-12-15	52624	1.16	1.29	0.13	–	–	1.40	1.66
2002-12-18	52627	1.15	1.25	0.10	–	–	1.34	1.62
2002-12-19	52628	1.15	1.23	0.08	–	–	1.42	1.59
2002-12-20	52629	1.15	1.22	0.07	–	–	1.31	1.56
2002-12-21	52630	1.15	1.19	0.05	–	–	2.15	2.49
2002-12-22	52631	1.14	1.26	0.11	–	–	1.91	2.27
2005-04-08	53469	1.11	1.15	0.04	–	–	0.95	1.26
2005-04-09	53470	1.11	1.15	0.04	–	–	0.96	1.24
2005-04-13	53474	1.11	1.15	0.04	–	–	1.59	2.24
2005-04-14	53475	1.11	1.20	0.09	–	–	1.08	1.43
2005-04-15	53476	1.11	1.18	0.06	–	–	1.16	1.49
2005-04-16	53477	1.11	1.17	0.06	–	–	1.27	1.61
2005-04-17	53478	1.11	1.21	0.10	–	–	1.89	2.41
2005-04-18	53479	1.11	1.17	0.06	–	–	1.58	2.36
2006-01-07	53743	1.20	1.35	0.14	–	–	2.35	2.96
2006-01-08	53744	1.20	1.33	0.13	–	–	2.63	3.57
2006-01-09	53745	1.20	1.55	0.35	cont.	var.	2.23	2.92
2006-01-10	53746	1.20	1.51	0.31	cont.	var.	1.84	2.44
2006-01-11	53747	1.20	1.46	0.26	–	–	1.94	2.69
2006-01-12	53748	1.20	1.54	0.34	cont.	var.	2.17	2.60
2006-01-13	53749	1.20	1.59	0.39	cont.	var.	1.96	2.69
2006-01-14	53750	1.20	1.54	0.34	cont.	var.	1.63	2.21
2006-01-15	53751	1.20	1.91	0.71	cont.	const.	1.80	2.54
2006-01-16	53752	1.20	1.76	0.56	cont.	var.	2.02	2.57
2006-01-17	53753	1.20	1.73	0.53	cont.	var.	2.01	2.55
2006-02-14	53781	1.15	1.21	0.06	–	–	1.80	2.06
2006-02-15	53782	1.14	1.30	0.16	–	–	1.28	1.71
2006-02-16	53783	1.14	1.33	0.19	–	–	–	–

Table 7.6 – continued.

Date	LJD	Air mass			Extinction	Seeing [arcsec]		
		Min.	Max.	Range		Coverage	Min.	Median
2006-02-17	53784	1.14	1.44	0.30	–	–	–	–
2006-02-18	53785	1.14	1.56	0.41	cont.	–	–	–
2006-03-14	53809	1.11	1.79	0.67	cont.	var.	1.47	2.47
2006-03-15	53810	1.11	1.79	0.68	cont.	var.	1.85	2.61
2006-03-16	53811	1.11	1.28	0.17	–	–	1.96	2.96
2006-03-17	53812	1.11	1.36	0.25	–	–	1.50	2.61
2006-03-18	53813	1.11	1.78	0.67	cont.	var.	1.78	2.72
2006-03-19	53814	1.11	1.51	0.40	cont.	var.	1.61	2.60
2006-03-20	53815	1.11	1.28	0.17	–	–	2.03	2.88
2006-03-21	53816	1.11	1.58	0.47	cont.	var.	1.71	2.46
2006-03-22	53817	1.21	1.32	0.12	–	–	1.77	2.28
2006-03-23	53818	1.18	1.31	0.13	–	–	1.98	2.29
2006-03-24	53819	1.11	1.81	0.70	discont.	clouds	1.29	2.03
2006-03-25	53820	1.18	1.30	0.13	–	–	1.64	1.87
2006-03-26	53821	1.11	1.37	0.26	–	–	1.87	2.41
2006-03-27	53822	1.17	1.29	0.12	–	–	2.19	2.59
2007-01-31	54132	1.11	1.26	0.15	–	–	2.13	2.50
2007-02-01	54133	1.11	1.18	0.07	–	–	2.53	3.36
2007-02-02	54134	1.11	1.32	0.21	–	–	1.85	2.40
2007-02-03	54135	1.11	1.12	0.01	–	–	1.98	2.20
2007-02-04	54136	1.11	1.29	0.18	–	–	2.71	3.69
2007-02-05	54137	1.11	1.33	0.22	–	–	1.91	2.33
2007-02-06	54138	1.11	1.23	0.12	–	–	2.09	2.83
2007-02-08	54140	1.11	1.39	0.28	–	–	2.56	3.32
2007-02-12	54144	1.11	1.20	0.09	–	–	1.72	2.16
2007-02-19	54151	1.11	1.51	0.40	cont.	var.	2.05	2.98
2007-02-28	54160	1.11	1.45	0.34	cont.	var.	2.14	2.62
2007-03-01	54161	1.11	1.18	0.07	–	–	2.20	2.64
2007-03-05	54165	1.12	1.79	0.68	discont.	var.	1.63	1.85
2007-03-07	54167	1.44	1.79	0.35	cont.	const.	3.01	3.75
2007-03-08	54168	1.11	1.24	0.13	–	–	1.83	2.26
2007-03-09	54169	1.12	1.81	0.69	cont.	var.	1.79	2.32
2007-03-10	54170	1.40	1.82	0.42	cont.	const.	2.05	2.72
2007-03-11	54171	1.11	1.19	0.08	–	–	1.96	2.43
2007-03-12	54172	1.11	1.83	0.72	cont.	clouds	1.96	2.48
2007-03-13	54173	1.11	1.24	0.13	–	–	2.06	2.57

In order to study extinction, we selected nights on which NGC 3293 observations covered an air-mass range of 0.3 or more. 65 nights out of 203 met this criterion. Air-mass coverage was classified as continuous, discontinuous, or consisting of two snapshots. Extinction was classified as constant, variable, or variable due to passing clouds. Some nights exhibited constant extinction on one side of the meridian and variable on the other, in which cases the two parts were classified separately. Figure 7.6 shows Bouguer plots for four nights with different air-mass coverage and extinction behaviour.

From the selected 65 nights, 9 nights had constant extinction over the whole range of observed air masses and 4 nights had constant extinction on one side of the meridian. The Bouguer lines for stars #5, 6, 10, 26, 29, 33, and 34 were constructed and mean extinction coefficients were calculated. The coefficients for the La Silla Observatory are presented in Table 7.7.

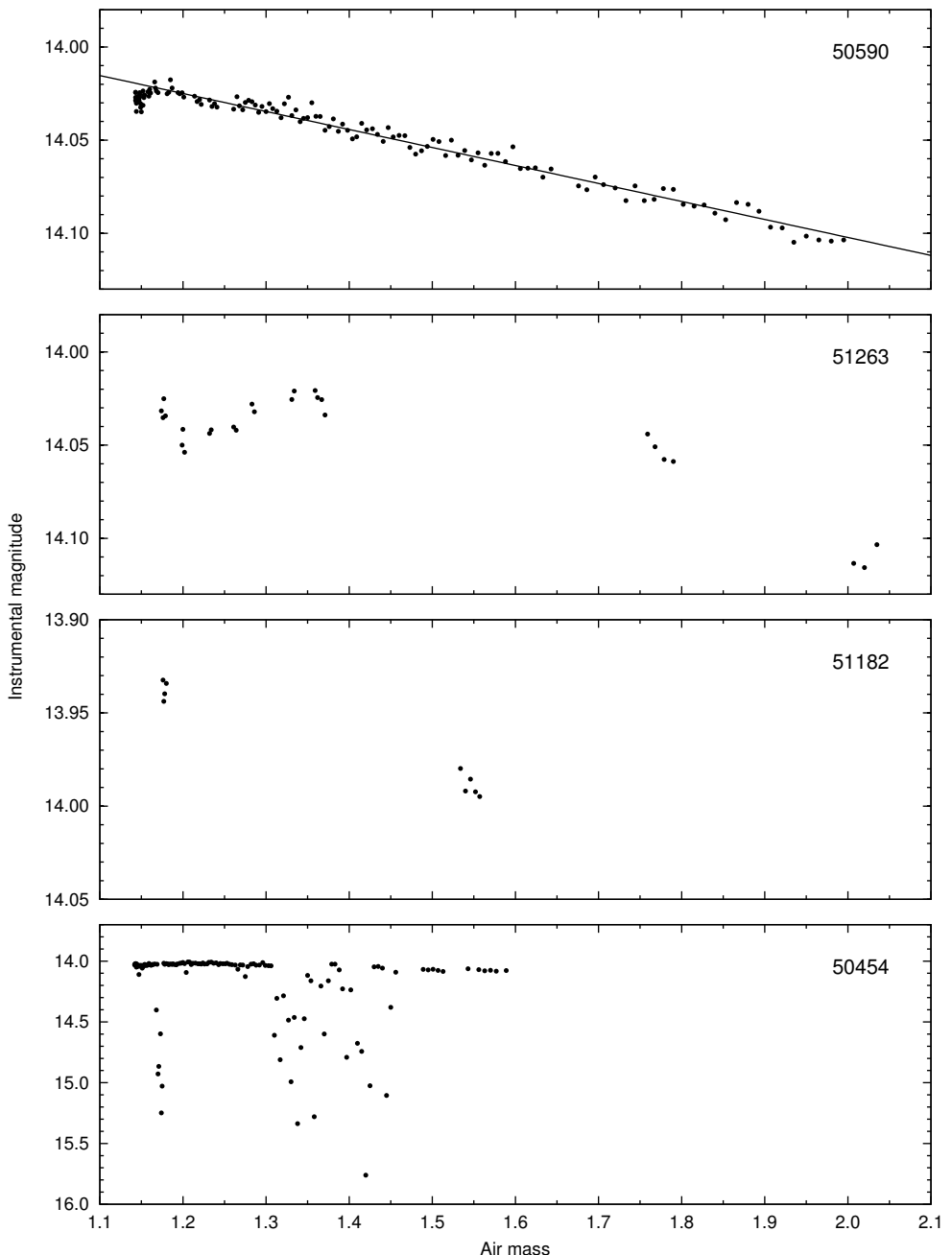


Figure 7.6: Bouguer plots for four nights, y -passband, star #5. LJD 50590 – continuous coverage, constant extinction (west of meridian); LJD 51263 – discontinuous coverage, variable extinction; LJD 51182 – two snapshots; LJD 50454 – continuous coverage, passing clouds.

Table 7.7: Atmospheric extinction coefficients in the Strömgren system for the La Silla Observatory.

Date	LJD	k_y	k_b	k_v	k_u
1997-02-03	50483	0.133 ± 0.010	0.193 ± 0.010		
1997-02-04	50484	0.169 ± 0.014	0.232 ± 0.009		
1997-02-07	50487	0.149 ± 0.011	0.214 ± 0.013		
1997-05-14	50583	0.116 ± 0.006	0.177 ± 0.007		
1997-05-21	50590	0.096 ± 0.009	0.151 ± 0.007		
1997-07-16	50646	0.132 ± 0.008	0.161 ± 0.008		
1997-07-18	50648	0.128 ± 0.012	0.182 ± 0.008		
1999-03-27	51265	0.129 ± 0.004	0.201 ± 0.007		
2001-03-10	51979	0.157 ± 0.006	0.223 ± 0.007		
2002-04-01	52366	0.122 ± 0.006	0.177 ± 0.011	0.290 ± 0.018	0.534 ± 0.009

We note that our time-series observations of NGC 3293 are not particularly suitable for studying atmospheric extinction. Observations made at a wide range of air masses are needed for that purpose, whereas the cluster has been preferably observed at low air masses.

7.7 Selection of comparison stars

In order to carry out differential photometry in the cluster, one or more comparison stars are needed. Initially we selected BVC 5 as a comparison star, as it was bright and had been used for differential photometry of BVC 13 (HD 92024) by Freyhammer et al. (2005). Other comparison-star candidates were required to be relatively bright, isolated from neighbouring stars, measurable (i.e. present and not saturated) on the majority of CCD frames, and without exhibiting any variability.

First we looked at the *uvby* dataset. We constructed *y*-passband light curves for the stars BVC 1–120 that appeared on at least 90% (i.e., 4072) of the *y*-frames during good nights, while poor-quality data were filtered out. A constant aperture radius of $2 \times \text{FWHM}$ and a maximum FWHM of 2.5 arcsec were used. Standard deviation as a function of differential magnitude is plotted in Fig. 7.7a. Comparison-star candidates were then selected among bright stars that exhibited low standard deviations and that were not previously classified as variables. The candidates are listed in Table 7.8.

Next we excluded stars with less than 90% valid measurements in *BV* passbands in the SAAO dataset, stars that exhibited variability, and stars whose aperture photometry was affected by neighbouring stars. From the remaining candidates, BVC 26 was the brightest, and therefore we constructed new sigma-magnitude diagrams, now using BVC 26 as a comparison star, see Fig. 7.7 (panels b and c). The four candidates (BVC 29, 33, 34, 64) remain to show the lowest scatter in their light curves, compared to stars with similar magnitudes. Curiously, stars BVC 5, 6, 7, 10, and 14, although being 1–2 magnitudes brighter than BVC 29 and 33, exhibit slightly higher scatter, being on par with the β Cep star BVC 18. The rest of β Cep stars can be

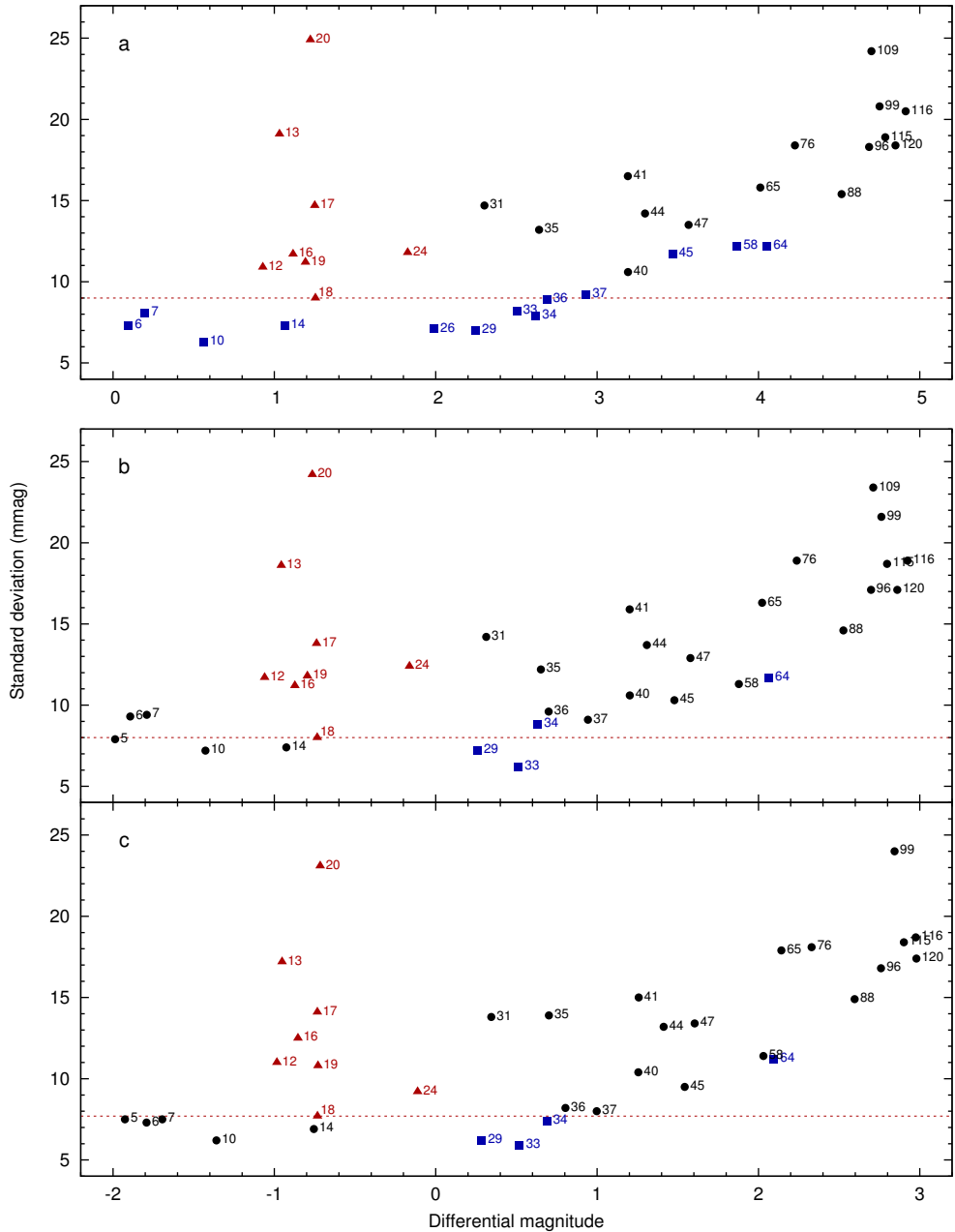


Figure 7.7: Sigma-magnitude diagram based on light curves with a single comparison star: (a) y passband, comparison star BVC 5; (b) y passband, comparison star BVC 26; (c) b passband, comparison star BVC 26. Red triangles denote known β Cep stars. Comparison-star candidates are plotted with blue squares. Red dashed lines depict the lowest standard deviation of a β Cep star (BVC 18).

Table 7.8: Comparison-star candidates. Data coverage is given in percent of the total number of frames in a specific passband.

BVC	Data coverage (%)				Remarks
	<i>b</i>	<i>y</i>	<i>B</i>	<i>V</i>	
5	98.1	98.4	31.6	30.1	limited data in <i>BV</i>
6	98.3	98.5	50.0	38.5	limited data in <i>BV</i>
7	97.9	97.9	59.6	48.9	crowded
10	98.5	98.7	84.8	76.8	limited data in <i>BV</i>
14	98.9	99.1	98.1	96.3	evidence of variability
26	98.7	99.1	98.3	97.6	
29	98.9	99.1	98.0	97.2	
33	98.7	99.1	98.4	97.8	
34	98.7	98.9	92.5	92.8	
36	98.7	98.8	92.9	93.1	evidence of variability
37	98.2	98.4	54.8	46.5	limited data in <i>BV</i>
45	96.7	96.6	91.9	92.9	evidence of variability
58	98.3	98.3	91.1	92.6	crowded
64	98.8	99.1	97.7	97.6	

Table 7.9: Colour indices of comparison-star candidates. The *UBV* photometry (columns 2–4) is from Baume et al. (2003) and the Strömgren photometry (columns 5–9) is from Balona (1994).

BVC	Baume et al. (2003)			Balona (1994)				
	<i>V</i>	<i>B</i> – <i>V</i>	<i>U</i> – <i>B</i>	<i>V</i>	<i>b</i> – <i>y</i>	<i>m</i> ₁	<i>c</i> ₁	β
26	9.97	–0.02	–0.76	10.017	0.003	0.075	0.072	2.622
29	10.22	0.04	–0.67	10.270	0.040	0.073	0.147	2.640
33	10.48	0.01	–0.67	10.517	0.026	0.068	0.162	2.650
34	10.61	0.10	–0.63	10.670	0.074	0.056	0.212	2.642
64	12.05	0.07	–0.39	12.071	0.096	0.019	0.485	2.688

easily distinguished by their higher standard deviations.

Figures 7.8–7.11 show the light curves of BVC 29–26, BVC 33–26, BVC 34–26, and BVC 64–26. Of these four, the first two are comparable in terms of constancy and low scatter, whereas the nightly means of BVC 34–26 vary more. The light curve of BVC 64–26 shows higher scatter due to BVC 64 being more than a magnitude fainter than the other candidates.

The nightly-averaged *y*-passband light curve of BVC 29–26 (Fig. 7.8c) has one outlier slightly exceeding the 3- σ limit at JD 52009. The light curve of BVC 33–26 has an outlier at JD 50830 (Fig. 7.9c). Both of these outliers can also be seen in the *b* passband.

The most favourable comparison-star candidates are thus BVC 26, 29, and 33. They are all located in a small area in the core of NGC 3293 (see Fig. 7.1) and they

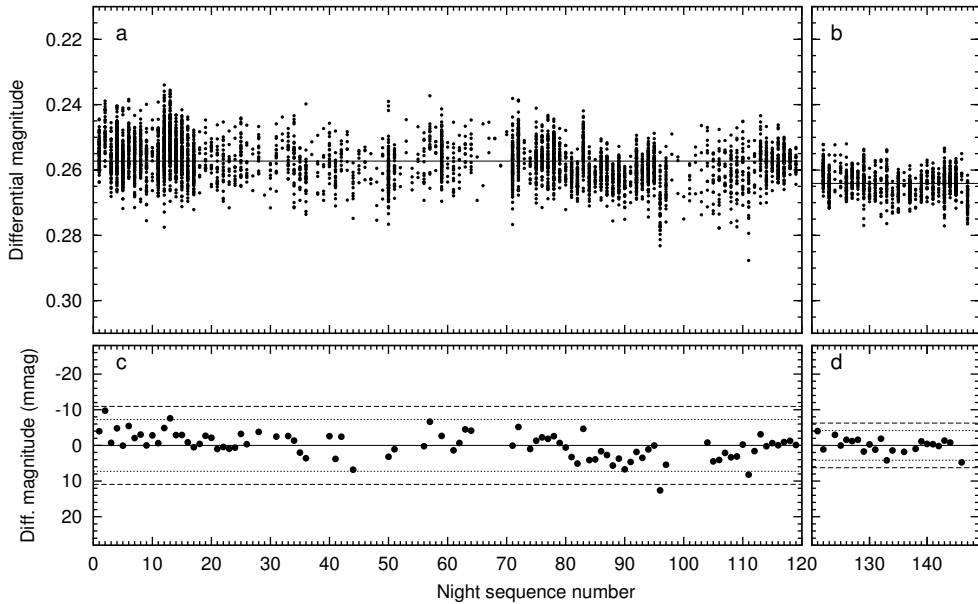


Figure 7.8: Light curve of BVC 29–26 in y (panels a, c) and V passbands (panels b, d). In panels a and b, data points are grouped by night sequence number. Panels c and d give nightly mean magnitudes (with at least 10 nightly measurements) from the same light curve. Dotted lines represent 2σ and dashed lines 3σ limits, where σ is the standard deviation of nightly mean values.

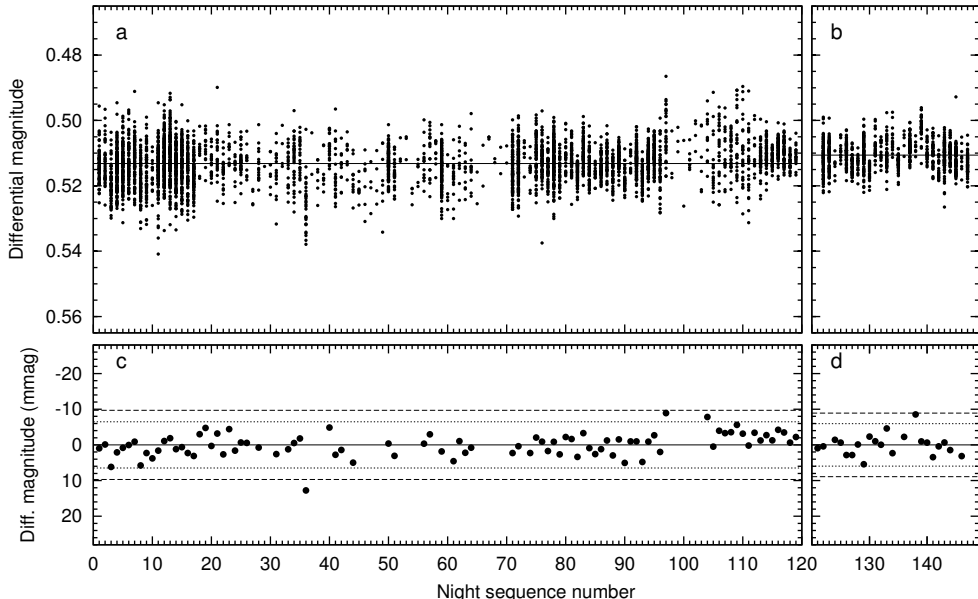


Figure 7.9: Light curve of BVC 33–26 in y and V passbands. See Fig. 7.8 for details.

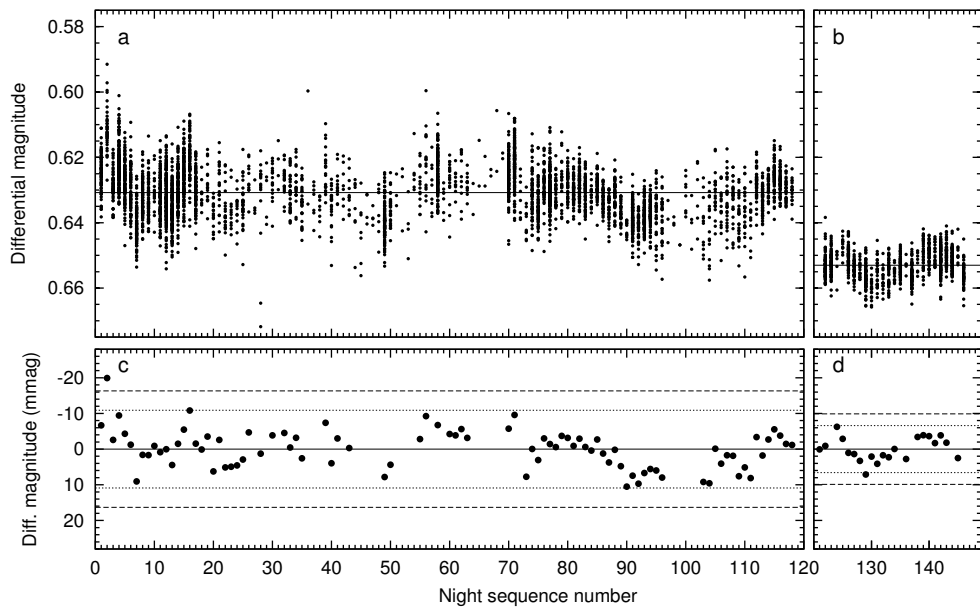


Figure 7.10: Light curve of BVC34–26 in y and V passbands. See Fig. 7.8 for details.

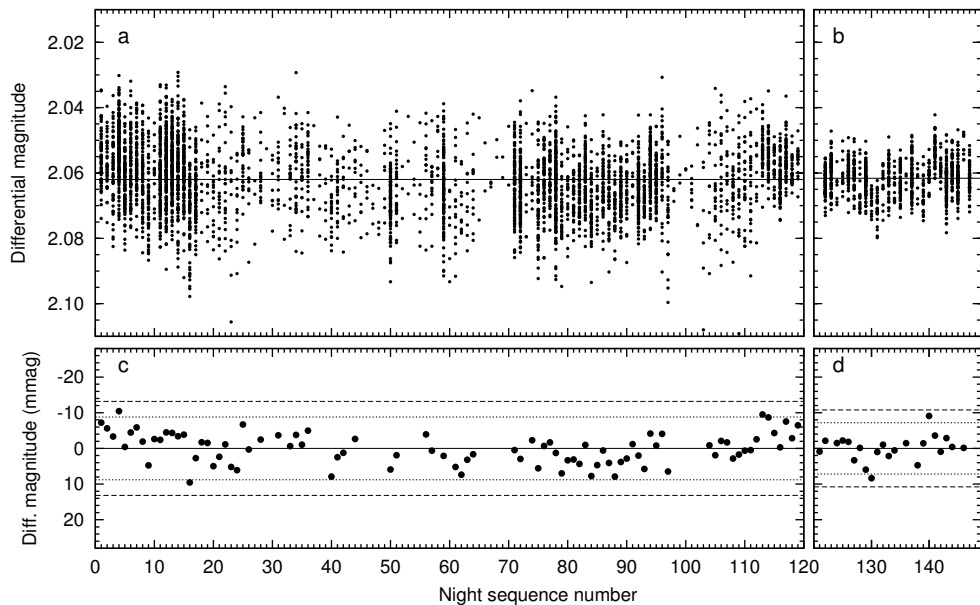


Figure 7.11: Light curve of BVC64–26 in y and V passbands. See Fig. 7.8 for details.

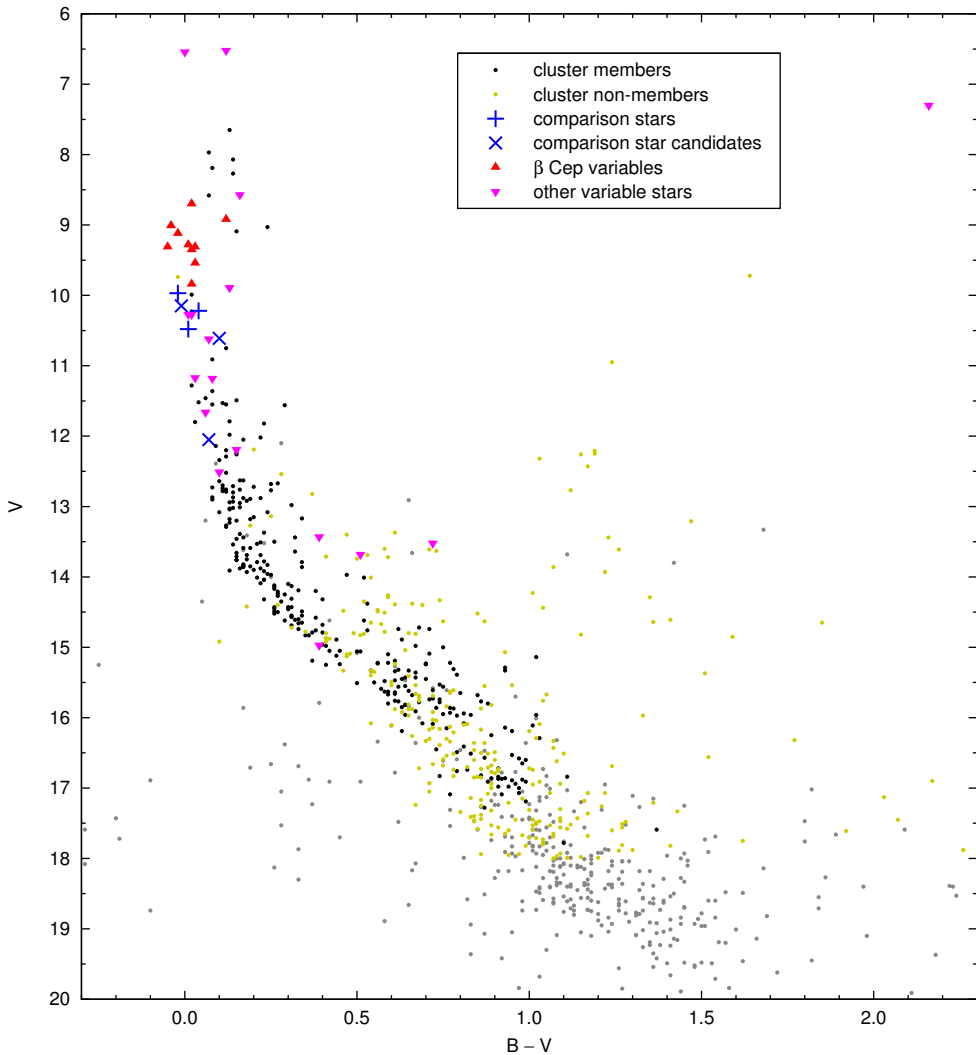


Figure 7.12: Colour-magnitude diagram based on photometry from Baume et al. (2003). Variable stars as known from the literature (see Table 7.1) are denoted with triangles. Comparison stars (BVC 26, 29, 33) and comparison star candidates (BVC 28, 34, 64) are marked with plusses and crosses, respectively.

have similar colour indices, as given in Table 7.9. The comparison stars can be seen in the colour-magnitude ($B - V, V$) diagram just below β Cep stars (Fig. 7.12).

For evaluating the benefits of using more than one comparison star, we look at point-to-point scatter in light curves. Point-to-point variance¹ is calculated as follows

¹Not to be confused with population variance of a variable.

(Kjeldsen & Frandsen 1992):

$$\sigma_{\text{pp}}^2 = \frac{1}{2(N-1)} \sum_{i=1}^{N-1} (m_i - m_{i+1})^2, \quad (7.2)$$

where m_i are individual magnitudes from the light curve of N data points. Point-to-point scatter, σ_{pp} , is the square root of the variance. σ_{pp} describes the precision of a single measurement if magnitude errors dominate over trends between two successive data points. This condition is met for nearly all light curves in our dataset, except for eclipses.

Figure 7.13 illustrates how the combination of three comparison stars (BVC 26, 29, 33) improves light curves in terms of σ_{pp} , compared to using just a single comparison

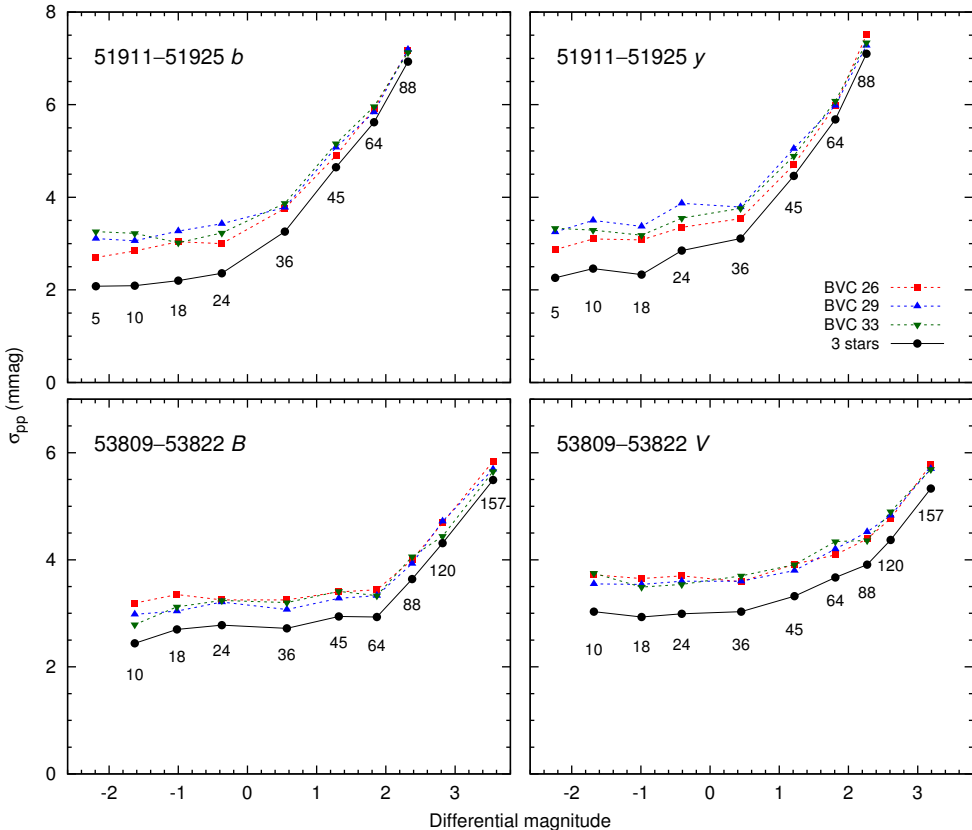


Figure 7.13: Point-to-point scatter in light curves of nine stars, using either a single comparison star (dotted lines) or three comparison stars combined (solid line). The numbers below data points refer to BVC identification numbers. The scatter is calculated for a specific observing run and passband, marked on each panel. The zero-point of the differential magnitude corresponds to the mean magnitude of the comparison stars (BVC 26, 29, 33).

star. As expected, the effect is bigger for bright stars that exhibit lower Poisson noise than a single fainter comparison star.

Hereafter we use the mean magnitude of BVC 26, 29, and 33 as an artificial comparison star. Differential magnitudes, if not noted otherwise, are provided with respect to this mean magnitude.

7.8 Quantification of variability

Following Kjeldsen & Frandsen (1992), we define the scatter ratio (named the detection level, or d value in the cited paper) as a ratio between the total and point-to-point scatter:

$$r_\sigma = \sigma_{\text{total}} / \sigma_{\text{pp}}. \quad (7.3)$$

The total scatter, σ_{total} , is the standard deviation of magnitudes in a differential light curve. The scatter ratio allows for preliminary detection of variable stars, as large values are mostly due to stellar variability. Constant stars have r_σ values close to 1.

Point-to-point scatter as a function of differential magnitude, based on two observing runs (2001 and 2006), is plotted in Fig. 7.14. The selection of stars in the plot is limited to isolated stars with the BVC number up to 500 ($V < 15.77$). The SAAO

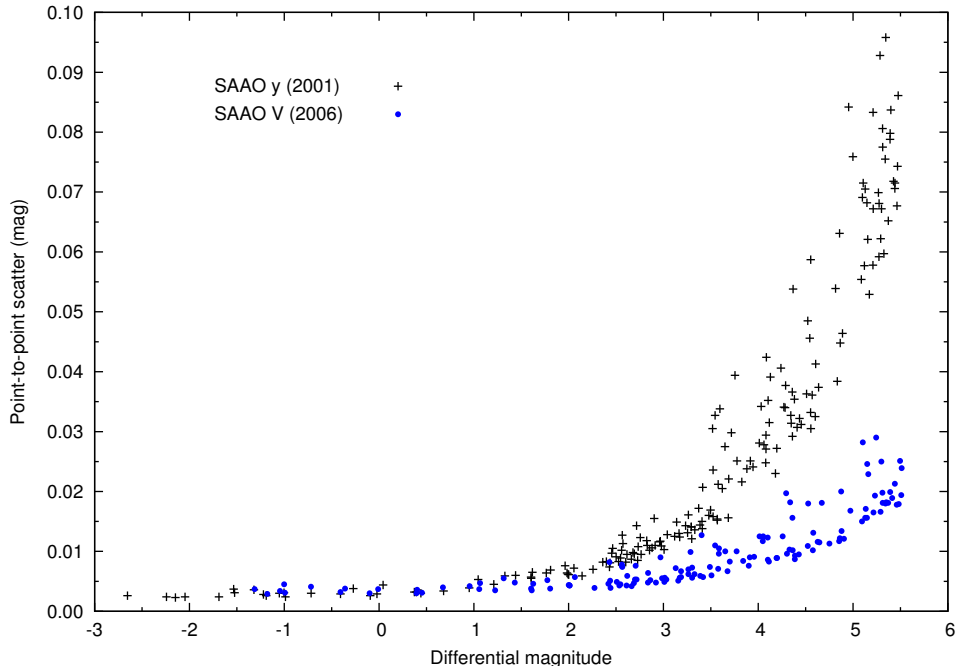


Figure 7.14: Point-to-point scatter as a function of differential magnitude. Crowded stars have been excluded.

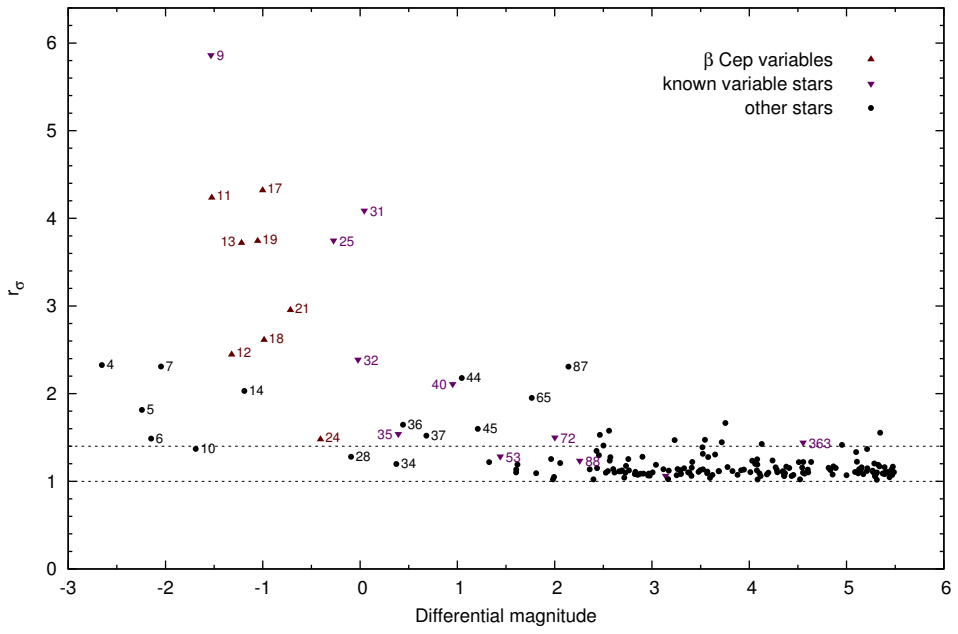


Figure 7.15: Scatter ratio (r_σ) as a function of differential magnitude, based on the SAAO y data (2001). Crowded stars have been excluded. Dashed lines represent r_σ values of 1.0 and 1.4.

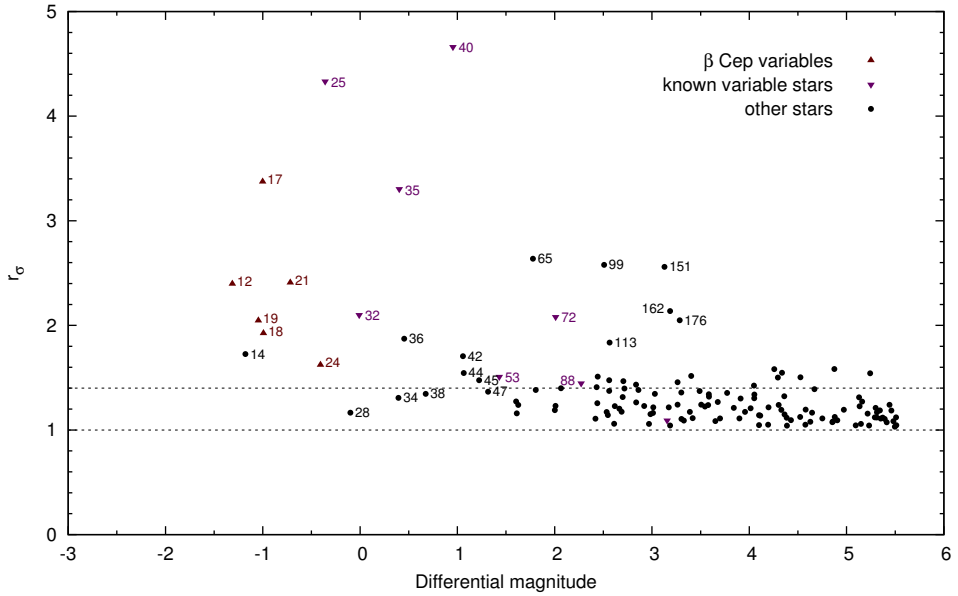


Figure 7.16: Same as Fig. 7.15, but based on the SAAO V data (2006).

observing run in 2001 was optimised for brighter stars, resulting in lower signal-to-noise ratio for fainter stars. During the 2006 run, on the other hand, brightest stars in the cluster were overexposed, but the signal-to-noise ratio of the fainter stars was improved. The scatter in the bright end of the magnitude range is similar for both observing runs.

The scatter ratio as a function of differential magnitude, based on the SAAO y (2001) data, is plotted in Fig. 7.15. β Cep stars and most of the other known variables have r_σ values higher than 1.4. At the bright end, a group of stars (BVC 4, 5, 6, 7, 10, and 14) exhibit higher r_σ values than what is expected for constant stars, so their variability needs further examination. Based on the plot, several new variables can also be suspected among slightly fainter stars, e.g. BVC 36, 37, 44, 45, 65, and 87. At the faint end, point-to-point scatter becomes too high to detect low-amplitude variables.

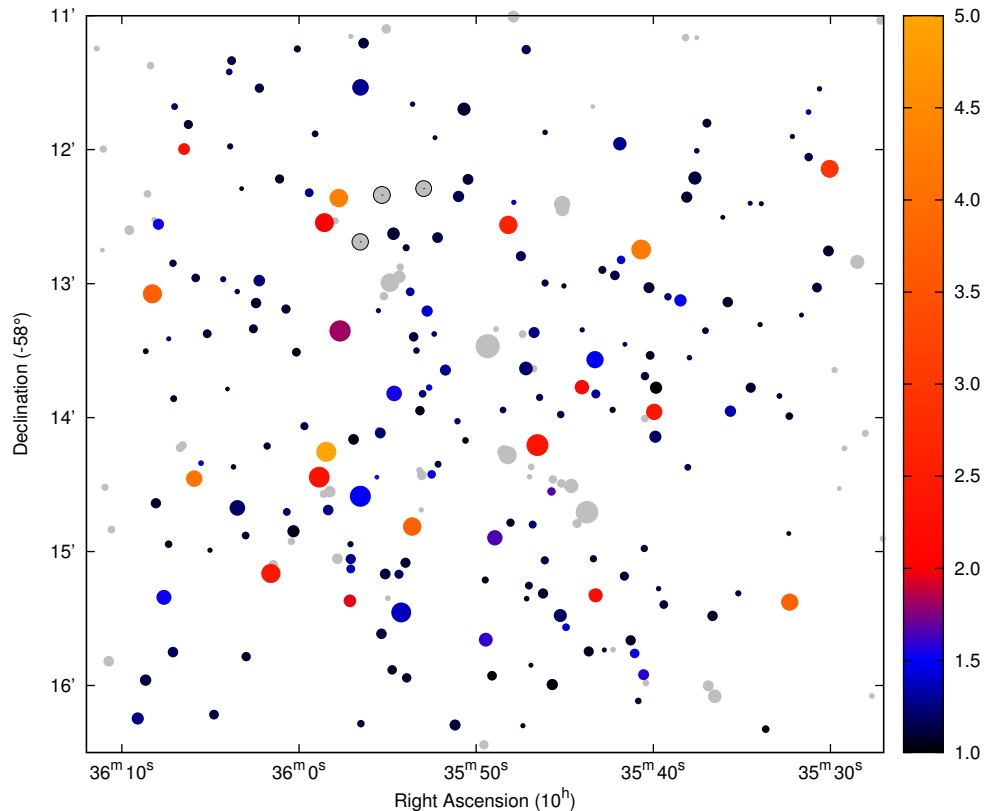


Figure 7.17: Variability map in y passband, based on the SAAO y data (2001). Point sizes correspond to the V magnitude (Baume et al. 2003), while colours refer to the scatter ratio (r_σ) values from 1 to 5. Grey points denote stars that have been excluded from the r_σ calculation, due to being saturated, crowded, or outside of the telescope field of view. The comparison stars are marked with a black outline.

Variability in the SAAO V (2006) photometry is shown in Fig. 7.16. The brightest stars are missing due to being saturated, but several fainter candidate variable stars emerge: BVC 99, 113, 151, 162, and 176.

The variability map of NGC 3293 in the y passband is shown in Fig. 7.17. No obvious clustering of variable stars is evident from the map.

7.9 Ensemble photometry

Each CCD frame of NGC 3293 typically contains several hundred stellar images that are registered by the magnitude-extraction routine. The question arises as to whether additional comparison stars from these hundreds can be used to improve signal-to-noise ratio in light curves of program stars.

Following Honeycutt (1992), we call strict ensemble photometry the technique where the comparison magnitude is obtained from magnitudes of a number of stars that appear in each exposure in the series. Honeycutt (1992) then describes a variation of ensemble photometry where the number and/or identity of comparison stars varies throughout the set of frames. We call this method inhomogeneous ensemble photometry. Inhomogeneity may be due to varying limiting magnitude (sky transparency, sky brightness, exposure time), or variations in telescope pointings. Also, data sets originating from various telescopes and instruments, as is the case in the present study, give inhomogeneous sets of available comparison stars.

We carried out ensemble photometry for data batches from two observing runs: SAAO by data from 2001 (JD 51911–51925) and SAAO BV data from 2006 (JD 53809–53822).

The ensemble stars were selected from the set of comparison stars (BVC 26, 29, 33, see Sect. 7.7) and from the pool of stars with a low scatter ratio ($1.0 < r_\sigma < 1.4$) in the respective data batch (Sect. 7.8). The stars were added to ensembles one by one, beginning with the comparison stars, while the rest of the stars were added in the order of their BVC number, which follows the V magnitude. For each number of ensemble stars, from 1 to 20 (by) or 21 (BV), the point-to-point scatter in light curves was computed.

Fig. 7.18 shows the point-to-point scatter in the light curves of well-exposed stars as a function of the number of ensemble stars. The scatter becomes rapidly smaller by using more than one or two comparison stars, but very little, if anything at all, is gained by using more than five stars in the ensemble. As seen in Fig. 7.19, the scatter in the light curves of poorly-exposed stars depends largely on the chosen aperture, and not so much on the number of ensemble stars. Very little is gained when using more than three comparison stars.

For well-exposed stars, aperture factors 1.6 and 2.0 produce lower scatter than the factor of 1.2. For poorly-exposed stars, the factor 1.2 is favoured, while larger apertures give clearly larger scatter in light curves.

The number of CCD frames that include all the comparison stars, decreases with the increase of the number of stars beyond 5 or 6. The decrease is the most prominent for larger apertures in the BV data set. This is a problem in the case of strict ensemble photometry, as a significant fraction of data points will be missing from light curves.

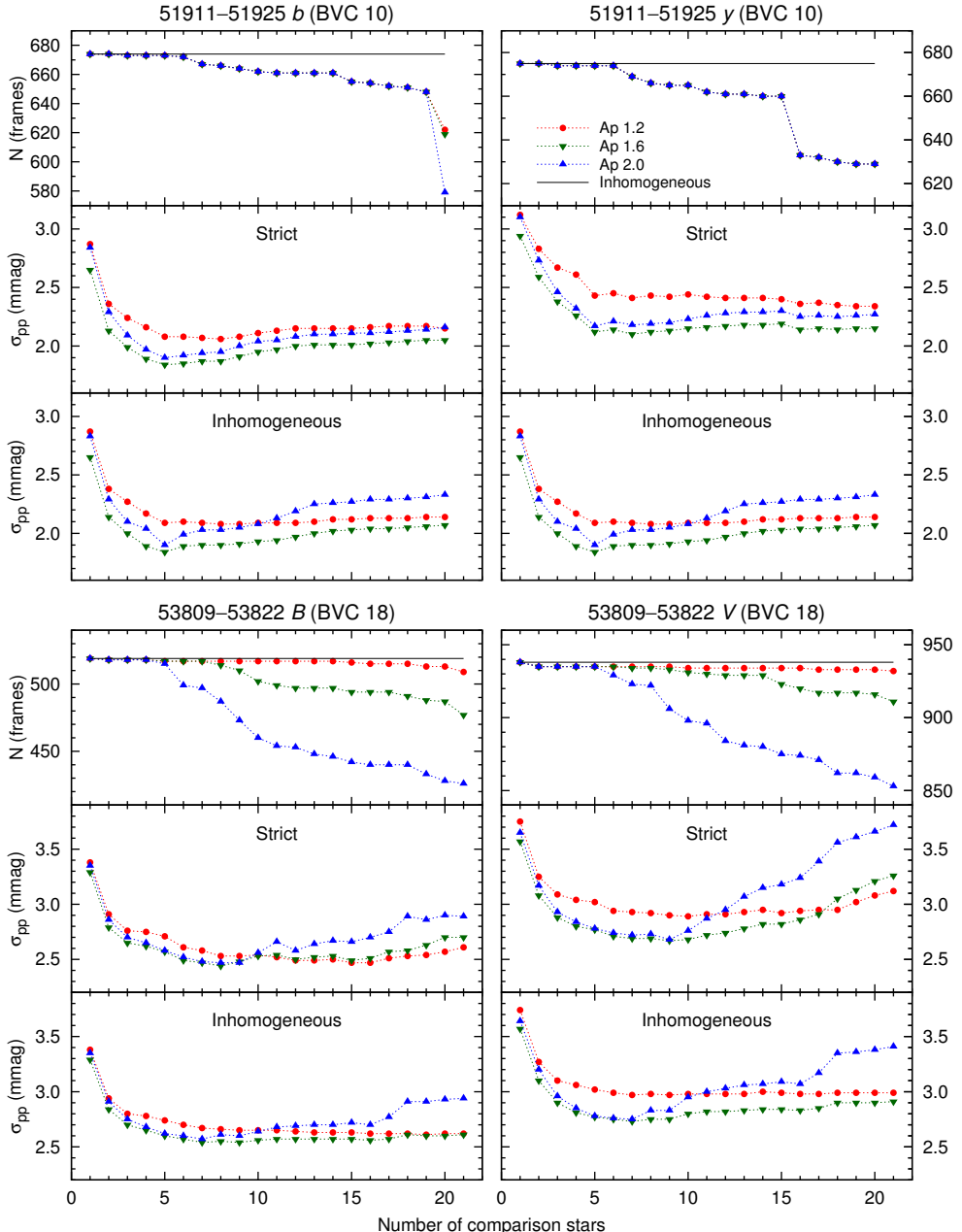


Figure 7.18: Point-to-point scatter in light curves of well-exposed stars (BVC 10, 18) as a function of the number of comparison stars. The top graph in each panel shows the number of frames contributing to a light curve. The middle and bottom graphs in each panel show the resulting scatter in case of strict and inhomogeneous ensemble photometry, respectively. Three curves refer to distinct aperture radii (1.2 , 1.6 , and $2.0 \times \text{FWHM}$).

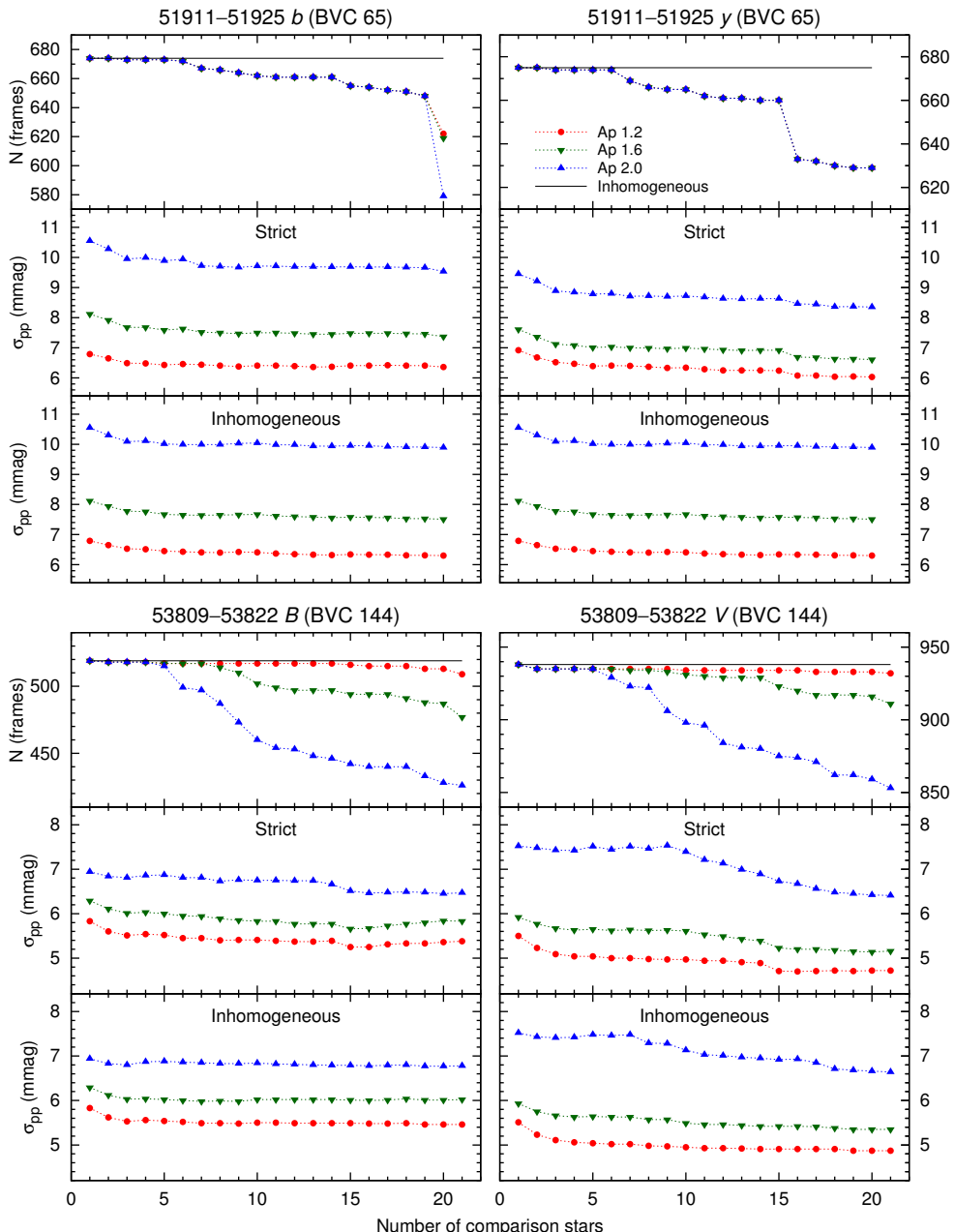


Figure 7.19: Point-to-point scatter in light curves of poorly-exposed stars (BVC 65, 144), as a function of the number of comparison stars. See the caption of Fig. 7.18 for further explanations.

Inhomogeneous ensemble photometry compensates for missing comparison stars, so the number of frames contributing to light curves stays constant.

Our test of ensemble photometry only shows the effect of using multiple comparison stars on the point-to-point scatter within a homogeneous data batch (one observing run). Systematic effects, arising from merging data from different observing runs (as seen in Fig. 7.10ab), or from using comparison stars with different colours, were not taken into account.

Considering that the gain in using more than three comparison stars is small or nonexistent, and that it may potentially introduce systematic errors, the preferred way is to use three comparison stars (BVC 26, 29, 33). Only for bright program stars the use of four or five comparison stars is justified (additional stars BVC 28, 34), after checking for systematic effects in data merging.

Our results do not support the notion that using a large number of comparison stars reduces noise in differential light curves. Honeycutt (1992) demonstrates the use of strict ensemble photometry with 25 stars and the inhomogeneous method with 92 stars. In a multi-site campaign of the open cluster NGC 884 (Saesen et al. 2010), ensemble photometry with an average of 25 comparison stars is used. Large numbers of comparison stars possibly give good results in cases with a different brightness distribution of stars in the field of view. In NGC 3293 the brightest five stars in the ensemble are more than a magnitude brighter than the next stars, and the magnitude errors of fainter ensemble stars are so much bigger that they reduce the overall signal-to-noise ratio.

7.10 Long-term variability in NGC 3293

Long-term variability in NGC 3293 was studied on the basis of nightly-averaged y - and V -passband data. For a few stars of interest, nightly-averaged b - and B -band magnitudes were included in the study. As about half of the observing nights of the decade-long monitoring were carried out with the Dutch 0.91-m telescope that has one of the smallest fields of view, we selected only those stars that appeared on at least 80% of the Dutch y -band frames for further study. The selection included 121 stars with BVC number 4–394 (corresponding magnitude range $7.65 \leq V \leq 15.19$), of which three were comparison stars. The selection was narrowed by excluding 24 crowded stars, for which aperture photometry was strongly affected by neighbouring stars, thus leaving 94 stars in the final selection.

The selected stars brighter than $V = 13.76$ (with an exception of BVC 359) with their published photometry and spectral types are listed in Table 7.10. Based on the spectral classification (Evans et al. 2005), we constructed the spectral type–luminosity class diagram for B-type stars (Table 7.11).

Mean magnitudes were calculated for nights that had at least five acceptable data points in the y or V passband. Prior to averaging, light curves were constructed with the following restrictions: maximum seeing value 3.0 arcsec, minimum integration time 1.0 s, and poor-quality data (flags –1 and 1, see Table 1.1) excluded.

Table 7.10: Photometry and spectral types of stars discussed in Section 7.10: BVC number and UBV photometry (columns 1–4) from Baume et al. (2003), identification number and Strömgren photometry (columns 5–9) from Balona (1994), ESL number and spectral type from Evans et al. (2005). Three comparison stars are listed at the end.

BVC	V	$B - V$	$U - B$	# B	V	$b - y$	m_1	c_1	ESL	Sp. type
4	7.65	0.13	-0.85	22	7.649	0.125	0.042	-0.015	3	B1 III
5	7.97	0.07	-0.82	20	8.044	0.076	0.037	-0.024	4	B1 III
6	8.07	0.14	-0.78	25	8.146	0.118	0.028	0.002	5	B1 III
7	8.19	0.08	-0.77	6	8.251	0.118	0.017	-0.010	6	B1 III
9	8.57	0.16	-0.85	26	8.743	0.132	0.013	-0.150	11	Be (B1:)
10	8.58	0.07	-0.79	7	8.630	0.084	0.046	0.017	8	B1 III
12	8.92	0.12	-0.78	27	8.978	0.123	-0.001	0.073	12	B1 III
13	9.01	-0.04	-0.81	5	9.030	0.029	0.042	0.043	13	B1 III
14	9.03	0.24	-0.72	19	9.093	0.189	0.015	-0.011	14	B0.5 IIIIn
16	9.12	-0.02	-0.81	133	9.147	0.060	0.024	0.014	15	B1 V
17	9.28	0.01	-0.80	18	9.285	0.012	0.066	0.039	18	B1 V
18	9.31	-0.05	-0.87	14	9.277	0.014	0.069	0.004	19	B1 V
19	9.31	0.03	-0.67	24	9.245	0.079	0.040	0.017	17	B1 V
24	9.84	0.02	-0.73	65	9.865	0.062	0.077	0.033	21	B1.5 III
31	10.27	0.01	-0.66	28	10.333	0.047	0.054	0.176	29	B0.5-B1.5 Vn
34	10.61	0.10	-0.63	33	10.670	0.074	0.056	0.212	31	B2 V
35	10.62	0.07	-0.66	29	10.678	0.054	0.074	0.155	32	B0.5-B1.5 Vn
36	10.75	0.12	-0.64	86	10.747	0.120	0.044	0.066	34	B2 IIIh
37	10.91	0.08	-0.65	89	10.972	0.077	0.040	0.170	37	B2 V
40	11.17	0.03	-0.57	63	11.246	0.062	0.081	0.266	40	Be (B3n)
41	11.18	0.08	-0.71	87	11.248	0.075	0.072	0.174	41	B2.5 V
45	11.46	0.06	-0.57	85	11.534	0.072	0.088	0.283		
47	11.52	0.04	-0.63	31	11.622	0.057	0.075	0.234		
58	11.82	0.23	-0.43	84	11.970	0.151	0.069	0.415	57	B3 V
64	12.05	0.07	-0.39	52	12.071	0.096	0.019	0.485	61	B5 V
65	12.05	0.17	-0.24	90	12.112	0.136	0.063	0.544	66	B5 V
76	12.24	0.15	-0.34	178	12.296	0.129	0.043	0.442		
87	12.43	1.17	0.05							
88	12.51	0.10	-0.25	93	12.544	0.091	0.071	0.545	84	B5 V
96	12.64	0.10	-0.18	30	12.706	0.079	0.107	0.674		
99	12.70	0.11	-0.20	55	12.790	0.099	0.119	0.613	98	B8 III-V
104	12.76	0.16	-0.14	66	12.902	0.120	0.079	0.819		
109	12.78	0.11	-0.23	58	12.746	0.097	0.098	0.553		
116	12.87	0.08	-0.27	34	12.938	0.047	0.124	0.588	106	B6-7 V
117	12.88	0.22	-0.06	166	12.952	0.143	0.094	0.668	105	B8 III-V
120	12.90	0.08	-0.13	32	12.909	0.115	0.129	0.648		
123	12.93	0.14	-0.21	160	13.003	0.096	0.096	0.543		
125	12.95	0.16	-0.21	88	13.019	0.130	0.062	0.603		
127	13.01	0.16	-0.16	100	13.089	0.130	0.069	0.647	113	B6-7 V
128	13.02	0.14	-0.22	91	13.018	0.115	0.115	0.601	111	B6-7 III-V
131	13.08	0.10	-0.11	94	13.106	0.089	0.092	0.732		
136	13.14	0.25	0.20	181	13.188	0.190	0.072	1.098		
138	13.17	0.34	0.00	157	13.286	0.234	0.079	0.866		
140	13.18	0.19	-0.08	167	13.262	0.112	0.089	0.765		
141	13.20	0.06	-0.09	169	13.166	0.108	0.077	0.725	115	B8 III-V
143	13.21	1.47	1.18	105	13.359	0.908	0.404	0.411		
144	13.23	0.13	-0.23	67	13.329	0.073	0.123	0.699	125	B8 III-V
147	13.29	0.12	-0.06	112	13.333	0.090	0.088	0.834		
160	13.46	0.15	-0.06	69	13.562	0.111	0.115	0.838		
166	13.50	0.26	0.16	56	13.578	0.168	0.116	1.041		
168	13.52	0.72	0.33	60	13.465	0.437	0.226	0.273		

Table 7.10 – continued.

BVC	<i>V</i>	<i>B</i> − <i>V</i>	<i>U</i> − <i>B</i>	# _{<i>B</i>}	<i>V</i>	<i>b</i> − <i>y</i>	<i>m</i> ₁	<i>c</i> ₁	ESL	Sp. type
178	13.63	0.73	0.27	96	13.703	0.428	0.175	0.432		
181	13.66	0.15	0.06	234	13.700	0.098	0.097	1.006		
191	13.71	0.15	-0.05	161	13.785	0.006	0.231	0.727		
197	13.75	0.18	0.02	210	13.846	0.138	0.123	0.897		
198	13.76	0.15	0.09	95	13.787	0.117	0.106	0.985		
359	14.92	0.10	0.29	214	14.479	0.295	0.140	0.788		
26	9.97	-0.02	-0.76	131	10.017	0.003	0.075	0.072	23	B1.5 III
29	10.22	0.04	-0.67	132	10.270	0.040	0.073	0.147	28	B2 V
33	10.48	0.01	-0.67	17	10.517	0.026	0.068	0.162	30	B2 V

Table 7.11: Distribution of stars in the NGC 3293 region in the spectral type–luminosity class diagram. Rows 1–6 include all B-type stars from the VLT-FLAMES survey (Evans et al. 2005). Rows 7–10 show a subset of stars as listed in Table 7.10.

I	1	1	—	—	—	—	—	—	—	—	
II	—	—	—	—	—	—	—	—	—	1	
III	—	1	9	4	3	—	—	2	2	5	
III–V	—	—	—	—	—	—	—	3	3	7	
V	—	—	6	—	5	6	7	13	10	—	
Be	—	—	3	1	—	—	1	—	—	—	
III	—	1	7	2	1	—	—	—	—	—	
III–V	—	—	—	—	—	—	—	—	1	4	
V	—	—	6	—	4	1	1	3	2	—	
Be	—	—	1	—	—	—	1	—	—	—	
	B0	B0.5	B1	B1.5	B2	B2.5	B3	B5	B6–7	B8	B9

We also checked all light curves for possible light spill from neighbouring stars by examining differential magnitude–seeing plots (Fig 7.20). The effect is most significant for faint stars in the vicinity of bright stars. We applied maximum seeing value of 2.5 arcsec for stars whose photometry was affected in the seeing range between 2.5 and 3.0 arcsec (BVC 47, 58, 76, 117, 125, 141, 160, 214, 330), and maximum seeing of 2.0 arcsec for stars that showed the effect between 2.0 and 2.5 arcsec (BVC 16, 41, 104, 127, 128, 140, 181, 191, 197, 198, 206, 221, 222, 224, 229, 250, 268, 273, 280, 359, 363, 366). Stars whose magnitude depended on seeing below 2.0 arcsec, were considered crowded and excluded from the study, as described above.

Aperture radii were scaled with the FWHM of star images. Optimal aperture scale factors were chosen on the basis of scatter in light curves of stars in three magnitude ranges. The aperture factors used are given in Table 7.12. An exception is BVC 16, for which we used aperture factors from the group BVC 34–63, due to a close neighbouring star.

Differential *V* magnitudes were transformed to the *y* scale using the transformation

$$y = V - 0.038(B - V) \quad (7.4)$$

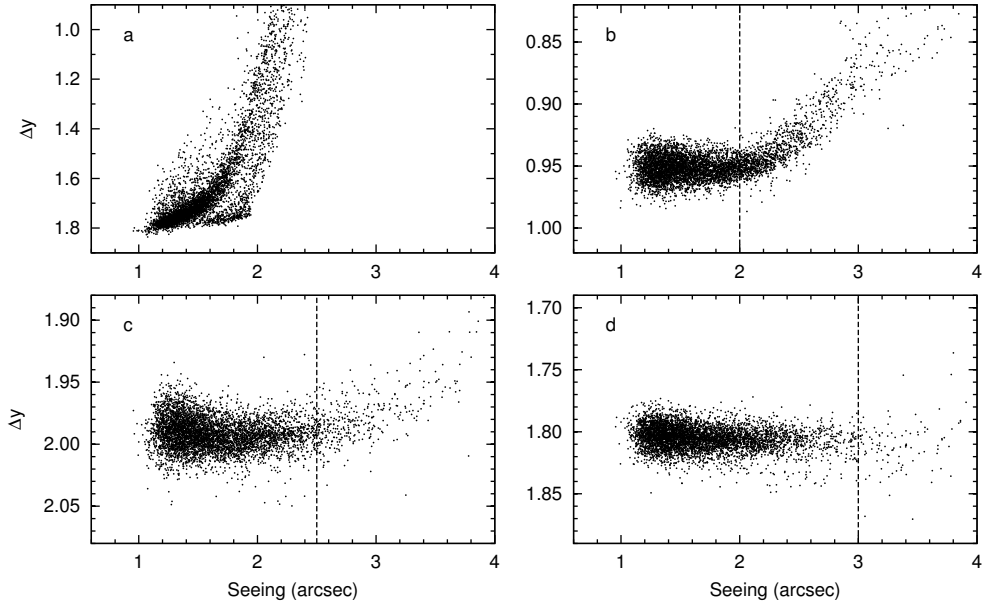


Figure 7.20: Light spill from neighbouring stars. Differential magnitude as a function of seeing in four cases: (a) crowded star BVC 60, aperture photometry impossible; (b) BVC 41, applied maximum seeing limit 2.0 arcsec; (c) BVC 76, limit 2.5 arcsec; (d) isolated star BVC 64, limit 3.0 arcsec.

(Cousins & Caldwell 1985) and assuming the mean $(B - V)$ of 0.01 for the comparison stars. The $(B - V)$ colour indices by Baume et al. (2003) were used.

For each star in our study, we calculated the standard deviation and range (maximum minus minimum) of the nightly mean y magnitudes. The calculations were based only on the Strömgren data (years 1997–2005) to avoid errors from merging the y and V data sets. Merging errors would arise from flat-fielding issues and from different seeing values, as most of the OCA and SAAO V data suffered from poorer seeing (partly due to defocusing).

The standard deviations of nightly mean magnitudes are plotted in Fig. 7.21. A few stars stand above the others in terms of spread in their nightly magnitudes: BVC 4, 9, 13, 24, 31, 35, 65, and 87. These stars are expected to show night-to-

Table 7.12: Aperture scale factors used for generating light curves. Four groups were treated separately, characterised by BVC numbers and corresponding V magnitudes.

Data batch	BVC	4–33	34–63	64–199	200–399
	$V \approx$	7.7–10.5	10.5–12.0	12.0–13.8	13.8–15.2
Strömgren y		2.0	1.6	1.2	1.0
OCA V		2.0	1.6	1.2	1.0
SAAO V		1.6	1.4	1.2	1.0

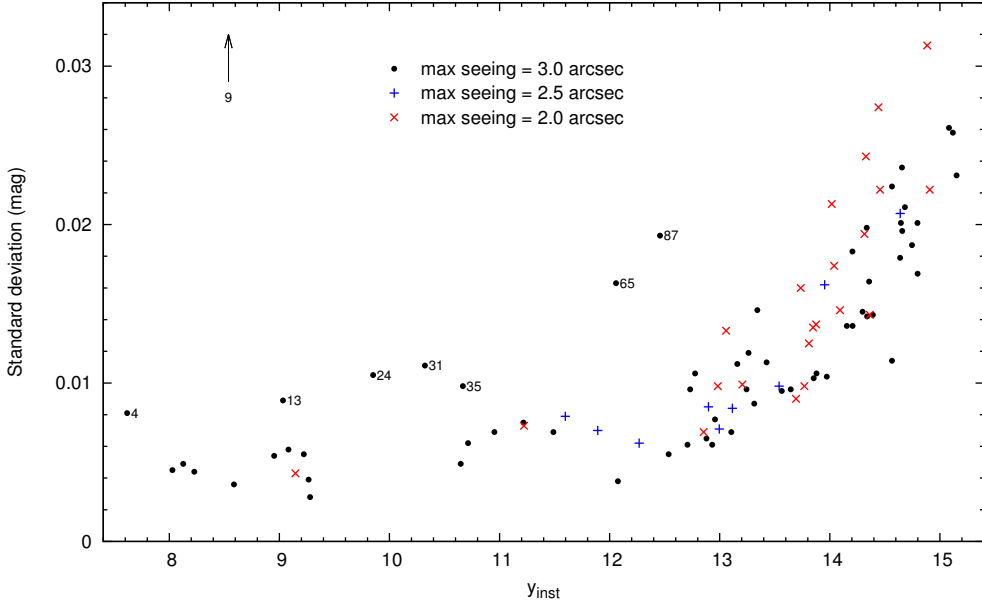


Figure 7.21: Standard deviation of nightly mean magnitudes as a function of instrumental y magnitude. Stars whose photometry was affected by neighbouring stars at seeing values below 3 arcsec, are shown with crosses (maximum seeing 2.0 arcsec) and plusses (maximum seeing 2.5 arcsec). BVC 9 ($\sigma = 0.12$) is outside the bounds of the plot and is marked with an arrow.

night or long-term variability. At the faint end ($y > 13$), the stars whose photometry was affected by neighbouring stars, yield higher standard deviations than isolated stars, although the maximum seeing limit was applied. This means that aperture photometry is not optimal for these stars and PSF photometry should be preferred in such cases.

The variability of the selected stars is discussed in the following subsections, beginning with the brightest stars in the cluster. Separate subsections are devoted to Be stars, β Cep stars, and slowly pulsating B-star (SPB) candidates, followed by a subsection on the remainder of the stars.

7.10.1 Bright stars BVC 4, 5, 6, 7, 10

BVC 4, 5, 6, 7, and 10 are among the brightest stars in NGC 3293, being about 1–2 magnitudes fainter than the blue supergiants BVC 1 and 2, and also fainter in y and V passbands than the red supergiant BVC 3. As BVC 1 is slightly out of the Dutch telescope field of view, and BVC 2 and 3 are saturated in the majority of our frames, BVC 4, 5, 6, 7, and 10 are the brightest stars in our variability study. They are located in the colour-magnitude diagram (see Fig. 7.12) just above the known β Cep stars. Evans et al. (2005) classify the five stars in question as B1 III.

The nightly-averaged magnitudes of BVC 4, 5, 6, 7, and 10 are shown in Fig. 7.22. No stars in this group exhibit significant long-term variability, but night-to-night

variations of up to a few hundredths of a magnitude are evident. The differences of mean magnitudes between the y and V data sets may be attributable to systematic effects in flat-fielding of CCD frames. The standard deviations and ranges of nightly mean magnitudes in the y data are given in Table 7.13.

BVC 4 has the largest standard deviation of the nightly mean magnitudes, while BVC 10 has the smallest in the group. We used the standard deviation (σ) of BVC 10

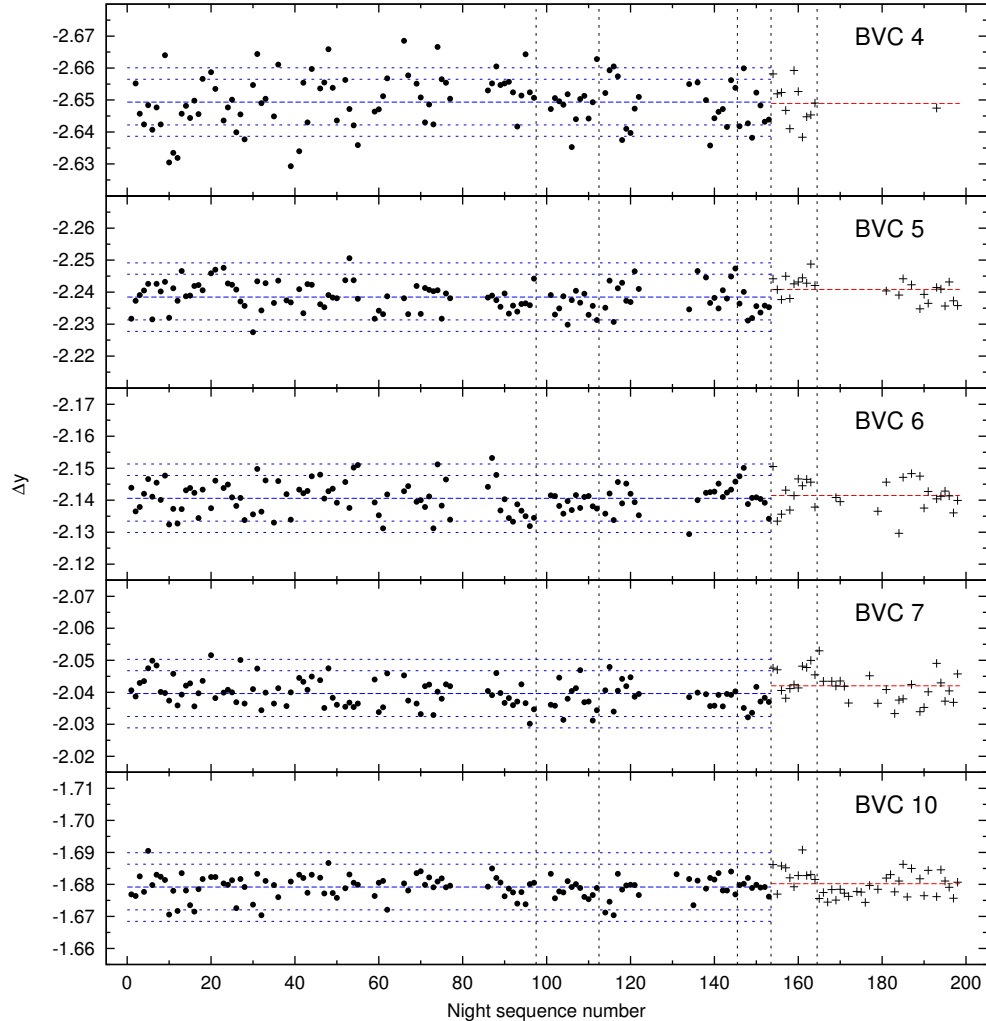


Figure 7.22: Nightly-averaged magnitudes of a group of bright stars in NGC 3293. Plusses denote differential V magnitudes transformed to the y scale. Vertical dotted lines separate data batches from different telescopes. The mean values of nightly means are plotted with dashed lines (blue: y data; red: V data). Horizontal dotted lines give 2σ and 3σ limits around the means, using the standard deviation of BVC 10.

Table 7.13: Standard deviations and ranges of the nightly mean y magnitudes of five bright cluster stars.

BVC	Std. dev.	Range	BVC	Std. dev.	Range
4	0.0081	0.039	7	0.0046	0.023
5	0.0043	0.023	10	0.0036	0.020
6	0.0050	0.027			

for plotting the 2σ and 3σ limits around the mean magnitudes in Fig. 7.22. BVC 4 has numerous data points exceeding the 3σ limit and thus can be considered variable. BVC 5 and 6 have two nightly means outside the 3σ limits, and BVC 7 and 10 have one, although there are more data points between 2σ and 3σ from the overall mean magnitude than what is expected from a Gaussian distribution.

To illustrate the variability further, the light and colour curves from two observing runs are shown in Figs. 7.23–7.27. BVC 4 exhibits light variations up to 0.03 mag from night to night, while the $(b - y)$ colour variations are below 0.01. BVC 5, 6, and 7 show similar light variability, although with lower amplitudes. BVC 10 is the least variable star in this group, but occasional deviations of the nightly mean magnitude by up to 0.01 from the overall mean magnitude can be seen.

Balona & Engelbrecht (1983) reported BVC 4, 5, 6, 7, and 10 to be constant, based

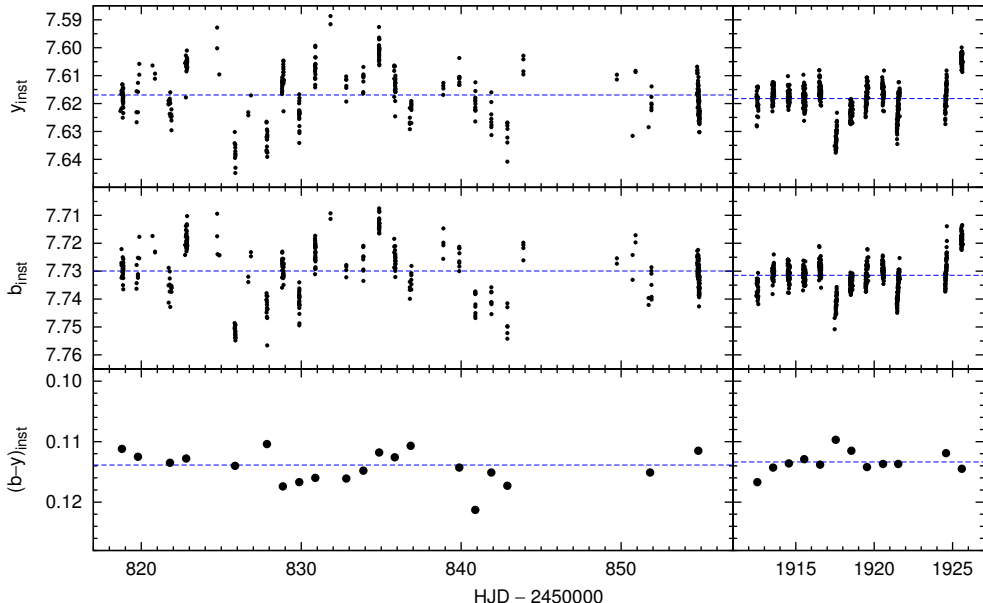


Figure 7.23: Light and colour curves of BVC 4 from two observing runs (JD 2450818–54 and 2451912–25). The mean magnitudes of observing runs are shown with dashed lines.

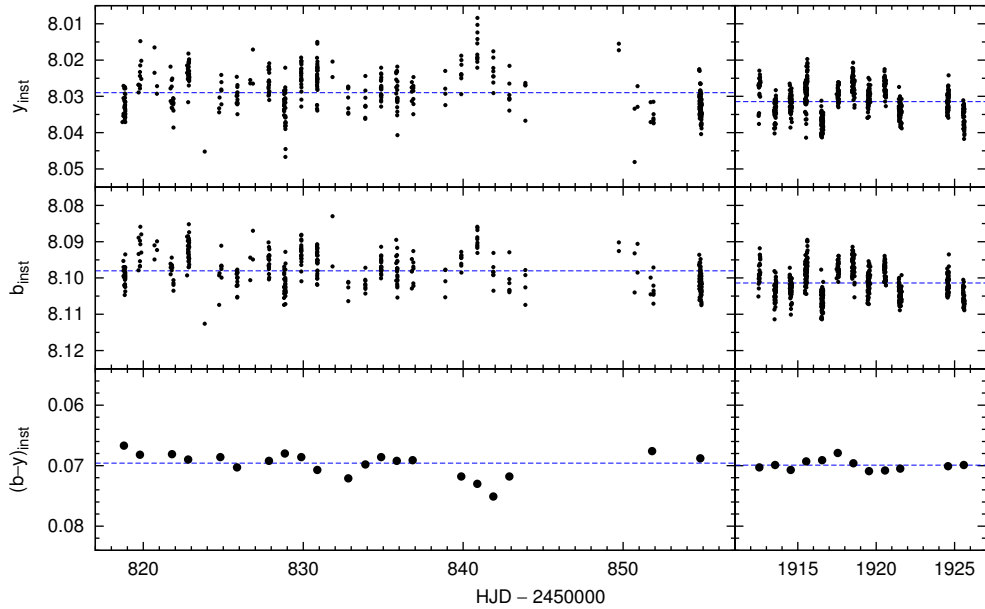


Figure 7.24: Light and colour curves of BVC 5 from two observing runs (JD 2450818–54 and 2451912–25). The mean magnitudes of observing runs are shown with dashed lines.

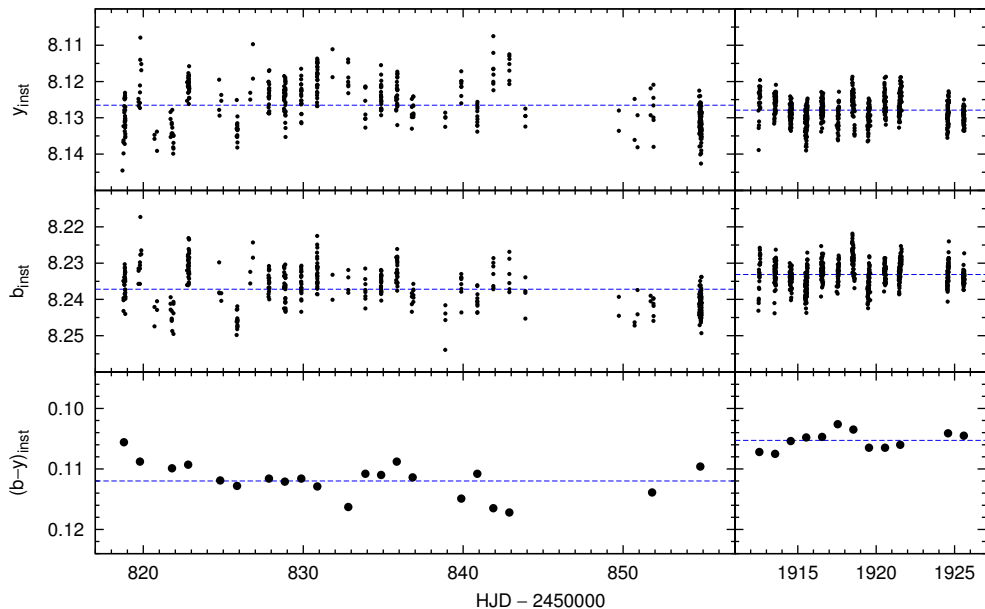


Figure 7.25: Light and colour curves of BVC 6 from two observing runs (JD 2450818–54 and 2451912–25). The mean magnitudes of observing runs are shown with dashed lines.

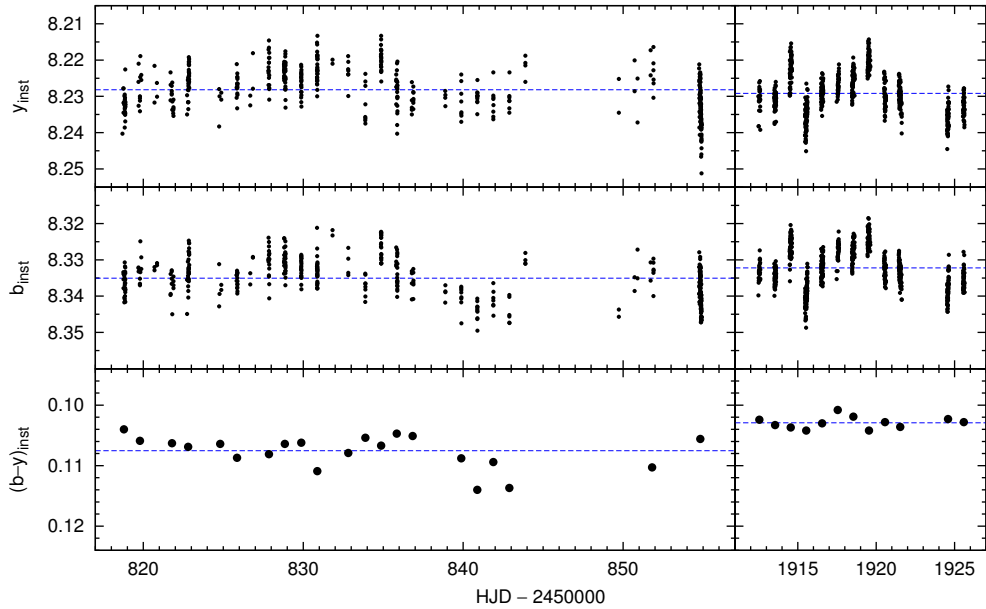


Figure 7.26: Light and colour curves of BVC 7 from two observing runs (JD 2450818–54 and 2451912–25). The mean magnitudes of observing runs are shown with dashed lines.

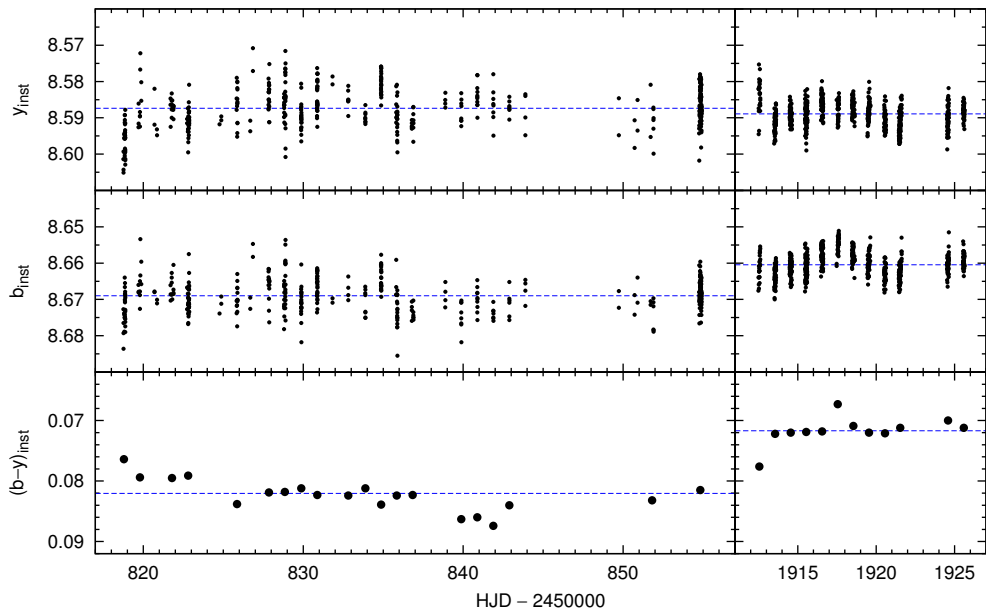


Figure 7.27: Light and colour curves of BVC 10 from two observing runs (JD 2450818–54 and 2451912–25). The mean magnitudes of observing runs are shown with dashed lines.

on observations for an average of 19 hours on 3.3 nights. Some of these stars have later been used as comparison for variability studies of β Cep stars in the cluster: e.g., Engelbrecht (1986) used BVC 4, 5, and 10, while Jerzykiewicz & Sterken (1992) and Freyhammer et al. (2005) used BVC 5. For future variability studies in NGC 3293, the variability of the stars discussed here should be taken into account.

7.10.2 Be stars

Be stars are non-supergiant B stars whose spectrum has, or had at some time, one or more Balmer lines in emission (Porter & Rivinius 2003, and references therein). This definition already includes variability as a common feature of Be stars.

BVC 9 = V379 Car

Feast (1958) classifies BVC 9 as B1 III, based on three spectra from 1956 April, 1957 April and June. He reports poor spectral lines, probably variable radial velocity, and possible indications of line doubling, which may be an evidence for being a binary or for the lines exhibiting emission cores (Shobbrook 1980). Balona (1975) measured rotational velocities from the same spectra and obtained $v \sin i = 203 \text{ km s}^{-1}$. Evans et al. (2005) obtained a spectrum of BVC 9 within the VLT-FLAMES survey in 2004 July. They report broad H α emission and classify BVC 9 as a Be star (spectral type B1).

The V -passband light curve of BVC 9 from the 1997–2007 monitoring is shown in Fig. 7.28. The star was at its maximum brightness during the first season (1997) of the monitoring, then began to fade during the second season. From the third to the fifth season (1999–2001), BVC 9 was 0.25–0.30 magnitudes fainter than in the maximum. Between the fifth and the sixth season (2001–2002), the star brightened by about 0.20 mag, then stayed at its maximum brightness until 2006. The data from 2007 suggest a beginning of another fading, as BVC 9 was about 0.1 mag fainter than during the previous season.

In Fig. 7.29 (top), our nightly-averaged V -passband magnitudes of BVC 9 are supplemented with available published data and new unpublished data. The following sources were used (in chronological order):

1. Feast (1958) listed the visual magnitude $m_V = 9.28$ (close to the Johnson V magnitude) and $B - V = -0.04$ from unpublished work by T. E. Houck. The observing date is uncertain, as it was “some years” before 1958, so we assume a date between 1954 and 1956.
2. Balona (1977) observed BVC 9 on two nights in 1976 March. On JD 2442853 he obtained $V = 9.34$ and a week later, on JD 2442860, $V = 8.84$. Based on light curves from these two nights, he found a period of 0.1753 days. He reports that the amplitudes on the two nights were different.
3. Turner et al. (1980) obtained photoelectric UBV data in 1975 and 1977, reduced both sets separately, intercompared them, and then averaged the data sets. BVC 9 was observed on five nights. They checked for variability during the period of their study but they did not find any light variation for this star.

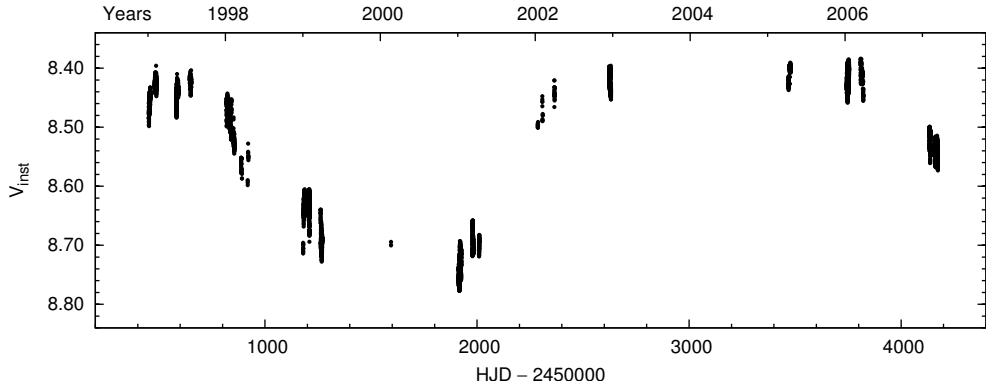


Figure 7.28: Long-term light curve of BVC 9. Differential y magnitudes have been transformed to the V scale.

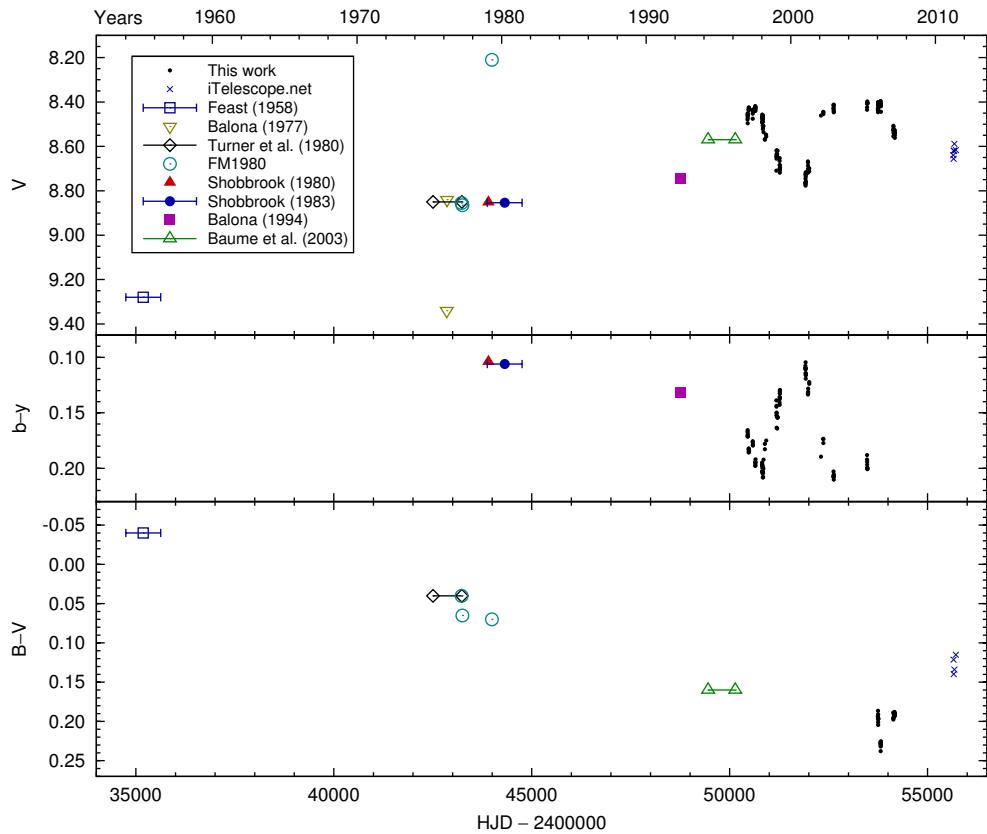


Figure 7.29: Nightly-averaged light and colour curve of BVC 9, supplemented with published data and with new data from 2011 (see text for details). Uncertain observing dates are marked with error bars or ranges. FM1980 refers to Feinstein & Marracco (1980).

4. Feinstein & Marraco (1980) observed NGC 3293 in BV passbands in 1977 March and April, and in $UBVRI$ passbands in 1979 April. For BVC 9 they report the V magnitudes of 8.86 and 8.85 from 2443228.60 (March 26, 1977), 8.87 and 8.86 from JD 2443246.61 (April 13, 1977), and 8.21 from JD 2443993.81 (April 30, 1979). The corresponding $B - V$ colour indices were 0.04, 0.04, 0.07, 0.06, and 0.07.
5. Shobbrook (1980) reports $uvby$ photometry of NGC 3293 from the total of 11 nights in 1979 February, March, April, and June. Yet, when discussing the variability of BVC 9, he mentions five observations from 1979 January and February, suggesting that BVC 9 was not observed in later months. He notes that the range of the five V magnitudes was 0.045 mag.
6. Shobbrook (1983) gives the $uvby$ photometry of NGC 3293 based on observations from January 1979 to May 1981, including his 1979 observations that were published in the previous paper (Shobbrook 1980). It is not clear whether BVC 9 was re-observed after 1979 February; it is possible that the 1979 observations were only re-reduced using new values for the standard system stars. He does not report any light variability of BVC 9.
7. Balona (1994) gives the $uvby$ photometry and B -passband variability monitoring based on a two-week observing run in 1992 May. He suggests that the star probably belongs to the λ Eri group (periodic Be stars) with a period of 0.877 days, or the double-wave period of 1.754 days.
8. Baume et al. (2003) observed NGC 3293 in $UBVRI$ passbands in 1994 April and 1996 February. They complemented their data set with unpublished $UBVRI$ data obtained in 1996 April. A single value is given for the V magnitude and each colour index; variability is not discussed.
9. Evans et al. (2005) used the BV frames of the ESO imaging survey from February 2000, but stars brighter than 10.75 in V , including BVC 9, were saturated and thus the authors list photometry by Turner et al. (1980) for these stars.
10. In 2011 remote observations with the iTelescope.net T9 telescope (located in Australia, formerly named GRAS-009) were carried out from the Tartu Observatory, Estonia. The cluster was observed using the BVI filters.

The $(b - y)$ colour curve of BVC 9 is shown in the middle panel of Fig. 7.29. The star is bluer in $(b - y)$ when fainter in V , and redder when brighter in V . The $(b - y)$ colour index as a function of the V magnitude is plotted in Fig. 7.30. The colour–magnitude relation is bi-valued (loop-like), a phenomenon that has been observed in many Be stars of the Small Magellanic Cloud (de Wit et al. 2006).

The light and colour variations of BVC 9 after 1997 can be interpreted by the formation and dissipation of a circumstellar disc that is viewed from a small inclination angle, i.e. not equator-on. Optical brightening then corresponds to the formation of the disc, of which the inner and optically thick part is called a pseudophotosphere (Harmanec 2000; Carciofi 2011). The pseudophotosphere simulates an increase of the radius of the star, which then appears brighter. Due to the pseudophotosphere being cooler than the photosphere of the star, the $(b - y)$ colour index becomes redder.

We note that the $(b - y)$ colour index also became redder at maximum brightness,

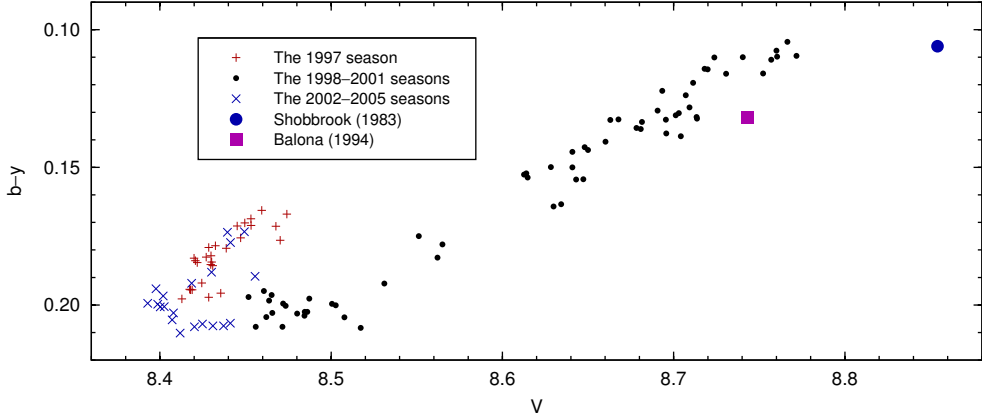


Figure 7.30: The $(b - y)$ colour index of BVC 9 as a function of the V magnitude.

just before fading in V was observed in 1998 and similarly, the star reddened in $(B - V)$ before fading in 2007. As there are no observations from between 2007 and 2011, it is not clear whether the star reached the same minimum brightness as around 2000.

There are two conspicuous episodes in the observational history of BVC 9. The first is the fading from $V = 8.85$ in 1975 to $V = 9.34$ in 1976 March, and then a rapid brightening by 0.5 mag to $V = 8.84$ just a week later. The second episode is brightening from $V = 8.84$ in 1979 January–February to $V = 8.21$ in 1979 April, while the $(B - V)$ colour index did not change significantly.

On top of the long-term behaviour, the star also exhibits light variability within hours and days. A sample two-week light curve from 2001 January is shown in Fig. 7.31. Multiple time scales are evident, as the magnitudes of maximum and minimum light vary on the order of days.

Curiously, different periods of short-term variability have been reported in the literature: 0.1753 d (Balona 1977), 0.877 d (single-wave) or 1.754 d (double-wave) (Balona 1994).

Our data suggest that the short-term variability time scale is on the order of 0.56–0.58 days. In panel (a) of Fig. 7.32 the light curve from six consecutive nights (JD 2453745–50) has been folded on the period of 0.559 d. The same period does not fit the light curve of the next three nights (JD 2453751–53), as seen from panel (b). Data from JD 2454160–70 are best fitted with the period of 0.576 d (panel c). If the observed periods are of rotational origin, then they are at the lower end for λ Eri stars, based on $v \sin i = 203 \text{ km s}^{-1}$ and the $v \sin i/P$ relationship (Balona 1995).

Lately it has been found that discs around Be stars are in Keplerian rotation and are best described with the viscous decretion disc model, although the mechanism responsible for ejecting material from the star is not known (Rivinius 2007; Carciofi 2011). Carciofi (2011) shows that different wavelengths probe different regions of the disc, and that the V -band excess is formed very close to the star, within about

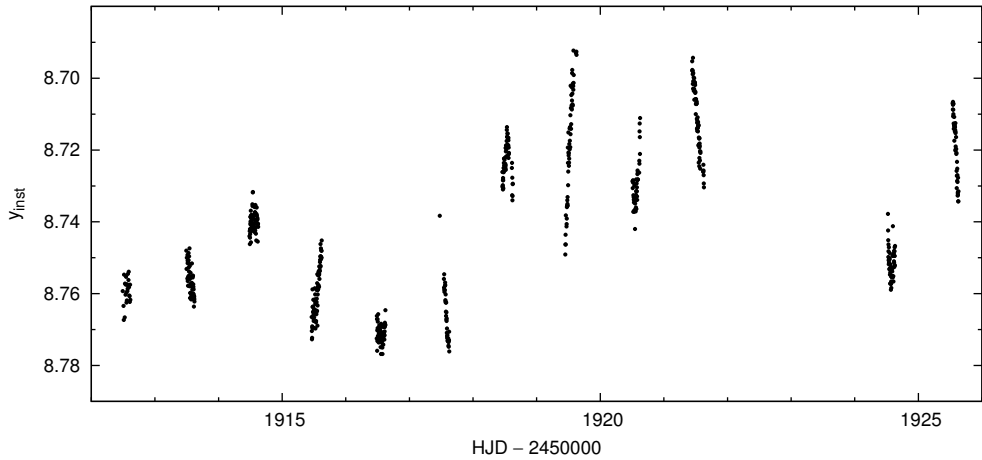


Figure 7.31: Short-term variability of BVC9 in the y passband during a two-week observing run.

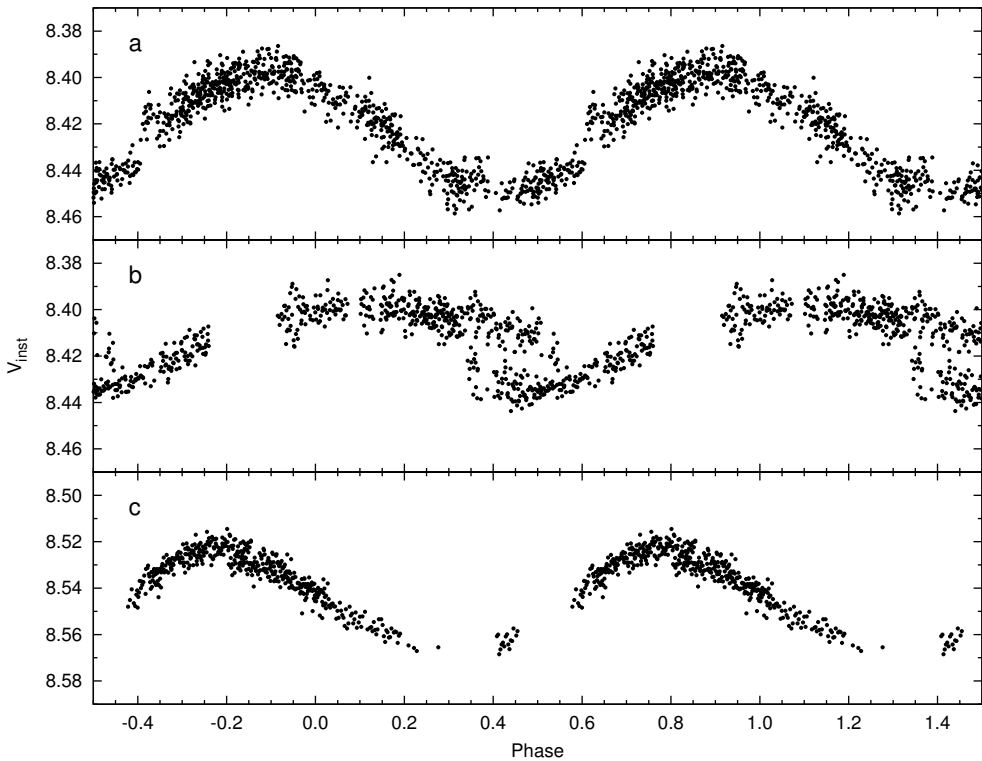


Figure 7.32: Phase diagrams of the BVC9 V -band light curve: (a) JD 2453745–50, folded on the period $P = 0.559$ d; (b) JD 2453751–53, $P = 0.559$ d; (c) JD 2454160–70, $P = 0.576$ d. The epoch of phase zero is HJD 2450000.0 in all three cases.

two stellar radii. Thus, the observed quasi-periods of 0.56–0.58 days may be due to inhomogeneities in orbit around the star, and variations in periods may be attributed to the inhomogeneities being observed at various distances from the star.

Further study of BVC 9 may provide important clues for answering the open questions about disc formation around Be stars.

BVC 14

BVC 14 is located to the right of the β Cep stars in the colour-magnitude diagram (see Fig. 7.12). According to Evans et al. (2005), the spectral type of BVC 14 is

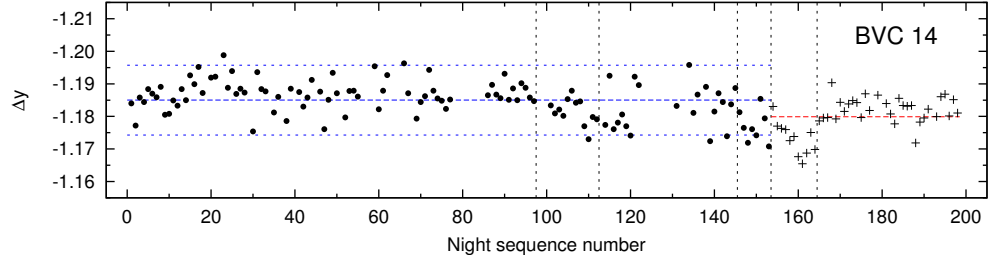


Figure 7.33: Nightly-averaged magnitudes of BVC 14. The designations are the same as in Fig. 7.22. The 3σ limits around the mean magnitudes are based on the standard deviation of BVC 10.

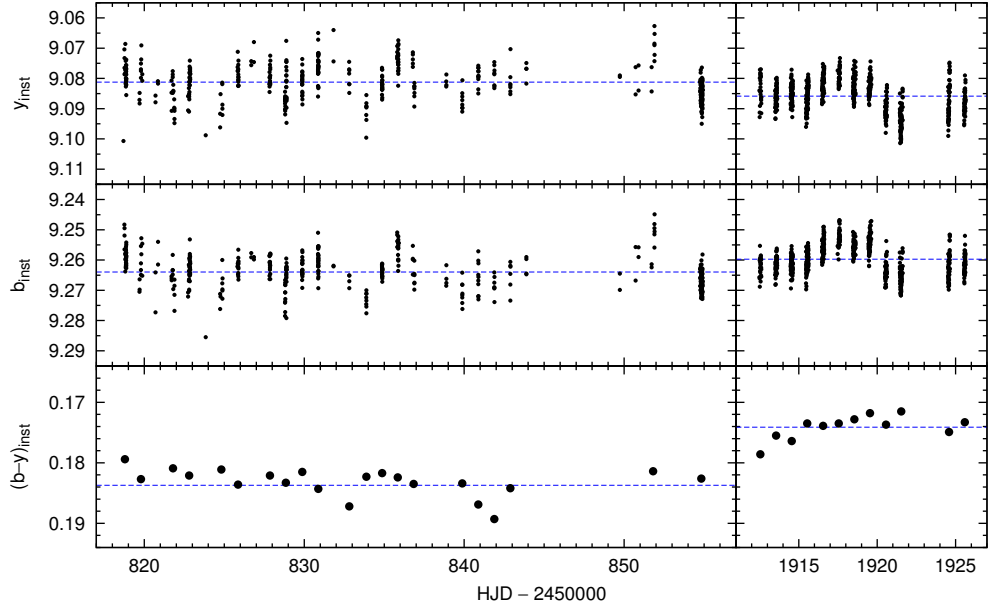


Figure 7.34: Light and colour curves of BVC 14 from two observing runs (JD 2450818–54 and 2451912–25). The mean magnitudes of observing runs are shown with dashed lines.

B0.5 IIIIn. McSwain & Gies (2005) and McSwain et al. (2009) report BVC 14 to be a Be star. The Be classification is supported by the high projected rotational velocity of 290 km s^{-1} , reported by Dufton et al. (2006).

The nightly-averaged magnitudes of BVC 14 are shown in Fig. 7.33. No significant long-term variations are evident, but the scatter suggests night-to-night variability on the order of 0.01 mag.

The b and y light curves and the $(b - y)$ colour curve of BVC 14 from two observing runs are plotted in Fig. 7.34. A sample V -band light curve from two nights in 2006 March is shown in Fig. 7.35. The light curves show variability on time scales of about 0.3 days and a few days. The $(b - y)$ colour variations are not significant from night to night.

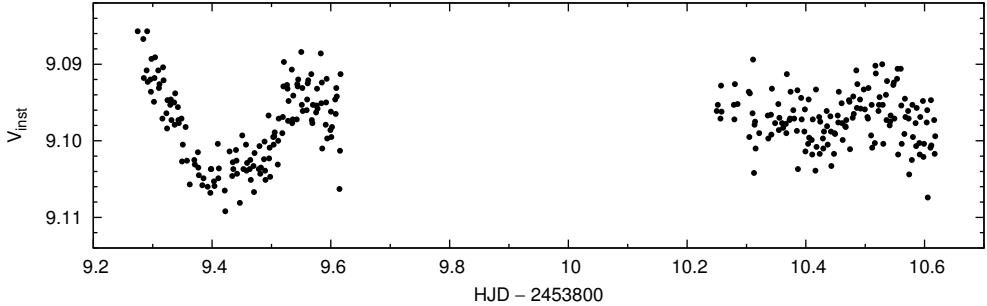


Figure 7.35: Short-term variability of BVC 14 in the V passband during two consecutive nights.

BVC 40

The light variability of BVC 40 was found by Balona (1994), who reported the period of 0.437 d, with a possible second period of 0.500 d. Evans et al. (2005) classified BVC 40 as a Be star (spectral type B3n).

The nightly-averaged light and colour curves are shown in Fig. 7.36. Our data are supplemented with published photometry from the same sources as in the case of BVC 9, described above. The published $uvby$ photometry has also been transformed to the $(B - V)$ colour indices (bottom panel of Fig. 7.36), using the formula

$$B - V = 1.584(b - y) + 0.681m_1 - 0.116, \quad (7.5)$$

applicable to stars of spectral types O, B, and A (Turner 1990).

The V -band light curve between 1997 and 2007 seems to follow a sine-wave with the period of about ten years. During the same time, the $(b - y)$ colour reddened by about 0.02 mag. Published photometry suggests that there have been brightenings in V by 0.05 mag between 1977 and 1979, and by 0.07 mag between 1992 and 1994–1996, although systematic differences of a few hundredths of a magnitude between different sources are common. Note also that our data has not been transformed to the standard system.

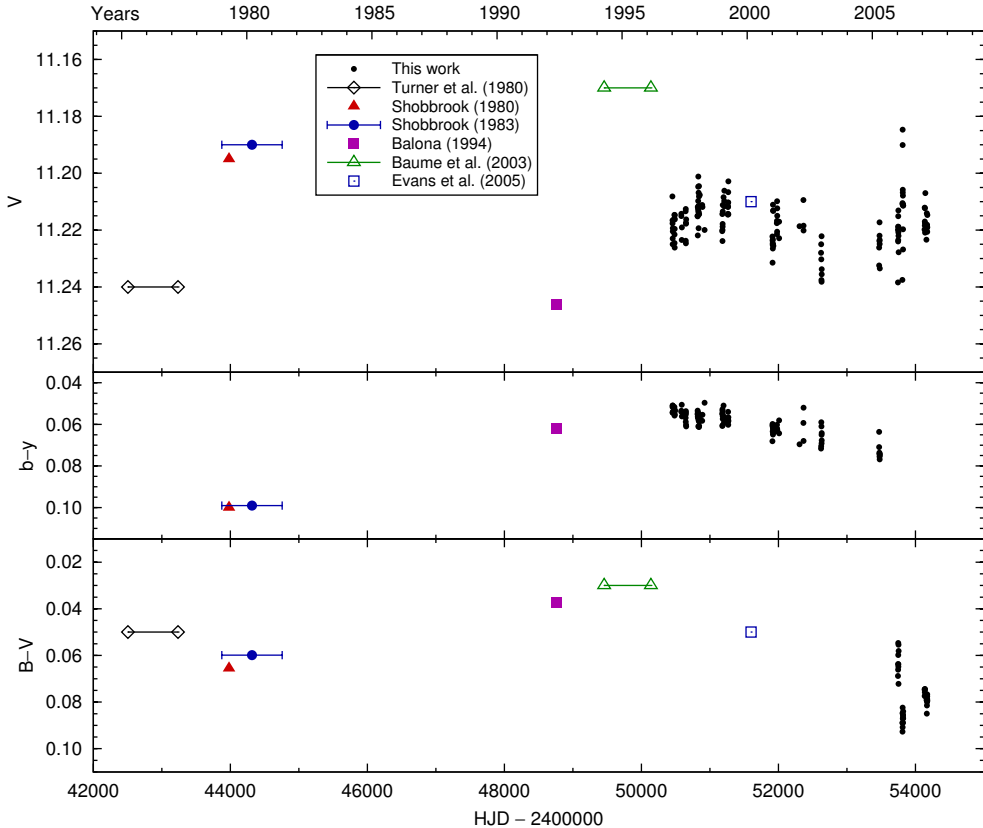


Figure 7.36: Nightly-averaged light and colour curve of BVC 40, supplemented with data from the literature. Uncertain observing dates are marked with error bars and ranges.

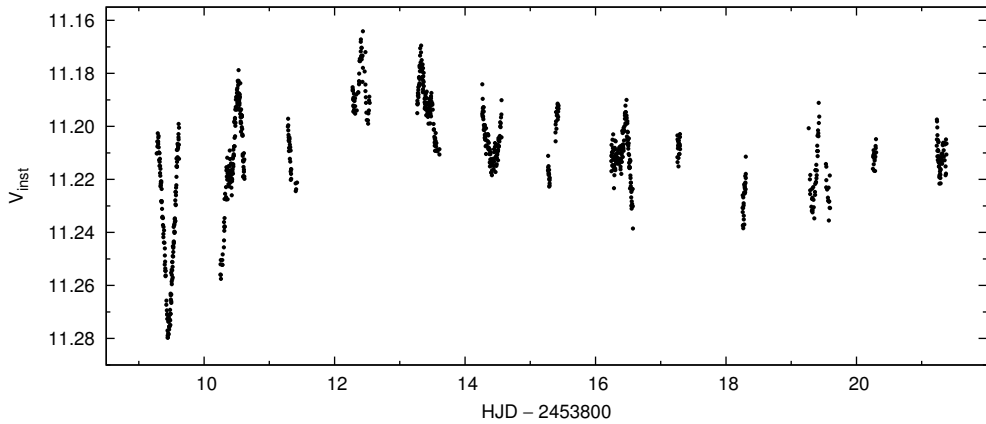


Figure 7.37: Short-term variability of BVC 40 in the V passband during a two-week observing run.

A sample V light curve of the short-term variability of BVC 40 is shown in Fig. 7.37. Light variations on multiple time scales are evident. Variability on the time scale of 0.3 days may be attributed to rotation, which is consistent with the $v \sin i/P$ relationship (Balona 1995), given that the projected rotational velocity $v \sin i = 335 \text{ km s}^{-1}$ (Dufton et al. 2006).

7.10.3 β Cep stars

β Cep stars are dwarfs and giants of spectral classes B0–B2 with pulsation periods of 2–6 hours (see Balona 2010, Chapter 2, for a review). As of 2010, there were 204 β Cep stars known, of which 11 were located in NGC 3293. In this section we do not concentrate on the short-period pulsations of these stars, but focus on the possible long-term variability.²

To calculate nightly-averaged magnitudes for β Cep stars, only nights with longer time span of observations than a full pulsation period of each star, were taken into account. Nightly light curves were then checked for gaps, and only such parts were accepted that had no longer gaps than 0.02 days (0.5 hours) and consisted of at least 20 data points. A nightly mean magnitude was calculated for an integer number of pulsation periods, as demonstrated in Fig. 7.38.

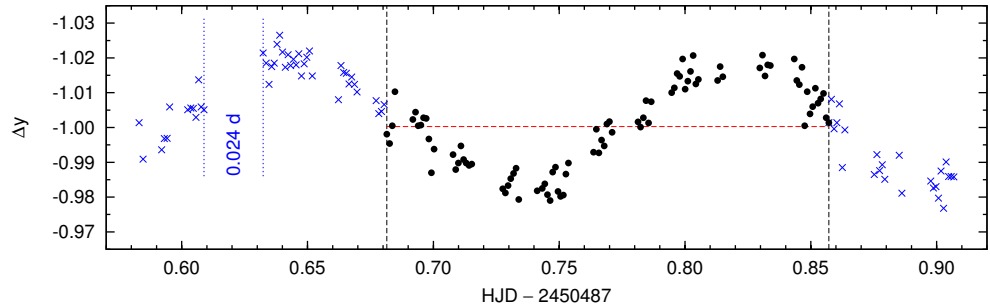


Figure 7.38: Nightly light curve of the β Cep star BVC 17. A full period was used for the nightly mean magnitude calculation, shown with dots between vertical dashed lines; other data (crosses) were not taken into account. Horizontal dashed line denotes the nightly mean magnitude. Also, a gap longer than 0.02 days is shown with dotted lines.

Five β Cep stars were suitable for studying the variability of nightly mean magnitudes: BVC 12, 16, 17, 18, and 24. Due to a close neighbouring star, it was impossible to get light curves of BVC 20 using aperture photometry. BVC 13 and 19 have multiple frequencies that make proper determining of their mean magnitudes complicated; the two stars are discussed separately below. The remaining β Cep stars, BVC 11, 21, and V400 Car, were located outside of the Dutch 0.91-m telescope field of view and thus were left out of the present study.

²An in-depth analysis of the high-frequency pulsational variability requires inclusion of multi-site data from the 2006 campaign (Section 7.3), and will be a topic of a forthcoming paper (Handler, Tuvikene, et al., in prep.).

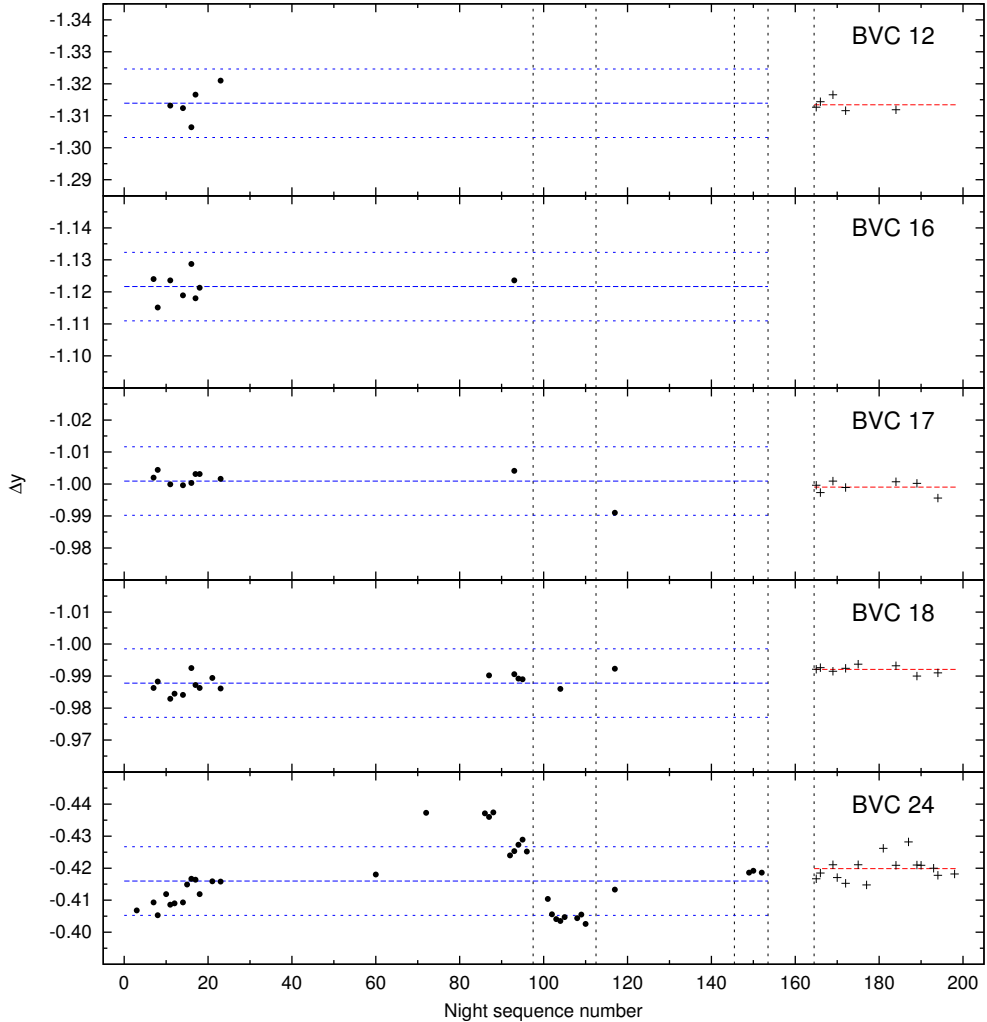


Figure 7.39: Nightly-averaged magnitudes of the β Cep stars BVC 12, 16, 17, 18, and 24. The designations are the same as in Fig. 7.22. The 3σ limits around the mean magnitudes are based on the standard deviation of BVC 10.

The resulting nightly-averaged magnitudes are shown in Fig. 7.39. Based on the limited number of nights for which averaging was possible, none of the nightly mean magnitudes of BVC 12, 16, 17, and 18 exceed 3σ from overall means, where σ is the standard deviation of the nightly means of BVC 10. Thus, our data do not support the brightness variability of BVC 12, 16, 17, and 18 on long time scales. The fifth star in this group, BVC 24, exhibits variability range of about 0.03 mag in the y passband.

The top panel of Fig. 7.40 shows the nightly-averaged V magnitudes of BVC 24 as a function of time. Our data are supplemented with available data from the literature;

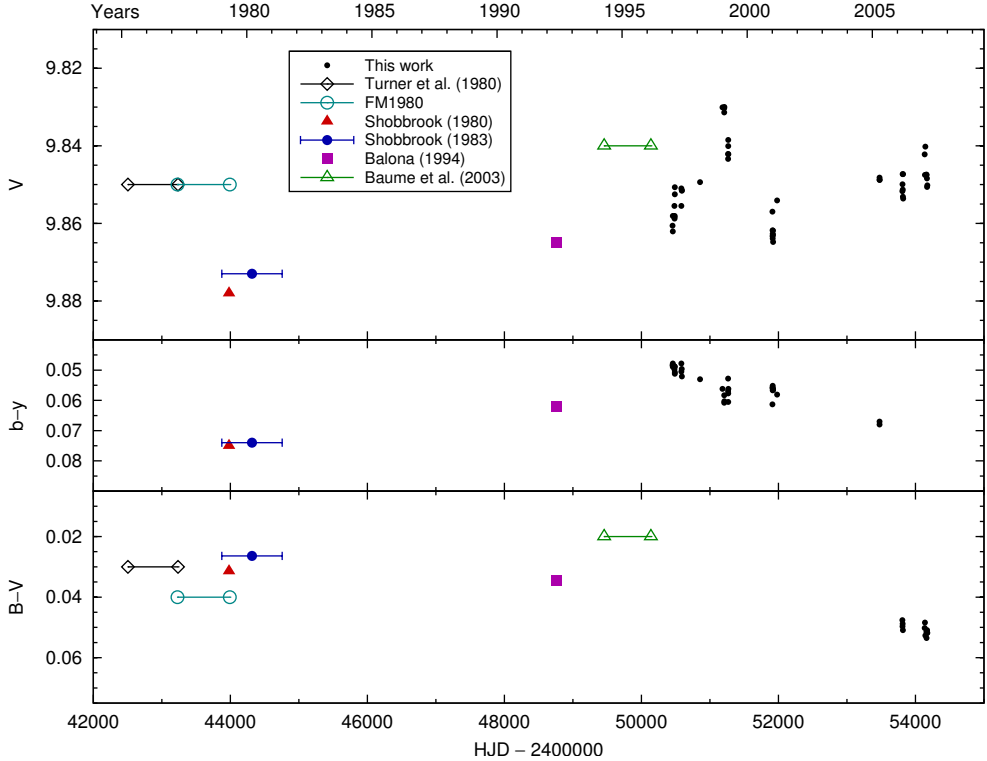


Figure 7.40: Light and colour curve of BVC 24, supplemented with data from the literature. Uncertain observing dates are marked with error bars and ranges.

the sources are common with the sources listed for BVC 9 (Section 7.10.2), however BVC 24 was not observed in early works on NGC 3293. Differences of a few hundredths of a magnitude in V between different sources may be due to transformation to the standard system, rather than the real variability of the star. Our data, however, reveals a brightening of the mean magnitude of the star by 0.02 mag in 1999 January, compared to the 1998 season. The V magnitude was constant between 1999 January 4 and 30 (JD 2451183–2451207), then faded by 0.01 mag by the end of March (JD 2451264–2451268). In 2001, the star was again fainter, with about the same brightness as in the 1997 season.

The $(b - y)$ and $(B - V)$ colour curves are given in the middle and bottom panels of Fig. 7.40. The $(b - y)$ colour curve does not follow variations in the light curve, while there is a trend evident: $(b - y)$ increases by 0.02 between 1997 and 2005. In the bottom panel, the $uvby$ photometry from Shobbrook (1980, 1983) and Balona (1994) has been transformed to the $(B - V)$ scale, using Eq. 7.5. It can be seen that the $(B - V)$ colour index of BVC 24 in 2006–2007 is redder by 0.02–0.04, compared to values from 1975–1996; however, the transformation of colour indices leads to some uncertainty.

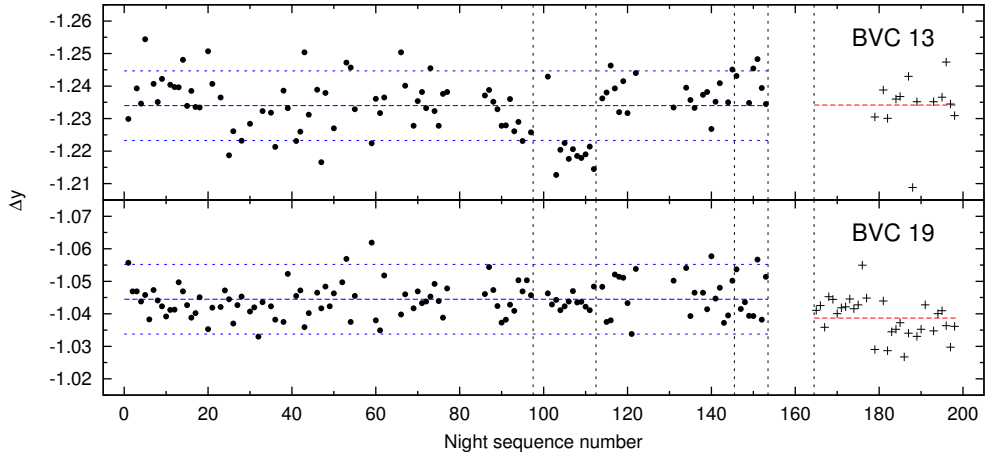


Figure 7.41: Nightly-averaged magnitudes of the β Cep stars BVC 13 and 19. The designations are the same as in Fig. 7.22. The 3σ limits around the mean magnitudes are based on the standard deviation of BVC 10.

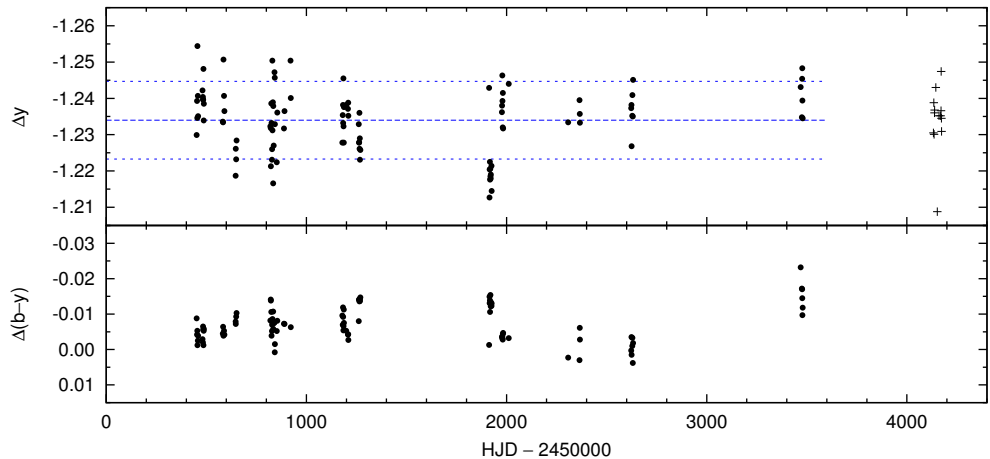


Figure 7.42: Light and colour curve of the β Cep star BVC 13. The designations are the same as in Fig. 7.22.

BVC 13 = HD 92024

BVC 13 is an eclipsing binary with a β Cep component. The orbital period is 8.32457 d (Freyhammer et al. 2005).

We calculated the nightly mean magnitudes of BVC 13 by excluding primary and secondary eclipses (phases 0.000–0.035, 0.472–0.542, and 0.965–1.000) from light curves, using the ephemeris by Freyhammer et al. (2005). As the β Cep component is multiperiodic, we were unable to average magnitudes over full periods, thus

we included all nights with at least five valid data points.

The nightly mean magnitudes of BVC 13 are plotted in Fig. 7.41. As expected, the spread is larger compared to the previously discussed β Cep stars, for which pulsation periods were taken into account. The nightly-averaged light and colour curves are shown in Fig. 7.42. No significant long-term variability is evident. The fadings of y magnitude by 0.02 during the SAAO 2001 observing run (JD 2451912–2451925) and on JD 2454151 are due to systematic effects in flat-fielding, as BVC 13 was located at the edge of CCD frames and proper flat-field correction was not possible using non-variable cluster stars.

BVC 19

Similarly to BVC 13, strict averaging over full pulsation periods was not possible for BVC 19, thus all nights with at least five measurements were used. The nightly-averaged magnitudes are plotted in Fig. 7.41. No significant long-term light variability is seen.

7.10.4 SPB-star candidates

Slowly pulsating B stars (SPB stars) are mid-B type dwarfs and giants with pulsation periods in the range 0.5–3 days (Balona 2010, p. 26).

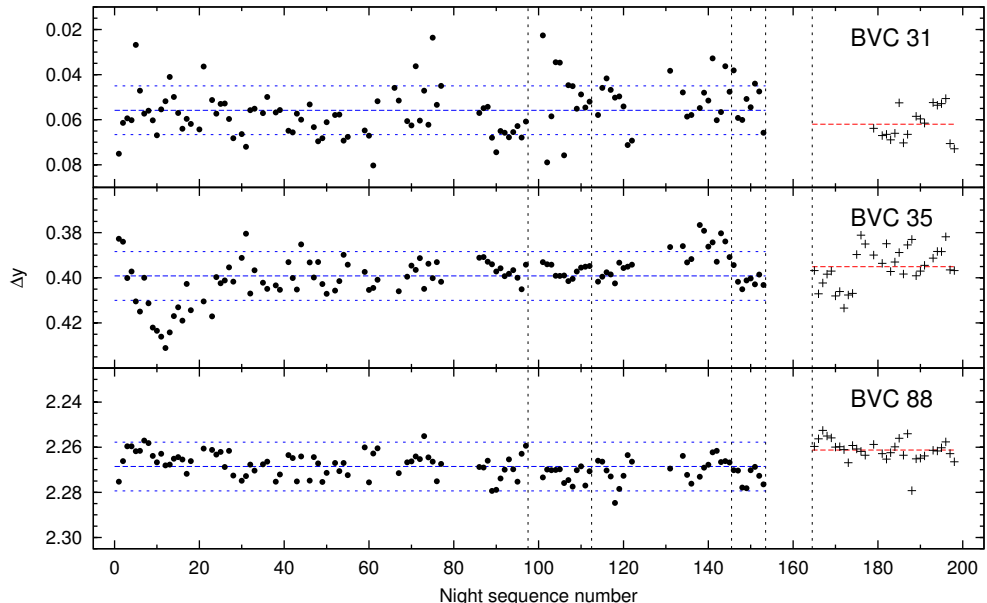


Figure 7.43: Nightly-averaged magnitudes of the SPB-star candidates BVC 31, 35, and 88. The designations are the same as in Fig. 7.22. The 3- σ limits around the mean magnitudes are based on the standard deviation of BVC 10.

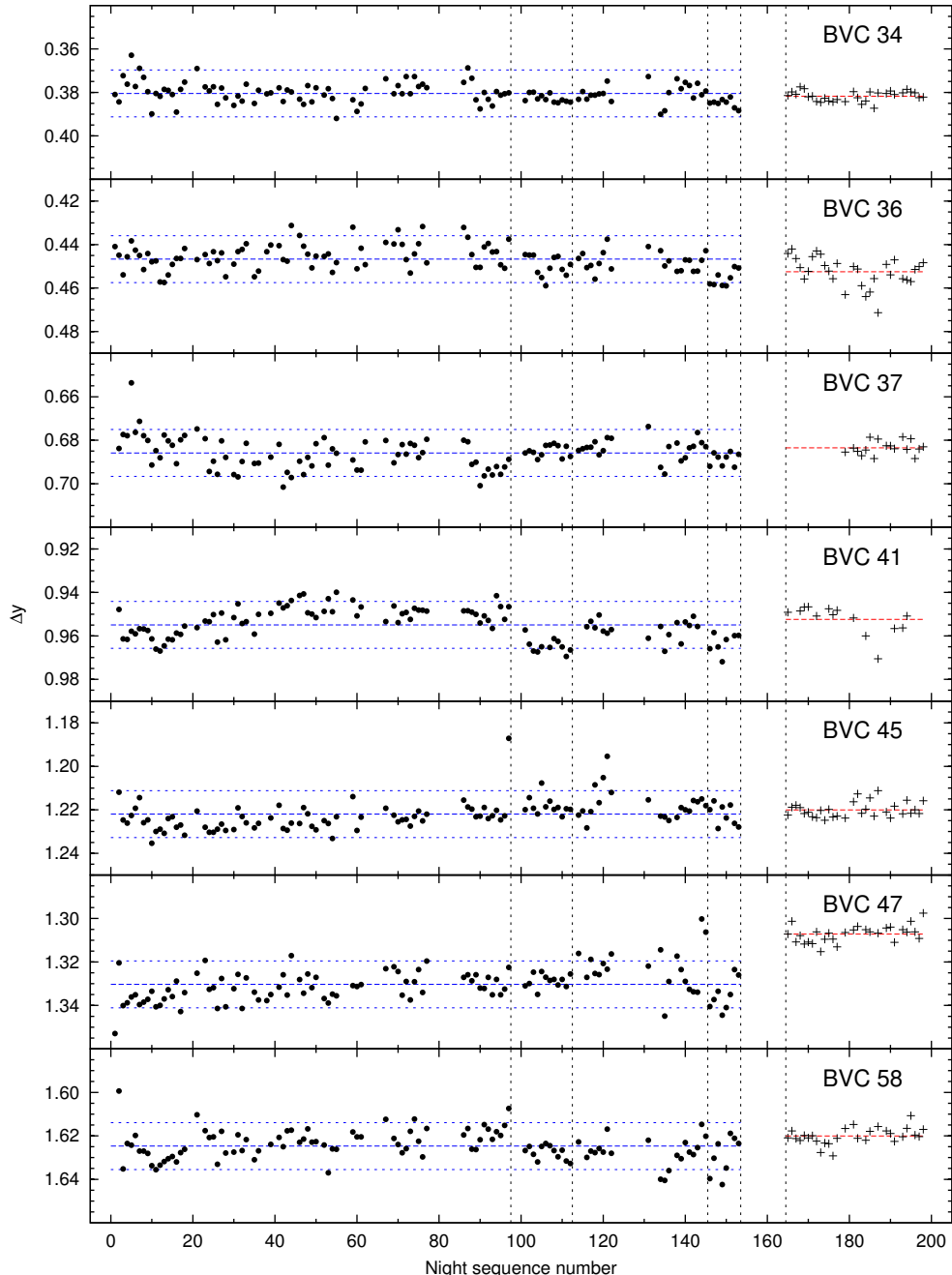


Figure 7.44: Nightly-averaged magnitudes of BVC 34, 36, 37, 41, 45, 47, and 58. The designations are the same as in Fig. 7.22. The 3- σ limits around the mean magnitudes are based on the standard deviation of BVC 10.

Handler et al. (2008) present amplitude spectra of five variable stars near the low-luminosity end of the β Cep instability strip: BVC 31, 32, 35, 40, and 88. They preliminarily classify these stars as SPB candidates and suggest that the variability of these stars may be connected to their rapid rotation. Of this group, BVC 32 is outside the Dutch telescope field of view and is not included in the present study. The Be star BVC 40 was already discussed in Section 7.10.2.

The nightly-averaged magnitudes of BVC 31, 35, and 88 are shown in Fig. 7.43. The variations of the nightly mean magnitudes of these stars are due to short-term variability, which is out of the scope of this work. We do not find any significant light variability on long time scales for these stars.

7.10.5 Other stars

In this subsection we discuss long-term variability of the rest of the bright stars ($V < 12$) in our selection, and of a few fainter stars of interest.

The nightly-averaged magnitudes of BVC 34, 36, 37, 41, 45, 47, and 58 are plotted in Fig. 7.44. None of these stars exhibit notable variability on long time scales.

BVC 36

BVC 36 is an early B-type giant (B2 IIIh, Evans et al. 2005), whose variability has not been reported before. We find that the star exhibits light variability with a period of 6.3631 days. The phase diagrams of the nightly-averaged y magnitudes and $(b - y)$ colour indices, folded with the above period, are shown in Fig. 7.45.

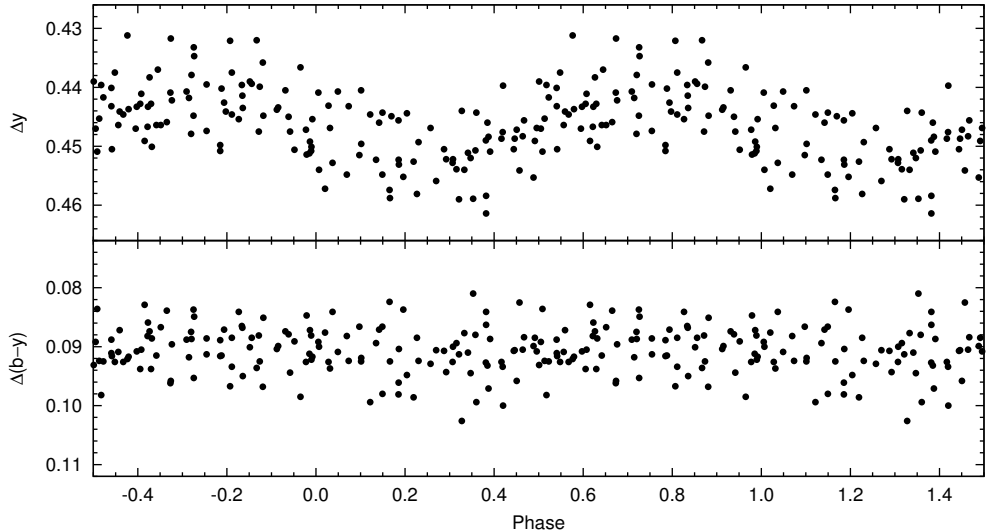


Figure 7.45: Phase diagrams of the nightly-averaged y -passband light curve and $(b - y)$ colour curve of BVC 36, folded on the period of 6.3631 days. The epoch of phase zero is HJD 2450000.0.

BVC 65

BVC 65 has a spectral type B2 V (Evans et al. 2005) and its variability has not been reported before. The long-term light and colour curves of BVC 65 are shown in Fig. 7.46. Variability on time scales of years is not evident. Large scatter in the light curve is due to variability on shorter time scales.

Fig. 7.47 shows a sample two-week V -band light curve, revealing that the short-term variability of this star is rather complicated.

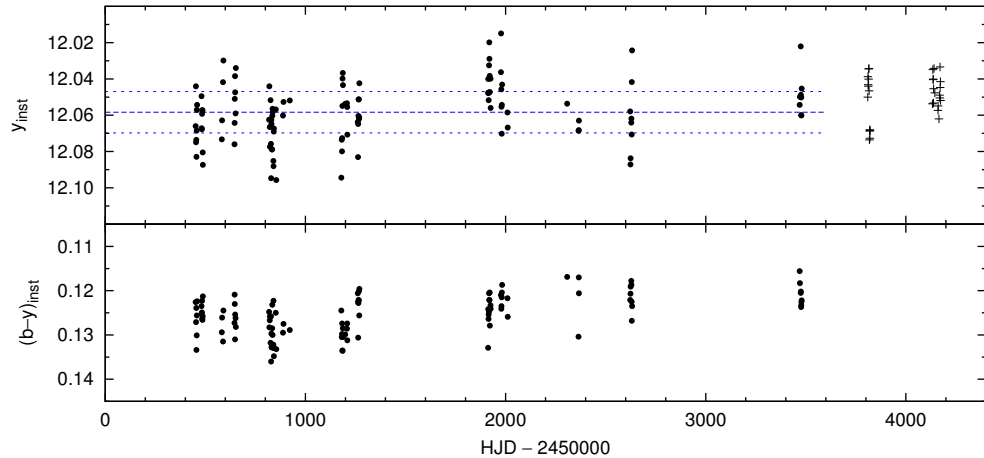


Figure 7.46: Nightly-averaged light and colour curve of BVC 65 (in the instrumental system). The V magnitudes (marked with plusses) have been transformed to the y scale. Dashed line denotes the mean of nightly mean magnitudes and dotted lines give 3σ limits around the mean, using the standard deviation of BVC 64.

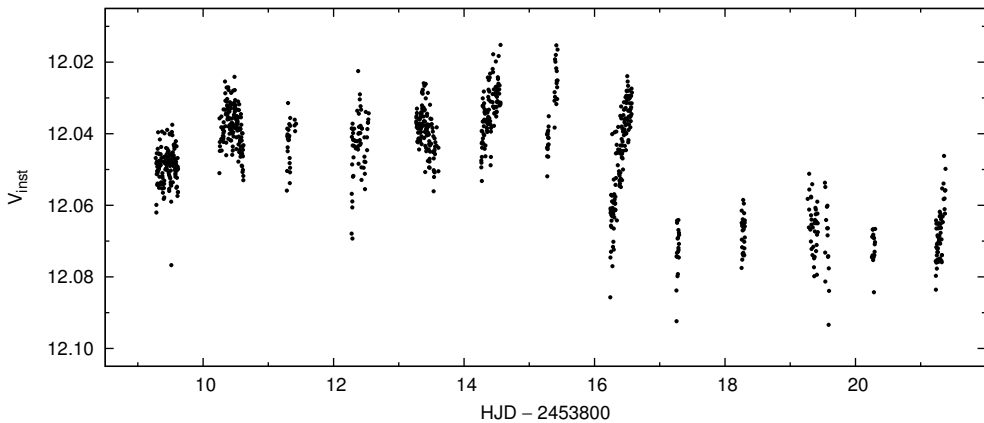


Figure 7.47: Short-term variability of BVC 65 in the V passband during a two-week observing run.

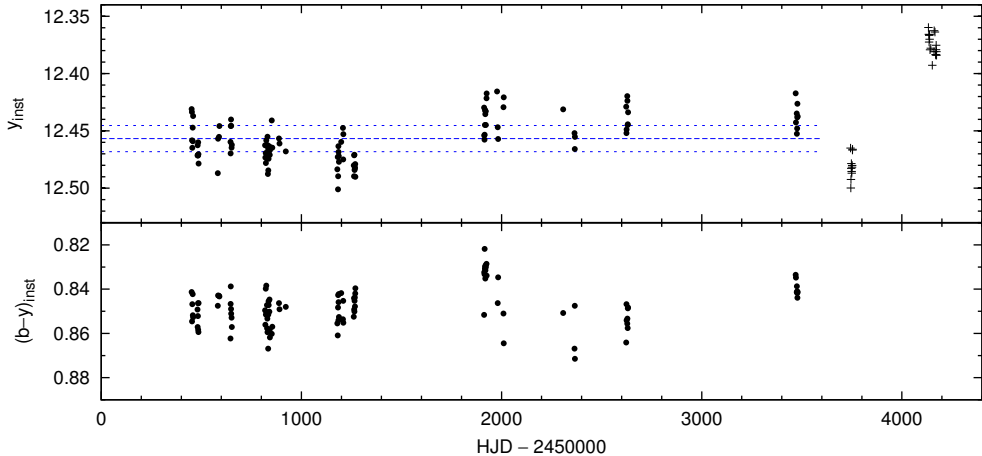


Figure 7.48: Nightly-averaged light and colour curve of BVC 87 (in the instrumental system). The V magnitudes have been transformed to the y scale. Designations are the same as in Fig. 7.46.

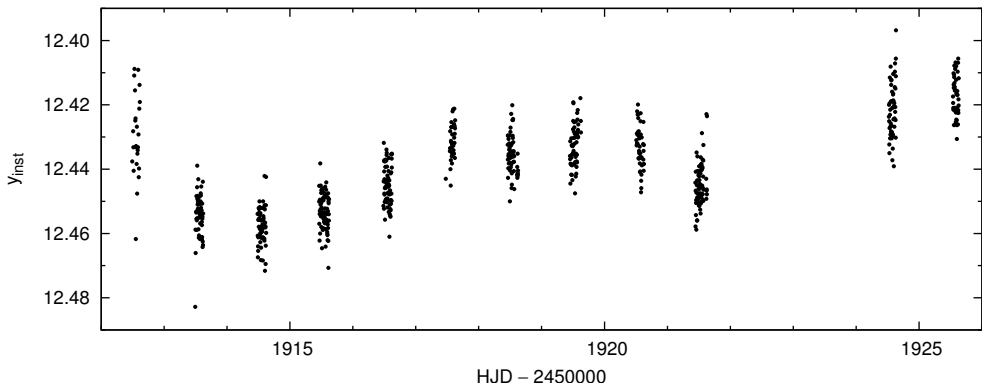


Figure 7.49: Short-term variability of BVC 87 in the y passband during a two-week observing run.

BVC 87

As seen in Fig. 7.21, BVC 87 exhibits much higher scatter of nightly mean magnitudes than what is expected from constant stars of the same brightness. In the literature, we find only two measurements of BVC 87: Herbst & Miller (1982) give $V = 12.42$, $B - V = 1.06$, and Baume et al. (2003) list $V = 12.43$, $B - V = 1.17$, classifying it as a non-member of NGC 3293. No spectra of this star has been published and light variability has not been reported before.

The nightly-averaged y -passband light curve and $(b - y)$ colour curve are shown in Fig. 7.48. Long-term variability of BVC 87 in the y passband is characterised by brightenings and fadings by a few hundredths of a magnitude between different seasons. However, we cannot rule out the possibility that the variations are caused by

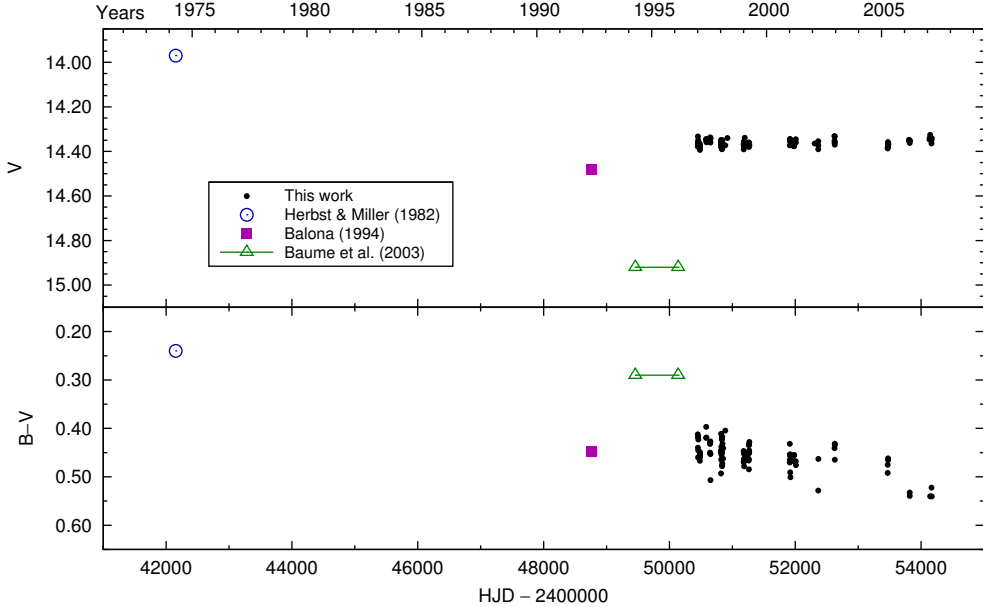


Figure 7.50: Light and colour curves of BVC 359, supplemented with data from the literature. Uncertain observing date is marked with a range.

systematic flat-field errors, as BVC 87 was located at the edge of the field of view of most telescopes we used. The large scatter of nightly means is due to night-to-night variability. A sample light curve from a two-week observing run is shown in Fig. 7.49, suggesting variability on the time scale of about 7 days.

BVC 359

BVC 359 is notable for the large range of published V magnitudes: 13.97 (Herbst & Miller 1982), 14.479 (Balona 1994), and 14.92 (Baume et al. 2003).

The V -passband light curve and the $(B - V)$ colour curve of BVC 359 are plotted in Fig. 7.50. The $(b - y)$ values have been transformed to the $(B - V)$ scale, using Eq. 7.5. Our data from 1997–2007 give rather constant light and colour curves and are close to the photometry by Balona (1994).

7.11 Conclusions

Based on the ten-year monitoring of NGC 3293, we studied long-term variability of 94 stars in the cluster. We report, for the first time, the light variability of the following stars: BVC 4, 5, 6, 7, 10, 14, 36, 65, and 87.

The Be star BVC 9 is found to exhibit cyclic variability on the time scale of ten years. This variability is attributed to the formation and dissipation of the circumstellar disc. Short-term light variations are found with quasi-periods of 0.56–0.58 days.

We suggest that this variability is related to inhomogeneities orbiting the star.

The variability of the Be stars BVC 14 and 40 were studied in the light of the Be phenomenon.

The β Cep star BVC 24 is found to show long-term light variations, in addition to short-period pulsations.

References

- Balona, L. A. 1975, MmRAS, 78, 51
- Balona, L. A. 1977, MmRAS, 84, 101
- Balona, L. A. 1994, MNRAS, 267, 1060
- Balona, L. A. 1995, MNRAS, 277, 1547
- Balona, L. A. 2010, Challenges In Stellar Pulsation (Bentham Publishers)
- Balona, L. A. & Engelbrecht, C. 1981, in *Pulsating B-Stars*, ed. C. Sterken & Groupe Etoiles Variables de L'Observatoire de Nice, p. 195
- Balona, L. A. & Engelbrecht, C. 1983, MNRAS, 202, 293
- Baume, G., Vázquez, R. A., Carraro, G., & Feinstein, A. 2003, A&A, 402, 549
- Carciofi, A. C. 2011, in IAU Symposium, Vol. 272, *IAU Symposium*, ed. C. Neiner, G. Wade, G. Meynet, & G. Peters, p. 325
- Cousins, A. W. J. & Caldwell, J. A. R. 1985, The Observatory, 105, 134
- de Wit, W. J., Lamers, H. J. G. L. M., Marquette, J. B., & Beaulieu, J. P. 2006, A&A, 456, 1027
- Dufon, P. L., Smartt, S. J., Lee, J. K., et al. 2006, A&A, 457, 265
- Engelbrecht, C. A. 1986, MNRAS, 223, 189
- Evans, C. J., Smartt, S. J., Lee, J.-K., et al. 2005, A&A, 437, 467
- Feast, M. W. 1958, MNRAS, 118, 618
- Feinstein, A. & Marraco, H. G. 1980, PASP, 92, 266
- Freyhammer, L. M., Hensberge, H., Sterken, C., et al. 2005, A&A, 429, 631
- Handler, G., Tuvikene, T., Lorenz, D., et al. 2007, Communications in Asteroseismology, 150, 193
- Handler, G., Tuvikene, T., Lorenz, D., et al. 2008, Communications in Asteroseismology, 157, 315

- Harmanec, P. 2000, in Astronomical Society of the Pacific Conference Series, Vol. 214, *IAU Colloq. 175: The Be Phenomenon in Early-Type Stars*, ed. M. A. Smith, H. F. Henrichs, & J. Fabregat, p. 13
- Herbst, W. & Miller, D. P. 1982, AJ, 87, 1478
- Honeycutt, R. K. 1992, PASP, 104, 435
- Jerzykiewicz, M. & Sterken, C. 1992, MNRAS, 257, 303
- Kjeldsen, H. & Frandsen, S. 1992, PASP, 104, 413
- McSwain, M. V. & Gies, D. R. 2005, ApJS, 161, 118
- McSwain, M. V., Huang, W., & Gies, D. R. 2009, ApJ, 700, 1216
- Porter, J. M. & Rivinius, T. 2003, PASP, 115, 1153
- Rivinius, T. 2007, in Astronomical Society of the Pacific Conference Series, Vol. 361, *Active OB-Stars: Laboratories for Stellar and Circumstellar Physics*, ed. A. T. Okazaki, S. P. Owocki, & S. Stefl, p. 219
- Saesens, S., Carrier, F., Pigulski, A., et al. 2010, A&A, 515, A16
- Schild, R. E. 1970, ApJ, 161, 855
- Shobbrook, R. R. 1980, MNRAS, 192, 821
- Shobbrook, R. R. 1983, MNRAS, 205, 1215
- Sterken, C. & Manfroid, J., eds. 1992, Astrophysics and Space Science Library, Vol. 175, Astronomical Photometry, A Guide
- Turner, D. G. 1990, PASP, 102, 1331
- Turner, D. G., Grieve, G. R., Herbst, W., & Harris, W. E. 1980, AJ, 85, 1193

Summary

Photometric observations of variable stars with CCD cameras yield large amounts of raw data in the form of CCD frames. Data reduction consists of initial calibration of raw frames, extraction of fluxes or magnitudes of stellar sources, identification of the sources, and construction of differential light curves by using one or more comparison stars from the same field of view.

In this study, the reduction of CCD frames was addressed via the design and implementation of a workflow. Our proposed CCD photometry workflow is especially suitable for working with heterogeneous data that have been obtained with a variety of telescopes and instruments. In this case, individual data batches may require different calibration steps to be carried out, or different parameters to be chosen for magnitude extraction. The workflow approach enables consistency in data reduction, from frame calibration to construction of a light curve.

The workflow was implemented in the software package PHOTWORK that was developed in the framework of this thesis. We used PHOTWORK for data reduction in the majority of cases throughout this study. Data batches varied in size from about 100 to 18000 frames, each frame containing from just a few stellar images in non-crowded fields to several hundred stellar images in the semi-crowded field centred on the open cluster NGC 3293. We used PHOTWORK to handle photometry databases with up to a few million entries, each entry consisting of 12 magnitudes, corresponding to 12 aperture radii.

In order to check for systematic errors arising from data reduction, we carried out comparative tests that involved independent reductions of the same CCD frames. In the first test, magnitudes of stellar sources were extracted from the same calibrated frames using three different software packages. In the second test, a batch of raw frames was calibrated and analysed independently using two different approaches. The resulting differential light curves were then compared. We found systematic discrepancies of the order of several millimagnitudes between light curves obtained with different software packages. Although we did not carry out extensive comparisons, it was evident that systematic errors arising from data reduction procedures were rather common. Thus, for high accuracy, data should be reduced in a consistent way, preferably using a single software package. Merging light curves from different reductions should be done with care, and possible systematic errors should be taken into account.

In Part II of this thesis, we presented five case studies involving CCD photometry of variable stellar sources.

We participated in observations of a stellar occultation by Pluto's moon Charon at Observatorio Cerro Armazones (OCA), Chile, on 11 July 2005. The spatial resolution with which Charon could be probed, was mainly limited by the time resolution of observations. The observations were carried out with the POETS system, a specialised instrument utilising a frame-transfer camera and a GPS receiver to trigger exposures and provide accurate timing. At OCA we achieved a data rate of 2 Hz, while at larger telescopes the maximum data rate was 10 Hz, corresponding to a spatial resolution of 2.13 km at Charon. Combining four occultation chords yielded Charon's mean radius of 606 ± 8 km. Later, Person et al. (2006, AJ, 132, 1575) combined all available data from the 2005 occultation to more accurately determine the mean radius of Charon: 606.0 ± 1.5 km. They found the density of Charon to be significantly smaller than Pluto's.

GSC 08613–02122 is a newly-discovered 12th-magnitude δ Scuti star in Carina. We found its variability from the wide-field images of the open cluster NGC 3293. The discovery proved the usefulness of the workflow approach, in which magnitudes of all stellar sources in CCD frames are extracted and stored in a database for further inspection. We carried out dedicated observations of GSC 08613–02122 in *BVRI* and *uvby* passbands, revealing a main pulsation period of about four hours with an amplitude of $0.^m05$ in the *V* passband. We found the pulsation amplitude to be variable. The $O - C$ diagram of the times of maximum light in 2007 revealed the existence of a 29.5-day cycle, resulting from the beating of the main pulsation frequency with a nearby frequency.

The variability of the previously unstudied 12th-magnitude eclipsing binary GSC 04778–00152 was detected by inspecting light curves of stars in the field of the δ Scuti star V1162 Orionis. We carried out follow-up photometric observations of GSC 04778–00152 in *UBVRI* and *uvby* passbands, and collected several spectra. Images obtained in good seeing conditions revealed a 1-mag fainter visual companion (star B) about 2 arcsec away from the binary (star A). Utilising point-spread-function (PSF) photometry allowed us to determine the *UBVRI* magnitudes of the companion B and to subtract its contribution from the unresolved light curves of stars A and B together. We found the shape of the binary to be typical of A-type W UMa type systems. Our spectra indicated that the spectral type of the primary component of the binary was F5V. From light-curve modelling we concluded that the secondary component had 18 percent of the mass of the primary and was about 500 K cooler.

CY Aquarii is an SX Phoenicis type pulsating star with a pulsation period of 87.9 minutes. The star has been studied since the discovery of its variability in 1934 and several investigations of its changing pulsation period using the $O - C$ diagram have been published. We obtained a large amount of photometric observations of CY Aquarii since the previous substantial study by Fu & Sterken (2003, A&A, 405, 685), who proposed a binary model with an orbital period of 52.5 years. We reduced the bulk of the data using PHOTWORK and determined the times of maximum light. A weighting scheme was established, based on data density and shape of the local maximum. We presented a total of 155 new times of maximum together with 20

times of maximum taken from the literature. The times of maximum led to a linear ephemeris for 2003–2011 with formally shorter period than the one given by Fu & Sterken (2003) for 1996–2002. Our data show that consistent monitoring of CY Aquarii with modest equipment, when sustained for at least 5 to 10 years, will provide enough evidence to conclude whether the binary model can fully account for all the period variability observed in this star. The decreasing internal variance of our $O - C$ residuals illustrates the importance of a systematic and careful approach in observing as well as in data reduction.

The young open cluster NGC 3293 was photometrically monitored from 1997 to 2007, providing a unique data set for studying stellar variability at a wide range of time scales, from less than an hour to ten years. We carried out the observations with five telescopes at three observatories, using Strömgren *uvby* filters in 1997–2005 and Johnson *UBV* filters in 2006–2007. CCD frames were reduced with the PHOTWORK software; stellar magnitudes were extracted by means of aperture photometry. Stars whose photometry was affected by neighbouring stars were left out of the present study. We further focused on the central part of the cluster, corresponding to the field of view of the 0.91-m Dutch telescope, as this region had the best data coverage. We chose comparison-star candidates among relatively bright isolated stars and checked for their constancy. We found three stars (BVC 26, 29, and 33) to be comparable in constancy and low scatter in differential light curves, and thus we chose their mean magnitude as an artificial comparison star for differential photometry in the cluster. By carrying out a test of ensemble photometry, we found the gain in using more than three comparison stars to be small or nonexistent.

We studied long-term variability of 94 stars in the centre field of NGC 3293 on the basis of nightly-averaged differential magnitudes. The bright stars BVC 4, 5, 6, 7, and 10, classified as spectral type B1 III, of which some had been used as comparison stars in earlier studies, were all found to exhibit night-to-night variability of up to a few hundredths of a magnitude. The Be star BVC 9 showed cyclic variability on a time scale of ten years. We attributed this variability to the formation and dissipation of a circumstellar disc. We suggested that the short-term light variations of BVC 9 with quasi-periods of 0.56–0.58 days were related to inhomogeneities orbiting the star. Another Be star, BVC 14, was found to show light variability on time scales of about 0^d.3 and a few days. In order to study long-term variability of β Cep stars, we averaged their magnitudes over full pulsation periods. Our data revealed a brightening of the mean magnitude of the β Cep star BVC 24 by 0.02 mag in 1999, compared to the previous season, and subsequent fading by the 2001 season. The other β Cep stars in NGC 3293 did not show any long-term variability. We also reported, for the first time, light variability of BVC 36, 65, and 87. It can be concluded that non-variable stars among the bright members of NGC 3293 are rather rare.

We intend to continue our variability study of the open cluster NGC 3293 by working on the following aspects:

- frequency analysis of pulsating stars;
- variability of stars outside the core of the cluster where data coverage is poorer;

- usage of PSF photometry technique to obtain light curves of stars with blended images or with close neighbouring stars.

As was shown in several case studies, our workflow approach was successful in producing light curves of high quality, which let us find even small light variations in stars that were previously considered constant. We plan to continue using the CCD photometry workflow in our upcoming studies of variable stars.

Samenvatting

Hedendaags fotometrisch onderzoek van veranderlijke sterren is gebaseerd op waarnemingen verkregen met CCD camera's. Enerzijds bieden CCD camera's heel wat voordelen, zoals een bijna lineair signaal, een hoge quantum efficiëntie, en de mogelijkheid om heel veel hemelobjecten op één enkel beeld vast te leggen. Anderzijds vergt de verwerking van CCD data een zorgvuldige benadering, vooral als resultaten met een hoge nauwkeurigheid worden beoogd. Bovendien gaat hiermee doorgaans een groot datavolume gepaard, in het bijzonder als elk beeldveld honderden sterren bevat, en als het onderzoek over een lange tijdbasis wordt uitgevoerd.

De verwerking van grote hoeveelheden CCD frames vergt een vrij hoge graad van automatisatie. Omdat de data vaak afkomstig zijn van verschillende telescopen en instrumenten, is het niet mogelijk om exact dezelfde stappen op alle data toe te passen. Een volautomatisch datareductie proces kan in de praktijk niet worden aangewend: een georganiseerde en systematische verzameling van reductieprocedures in een "workflow" is eerder aan de orde.

Het hoofddoel van deze studie bestond eruit om niet alleen nieuwe, maar ook gearriveerde fotometrische metingen van een aantal heel specifieke hemelobjecten te verzamelen. Alle geselecteerde objecten worden gekenmerkt door één of andere extreme observationele parameter – zoals een zeer kleine of een zeer grote amplitude, een steile gradiënt, of een zeer nabije begeleider – en vormen dus een uitdaging bij de waarneming, bij de datareductie of bij de analyse.

De motivatie voor onze systematische en grondige aanpak werd gedreven door ons verlangen om heel kleine fysische veranderingen in licht en kleur te onderscheiden van effecten van instrumentele origine, maar ook van effecten geproduceerd door datacalibratie, standaardisatie en datareductie. Een dergelijke bendering is uitermate belangrijk omdat doorbraken in hedendaags baanbrekend astrofysisch onderzoek niet alleen steunen op data verkregen met moderne grote telescopen, maar ook (en soms vooral) op de eerder vermelde aspecten van observationele en data-verwerkende procedures. Dit is, in het bijzonder, het geval voor studies van objecten op cosmologische afstanden en voor fenomenen die veroorzaakt worden door exotische fysische processen.

Deel I van deze thesis beschrijft het concept, het ontwerp en de implementatie van onze workflow. Een belangrijk aspect is de inschatting van de nauwkeurigheid: dit wordt in Hoofdstuk 2 beschreven aan de hand van een vergelijkende test van verschillende datareductie procedures. Aan de discussie in Deel I is Appendix B toegevoegd:

een “User Guide” voor de workflow tool PHOTWORK, omvattende een beschrijving van de modulaire opbouw, het gebruik, en de structuur van de geïmplementeerde database.

Deel II is gewijd aan case studies van enkele veranderlijke hemelobjecten. Hoofdstuk 3 behandelt de bepaling van de diameter van Charon – de maan van Pluto – via de waarneming van een sterbedekking. Het gecombineerd licht van Pluto, Charon, en een achtergrondster verandert als Charon vóór de ster heen passeert. De observatie van een dergelijke gebeurtenis vereist snelle fotometrie gecombineerd met een accurate timing van de CCD frames. Dezelfde techniek werd ook toegepast op de pulserende ster CY Aquarii, wat leidde tot een unieke hoge-resolutie lichtkromme over bijna twee periodes (zie Hoofdstuk 6).

Hoofdstuk 4 is gewijd aan de nieuw-ontdekte δ Scuti ster GSC 08613–02122. De ster ligt in de nabijheid van de open cluster NGC 3293, en werd als veranderlijke ontdekt gedurende de fotometrische monitoring van de cluster. Een dergelijke ster kan als een klassiek geval worden beschouwd, alhoewel onze resultaten de aanwezigheid aantoonden van onregelmatige variaties in amplitude en fase, die niet kunnen toegeschreven worden aan instrumentele effecten of aan de gevolgde procedures.

Een diepgaande studie van de nauwe dubbelster GSC 04778–00152 wordt in Hoofdstuk 5 beschreven, en omvat ook spectroscopische en astrometrische waarnemingen. De ster heeft een 1 mag zwakkere visuele begeleider op 2 arcsec afstand, wat de dataverwerking erg bemoeilijkt omdat de begeleider niet zichtbaar is op de meeste CCD beelden. De parameters van het dubbelster systeem werden afgeleid uit het modeleren van de lichtkromme.

Hoofdstuk 6 behandelt de variabiliteit van de SX Phoenicis ster CY Aquarii. De ster heeft een korte pulsatieperiode (87.9 min) en een grote amplitude ($0.^m71$ in V), en de lichtkromme wordt gekenmerkt door een bijzonder steil verloop naar het maximum. In dit Hoofdstuk werden data van 2010 en 2011 gecombineerd met een grote hoeveelheid data verkregen aan 10 observatoria wereldwijd gedurende een tiental jaar. De resulterende tijdstippen van maximum licht, samen met de timings verkregen over 75 jaar, werden geanalyseerd in een $O - C$ diagram dat de lange-termijn periodevariaties van CY Aqr aantoont. Het databestand van het 2011 seizoen illustreert overduidelijk dat een zorgvuldige en systematische aanpak – zowel in de waarnemingen als in de datareductie – leidt tot de kleinste $O - C$ residu’s verkregen over de laatste tien jaar.

In Hoofdstuk 7, tenslotte, wordt de workflow toegepast op een object waarvoor de procedure oorspronkelijk werd ontwikkeld – de open cluster NGC 3293, die 11 β Cephei-type pulsators en talloze andere veranderlijken omvat. De cluster werd fotometrisch over een tijdsperiode van 10 jaar gevolgd (1997–2007), hetgeen resulteerde in een massieve database van meer dan 22 000 CCD frames. Zorgvuldige en nauwlettende datareductie en analyse leidde tot de conclusie dat echt constante sterren vrij zeldzaam zijn. Speciale aandacht werd besteed aan de lange-termijn variabiliteit van de cluster sterren behorend tot deze cluster.

Appendix A bevat een lijst met abstracts van 7 papers die een wijde verscheidenheid van hemelobjecten behandelen: van een cataclysmische ster tot de Andromeda galaxie. Al deze studies zijn gebaseerd op CCD fotometrie, met verschillende vereisten omtrent waarnemingen en datareductie.

Appendices

Appendix A

Other publications

CCD photometry of WX Ceti in quiescence and outburst

C. Sterken, N. Vogt, M. Uemura, T. Tuvikene, M. Knudsen, and H. W. Duerbeck

WX Cet (Nova Cet 1963) – a SU UMa type dwarf nova – was observed in 2001 and in 2004-2005 during superoutburst and subsequent quiescence. This paper presents the complete light curve material in digital form, and provides a number of nightly-averaged *BVR* CCD frames of the WX Ceti field for calibration purposes.

2005, The Journal of Astronomical Data, 11, 1

WX Ceti: a closer look at its behaviour in quiescence and outburst

C. Sterken, N. Vogt, M. R. Schreiber, M. Uemura, and T. Tuvikene

Context: WX Cet is a dwarf nova with rare outbursts of large amplitude.

Aims: We compile the available data of WX Cet, compare the results with other SU UMa stars, and discuss our findings in the context of current theories of superhumps and superoutbursts to progress with our understanding of SU UMa stars.

Methods: We analyse all recorded outbursts of WX Cet, based on the AAVSO archive and other published sources, and present new CCD photometry during two recent superoutbursts, including the determination of the corresponding periodicities. We perform numerical disc instability model calculations and compare its predictions with the observations.

Results: WX Cet is a SU UMa type dwarf nova with a superoutburst cycle of 880 days on average, and short eruptions every 200 days. It seems that the outburst cycle length increased by nearly a factor of 2 during the past 70 years. According to our numerical simulations, this can be explained in the context of the disc instability model by assuming enhanced mass transfer during outburst and a decreasing mean mass

transfer rate during the last decades. Using the data available, we refine the orbital period of WX Cet to 0.0582610 ± 0.0000002 days and interpret the orbital hump found in quiescence as emission from the hot spot. During two recent superoutbursts in July 2001 and December 2004 we observed superhumps, with a rather large positive period derivative of $\dot{P}_s/P_s = 1.6 \times 10^{-4}$, present only during the first 9 days of a superoutburst. Afterwards and during decline from the “plateau” phase, a constant superhump period of about 0.05922 days was observed. Late superhumps are present for at least 12 days after the decline from the “plateau”, with a period of 0.05927 days. We find this phenomenology difficult to interpret in the context of the standard explanation for superhumps, i.e. the thermal tidal instability model.

Conclusions: We interpret the long-term light curve of WX Cet as the result of a significantly decreasing mean mass transfer rate. Highlighting the complexity of the observed superhump light curves, we emphasise the importance of WX Cet for a proper understanding of the SU UMa star outburst physics and the evolution of ultra-short period cataclysmic variables.

2007, Astronomy and Astrophysics, 463, 1053

Pulsating variables in NGC 3293, the open cluster with the most β Cephei stars known

G. Handler, T. Tuvikene, D. Lorenz, S. Saesen, J. L. Provencal, R. R. Shobbrook, M. Pagani, B. Quint, M. Desmet, C. Sterken, A. Kanaan, and C. Aerts

We carried out an extensive CCD photometry campaign of the open cluster NGC 3293 that contains eleven known β Cephei stars. Preliminary results indicate that none of these is singly periodic. Several objects are among the most multiperiodic of these massive pulsators, giving us strong hope to perform precision asteroseismology in an open cluster for the first time. We also report a peculiar group of variables in NGC 3293 that is located near the low-luminosity end of the β Cephei instability strip. The variability periods of these stars are too long for classical β Cephei pulsation, but too short for binarity or rotational effects, or for SPB-type pulsation. In addition, we discovered about a dozen δ Scuti stars in the field.

2007, Communications in Asteroseismology, 150, 193

Asteroseismology in the young open cluster NGC 3293

G. Handler, T. Tuvikene, D. Lorenz, R. R. Shobbrook, S. Saesen, J. L. Provencal, M. Pagani, B. Quint, M. Desmet, C. Sterken, A. Kanaan, and C. Aerts

This is a progress report on the analysis of our extensive CCD *UBV* photometry campaign of the open cluster NGC 3293 that contains eleven known β Cephei stars. All of them are multiperiodic with up to seven independent mode periods detected so far. Another group of variables is located near the low-luminosity end of the β Cephei instability strip; it probably consists of rapidly rotating SPB stars. More

than a dozen δ Scuti stars have been confidently identified in the field so far. All are new discoveries; about half of them belong to the cluster. To date, we have also discovered five eclipsing variables in and around NGC 3293.

2008, Communications in Asteroseismology, 157, 315

On the Relative Distances of ω Centauri and 47 Tucanae

G. Bono, P. B. Stetson, N. Sanna, A. Piersimoni, L. M. Freyhammer, Y. Bouzid, R. Buonanno, A. Calamida, F. Caputo, C. E. Corsi, A. Di Cecco, M. Dall’Ora, I. Ferraro, G. Iannicola, M. Monelli, M. Nonino, L. Pulone, C. Sterken, J. Storm, T. Tuvikene, and A. R. Walker

We present precise optical and near-infrared ground-based photometry of two globular clusters (GCs): ω Cen and 47 Tuc. These photometric catalogs are unbiased in the red giant branch (RGB) region close to the tip. We provide new estimates of the RGB tip (TRGB) magnitudes— $m_I(\text{TRGB}) = 9.84 \pm 0.05$, ω Cen; $m_I(\text{TRGB}) = 9.46 \pm 0.06$, 47 Tuc—and use these to determine the relative distances of the two GCs. We find that distance ratios based on different calibrations of the TRGB, the RR Lyrae stars, and kinematic distances agree with each other within 1σ . Absolute TRGB and RR Lyrae distance moduli agree within 0.10–0.15 mag, while absolute kinematic distance moduli are 0.2–0.3 mag smaller. Absolute distances to 47 Tuc based on the zero-age horizontal branch and on the white dwarf fitting agree within 0.1 mag, but they are 0.1–0.3 mag smaller than TRGB and RR Lyrae distances.

2008, The Astrophysical Journal, 686, L87

SDSS surface photometry of M 31 with absorption corrections

E. Tempel, T. Tuvikene, A. Tamm, and P. Tenjes

Aims. The objective of this work is to obtain an extinction-corrected distribution of optical surface brightness and colour indices of the large nearby galaxy M 31 using homogeneous observational data and a model for intrinsic extinction.

Methods. We process the Sloan Digital Sky Survey (SDSS) images in $ugriz$ passbands and construct corresponding mosaic images, taking special care of subtracting the varying sky background. We apply the galactic model developed in Tempel et al. (2010, A&A, 509, A91) and far-infrared imaging to correct the photometry for intrinsic dust effects.

Results. We obtain observed and dust-corrected distributions of the surface brightness of M 31 and a map of line-of-sight extinctions inside the galaxy. Our extinction model suggests that either M 31 is intrinsically non-symmetric along the minor axis or the dust properties differ from those of the Milky Way. Assuming the latter case, we present the surface brightness distributions and integral photometry for the Sloan

filters as well as the standard *UBVRI* system. We find the following intrinsic integral colour indices for M 31: $(U - B)_0 = 0.35$; $(B - V)_0 = 0.86$; $(V - R)_0 = 0.63$; $(R - I)_0 = 0.53$; the total intrinsic absorption-corrected luminosities of M 31 in the *B* and the *V* filters are 4.10 and 3.24 mag, respectively.

2011, Astronomy and Astrophysics, 526, A155

Variability survey of massive stars in northern OB-associations: preliminary results on the Cygnus region

J. Laur, T. Tuvikene, T. Eenmäe, I. Kolka, and L. Leedjärv

We present *V*- and *I*-passband photometry of massive stars in the Cyg OB1 and Cyg OB2 associations, based on about 80 observing nights spanning 300 days in the 2011 season. The variability of 22 supergiants and 48 OB-stars with luminosity classes III–V is analysed. We report two new variable OB stars and 15 variable supergiants of which four are new discoveries. The light variations of Schulte 12 are interpreted as microvariability. We also present light curves of the red supergiants BC Cyg and BI Cyg, which exhibit brightness drop of more than 0.4 magnitudes during the season.

2012, Baltic Astronomy, accepted

Appendix B

PHOTWORK user guide

B.1 Introduction

PHOTWORK is a software package for reducing raw CCD frames in FITS format, carrying out aperture photometry, identifying stars in the images, and handling photometric data. PHOTWORK stands for ‘photometry workflow’ which means an organised and consistent data reduction process. The package is written in the Interactive Data Language (IDL) and relies on the IDL Astronomy User’s Library (Landsman 1995), hereafter IDLASTRO¹. The minimum required IDL version is determined by IDLASTRO.

The core of PHOTWORK is a database system. It allows the user to manage large amounts of data without having to read and write multiple text files. It also enables sorting and filtering of photometric data according to various parameters, like observation time, passband, air mass, seeing, etc. Differential light-curves can be easily formed by extracting only the magnitudes of the program star and comparison stars from the database.

The majority of the PHOTWORK tasks run in text mode. A graphical user interface (GUI) has been developed for frame inspection and identification of stars.

B.1.1 Installation

The PHOTWORK scripts should be included in the IDL path. A natural choice is to copy the package to the IDL library folder.

B.1.2 Getting started

Run the `photwork` procedure at the IDL command prompt. The program prints the current settings (working directory, database directory, and configuration file), the main menu, and the ‘Your choice’ prompt (Fig. B.1). The available commands are detailed in Sect. B.2.

¹<http://idlastro.gsfc.nasa.gov/>

```

-----
PHOTWORK (updated 03/10/2011)
-----
Current working directory: /data/ngc3293
Database directory:      /data/db-ngc3293
Configuration file:     /data/ngc3293/saao.cfg

Step 1: 11 - create master bias
        12 - create master dark
        13 - create master flat field
Step 2: 21 - calibrate object frames
Step 3: 31 - read frame headers
        32 - aperture photometry
Step 4: 41 - display images & identify stars
        42 - batch-identify stars
Option: 91 - change working directory
        92 - change configuration file
        93 - create empty database
        94 - output frame logbook
        0 - exit

```

Your choice:

Figure B.1: The PHOTWORK main menu.

The working directory is where PHOTWORK finds FITS files for data reduction and where output files will be written. By default, it is the same as the current working directory of the IDL session. The database directory specifies the location of database files.

Configuring of PHOTWORK is accomplished through a single configuration file. The file should be edited outside of PHOTWORK, with any text editor of choice. Users are advised to create a configuration file for each data batch that requires different parameters for the reduction, and to change the file accordingly from the main menu. See Sect. B.10 for explanations on the structure of the configuration file.

A typical run begins with selecting an appropriate configuration file (step 92). Then the necessary master calibration files are made (steps 11, 12, and 13), followed by calibrating object frames (step 21). To continue with the reduction, an existing database is required. Step 93 can be used to create an empty database. The headers of object frames are processed in step 31, after which aperture photometry can be carried out (step 32). Finally, in step 41 or 42 the extracted magnitudes are matched with real stars.

Most of the PHOTWORK routines require the selection of file names. These can be provided by typing the names in text mode (using wildcard characters where appropriate), by entering a file name that contains the listing (one filename per line), or by selecting from the file dialog. The dialog window appears when no text has been typed and the ‘Enter’ key has been hit. The supported wildcard characters are based on the IDL function `file_search`. Input files may be located outside of the

working directory and they may be specified equally with relative or absolute paths.

When PHOTWORK asks for user input interactively, the values printed on screen in square brackets are the default values, which can be accepted by hitting the ‘Return’ key.

B.2 The main menu

The `photwork` procedure provides the user with a menu from where the data reduction steps can be initiated (Fig. B.1). The tasks are invoked by entering the corresponding number at the ‘Your choice’ prompt, e.g. ‘11’ to create master bias, ‘21’ to calibrate object frames.

The main menu also allows the user to change the working directory and to select configuration files from disk. The database directory cannot be selected directly, as it has to be specified in the configuration file.

11 – create master bias

This command combines individual bias frames into a master bias frame. See Sect. B.3.2 for details.

12 – create master dark

Creates a master dark by combining individual dark frames. The details are given in Sect. B.3.3.

13 – create master flat

This task scales individual flat field frames to unity and combines them into a master flat. See Sect. B.3.4 for further details.

21 – calibrate object frames

Calibrates object frames, using master bias, master dark, and master flat. The calibrated frames are saved to disk. See Sect. B.4 for detailed explanation.

31 – read frame headers

The headers of the calibrated frames are processed, in order to extract information about the time of observation, target coordinates, filters, etc. The extracted data are stored in the database. See Sect. B.5 for details.

32 – aperture photometry

This task locates stellar sources in the calibrated frames and carries out aperture photometry. The extracted magnitudes are stored in the database and are optionally written to text files. See Sect. B.6 for options and further details.

41 – display images and identify stars

Invokes the graphical user interface which allows the user to examine frames and identify the measured stars. The available tools are explained in Sect. B.7.

42 – batch-identify stars

This option enables automatic identification of stars without any interaction with the user. It is required that the frames have been analysed with PHOTWORK before and the identification data is available in the database.

91 – change working directory

Changes the directory where PHOTWORK finds CCD frames and where output files are written.

92 – change configuration file

Allows the user to select a configuration file which corresponds to the frames being analysed.

93 – create empty database

Creates an empty database for data storage or deletes the existing data on table-by-table basis.

94 – output frame logbook

Creates a text file with the details of object frames. The information has to exist in the database.

0 – exit

Quits the program and returns to the IDL prompt.

B.3 Creating master files

B.3.1 Overscan correction

PHOTWORK allows the user to define one continuous overscan area, where the pixel values are averaged, in order to subtract the mean value from each pixel on the frame. The area can be defined with the `overscan_test` parameter in the `[Reductions]` section of the configuration file. The `use_overscan` parameter controls whether the mean overscan value is subtracted from the bias, dark, flat, and object frames.

B.3.2 Creating a master bias

This module allows the user to subtract the mean overscan value from individual bias frames and to median-average the frames into a master bias. The master frame is written to disk under the name provided by the user.

In the following sample run, 5 bias frames are corrected for overscan and combined together. The underlined text is entered by the user. Note that a wildcard character (*) is used to select files from the working directory.

```
| Your choice: 11
|
| Creating master bias
|
| Bias frame(s): a64027*
| a6402744.fits a6402745.fits a6402746.fits a6402747.fits a6402748.fits
|
| Filename for master bias: mbias.fit
|
| Reading bias frame: a6402744.fits
| Subtracting overscan: 187.78
|
```

```

| Reading bias frame: a6402745.fits
| Subtracting overscan: 187.57
|
| Reading bias frame: a6402746.fits
| Subtracting overscan: 187.94
|
| Reading bias frame: a6402747.fits
| Subtracting overscan: 187.70
|
| Reading bias frame: a6402748.fits
| Subtracting overscan: 187.45
|
| Computing median
| Master bias frame was written to mbias.fit
|
| Master bias created

```

B.3.3 Creating a master dark

This routine corrects individual dark frames for overscan, subtracts master bias and combines the frames into a master dark. The resulting frame is written to disk. The subtraction of master bias is controlled by the `use_bias` parameter in the [Reductions] section of the configuration file.

In the following example a master dark is created from 5 individual dark frames. The files are selected with a regular expression, providing a range of numbers between the '[' and ']' wildcards. Also note the relative path which is used to select the master bias frame from another directory.

```

| Your choice: 12
|
| Creating master dark
|
| Dark frame(s): a640275[0-4].fits
| a6402750.fits a6402751.fits a6402752.fits a6402753.fits a6402754.fits
|
| Warning: Be sure to use bias from which overscan has been subtracted!
|
| Master bias: ../bias/mbias.fit
| ../bias/mbias.fit
|
| Filename for master dark: mdark.fit
|
| Reading bias frame: ../bias/mbias.fit
|
| Processing: a6402750.fits
| Subtracting overscan: 187.67
| Subtracting bias frame
|
| Processing: a6402751.fits
| Subtracting overscan: 187.66
| Subtracting bias frame
|
| Processing: a6402752.fits
| Subtracting overscan: 187.37
| Subtracting bias frame

```

```

| Processing: a6402753.fits
| Subtracting overscan: 187.65
| Subtracting bias frame
|
| Processing: a6402754.fits
| Subtracting overscan: 187.85
| Subtracting bias frame
|
| Computing median
| Master dark frame was written to mdark.fit
|
| Master dark created

```

B.3.4 Creating a master flat

This data reduction step involves subtracting overscan, master bias, and master dark from individual flat frames, scaling the flats to unity, and median-averaging them into a master flat. The subtraction of bias and dark are controlled by the `use_bias` and `use_dark` parameters in the [Reductions] section of the configuration file. The master dark is scaled with the integration time if the `scale_dark` parameter is set. The `flat_test` parameter specifies the frame area which is used for calculating the median pixel value, in order to scale the frame to unity. The resulting master flat is written to disk.

In the following example, four *V*-band flats are used to create a master flat, omitting dark frame subtraction. Note the use of a wildcard character (*) to conveniently select files, even if only one file is expected, as is the case with the master bias.

```

| Your choice: 13
|
| Creating master flat field
|
| Flat field frame(s): a640278*
| a6402782.fits a6402783.fits a6402784.fits a6402785.fits
|
| Warning: Be sure to use bias frame from which overscan has been subtracted!
|
| Master bias: ../bias/mb*
| ../bias/mbias.fit
|
| Filename for master flat field: mflatV.fit
| Reading bias frame: ../bias/mbias.fit
|
| Processing: a6402782.fits
| Subtracting overscan: 200.52
| Subtracting bias frame
|
| Processing: a6402783.fits
| Subtracting overscan: 199.32
| Subtracting bias frame
|
| Processing: a6402784.fits
| Subtracting overscan: 199.24
| Subtracting bias frame

```

```

| Processing: a6402785.fits
| Subtracting overscan: 199.95
| Subtracting bias frame
|
| Computing median
| Master flat frame was written to mflatV.fit
|
| Master flat field created

```

B.4 Calibration of object frames

This routine takes care of the overscan, bias, and dark subtraction, and flat-fielding of object frames. The `use_overscan`, `use_bias`, `use_dark`, and `use_flat` parameters in the `[Reductions]` section of the configuration file individually control whether to carry out these reduction steps. See Sect. B.3.1 for details on overscan correction. The `scale_dark` parameter specifies whether the master dark is scaled with the integration time before subtracting from object frames.

The user may choose to save a subframe or the entire calibrated frame. Specifying a subframe is especially useful for trimming overscan areas. The `crop_region` configuration parameter in the `[Reductions]` section can be used to define the area that will be saved to disk. The configuration file section `[Files]` includes `filename_suffix` and `extension_reduced` parameters which control the naming of the calibrated frames.

The following sample session illustrates calibration of two object frames, including overscan, bias, and dark subtraction, dark frame scaling, and flat-fielding. The same master dark is provided in both cases, letting PHOTWORK scale the dark frame according to the actual exposure times of the frames. The calibrated frames are saved to disk under modified names, leaving the original data intact.

```

| Your choice: 21
|
| Reducing data frame(s)
|
| Data frame(s): a640287[35].fits
| a6402873.fits a6402875.fits
|
| Warning: Be sure to use bias frame from which overscan has been subtracted!
|
| Bias frame: mbias.fit
| mbias.fit
|
| Warning: Be sure to use dark frames from which overscan and/or bias
| has been subtracted!
|
| Dark frame for 16.04 sec exposure(s): mdark60.fit
| mdark60.fit
|
| Dark frame for 20.04 sec exposure(s): mdark60.fit
| mdark60.fit
|

```

```

| Flat field frame: mflatV.fit
| mflatV.fit
|
| Do you want to continue with the reduction (y/n)? [y]: y
|
| Reading bias frame: mbias.fit
| Reading dark frame(s): mdark60.fit mdark60.fit
| Reading flat frame: mflatV.fit
|
| Processing: a6402873.fits
| Subtracting overscan: 194.65
| Subtracting bias frame
| Subtracting dark frame (scale factor: 0.2671)
| Dividing by flat frame
| Reduced frame was written to a6402873f.fit
|
| Processing: a6402875.fits
| Subtracting overscan: 194.68
| Subtracting bias frame
| Subtracting dark frame (scale factor: 0.3337)
| Dividing by flat frame
| Reduced frame was written to a6402875f.fit
|
| Data frame(s) reduced
| a6402873f.fit a6402875f.fit

```

B.5 Processing of frame headers

The headers of CCD frames usually contain information about the file format, telescope, filters, camera, target, and exposure. During the calibration, PHOTWORK takes care that all the information in the headers are kept intact and saved within the calibrated FITS files.

The processing of calibrated frames begins with reading the FITS headers, extracting useful information, and storing it in the database system. The keywords in FITS headers are not standardised, and a parameter, like filter name, may be described with various keywords, depending on the software used during the observations. The user has to indicate appropriate keywords in the [FITS_header] section of the PHOTWORK configuration file. One may create several configuration files, each to reflect the settings of certain data batches.

PHOTWORK can be configured to extract the following time-related parameters from FITS headers:

1. date and time of the start or end of exposure;
2. modified Julian date (MJD) of the start or end of exposure;
3. Julian date (JD) of mid-exposure;
4. heliocentric Julian date (HJD) of mid-exposure;
5. local Julian day number (LJD);
6. integration time (exposure time).

If JD, HJD, or LJD are missing from the header, the values are calculated using either

the date and time, or the MJD, and by applying the mid-exposure and heliocentric corrections.

The headers of CCD frames may also contain the right ascension (RA) and declination (DEC) of the observed target which can be extracted by PHOTWORK and stored in the database. Alternatively, RA and DEC values may be specified in the configuration file and applied to a batch of frames.

The celestial coordinates (RA and DEC) together with the time (JD) and geographical coordinates of observation are used to calculate the true zenith angle and the corresponding air mass at mid-exposure.

The extracted and calculated quantities are then stored in the ‘frames’ table in the database, leaving the frames and their headers unmodified. It is assumed that there are no files with the same name obtained during the same night. When a frame with the same name and LJD exists in the database, then the information in the database will be overwritten.

In the following example the header of a calibrated frame is processed. The extracted information is printed on the screen in addition to storing in the database.

```
| Your choice: 31
|
| Reading frame headers
|
| Data frame(s): a6401613f.fit
| a6401613f.fit
|
| OBSERVATORY = saao
| LATITUDE    = -32.37944
| LONGITUDE   = 20.81070
| ALTITUDE    = 1798.0
| TIMEZONE    = 2.0
|
| ****
| Processing: a6401613f.fit
| ****
| LJD        = 54137
| OBSDATE   = 2007-02-05
| OBSTIME   = 22:17:26
| MJD        = 54136.92877
| MID_JD    = 54137.42881
| MID_HJD   = 54137.43020
| EXPTIME   = 7.04
| FILTER     = V
| XSIZE      = 1024
| YSIZE      = 1024
| OBJECT     = NGC3293
| RA         = 158.95419
| DEC        = -58.22420
| TELESCOPE  = SAAO 1.0m
| INSTRUMENT = STE4 CCD
| OBSERVER   = Taavi Tuvikene
| AIRMASS    = 1.180
|
| Frame headers processed
```

B.6 Aperture photometry

PHOTWORK uses star finding, sky level determination, and aperture photometry routines from IDLASTRO, namely `find`, `sky`, and `aper`. These routines are adapted from the DAOPHOT software.

The following scheme is followed for each frame:

1. FWHM of stellar profiles is determined for a frame. First, star-finding and aperture photometry routines, `find` and `aper`, are run with an approximate FWHM value, given by the user in the [FWHM] section of the PHOTWORK configuration file. The magnitudes are then sorted, and up to a maximum number (`maxnum`) of the brightest stars in the frame (with the magnitude error less than `limit_err`) are selected. For each star in the selection, a two-dimensional Gaussian function is fitted and the FWHM is taken from the fit. The fit is carried out in a box around the star; the half-width of the box can be configured with the `bsize` parameter. The median of the FWHM values is adopted for the whole frame. By specifying the `pixscale` parameter (section [CCD]), the seeing in arcsec is calculated.
2. The star detection threshold is calculated on the basis of the standard deviation of sky-background values, σ_{sky} , determined with the `sky` function. To obtain the threshold, σ_{sky} is multiplied with the parameter `sigma`, specified in the [Photometry] section of the configuration file. Alternatively, the threshold can be set directly in ADUs, using the `threshold` parameter.
3. The star-locating routine (`find`) is run, using the obtained FWHM value and the derived detection threshold. This reduction step is affected by the following configuration parameters: `badpix`, `phpadu`, and `readnoise` (section [CCD]), `fullframe`, `subframe`, `out_of_focus`, `find_rebin`, `remove_cosmic`, `sharplim`, and `roundlim` (section [Photometry]).
4. Aperture photometry is performed with the `aper` procedure. The user may specify up to 12 aperture radii, either directly in pixels, or in dimensionless units (*aperture factors*) which are multiplied by the FWHM value. The `auto_aperture` parameter (section [Photometry]) controls whether apertures will be scaled with the FWHM, or fixed apertures will be used. Dimensionless aperture factors can be set with the `aprad` parameter, and fixed apertures with the `aprad_px` parameter. Similarly, the inner and outer radius of a sky annulus can be specified (parameters `skyrad` and `skyrad_px`). The modal value of the sky-background level is determined locally for each star.

The procedure sums ADUs in concentric apertures, centred on the detected stellar images, and calculates magnitudes using the following formula:

$$m = 25 - 2.5 \log_{10} (I - I_{\text{sky}}), \quad (\text{B.1})$$

where I is the sum of ADUs for a given star and aperture size, and I_{sky} is the total count of sky values in the aperture. Note that the magnitude zero-point is

arbitrary. The corresponding magnitude error is added up from 3 components: random photon noise, the uncertainty in the mean sky value, and the scatter in sky values.

The `writedb` and `writefile` configuration parameters (section [Photometry]) control whether the results will be stored in the database and in a text file, respectively. Only the measurements where the magnitude error is less than the limiting error (the `limit_err` parameter), are saved. The stars are ordered in ascending magnitude and numbered sequentially within each frame, but there is no identification made at this stage.

When storing the results in the database, the centroids of stellar images, sky-background values, magnitudes, and magnitude errors are written to the ‘aperphot’ table, while the ‘frames’ table is updated with the FWHM and seeing values, and with the radii of apertures and sky annuli. The text files, when requested by the user, are created in the current working directory and contain the same information as is written to the database. The filename extension can be configured with the `extension_ap` parameter in the [Files] section.

The following example demonstrates how aperture photometry is carried out on a single frame. The parameters are specified in the configuration file and the user chooses not to change them interactively.

```
| Your choice: 32
|
| Doing aperture photometry
|
| Data frame(s): a6401613f.fit
| a6401613f.fit
|
| Full frame: yes
| Remove cosmic rays: no
| Threshold in sigmas: 3.0
| Out of focus: no
| Rebin image for find: no
| Pixel scale ("/px): 0.310
| Bad pixel values: -20 60000
| Photons per ADU: 2.8
| CCD readout noise (electrons): 6.5
| Sharpness limits: 0.2 1.0
| Roundness limits: -1.0 1.0
| FWHM: automatic
| Apertures: depending on FWHM
| Apertures (FWHM): 1.00 1.10 1.20 1.40 1.60 1.80 2.00 2.25 2.50 2.75 3.00
| 3.50
| Sky radii (FWHM): 5.00 7.00
| Limiting magnitude error for saving data: 0.1
| Output to database: yes
| Output to file: no
|
| Do you want to change the parameters (y/n) [n]? n
|
| Do you want to continue with aperture photometry (y/n)? [y]: y
|
| *****
```

```

| Processing: a6401613f.fit
| ****
|
| Determining FWHM
|
| Photons per ADU: 2.8
| Threshold in sigmas: 3.0
| Bad pixel values: -20 60000
| Sharpness limits: 0.2 1.0
| Roundness limits: -1.0 1.0
| Approximate FWHM (px): 8.0
| Box size (px): 32
| Fullframe: yes
| Limiting error: 0.05
|
| FWHM: 6.92
| Apertures (px): 6.9 7.6 8.3 9.7 11.1 12.5 13.8 15.6 17.3 19.0 20.8
| 24.2
| Sky radii (px): 34.6 48.4
|
| Finding stars in image
| Extracting magnitudes
| Number of bad stars: 15 (errors >= 0.10)
| Number of good stars: 247
|
| Aperture photometry completed
|
| Do you want to continue with identification (y=yes,b=batch,n=no)? [y]: n
```

B.7 Identification of stars

In this step, the estimated magnitudes are linked to the known stellar objects. Identification is carried out frame by frame, without any restrictions on field rotation, scale, or offsets. Stars can be identified either manually, or automatically on the basis of reference coordinates. In case of a sequence of frames, PHOTWORK is also able to identify stars based on a previous frame in the sequence.

PHOTWORK allows the user to set up reference fields from the stars in the database. The stars in a reference field have x and y coordinates associated with unique identification (ID) numbers. Same star may belong to several fields. In every field the same star carries the same ID number. The information about fields and stars are stored in the ‘fields’ and ‘stars’ tables in the database.

B.7.1 Graphical user interface

PHOTWORK provides the user with a graphical user interface (GUI) which can be used for frame inspection and identification of stars (Fig. B.2). The GUI can handle a sequence of an unlimited number of frames.

The left part of the GUI displays a frame and allows the user to change the brightness and contrast of the image. The right part of the GUI is dedicated to matching the stars on the frame with a reference field. The right side also features buttons for navigating through a frame sequence.

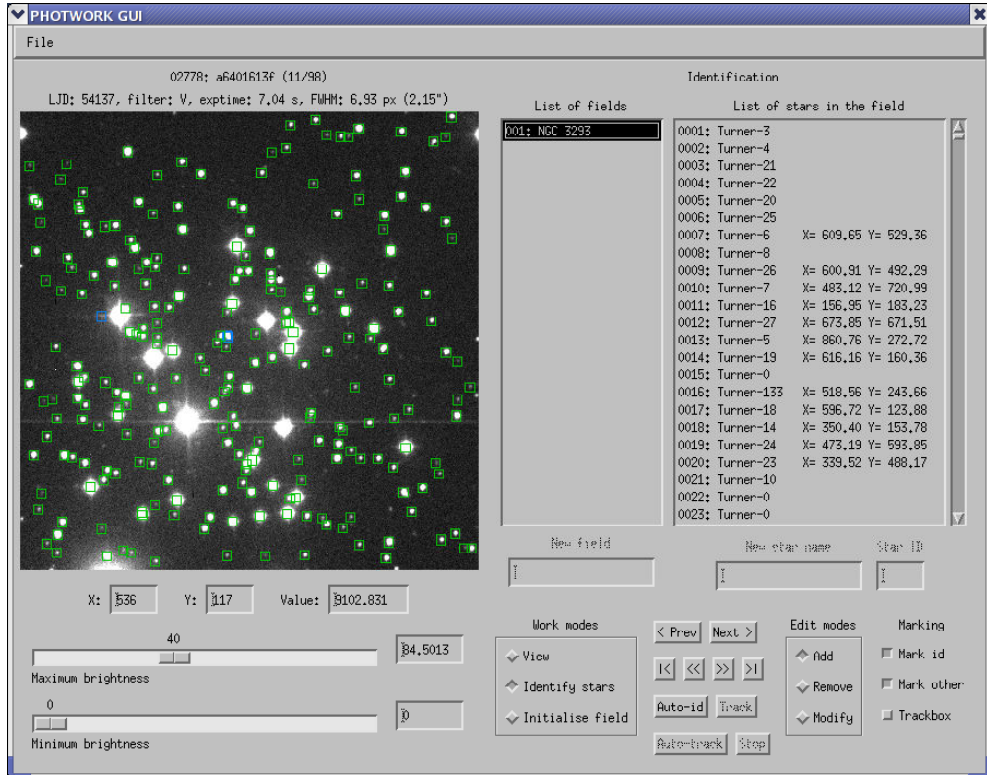


Figure B.2: Graphical user interface for inspecting CCD frames and identifying stars.

Image area

The size of the image area is 450×450 pixels. Upon loading, frames are always resized to fit the area.

Clicking in the image with the left mouse button shows the frame coordinates (x and y), and the image value in that pixel. The values are displayed in the dedicated text boxes below the image area. Holding the button down and dragging in the image updates the values on the fly.

Clicking with the right mouse button initiates zooming. Right-click and drag in the image to define a rectangle for zooming in. Right-click without dragging to zoom out for full-frame view.

Stellar images with extracted magnitudes in the database are marked with blue rectangles. Stellar images that have been identified on the frame, are marked with green rectangles. These markings can be switched on and off with the ‘Mark id’ and ‘Mark other’ check boxes in the bottom-right corner of the GUI. An identified star that has been selected in the star list, is marked with a red rectangle.

Brightness sliders

The brightness sliders determine the image values which are displayed as pure black and pure white. The values between these extremes are rendered as different shades of grey, using a linear greyscale. The sliders themselves exhibit a logarithmic scale. The image value which corresponds to the slider position, is shown to the right of the slider. It is also possible to enter the image value directly in the input box, next to the slider.

Moving the maximum brightness slider to the left, increases both brightness and contrast. Moving the minimum brightness slider to the right, decreases brightness, but increases contrast.

When navigating through a frame sequence, the brightness sliders keep their values. This helps to see changes in the sky-brightness levels.

Navigation in a frame sequence

For navigation there are dedicated buttons located in the bottom-right part of the GUI.

The ‘< Prev’ and ‘Next >’ buttons display respectively the previous and the next frame in the sequence.

The ‘<<’ button moves 10 frames backward in the sequence. Likewise, the ‘>>’ button moves 10 frames forward in the sequence. If there are less than 10 frames missing from the beginning or the end of the sequence, then the buttons move to the beginning or the end, respectively.

The ‘|<’ and ‘>|’ buttons display respectively the first and the last frame in the sequence.

Field list and star list

The GUI features two list boxes, a narrow box for the list of fields, and a wide box for the list of stars. By clicking on a field name in the field list, the corresponding star list is displayed.

The star list box shows the ID number and name for each star. For identified stars, also their x and y frame coordinates are shown. Stars may have up to 5 alternate names stored in the ‘stars’ table of the database. Which of the names is displayed in the list box, is determined with the `which_star_name` parameter in the [Show_Image] section of the configuration file.

B.7.2 Creating a reference field

A reference field can be created with the following steps:

1. Switch to the ‘Initialise field’ work mode. The ‘New field’ text box becomes active. Make sure that the ‘Add’ edit mode is selected.
2. Type a field name in the ‘New field’ text box and hit the ‘Enter’ key.

3. Click on the new field name in the field list. The ‘New star name’ and ‘Star ID’ boxes become active.
4. Type a star name in the ‘New star name’ box, or the ID number of an existing star in the ‘Star ID’ box. Then click on the stellar image on the frame with the left mouse button. The star appears in the star list.
5. Add as many fields and stars as necessary by repeating steps 2–4.
6. Finish with switching back to the ‘View’ or ‘Identify stars’ mode.

To remove a star from the reference field:

1. Switch to the ‘Initialise field’ work mode and select the ‘Add’ edit mode.
2. Click on the field name.
3. Select the ‘Remove’ edit mode.
4. Click on the star name to be removed. Confirm removing in the dialog window.

The star will be removed only from the selected reference field. The star will remain in the other fields and in the ‘stars’ table in the database.

To remove a reference field:

1. Switch to the ‘Initialise field’ work mode and select the ‘Remove’ edit mode.
2. Click on the field name to be removed. Confirm removing in the dialog window.

Alternatively, a reference field can be created and modified using the database routines in `IDLASTRO`. This is the preferred method when dealing with a large number of stars.

B.7.3 Manual identification

In order to identify stars manually:

1. Switch to the ‘Identify stars’ work mode. Make sure that the ‘Add’ edit mode is selected.
2. Click on a field name in the field list. The corresponding star list will appear.
3. Click on a star name (ID) in the star list.
4. Click on the stellar image on the frame.

The ‘aperphot’ table in the database is searched for measured stars on the frame that are located within a given radius around the click coordinates. The radius is determined with the `ident_radius` configuration parameter (section [Show_Image]). If there is only one star found in the area searched, then the star will be assigned the ID from the star list. If more than one star is found, then a warning message will be printed on the screen, and no stars will be identified.

5. Repeat steps 3–4 for each star to be identified.

If a wrong stellar image was chosen on the frame:

1. Click again on the star name (ID) in the list.
2. Click on the correct stellar image on the frame.

To remove an identification:

1. Switch to the ‘Remove’ edit mode.
2. Click on the star name (ID) in the list. Confirm removing the identification in the dialog window.
3. Switch back to the ‘Add’ edit mode.

To remove all identifications from the frame:

1. Switch to the ‘Remove’ edit mode.
2. Click on the ‘Auto-id’ button. Confirm removing the identifications in the dialog window.
3. Switch back to the ‘Add’ edit mode.

B.7.4 Automatic identification

In order to carry out automatic identification of stars, at least one star on the frame has to be manually identified. Based on the number of identified stars, the following transformations can be determined: translation (shift), scaling, reflection, and rotation (Table B.1). The coordinates of the reference stars, $(x_{\text{ref},i}, y_{\text{ref},i})$, are transformed to the frame coordinates, (x_i, y_i) , by:

$$x_i = s \times (r_x x_{\text{ref},i} \cos \theta - r_y y_{\text{ref},i} \sin \theta) + \delta_x, \quad (\text{B.2})$$

$$y_i = s \times (r_y y_{\text{ref},i} \cos \theta + r_x x_{\text{ref},i} \sin \theta) + \delta_y, \quad (\text{B.3})$$

where s is the scale factor, θ is the rotation angle, and (δ_x, δ_y) are the translation offsets. The parameters (r_x, r_y) determine whether the x and y axis are reversed (-1) or not (1).

Table B.1: Coordinate transformations on the basis of identified stars on the frame.

Identified stars	Translation	Scaling	Reflection	Rotation
1	+	—	—	—
2	+	+	+	—
3 or more	+	+	+	+

The calculated coordinates (x_i, y_i) are then used to match the reference stars with the sources on the frame. If a star is found within a certain distance from the

coordinates, then the star will be assigned the ID from the reference star list. If more than one star is found within the area, then the brightest star will be assigned the ID, and a warning message will be printed on the screen.

The search radius around the transformed coordinates is determined with the `autoindent_radius` parameter in the [Show_Image] section of the configuration file. The `auto_scale`, `auto_rotation`, and `auto_dir` parameters specify whether scaling, rotation and reflection will be determined in the coordinate transformation. The `transform_scale`, `transform_rotation`, `transform_xdir`, and `transform_ydir` parameters specify the coefficients (scale factor, rotation angle, reversing of x and y axis) that will be fixed in the transformation.

To carry out automatic identification:

1. Identify at least one star manually as described in Sect. B.7.3. Three or more identified stars are required for arbitrary coordinate transformations.
2. Make sure that the ‘Identify stars’ work mode and the ‘Add’ edit mode are selected.
3. Click on the ‘Auto-id’ button. Based on the manually identified stars, transformation between the reference field and the current frame will be determined. The transformation will be used to identify stars on the frame. At the end, the transformation coefficients will be revised on the basis of all identified stars, and the revised coefficients will be stored in the ‘ident’ table in the database.

Occasionally, PHOTWORK is unable to determine a transformation based on only a few identified stars. The solution is to manually identify a few more stars, or fix some transformation coefficients in the configuration file, before trying the automatic identification again.

Please refer to Sect. B.7.3 on how to remove identifications from the frame.

B.7.5 Tracking

Tracking allows the user to automatically identify stars on the next frame, assuming that the orientation and scale of the stellar field remains constant. Tracking works well, when a batch of frames originates from the same telescope and instrument, and when the field does not shift significantly between two consecutive frames.

The following steps are required for tracking:

1. Identify one or more stars manually (Sect. B.7.3) and run automatic identification as described in Sect. B.7.4.
2. Make sure that the ‘Identify stars’ work mode and the ‘Add’ edit mode are selected.
3. Mark the ‘Trackbox’ check box in the bottom-right corner of the GUI.
4. Click on an isolated star on the frame. The star must have its location determined and stored in the ‘aperphot’ table in the database. If there are no neighbouring stars within a tracking radius from the star, a red box will be drawn

around the star. The tracking radius is determined with the `trackbox_radius` parameter in the [Show_Image] section of the configuration file.

If the tracking box contains more than one star, an error message will be printed on the screen and tracking will fail. In this case, choose another, more isolated star, or reduce the value of the `trackbox_radius` parameter.

5. Click on the ‘Track’ button. The next frame in the sequence will be displayed. If the tracking box contains one star, then the star is assumed to be the same as in the previous frame, and translation offsets will be calculated on the basis of the coordinates on both frames. Automatic identification will be carried out by taking the transformation coefficients from the previous frame and by combining them with the calculated offsets. Once stars have been identified, all transformation coefficients will be revised and stored in the ‘ident’ table in the database.
6. To continue tracking, click again on the ‘Track’ button.

Automatic tracking can be started by clicking on the ‘Auto-track’ button instead of the ‘Track’ button. In this case the star in the tracking box will be followed continuously from one frame to the next, and automatic identification will be carried out on each frame, until the end of the sequence is reached, or until tracking fails. The continuous tracking can also be stopped by clicking on the ‘Stop’ button.

B.7.6 Batch-identification

Batch-identification of stars is a PHOTWORK procedure that is separate from the GUI and should be started from the main menu (step 42). The procedure identifies stars automatically on a batch of frames, based on coordinate transformations stored in the database. Thus, batch-identification requires that automatic identification has already been carried out on those frames, and proves to be useful when, for example, aperture photometry has been repeated with modified settings.

The following example demonstrates batch-identification on one frame:

```
| Your choice: 42
|
| Batch-identify stars
|
| Frame(s) for batch-identification: a6401613f.fit
| a6401613f.fit
|
| 1 fields available:
|   1: NGC 3293
|
| Enter field number [1]: 1
|
| Automatic identification in frame a6401613f
| Reading coordinate transformation from database
| Scale:          2.6269
| Theta (rad):    0.0273
| Theta (deg):    1.56
```

```

| X direction:      -1
| Y direction:      -1
| X offset:        1290.41
| Y offset:        1447.87
| a6401613f - Warning: found 2 stars around ( 462.42, 522.04) !
|
| Automatic identification: 242 stars
|
| Store coordinate transformation for a6401613f
|
| Batch-identification completed

```

B.8 Annotating data

Aperture photometry results can be annotated with the `flagdata` procedure that is included in the PHOTWORK package. Annotations are written in the 'annot' database table. The syntax is the following (optional keywords are in square brackets):

```

flagdata, flag [, LJD=integer/integer array]
    [, FILE_ID=integer/integer array]
    [, STAR_ID=integer] [, COMMENT=string]
    [, OLDFLAG=integer] [, FILTER=string] [, TELESCOPE=string]
    [, HJD_RANGE=[min_hjd, max_hjd]] [, HA_RANGE=[min_ha, max_ha]]
    [, MIN_AIRMASS=value] [, MAX_AIRMASS=value]
    [, MIN_FWHM=value] [, MAX_FWHM=value]
    [, MIN_SEEING=value] [, MAX_SEEING=value]
    [, EXCL_FILES=integer/integer array] [, /SILENT]

```

Procedure arguments:

flag Numerical code that characterises data. When set to 0, the existing annotations, matching the search criteria, will be deleted from the database.

Optional keywords:

LJD	A single LJD value or a vector of LJD values. Annotations will be restricted to the specified Julian day numbers.
FILE_ID	Frame ID number or a vector of ID numbers. Only the data corresponding to the specified frames will be annotated. When set, the LJD, FILTER, TELESCOPE, HJD_RANGE, HA_RANGE, MIN_AIRMASS, MAX_AIRMASS, MIN_FWHM, MAX_FWHM, MIN_SEEING, and MAX_SEEING parameters will be ignored.
STAR_ID	Star ID number. When not specified or set to 0, the entire frame will be affected. Use positive values for specific stars.
COMMENT	Textual annotation.
OLDFLAG	Previous flag code. Only data that has been annotated with the specified flag code, will be included in the selection.

FILTER	Filter name. Only data corresponding to the specified filter will be annotated.
TELESCOPE	Telescope name. Useful for annotating data from a single telescope only.
HJD_RANGE	A two-element vector of HJD values that determine the start and end of the data to be annotated.
HA_RANGE	A two-element vector of hour-angle values (in hours relative to the transit time) that determine the start and end of the data to be annotated.
MIN_AIRMASS	Minimum air-mass value.
MAX_AIRMASS	Maximum air-mass value.
MIN_FWHM	Minimum FWHM value (in px).
MAX_FWHM	Maximum FWHM value (in px).
MIN_SEEING	Minimum seeing value (in arcsec).
MAX_SEEING	Maximum seeing value (in arcsec).
EXCL_FILES	Frame ID number or a vector of ID numbers. The data points corresponding to the specified frames will be excluded from the selection.
SILENT	If set, the screen output will be suppressed.

Examples:

```
| flagdata, 5, ljd=54145, comment='Photometric night'
| flagdata, 1, file_id=[1001,1002,1010], comment='Clouds'
| flagdata, -1, file_id=3217, star_id=26, comment='Cosmic ray'
```

B.9 Constructing light curves

Light curves can be easily constructed with the `get_lightcurve` function in the PHOTWORK package. The syntax is the following:

```
result = get_lightcurve( prg_id, cmp_id, filter, aperture
    [, WEIGHTS=value/vector] [, LJD=integer/integer array]
    [, EXCL_LJD=integer/integer array]
    [, TELESCOPE=string] [, HJD_RANGE=[min_hjd, max_hjd]]
    [, MIN_AIRMASS=value] [, MAX_AIRMASS=value]
    [, MIN_FWHM=value] [, MAX_FWHM=value]
    [, MIN_SEEING=value] [, MAX_SEEING=value]
    [, MIN_EXPTIME=value] [, MAX_EXPTIME=value]
    [, MIN_XSIZE=value] [, MAX_XSIZE=value]
    [, MIN_YSIZE=value] [, MAX_YSIZE=value]
    [, INCL_FLAGS=integer/integer array]
    [, EXCL_FLAGS=integer/integer array]
    [, INCL_FILES=integer/integer array]
```

```
[, EXCL_FILES=integer/integer array]  
[, ERR_OUT=variable] [, PHOTINFO=variable] [, FRAMEINFO=variable]
```

Function arguments:

- prg_id** ID number of a program star.
- cmp_id** ID number of a comparison star, or a vector of ID numbers, when multiple comparison stars are desired. The magnitudes of comparison stars can be weighted with the **WEIGHTS** keyword. If set to 0, then **get_lightcurve** returns raw instrumental magnitudes.
- filter** Filter name.
- aperture**
 - Aperture number (1–12) or a vector of aperture numbers. If a vector is specified then **get_lightcurve** returns a 2-dimensional array that contains light curves corresponding to the given aperture numbers.

Optional keywords:

WEIGHTS	A vector of weights for comparison stars. Must be with the same length as the number of comparison stars.
LJD	A single LJD value or a vector of LJD values. The returned light curve will be restricted to the specified Julian day numbers.
EXCL_LJD	A single LJD value or a vector of LJD values. Data corresponding to the specified Julian day numbers will be excluded from the returned light curve.
TELESCOPE	Telescope name. Useful for retrieving a light curve from a single telescope only.
HJD_RANGE	A two-element vector of HJD values that determine the start and end of the returned light curve.
MIN_AIRMASS	Minimum air-mass value.
MAX_AIRMASS	Maximum air-mass value.
MIN_FWHM	Minimum FWHM value (in px).
MAX_FWHM	Maximum FWHM value (in px).
MIN_SEEING	Minimum seeing value (in arcsec).
MAX_SEEING	Maximum seeing value (in arcsec).
MIN_EXPTIME	Minimum integration time (in sec).
MAX_EXPTIME	Maximum integration time (in sec).
MIN_XSIZE	Minimum frame size in X (number of columns).
MAX_XSIZE	Maximum frame size in X (number of columns).
MIN_YSIZE	Minimum frame size in Y (number of rows).
MAX_YSIZE	Maximum frame size in Y (number of rows).
INCL_FLAGS	Flag code or a vector of codes. Only the data points annotated with the specified flags will be included in the returned light curve.

EXCL_FLAGS	Flag code or a vector of codes. The data points annotated with the specified flags will be excluded from the returned light curve.
INCL_FILES	Frame ID number or a vector of ID numbers. Only the data points corresponding to the specified frames will be included in the returned light curve.
EXCL_FILES	Frame ID number or a vector of ID numbers. The data points corresponding to the specified frames will be excluded from the returned light curve.
ERR_OUT	A named variable that will receive the magnitude errors. The array dimensions will be the same as that of the function return value.
PHOTINFO	A named variable that will receive the photometry information structure. The structure contains the following tags: .X – X coordinate of stellar centroid, .Y – Y coordinate of stellar centroid, .SKY – sky-background value, .SKYSIG – error in sky-background value, .X_CMP – X coordinates of comparison stars (array), .Y_CMP – Y coordinates of comparison stars (array), .SKY_CMP – sky-background value for comparison stars (array), .SKYSIG_CMP – error in sky-background value for comparison stars (array).
FRAMEINFO	A named variable that will receive the frame information structure. The structure contains the following tags: .FILE_ID – frame ID number, .FILENAME – frame name (filename), .HJD – HJD of mid-exposure, .JD – JD of mid-exposure, .LJD – LJD number, .OBSDATE – date of observation, .OBSTIME – time of observation, .EXPTIME – integration time, .FILTER – filter name, .XSIZE – frame size in X (number of columns), .YSIZE – frame size in Y (number of rows), .FWHM – FWHM value (in px), .SEEING – seeing value (in arcsec), .AIRMASS – air mass at mid-exposure, .OBSERVER – observer's name.

In the following example, the *V*-band light curve of star #13 is constructed, using three comparison stars (#26, #33, #34) with weights (2, 1, 1). Aperture number 7 is used, and only the data from a single night (LJD 53812) are selected. The magnitudes are returned in the IDL variable `mags` and the frame information structure in the variable `fr`.

```
| mags = get_lightcurve(13, [26,33,34], 'V', 7, weights=[2,1,1], $  
| ljd=53812, frameinfo=fr)
```

The retrieved data is ready to be used in IDL. For example, the light curve can be immediately plotted on the screen:

```
| plot, fr.hjd, mags
```

B.10 Configuration files

PHOTWORK recognises configuration files with **.cfg**, **.conf**, and **.ini** extensions. The basic element of a configuration file is a parameter which has a name and a value, delimited by an equals sign (=). Parameters are grouped into sections. Sections begin with a section name on a line by itself, enclosed in square brackets ([and]). Sections end with a declaration of a new section, or with the end of the file. Section names and parameters are case-insensitive. Comments are allowed only on separate lines and must start with a number sign (#).

Sections and parameters

[Files]

This section holds parameters which describe the database location and file naming, and are used throughout PHOTWORK.

zdbase	Specifies the database directory.
fits_filter	Filter for selecting FITS files from disk. Default: *.fit;*.fts;*.fits
remove_extension	If set to 1, extensions will be removed from FITS filenames when storing data in the database. Default: 0
filename_suffix	Filename suffix which will be added to original filenames when saving calibrated data frames. Default: f
extension_reduced	Filename extension for calibrated data frames. If not set, then the original extension will be retained. Example: .fit
extension_ap	Filename extension for aperture photometry data. Default: .ap
extension_list	Filename extension for filename listings. Default: .list

[Time]

Time parameters are used in step 31, and occasionally in steps 32, 41, and 42.

reduced_jd	If set to 1, Julian dates will be converted to reduced Julian dates, i.e. 2 400 000 will be subtracted. Default: 0
-------------------	--

[Reduction]

The following parameters control the master file creation steps 11, 12, 13, and the object frame calibration step 21.

<code>use_overscan</code>	Controls whether to subtract mean overscan from bias, dark, flat, and object frames (yes = 1, no = 0). Default: 0
<code>overscan_test</code>	Coordinates (x_1, y_1, x_2, y_2) of the overscan area which will be used for the mean overscan value determination. Coordinates start from 0,0. Example: 1024,0,1039,1023
<code>use_bias</code>	Controls whether to subtract master bias from dark, flat, and object frames (yes = 1, no = 0). Default: 1
<code>use_dark</code>	Controls whether to subtract master dark from flat and object frames (yes = 1, no = 0). Default: 0
<code>scale_dark</code>	Controls whether to scale master dark with the integration time before subtracting from flat and object frames (yes = 1, no = 0). Default: 0
<code>use_flat</code>	Controls whether to divide object frames by master flat (yes = 1, no = 0). Default: 1
<code>flat_test</code>	Coordinates (x_1, y_1, x_2, y_2) of the frame area which will be used for scaling a master flat field to unity. Coordinates start from 0,0. If not set, then full frame is used for the calculation. Example: 200,200,399,399
<code>crop_region</code>	Coordinates (x_1, y_1, x_2, y_2) of the frame area that will be saved to file after calibrating object frames. Useful for throwing away overscan areas. Coordinates start from 0,0. If not set, then full frames will be saved. Example: 10,0,1033,1023

[Photometry]

This section lists parameters that affect aperture photometry (step 32).

<code>fullframe</code>	Controls whether photometry will be carried out in the full frame (1) or in a subframe (0). Default: 1
<code>subframe</code>	Coordinates of the subframe in which photometry will be carried out. Only effective when <code>fullframe</code> =0. Coordinates start from 0,0. Example: 100,100,899,899
<code>threshold</code>	Star detection threshold in ADUs above the sky level. If not set, or equals to 0, then <code>sigma</code> will be used instead. Default: 0.0
<code>sigma</code>	Star detection threshold in sigmas above the sky level. If <code>threshold</code> is set and non-zero then <code>sigma</code> will not be used. Default: 3.0
<code>out_of_focus</code>	When set to 1, stars are assumed to be severely out of focus (donut-shaped) and smoothing is applied before locating the

	sources. This prevents multiple peaks from being registered. The parameter affects only star finding and image centring, as aperture photometry is carried out on unmanipulated frames. Default: 0
<code>find_rebin</code>	When set to 1, frames are rebinned 2x2 before locating stars. Useful when the FWHM is larger than about 10 px. The parameter affects only star finding and image centring, as aperture photometry is carried out on unmanipulated frames. Default: 0
<code>remove_cosmic</code>	When set to 1, frames are cleaned from cosmic rays before locating the stars. The parameter affects star finding as well as aperture photometry routines. Default: 0
<code>sharplim</code>	Low and high cutoff for the sharpness statistic. Needed for the IDLPHOT <code>find</code> procedure. Default: 0.2,1.0
<code>roundlim</code>	Low and high cutoff for the roundness statistic. Needed for the IDLPHOT <code>find</code> procedure. Default: -1.0,1.0
<code>fwhm</code>	FWHM (in pixels) of stellar images. If not set, then PHOTWORK determines FWHM automatically.
<code>auto_aperture</code>	When set to 1, aperture radii will be scaled with FWHM. Use <code>aprad</code> and <code>skyrad</code> to set the aperture factors. When set to 0, aperture radii will be fixed, and <code>aprad_px</code> together with <code>skyrad_px</code> will be used. Default: 1
<code>aprad</code>	Up to 12 aperture factors which will be multiplied by the FWHM value to get aperture radii. Used when <code>auto_aperture=1</code> . Default: 1.0, 1.2, 1.4, 1.6, 1.8, 2.0, 2.2, 2.4, 2.6, 2.8, 3.0, 3.2
<code>skyrad</code>	Aperture factors which will be multiplied by the FWHM value to get the radii of the inner and outer sky annulus. Used when <code>auto_aperture=1</code> . Default: 5.0, 7.0
<code>aprad_px</code>	Aperture radii in terms of pixels. Used when <code>auto_aperture=0</code> .
<code>skyrad_px</code>	The radii of the inner and outer sky annulus in pixels. Used when <code>auto_aperture=0</code> .
<code>limit_err</code>	Limiting error for saving magnitudes. Magnitudes which have larger error than this value will not be saved. Default: 1.0
<code>writedb</code>	If set to 1, the aperture photometry results will be written to the database. Default: 1
<code>writefile</code>	If set to 1, the aperture photometry results will be written to a text file (filename extension specified with the <code>extension_ap</code> parameter in the [Files] section). Default: 0

[FWHM]

The following parameters are used by the FWHM-determination script (step 32). These parameters are ignored when the `fwlm` parameter in the [Photometry] section is defined and non-zero.

<code>approx_fwhm</code>	Approximate FWHM in pixels. Default: 6.0
<code>maxnum</code>	Maximum number of stars in magnitude order to include in FWHM calculation. Default: 25
<code>bsize</code>	Box half-width around a star in terms of approximate FWHM (<code>approx_fwhm</code>) in which Gaussian fit will be carried out. Box width is twice this value. Default: 4.0
<code>limit_err</code>	Limits error. Stars which have larger error will not be taken into account in the FWHM determination. Default: 0.05

[Show_Image]

The parameters in this section control the behaviour of the GUI (step 41).

<code>markbox_radius</code>	Defines the box half-width in pixels which is drawn around the detected stars in the graphical user interface. Box width is twice this value. Default: 6.0
<code>ident_radius</code>	Defines the box half-width in pixels in which a star is found when clicked on the image. Default: 4.0
<code>autoindent_radius</code>	Defines the box half-width in pixels in which a star is found during automatic identification. Default: 2.0
<code>track_radius</code>	Defines the box half-width in pixels which is used in the tracking mode. When only one star appears in the box, then it is assumed to be the same star as in the previous frame. Default: 20.0
<code>which_star_name</code>	Controls which of the 5 possible star names from the database is shown in the star list. Default: 1
<code>auto_scale</code>	If set to 1, then the scale factor between the current frame and the reference field will be determined. Affects automatic identification of stars. Default: 1
<code>auto_rotation</code>	If set to 1, then the rotation angle between the current frame and the reference field will be determined. Affects automatic identification of stars. Default: 1
<code>auto_dir</code>	If set to 1, then the coordinate transformation between the current frame and the reference field will include reflections. Affects automatic identification of stars. Default: 1
<code>transform_scale</code>	Scale factor between the current frame and the reference field.

transform_rotation	Rotation angle (in degrees) between the current frame and the reference field.
transform_xdir	Determines the direction of x-axis in coordinate transformation between the current frame and the reference field. If set to -1, then the x-axis will be reversed. Allowed values: -1, 1
transform_ydir	Determines the direction of y-axis in coordinate transformation between the current frame and the reference field. If set to -1, then the y-axis will be reversed. Allowed values: -1, 1

[Observatory]

The following parameters describe the observatory site where the observations were carried out. Used in step 31, and occasionally in steps 32, 41, and 42.

observatory	Observatory name as described in the <code>observatory</code> script in IDLASTRO. Example: <code>sao</code>
latitude	Geographical latitude of the observatory site, in degrees. If <code>observatory</code> parameter is missing, then <code>latitude</code> is required.
longitude	Geographical longitude of the observatory site, in degrees east. West longitudes should be given with a minus sign. If <code>observatory</code> parameter is missing, then <code>longitude</code> is required.
altitude	Altitude of the observatory site in meters above sea level. Default: 0.0
timezone	Observatory timezone in hours east of Greenwich. For example, use 2 for UTC+2 and -4 for UTC-4. If <code>observatory</code> parameter is missing, then <code>timezone</code> is required.

[CCD]

The following parameters describe the CCD camera. Necessary for aperture photometry (step 32).

badpix	Minimum and maximum value of a good pixel. If both values are the same, then it is assumed that there are no bad pixels. The parameter is passed on to the IDLPHOT <code>aper</code> script. Default: -32765,32767
phpadu	Photons per analog-to-digital unit (ADU). Also known as the gain factor. The parameter is passed on to the IDLPHOT <code>aper</code> script. Default: 1.0
readnoise	CCD readout noise in electrons. The parameter is passed on to the IDLPHOT <code>aper</code> and <code>sky</code> scripts. Default: 0.0
pixscale	Pixel scale (arcsec px^{-1}). If not specified or equals to 0, then the seeing (in arcsec) will not be calculated. Default: 0.0

[FITS_header]

The parameters in this section describe the keywords in FITS headers. Mostly used in step 31, but occasionally throughout PHOTWORK.

obsdate_header	Keyword that holds the observation date. Example: DATE-OBS
obsdate_header_comment	If set to 1, the observation date will be read from the comment part of the header line. Default: 0
obsdate_pos	The starting and ending positions of the substring that contains the observation date. The first character position is 1. Example: 5,14
obsdate_pattern	The format of the observation date. Allowed values: YYYY-MM-DD, YYYY/MM/DD, YY/MM/DD, DD/MM/YY, DD/MM/YYYY, and DD-MM-YYYY.
obsdate_value	The observation date. Overrides the dates in FITS headers.
obstime_header	Keyword that holds the observation time (hour, minute, and second). Example: TIME-OBS
obstime_header_comment	If set to 1, the observation time will be read from the comment part of the header line. Default: 0
obstime_pos	The starting and ending positions of the substring that contains the observation time. The first character position is 1. Example: 5,14
obstime_local	Specifies whether the observation time is local (1) or UT (0).
obstime_timezone	The timezone of the observation time in the FITS header, in hours east of Greenwich. Specify even when obstime_local =0 (required for LJD calculation).
obstime_mode	Specifies whether the time in the FITS header corresponds to the start or end of exposure. Allowed values: start , end
datetime_header	Keyword that holds both the date and the time of observation. The value must be in standard ASCII format: DOW MON DD HH:MM:SS YYYY, where DOW is the day of the week, MON is the month, DD is the day of month, HH:MM:SS is the time, and YYYY is the year.
datetime_local	Like obstime_local , but for the date/time field.
datetime_timezone	Like obstime_timezone , but for the date/time field.
datetime_mode	Like obstime_mode , but for the date/time field.
mjd_header	Keyword that holds the modified Julian date (MJD). Exam-

	ple: MJD-OBS
mjd_mode	Like obstime_mode , but for the MJD field.
mid_jd_header	Keyword that holds the Julian date (JD) of the mid-exposure.
mid_hjd_header	Keyword that holds the heliocentric Julian date (HJD) of the mid-exposure.
ljd_header	Keyword that holds the local Julian day number (LJD).
ljd_value	The LJD value. Overrides the LJD in FITS headers, and LJD calculations.
exptime_header	Keyword that holds the exposure time (integration time). Example: EXPTIME
filter_header	Keyword that holds the name of the filter used.
filter_pos	Like obstime_pos , but for the filter name.
filter_value	Filter name. Overrides the values in FITS headers.
object_header	Keyword that holds the object name. Example: OBJECT
object_pos	Like obstime_pos , but for the object name.
object_value	Object name. Overrides the values in FITS headers. Example: NGC 3293
ra_header	Keyword that holds the right ascension (RA) value.
ra_mode	Specifies whether RA is given in decimal degrees, decimal hours, or sexagesimal hours (HH:MM:SS.SS or HH MM SS.SS). Allowed values: deg , hour , hms
ra_value	RA value. Overrides RA values in FITS headers. Example: 158.9542
dec_header	Keyword that holds the declination value.
dec_mode	Specifies whether declination is given in decimal degrees or sexagesimal degrees (DD:MM:SS.SS or DD MM SS.SS). Allowed values: deg , dms
dec_value	Declination value. Overrides the values in FITS headers. Example: -58.2242
telescope_header	Keyword that holds the telescope name and/or characteristics. Example: TELESCOP
telescope_value	Telescope name. Overrides the values in FITS headers. Example: OCA 41cm
instrument_header	Keyword that holds the instrument name and/or characteristics. Example: INSTRUME
instrument_value	Instrument name. Overrides the values in FITS headers. Ex-

	ample: SBIG STL-6303E
observer_header	Keyword that holds the observer name. Example: OBSERVER
observer_value	Observer name. Overrides the values in FITS headers.

B.11 Database structure

The PHOTWORK database consists of 6 tables: ‘aperphot’, ‘frames’, ‘stars’, ‘fields’, ‘ident’, and ‘annot’. The data in the tables are linked with the use of unique identification numbers (ID) for frames, stars, and reference fields.

The ‘aperphot’ table stores aperture photometry results. Each row corresponds to a detected star on a frame and holds centroid coordinates and extracted magnitudes. The structure of the table is given in Table B.2. The ‘aperphot’ table is linked to the ‘frames’ table through the FILE_ID item, and to the ‘stars’ table through STAR_ID.

Table B.2: Structure of the ‘aperphot’ table.

Item	Type	Description
FILE_ID	long integer	Frame ID number
STAR_NO	integer	Star number on the frame
STAR_ID	integer	Star ID number
X	real	X coordinate of stellar centroid
Y	real	Y coordinate of stellar centroid
SKY	real	Sky-background value
SKYSIG	real	Error in sky-background value
MAG_1	real	Magnitude in aperture 1
ERR_1	real	Magnitude error in aperture 1
MAG_2	real	Magnitude in aperture 2
ERR_2	real	Magnitude error in aperture 2
:	:	:
MAG_12	real	Magnitude in aperture 12
ERR_12	real	Magnitude error in aperture 12

The ‘frames’ table contains information about frames. Each row corresponds to a frame that has its header processed. The table structure is given in Table B.3.

Table B.3: Structure of the ‘frames’ table.

Item	Type	Description
FILE_ID	long integer	Frame ID number
FILENAME	string (80)	Frame name (filename)
LJD	long integer	Local Julian day number
OBSDATE	string (10)	Date of observation (yyyy-mm-dd)
OBSTIME	string (12)	Time of observation (hh:mm:ss.sss)

Table B.3 – continued.

Item	Type	Description
MJD	double	Modified Julian date of observation
MID_JD	double	Julian date of mid-exposure
MID_HJD	double	Heliocentric Julian date of mid-exposure
EXPTIME	real	Integration time
FILTER	string (8)	Filter
XSIZE	integer	Frame size in X (number of columns)
YSIZE	integer	Frame size in Y (number of rows)
OBJECT	string (20)	Object name
RA_FRAME	real	Right ascension of the pointing
DEC_FRAME	real	Declination of the pointing
TELESCOPE	string (80)	Name of the telescope
INSTRUMENT	string (80)	Name of the instrument
OBSERVER	string (80)	Name of the observer
LAT	real	Latitude of the observatory
LON	real	Longitude of the observatory
ALT	real	Altitude of the observatory
TZ	real	Timezone of the observatory
AIRMASS	real	Air mass at mid-exposure
FWHM	real	FWHM of stellar images (in px)
SEEING	real	Seeing (in arcsec)
AP_1	real	Radius of aperture 1 (in px)
AP_2	real	Radius of aperture 2 (in px)
:	:	:
AP_12	real	Radius of aperture 12 (in px)
IS	real	Radius of inner sky annulus (in px)
OS	real	Radius of outer sky annulus (in px)

The ‘stars’ table contains information about the stars that have been entered by the user. The table structure is given in Table B.4.

Table B.4: Structure of the ‘stars’ table.

Item	Type	Description
STAR_ID	integer	Star ID number
STAR_NAME1	string (20)	Star name 1
STAR_NAME2	string (20)	Star name 2
STAR_NAME3	string (20)	Star name 3
STAR_NAME4	string (20)	Star name 4
STAR_NAME5	string (20)	Star name 5
RA_2000	string (12)	Right ascension (J2000)
DEC_2000	string (12)	Declination (J2000)
RA	real	Right ascension (J2000, degrees), for search
DEC	real	Declination (J2000, degrees), for search

Reference fields are stored in the ‘fields’ table. Table rows correspond to stars in reference fields. The table structure is presented in Table B.5. Same star may appear in multiple fields. An empty field is defined with a row where the **STAR_ID** item is zero. The ‘fields’ table is linked with the ‘stars’ table through **STAR_ID**.

Table B.5: Structure of the ‘fields’ table.

Item	Type	Description
FIELD_ID	integer	Reference field ID number
FIELD_NAME	string (20)	Reference field name
STAR_ID	integer	Star ID number
X	real	X coordinate of the star
Y	real	Y coordinate of the star
ORDER	integer	Sequence number in the field

The ‘ident’ table contains information about coordinate transformations between reference fields and object frames. Each row corresponds to a frame, where stars have been automatically identified, using a certain reference field. Thus, a frame may have multiple transformations stored, one per reference field. The table structure is given in Table B.6. The ‘ident’ table is linked with the ‘frames’ table through the **FILE_ID** item, and to the ‘fields’ table through **FIELD_ID**.

Table B.6: Structure of the ‘ident’ table.

Item	Type	Description
FILE_ID	long integer	Frame ID number
FIELD_ID	integer	Reference field ID number
SCALE	real	Scale factor
THETA	real	Rotation angle
XDIR	integer	Reversing of X axis
YDIR	integer	Reversing of Y axis
XDELTA	real	Translation offset in X
YDELTA	real	Translation offset in Y

The structure of table ‘annot’ is shown in Table B.7. Annotations, stored one per row, either apply to a single magnitude or a whole frame. Annotations that apply to frames, have the **STAR_ID** item set to zero. The ‘annot’ table is linked to the ‘frames’ table through the **FILE_ID** item, and to the ‘stars’ table through **STAR_ID**.

Table B.7: Structure of the ‘annot’ table.

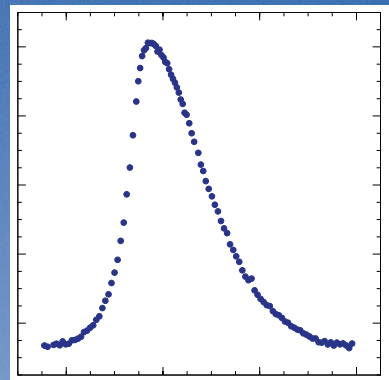
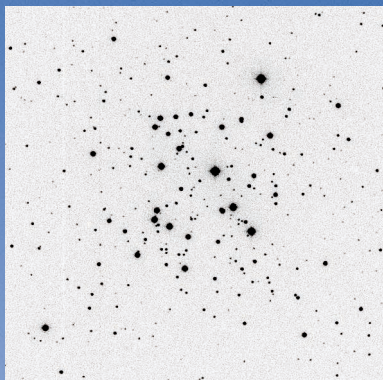
Item	Type	Description
FILE_ID	long integer	Frame ID number
STAR_ID	integer	Star ID number
FLAG	integer	Flag code
COMMENT	string (80)	Comment

B.12 Acknowledgements

The development of PHOTWORK was started at the Tartu Observatory in 2002. Initially the program was dedicated only for reducing CCD frames from the local 60-cm telescope. The GUI was developed by Anti Hirv on the basis of the XIMAGE program, written by David Fanning and originally available from the Coyote Library². Tõnis Eenmäe and Indrek Kolka are acknowledged for their help and constructive comments.

Since 2004 PHOTWORK has been extensively upgraded at Vrije Universiteit Brussel. The second generation of PHOTWORK allows for reducing CCD data from various observatory sites. The program has been developed into a general photometry workflow tool.

²<http://www.idlcoyote.com/documents/programs.php>



ISBN 978-9949-30-595-7